DTT
S.c. a r.l.

Divertor Tokamak Test facility
Research Plan

1st edition

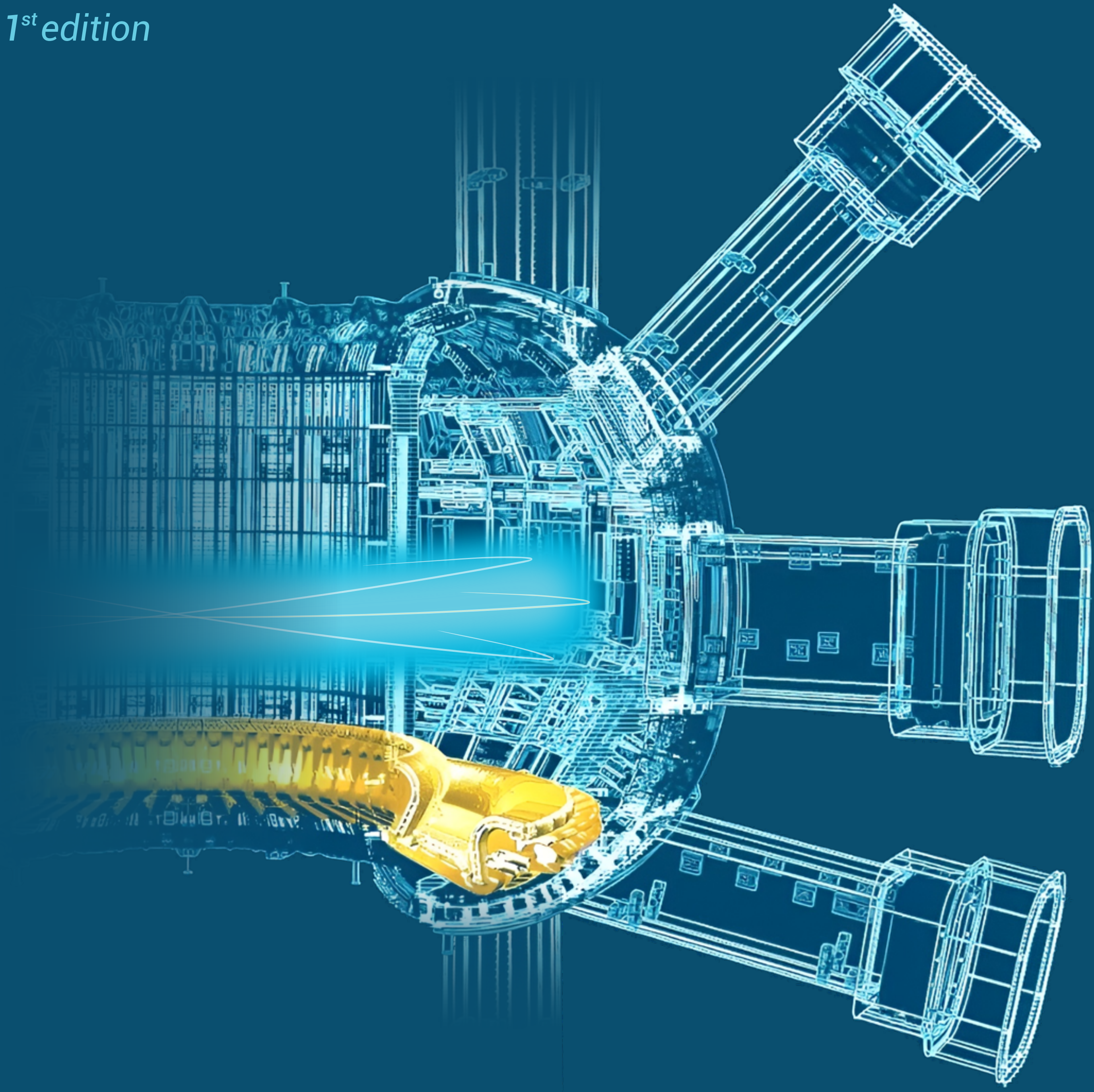

A milestone along the roadmap
to the realization of fusion energy

DTT

DIVERTOR TOKAMAK TEST facility

Research Plan

Version 1.0 - May 2024

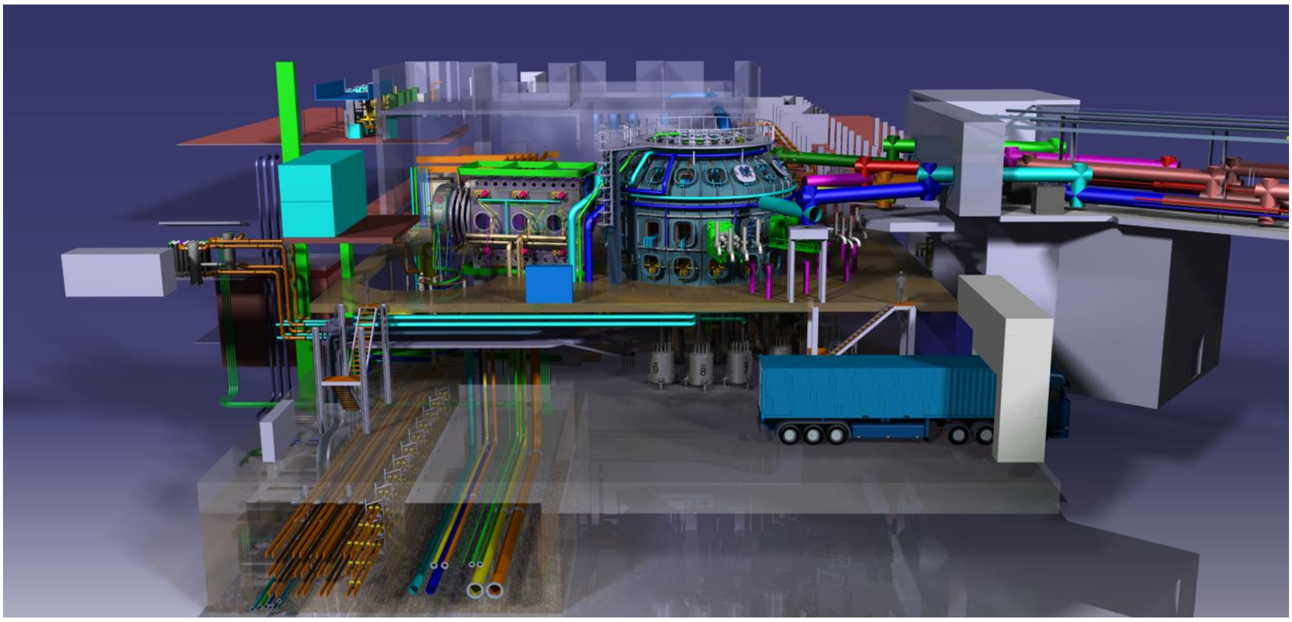

ENEA
Agenzia nazionale per le nuove tecnologie, l'energia e lo sviluppo economico sostenibile

CETMA

Consiglio Nazionale delle Ricerche

Create

CONSORZIO RFX
Ricerca Formazione Innovazione

eni

INFN
Istituto Nazionale di Fisica Nucleare

Politecnico di Torino

Università degli Studi di Milano Bicocca

Università di Roma Tor Vergata

Università degli Studi della Tuscia

DTT
Divertor Tokamak Test facility – Research Plan

Edited by F. Crisanti, G. Giruzzi and P. Martin

ISBN: 978-88-8286-474-3 (digital version)
978-88-8286-475-0 (printed version)

Cover designed by G. Di Gironimo and V. Golia

Printed in May 2024 at ENEA Frascati Research Center,
Via Enrico Fermi 45, 00044 Frascati (Roma), Italy

DTT Research Plan

Coordinators

F. Crisanti *(DTT S.C.a.r.l. & University of Tuscia, Italy)*

G. Giruzzi *(CEA, IRFM, France)*

P. Martin *(DTT S.C.a.r.l., Consorzio RFX & University of Padova, Italy)*

Leading Authors

Chapter 1: DTT power exhaust strategy	F. Crisanti G. Giruzzi P. Martin	*DTT S.C.a.r.l. & University of Tuscia, Italy* *CEA, IRFM, France* *DTT S.C.a.r.l., RFX & University of Padova, Italy*
Chapter 2: Plasma scenarios	P. Mantica C. Angioni	*CNR – ISTP, Italy* *Max Planck IPP, Germany*
Chapter 3: Divertor and SOL physics, plasma-wall interactions	P. Innocente E. Tsitrone M. Wischmeier	*Consorzio RFX, Italy* *CEA, IRFM, France* *Max Planck IPP, Germany*
Chapter 4: Transport physics and integrated modelling	C. Angioni P. Mantica	*Max Planck IPP, Germany* *CNR – ISTP, Italy*
Chapter 5: MHD, disruptions and control	E. Nardon G. Vlad M. Falessi	*CEA, IRFM, France* *ENEA, Italy* *ENEA, Italy*
Chapter 6: Physics of heating, current drive and fuelling	C. Sozzi D. Van Eester P. Vincenzi D. Terranova	*CNR – ISTP, Italy* *LPP-ERM/KMS, Belgium* *Consorzio RFX, Italy* *Consorzio RFX, Italy*
Chapter 7: Energetic particle physics	G. Vlad M. Falessi E. Nardon	*ENEA, Italy* *ENEA, Italy* *CEA, IRFM, France*
Chapter 8: Theory and simulation	M. Falessi G. Vlad E. Nardon	*ENEA, Italy* *ENEA, Italy* *CEA, IRFM, France*
Chapter 9: Fusion technology developments	S. Brezinsek C. Day G. Dose	*FZJ, Germany* *KIT, Germany* *ENEA, Italy*

Contributors

ENEA, Italy
L. Boncagni
A. Cardinali[6]
N. Carlevaro[3]
A. Castaldo[2]
C. Castaldo[6]
S. Ceccuzzi[6]
M. Ciotti[1]
D. Fiorucci
M. Iafrati[9]
C. Piron
G. Ramogida[5]
F. Zonca[1,5,7,8]

CNR/ISTP, Italy
E. Alessi[5]
B. Baiocchi[5,6]
N. Bonanomi[2]
I. Casiraghi[2,4,5]
A. Dal Molin[7]
L. Figini[6]
F. Ghezzi
P. Mantica[6]
A. Mariani[2]
S. Nowak[5]
D. Ricci
G. Rubino[2]
E. Vassallo

Università di Milano Bicocca, Italy
L. Aucone[6]
M. Cavedon[2,3]
M. Nocente[5,7,8]

Politecnico di Torino, Italy
R. Bonifetto[9]
G. Nallo[3]
F. Porcelli[5,7]
F. Subba[3]

Consorzio RFX, Italy
F. Auriemma[2]
P. Agostinetti
T. Bolzonella[1]
D. Bonfiglio[5]
M. Dalla Palma[9]
C. De Piccoli[6,8]
M. Gobbin[5,7,8]
P. Innocente[6]
A. Murari
S. Peruzzo[9]
L. Pigatto[5]
L. Piron[5]
G. Spizzo[7,8]
F. Veronese
N. Vianello[3,5]
P. Vincenzi[8]
M. Zuin[7,8]

CEA, IRFM, France
J.F. Artaud
H. Bufferand[3]
G. Ciraolo[3]
Y. Corre[3]
R. Dumont
G. Falchetto[8]
M. Firdaouss[9]
A. Gallo[3]
J. Garcia[1]
J. Hillairet[6]
E. Joffrin[1]
X. Litaudon[1]
P. Maget[5]
M. Missirlian[9]
J. Morales
M. Richou[9]
R. Sabot[1]

Aix-Marseille University, CNRS, France
J. Gaspar[3]

Consorzio CREATE, Italy
R. Albanese
R. Ambrosino[5]

Università della Tuscia, Italy
L. Balbinot

Max-Planck IPP, Germany
C. Hopf[6]
P. Lauber[8]
R. Neu[3]

KIT, Germany
T. Giegerich[9]
S. Varoutis

FZJ, Germany
S. Brezinsek[3]
J.W. Coenen[3,9]
M. Wirtz[3,9]

DIFFER, The Netherlands
S. Wiesen[3]

NCSRD, Greece
Y. Kominis[5,7,8]
C. Tsironis[6]

EPFL, Switzerland
C. Theiler[3]
D. Testa[5,7]

KTH, Sweden
L. Frassinetti[5]

Technical University of Denmark
M. Salewski[8]

ITER organisation
G. Brochard[8]

UKAEA, UK
P. Jacquet[6]
D. King[6]

[1] Co-author of Chapter 1
[2] Co-author of Chapter 2
[3] Co-author of Chapter 3
[4] Co-author of Chapter 4
[5] Co-author of Chapter 5
[6] Co-author of Chapter 6
[7] Co-author of Chapter 7
[8] Co-author of Chapter 8
[9] Co-author of Chapter 9

DTT community

D. Abate, E. Acampora, D. Agguiaro, R. Agnello, P.Agostinetti, M. Agostini, A. Aimetta, R. Albanese, G. Alberti, M. Albino, E. Alessi, S. Almaviva, M. Alonzo, R. Ambrosino, P. Andreoli, M. Angelone, M. Angelucci, C. Angioni, A. Angrisani Armenio, P. Antonini, D. Aprile, G. Apruzzese, M. Aquilini, G. Aragone, P. Arena, M. Ariola, G. Artaserse, L. Aucone, A. Augieri, F. Auriemma, J. Ayllon Guerola, N. Badodi, B. Baiocchi, L. Balbinot, C. Baldacchini, A. Balestri, T. Barberis, G. Barone, L. Barucca, M. Baruzzo, S. Begozzi, V. Belardi, F. Belli, A. Belpane, F. Beone, S. Bertolami, S. Bianucci, S. Bifaretti, S. Bigioni, W. Bin, P. Boccali, B. Boeswirth, E. Bogazzi, R. Bojoi, S. Bollanti, T. Bolzonella, F. Bombarda, M. Bonan, N. Bonanomi, A. Bonaventura, L. Boncagni, M. Bonesso, D. Bonfiglio, R. Bonifetto,D. Bonomi, D. Borgogno, T. Borzone, S. Botti, E. Boz, F. Braghin, M. Brena, S. Brezinsek, M. Brombin, A. Bruschi, S. Buonocore, P. Buratti, P. Buratti, D. Busi, G. Calabrò, M. Caldora, G. Camera, G. Campana, S. Candela, V. Candela, F. Cani, L. Cantone, F. Capaldo, S. Cappello, M. Caponero, S. Carchella, A. Cardinali, D. Carnevale, L. Carraro, C. Carrelli, V. Casalegno, I. Casiraghi, C. Castaldo, A. Castaldo, G. Castro, A. Carpignano, F. Causa, R. Cavazzana, M. Cavedon, M. Cavenago, M. Cecchini, S. Ceccuzzi, G. Celentano, L. Celona, C. Centioli, G.V. Centomani., S. Cesaroni, A.G. Chiariello, R. Chomicz, C. Cianfarani, F. Cichocki, M. Cinque, A. Cioffi, M. Ciotti, M. Cipriani, S. Ciufo, V. Claps, G. Claps, V. Coccorese, D. Coccorese, A. Colangeli, T. Coltella, F. Consoli, F. Cordella, D. Corradini, O. Costa, F. Crea, A. Cremona, F. Crescenzi, F. Crisanti, G. Cristofari, G. Croci, A. Cucchiaro, D. D’Ambrosio, M. Dal Molin, M. Dalla Palma, F. Danè, C. Day, M. De Angeli, V. De Leo, R. De Luca, E. De Marchi, G. De Marzi, G. De Masi, E. De Nardi, C. De Piccoli, G. De Sano, M. De Santis, G. De Tommasi, A. Del Nevo, A. Delfino, A. Della Corte, P. Deodati, S. Desiderati, E. Di Ferdinando, M.G. Di Florio, G. Di Gironimo, L.E. Di Grazia, V. Di Marzo, F. Di Paolo, E. Di Pietro, M. Di Pietrantonio, M. Di Prinzio, A. Di Silvestre, A. Di Zenobio, R. Dima, A. Domenichelli, A. Doria, G. Dose, S. Dubbioso, S. Dulla, I. Duran, M. Eboli, M. Elitropi, E. Emanuelli, B. Esposito, P. Ettorre, C. Fabbri, F. Fabbri, M. Fadone, M.M. Faggiano, F. Falcioni, M.V. Falessi, F. Fanale, P. Fanelli, A. Fassina, A. Fassina, M. Favaretto, G. Favero, M. Ferraris, F. Ferrazza, C. Ferretti, A. Ferro, N. Ferron, C. Fiamozzi Zignani, L. Figini, F. Filippi, M. Filippini, A. Fimiani, M. Fincato, F. Fiorenza, D. Fiorucci, D. Flammini, F. Flora, N. Fonnesu, P. Franz, L. Frassinetti, A. Frattolillo, R. Freda, R. Fresa, A. Frescura, P. Frosi, M. Fulici, M. Furno Palumbo, V. Fusco, P. Fusco, L. Gabellieri, P. Gaetani, E. Gaio, E. Gajetti, P. Gaetani, A. Galatà, J. Galdon Quiroga, D.L. Galindo, S. Gammino, G. Gandolfo, S. Garavaglia, J. Garcia Lopez, M. Garcia Muñoz, P. Gaudio, M. Gelfusa, G. Gervasini, L. Giannini, M. Giarrusso, C. Gil, F. Giorgetti, E. Giovannozzi, G. Giruzzi, L. Giudicotti, M. Gobbin, G. Gorini, G. Granucci, D. Grasso, T. Grasso, S. Grazioso, H. Greuner, G. Griva, G. Grosso, S. Guerini, J.P. Gunn, V. Hauer, J. Hidalgo Salaverri, M. Hoppe, M. Houry, M. Hoelzl, A. Iaboni, M. Iafrati, A. Iaiunese, V. Imbriani, D. Indrigo, P. Innocente, F. Koechl, B. Končar, A. Kryzhanovskyy, L. Laguardia, D.A. Lampasi, C. Lanchi, F. Lanzotti, A. Lanzotti, M. Laquaniti, F. Leone, J. Li, M. Libè, F. Lisanti, D. Liuzza, F. Locati, R. Lombroni, R. Lorenzini, P. Lorusso, L. Lotto, J. Loureiro, F. Lucca, T. Luda di Cortemiglia, P. Maccari, G. Maddaluno, S. Magagnino, G. Manca, A. Mancini, P. Mandalà, B. Mandolesi, F. Mandrile, G. Manduchi, S. Manfrin, M. Manganelli, P. Mantica, G. Marchiori, N. Marconato, G. Marelli, A. Mariani, A. Marin, M. Marinelli, F. Marino, P. Marino, D. Marocco, R. Marsilio, E. Martelli, P. Martin, F. Martinelli, G. Martini, R. Martone, A. Marucci, D. Marzullo, V. Masala, D. Mascali, F. Mascari, A. Masi, N. Massanova, S. Mastrostefano, M. Mattei, G. Mauro, S. Mauro, C. Meineri, L. Melaragni, A. Mele, P. Meller, S. Meloni, I. Menicucci, G. Messina, L. Mezi, G. Miccichè M. Micheletti, S. Migliori, D. Milanesio, F. Milazzo, R. Milazzo, P. Minelli, S. Minucci, F. Mirizzi, M. Missirlian, D. Monarca, C. Monti, M. Mori, A. Moriani, L. Morici, A. Moro, A. Moro, F. Moro, P. Mosetti, R. Mozzillo, A. Murari, A. Muraro, D. Murra, P. Muscente, S. Musumeci, L. Muzzi, G.F. Nallo, F. Napoli, E. Nardon, E. Naselli, R. Neu, M. Nocente, M. Notazio, S. Nowak, E. Ocello, A. Oliva, V. Orsetti, A. Orsini, F.P. Orsitto, M. Ortino, M. Ottavi, G. Paccagnella, D. Pacella, I. Pagani, N. Paganucci, A. Pagliaro, V. Palazzolo, M. Palermo, S. Palomba, F. Panza, D. Paoletti, M. Parisi, R. Pasqualotto, S. Passarello, M. Passoni, T. Patton, L. Pelliccia, A. Peloso, A. Pepato, E. Perelli, A. Perencin, S. Peruzzo, A. Pesenti, N. Pedroni, P. Petrolini, V. Piergotti, A. Pidatella, L. Pigatto, M. Pillon, T. Pinna, S. Pipolo, S. Piras, C. Piron, L. Piron, A. Pironti, M. Pistilli, D. Placido A. Pizzuto, P. Platania, A. Polimadei, F. Pollastrone, G.M. Polli, N. Pomaro, F. Pompili, C. Ponti, F. Porcelli, V. Prandelli, A. Previti,

A. Princiotta, G. Pucino, F. Quaglia, A. Quercia, F. Raffaelli, G. Ramogida, G. Ranieri, B. Raspante, D. Ravarotto, G.L. Ravera, A. Reale, P. Rebesan, M. Recchia, D. Regine, F. Renno, B. Riccardi, D. Ricci, D. Rigamonti, M. Ripani, N. Rispoli, S. Roccella, G. Rocchi, H. Roche, M. Romanato, F. Romanelli, F. Romanelli, G. Romanelli, R. Romaniello, A. Romano, M. Romano, R. Romano, R. Rossi, G. Rubinacci, G. Rubino, G. Rubino, S. Rubino, J. Rueda Rueda, A. Rufoloni, M. Salewski, C. Salvia, P. Salvini, A. Salvitti, L. Salvò, S. Sandri, F. Santoro, A. Satriano, L. Savoldi, C. Scardino, M. Scarpari, S. Schmuck, J. Scionti, M. Sciscìò, M. Scungio, K. Sedlak, L. Senni, G. Sias, A. Sibio, A. Simonetto, L. Singh, A. Sirignano, C. Sozzi, I. Spada, S. Spagnolo, L. Spinicci, G. Spizzo, M. Spolaore, C. Stefanini, H. Strobel, F. Subba, F. Taccogna, B. Taheri, C. Tantos, A. Tarallo, M. Tarantino, G. Tardini, M. Tardocchi, P. Tarfila, A. Tenaglia, C. Terlizzi, D. Terranova, D. Testa, E. Testa, R. Testoni, V. Toigo, G. Torrisi, A. Trotta, G. Trovato, E. Tsitrone, A. Tuccillo, O. Tudisco, M. Turcato, S. Turtù, A. Uccello, M. Ugoletti, O. Uras, M. Uras, M. Utili, V. Vaccaro, F. Valentini, L. Valletti, M. Valisa, D. Van Eester, D. Vanzan, E. Vassallo, G. Vecchi, M. Vellucci, I. Venneri, G. Ventura, M. Veranda, L. Verdini, C. Verona, G. Verona Rinati, F. Veronese, N. Vianello, F. Viganò, O. Villano, R. Villari, F. Villone, P. Vincenzi, V. Vitale, F. Vivio, G. Vlad, M. Wischmeier, H.S. Wu, I. Wyss, R. Zanino, B. Zaniol, F. Zanon, A. Zappatore, G. Zavarise, P. Zito, A. Zoppoli, M. Zucchetti, M. Zuin, P. Zumbolo

Contents

Appendices

Foreword

Fusion has achieved significant milestones in the past two years with the demonstration on JET and NIF of the controlled production of fusion power in conditions close to or even above breakeven. These results confirm our expectations that ITER will achieve its goals. A number of private companies are entering this field with a total of investments above 6B$. There is a strong expectation on fusion in the public opinion. To deploy fusion in the shortest possible time the fusion challenges must be investigated in a number of devices of smaller but significant size and adequate performance, in order to prepare and accompany the exploitation of ITER and to qualify innovative technologies for DEMO and fusion power plants.

The 2012 European Roadmap for the realisation of fusion energy identified two high performance tokamaks that should accomplish the task of supporting ITER and preparing DEMO after the conclusion of the JET exploitation. They are JT-60SA (already in the construction phase in 2012), whose main mission was to qualify steady-state regimes, and a new Divertor Tokamak Test (DTT) facility, to be conceived, designed, built and then operated in parallel with ITER, with the main mission of tackling the key issue of heat exhaust.

This strategy has been confirmed and reinforced by the second version of the European Roadmap (2018) and by the EUROfusion Facilities Review (2023). In the meantime, feasibility studies of a DTT device have been carried out in the framework of the EUROfusion consortium, by means of a dedicated work package. Since the beginning, the Italian fusion institutes have been at the forefront of this activity and in 2015 ENEA has produced a comprehensive project proposal of a DTT device that could be developed within the Italian fusion programme. A financial contribution was subsequently allocated by the Italian government to the project in 2017. In the same year, a EUROfusion DTT workshop was held to present the project to the European fusion community and provide the opportunity for broad discussion and exchanges. Following this event, by the end of 2017, the involvement of EUROfusion in the project for the procurement of the divertor system was approved by the EUROfusion General Assembly. At this point, the development of DTT could officially start as an Italian project, partially supported by EUROfusion.

The following steps were quickly undertaken. In 2018, ENEA/Frascati was selected as the DTT site, following a call for interest with nine candidates. In 2019, an Interim Design Report was published by ENEA and the DTT Consortium was established. In 2021, an international Scientific Technical Committee was appointed, to provide regular evaluations of the project progress and relevant recommendations. The DTT consortium includes all the public Italian institutions working in fusion and the largest Italian energy company and is the best example of public-private partnership in fusion. In 2024, the EUROfusion Facilities Review report stressed the potential of DTT "for major impact on the design of DEMO", as a device "ideal for testing ITER and DEMO scenarios in relevant conditions". Based on these considerations, DTT was classified by the Facilities Review international panel as one of the few "indispensable" tokamak facilities of the future European fusion programme, without which "the programme goals cannot be realized on the required timescale".

The DTT project is at present in its construction phase, with about one third of the budget already committed in industrial contracts and the prospect of an exploitation starting by the end of the 2020 decade. The design and construction activities are accompanied by intensive physics studies, carried out by various Italian institutes with international collaborations, including theory, modelling, diagnostics and control schemes developments. These studies are not limited to the DTT main mission of heat exhaust, but involve topics such as transport, MHD, heating and current drive, energetic particle physics, because the solution to the heat exhaust challenge requires an approach that ensures core-edge integration.

In 2022, it was decided to build on these studies to produce a DTT Research Plan (DTT-RP), involving the broadest possible community of European fusion institutes. An open DTT Research Plan workshop was held at ENEA/Frascati in June 2022, with ~130 participants (100 from Italy and 30 from various European institutes). Subsequently, a call for voluntary participation in the DTT-RP activity was issued, open to all the EUROfusion partners. The response of the community to this call was highly successful: 92 participants were officially appointed by their institutes (35 from Italian and 57 from non-Italian institutes), including 20 research institutes (12 non-Italian) from 10 different countries. The activity was organised in six Expert Groups, chaired by Responsible Officers (for each group, at least one from a non-Italian institute), and with three Coordinators of the ensemble (one from a non-Italian institute). The Responsible Officers and the Coordinators constitute the DTT-RP Team, which held various meetings, including four in-person ones, from 2022 to 2024.

The result of this activity is the first version of the DTT-RP, which is organised in nine chapters and nine technical appendices. The document describes the objectives and research strategy of the DTT experiment, culminating in a set of programmatic headlines. It should be stressed that the DTT-RP is a living document, which will be regularly updated during the construction phase and which will constitute the basis for the construction of the DTT scientific programme and of subsequent device upgrades. It will also catalyse and guide the research activities in preparation of the experimental phase. In the elaboration of the DTT-RP, ITER and EU-DEMO groups have been informed and consulted. In the future, the participation of international partners will be very welcome and is expected to enrich the scientific vision and programme of the DTT project.

For these reasons, a European DTT-RP Team, open to other international collaborators, will remain in charge of updating the Research Plan, following the evolution, along the years, of the scientific knowledge, from both a theoretical and an experimental point of view. The participation of scientists from international partners will be encouraged.

Chapter 1

DTT POWER EXHAUST STRATEGY

F. Crisanti, G. Giruzzi, P. Martin,
T. Bolzonella, M. Ciotti, J. Garcia, E. Joffrin, X. Litaudon, R. Sabot, F. Zonca

The challenge of power exhaust for fusion energy production in magnetically confined plasmas is described and the main research needs in this area for ITER and DEMO are specified. The role of DTT in this field is defined, together with its objectives and priorities. Besides its main mission, related to the assessment of viable power exhaust solutions for DEMO, DTT will provide significant contributions to other fusion energy research fields. The headlines of the DTT research programme are presented, together with the various research phases accompanying the facility evolutions.

1.1 Introduction

A fusion reactor is characterized by challenging bulk plasma properties (achievement of plasma temperature T > 10 keV and triple product (density.temperature.energy confinement time) $nT\tau_E \sim 10^{22}$ m^{-3} keV.s) and consequently with very large power and particle fluxes to the reactor Plasma Facing Components (PFC). The successful resolution of such integration issues is essential for the success of ITER, presently under construction, the demonstration reactor DEMO and any other future fusion power devices, given the foreseen large edge power and particle fluxes and the necessary very long duration of plasma discharges (from several minutes to continuous operation). Moreover, the presence of 14 MeV neutrons and the necessity of a good reliability of the Tritium self-production largely limits the number of usable plasma facing materials. Presently the most suitable candidate material is Tungsten (in various forms or alloys), which has already been implemented and tested in various fusion devices. Light liquid metals, as Tin or Lithium, are also considered, but experimental validation at significant scale is still far to be achieved. The highest power flux, considered compatible with the use of Tungsten monoblock technology for the divertor, is of the order of 10-20 MW/m^2, a figure still far from the energy flux foreseen for DEMO and the very limit for ITER.

Moreover, the challenge of developing adequate power exhaust solutions for fusion reactors is not limited to the choice of appropriate plasma facing materials. The overall features of the divertor, first wall surrounding the plasma and other PFCs need accurate optimization by design and validation tests (magnetic configuration, shaping, cooling, etc.). On the basis of these considerations, the two versions [1.1, 1.2] of the European roadmap towards the realization and the success of a DEMO fusion reactor have identified as mandatory a scaled experiment challenging the present PFC design and materials with plasma core conditions as close as possible to those of a reactor. In the absence of such a facility, it would be difficult to find a technical solution compatible with the plasma core performances necessary for a reactor that has to produce energy economically. This has provided a strong motivation for the Divertor Tokamak Test project (DTT), confirmed by a subsequent evaluation of the European fusion facilities by an international panel, which has classified the DTT device as "indispensable" for the EU fusion programme.

1.2 Main features of the DTT tokamak

Table 1.1. Main DTT parameters

R (m)	2.19
a (m)	0.7
Volume (m^3)	35
I_p (MA)	5.5
B_T (T)	5.85
$\overline{n}_e$ (10^{20} m^{-3})	1.5
P_{Tot} (MW)	45
P_{ECRH} (MW)	29
P_{ICRH} (MW)	6
P_{NNBI} (MW)	10

DTT has been designed in order to approach, as much as possible in a scaled facility, bulk and edge plasma conditions relevant to a fusion reactor. It is well known that, in order to reproduce in a scaled machine the main important features of a reactor plasma, the most important dimensionless plasma physics parameters must be preserved. These are: the plasma kinetic pressure normalised to the magnetic pressure (β), the plasma collisionality (ν^*) and the Larmor radius normalized to the machine dimension (ρ^*). In addition, the plasma temperature (T) should be in the same range as in a reactor-grade plasma. However, it is also well known that the simultaneous preservation of all these quantities cannot be achieved in a scaled experiment. Consequently, in order to fulfil such a challenging task DTT has been designed by using the weak Kadomtsev scaling approach [1.3] that has allowed preserving the above mentioned important dimensionless parameters, with the exception of the normalized Larmor radius. “Weak” here is to be intended as in its rigorous mathematical definition, i.e., as an argument reproducing a general result under less stringent assumptions, which are relaxed in a controlled way and yield the original “strong” result in the appropriate limit. This can be done assuming that $\rho^* R^{\varepsilon}$, β and ν^* are fixed (for instance to the ITER values, with ε an adjustable parameter) and appropriately rescaling T with respect to the ITER reference value (see Sec. 8.1 for a detailed discussion). This approach has led to design (see Tab. 1.1) a scaled tokamak with major and minor radii respectively R=2.19 m and a=0.7m, toroidal field B_T=5.85 T, plasma current I_P=5.5 MA, and a flat-top discharge lasting several tens of seconds (a few current diffusion times). DTT will be equipped with a large heating power (a total of 45 MW), composed by three heating systems ECRH, ICRH and NNBI, delivering at the plasma the powers 29MW, 6MW and 10MW, respectively. This heating mix has been selected in order to provide robust dominant electron heating, while also allowing non-negligible ion heating and non-inductive current, as well as the possibility to generate a significant fast ion tail.

Table 1.2. DTT important parameters versus the ITER and DEMO ones.

	DTT	**ITER**	**EU-DEMO 2018**
Psep/R [MW/m]	15	14	18.9
β_N [%]	1.6	2.1	2.5
ρ^* at mid-radius [10^{-3}]	3.8	2.0	1.5
ν^* at mid-radius [10^{-2}]	1.2	0.3	0.3
ρ^* at pedestal [10^{-3}]	2.7	1.4	0.8
ν^* at pedestal [10^{-2}]	5	2.2	4.4
q_{95}	3.0	3.2	3.89
n_{GW} [10^{20} m^{-3}]	3.6	1.2	0.66

The extensive use of state-of-the-art integrated modelling tools and transport models has confirmed the robustness of the initial parameter selection. In Table 1.2, some of the most important DTT dimensional and dimensionless parameters are reported versus those expected for ITER and (European) DEMO [1.4]. These are: the power crossing the separatrix divided by the major radius, the normalised β, i.e., $\beta_N = \beta(aB_T/I_p)$, the normalized ρ^* and ν^* evaluated at mid radius and at the pedestal, the safety factor at 95% of the magnetic flux (q_{95}) and the Greenwald density. In the spider plot of Fig. 1.1, some of these quantities are plotted, together with the normalized fast particles Larmor radius and kinetic pressure ρ^*_{fast} and β_{fast}. Thanks to the careful design of the machine characteristics, dimensionless parameters that are similar to those of ITER and DEMO are achievable for the plasma bulk and the plasma edge. Moreover, and most important, also the key quantity P/R is very similar, allowing a DTT divertor power flux similar to those of the ITER and DEMO.

The DTT device has been designed following the flexibility concept, namely the capability to incorporate the best candidate divertor and first wall concepts even at a later stage of its realization. An overall view of the tokamak, in its present state of design, is shown in Fig. 1.2. The toroidal field system is composed by 18 superconducting cable-in-conduit conductor (CICC) coils in Nb3Sn with B_{peak} = 11.9T and I_{max} = 42.5kA, able to provide up to ~6 T at the plasma major radius. The central solenoid (CS) is divided in 6 independently fed superconducting modules, made of Nb3Sn CICC coils with B_{peak} = 13.6T and I_{max} = 31.3kA. The CS is able to provide an ideal solenoidal flux of 16.6Vs and a real premagnetization flux of 16.2Vs in the plasma breakdown. The poloidal field (PF) coil system is composed by 6 independent superconducting coils, as shown in Fig. 1.3. They are made of Nb3Sn (top and bottom coils) and of NbTi for the other coils. The PF system is particularly flexible, since each coil has its own four quadrants power generator. This will allow obtaining a large class of plasma equilibrium configurations: from the standard X point, to the opposite one with negative triangularity. Moreover, a large space available

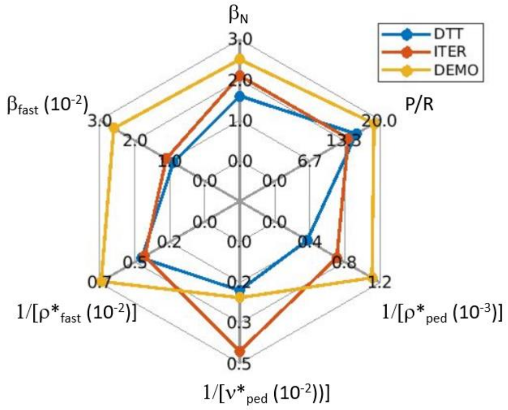

Fig. 1.1: Spider plot of some parameters connected with high-performance plasmas for DTT, ITER and DEMO

on the top of the machine will allow realizing double null configurations. Examples of such configurations are shown in Fig. 1.4, where cross-sections of the last closed magnetic surfaces are displayed. A fine-tuning of the second null will be possible thanks to the presence of four in-vessel copper coils in the divertor region. The in-vessel coil system, shown in Fig. 1.5, will also allow control of the vertical stability (VS) by means of two VS coils, as well as error field correction and ELM control by means of 27 non-axisymmetric (NAS) copper coils.

Since the beginning, DTT will be equipped with an actively cooled divertor, with W monoblocks (Fig. 1.6). This first divertor has been conceived with the aim of providing the possibility of different magnetic configurations, as shown by the examples of Fig. 1.4. To this end, most of its plasma facing surface is equipped with high heat flux components. Nevertheless, a remote handling system will allow replacing the divertor in order to study the role played by its shape and materials. In order to facilitate this task, four divertor test modules (DTM) are foreseen for dedicated experiments. Moreover, the design of vacuum vessel, ports and remote handling devices takes into account the possible application and testing of a Liquid Metal Divertor.

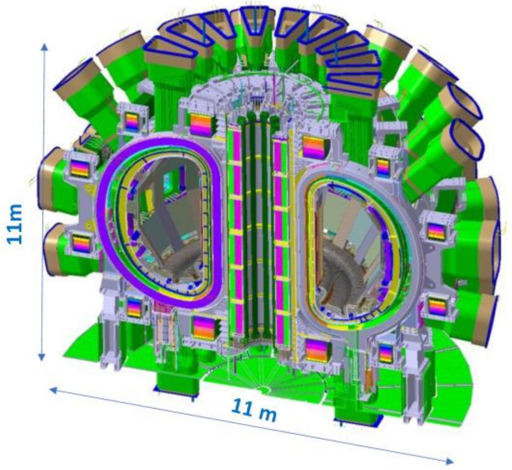

Fig. 1.2: Sectional view of DTT

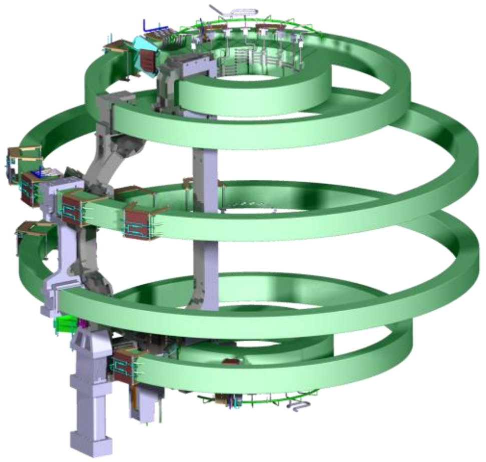

Fig. 1.3: DTT poloidal field coil system

The DTT heating and current drive capability, at the end of its progressive implementation, will be provided by three different systems (Fig. 1.7):

- ECRH: based on 4 clusters of 8 gyrotrons at 170 GHz/1 MW (to resonate at the fundamental electron cyclotron frequency for B_T ~ 6 T or at the second harmonic for B_T ~ 3 T), with an installed power up to 32 MW.
- ICRH: two modules composed by two antennas fed in parallel by a couple of tetrodes at 60− 90 MHz with 1 MW/Tetrode, with an installed power up to 9.5 MW.
- NNBI: one neutral beam injector based on the negative ion technology, at the energy of 510 keV and an installed power of 10 MW.

Machine protection, plasma control and scientific exploitation will be guaranteed by an exhaustive system of about 80 diagnostics, 40 of which will be available in the Phase 1 of DTT operation (see Appendix F).

1.3 DTT Role, Objectives and Priorities

Given the importance and peculiarity of the parameters achievable (see Table 1.2) DTT will be able to tackle the challenging task of power exhaust in reactor relevant conditions, as an integrated problem. Its main target will be to test the role played by different magnetic configurations, combined with the local divertor radiation, to minimize the power flux to the divertor tiles. As mentioned in the previous section, the presence of the test divertor modules will also allow studying the role played by different divertor materials. The final goal of DTT will be to propose a reliable and robust divertor concept for DEMO. The very recent modifications proposed for ITER, i.e., a change of the First Wall (from beryllium to tungsten) and a large increase of the ECRH injected power, enhance the similarity in physics and technology between ITER and DTT.

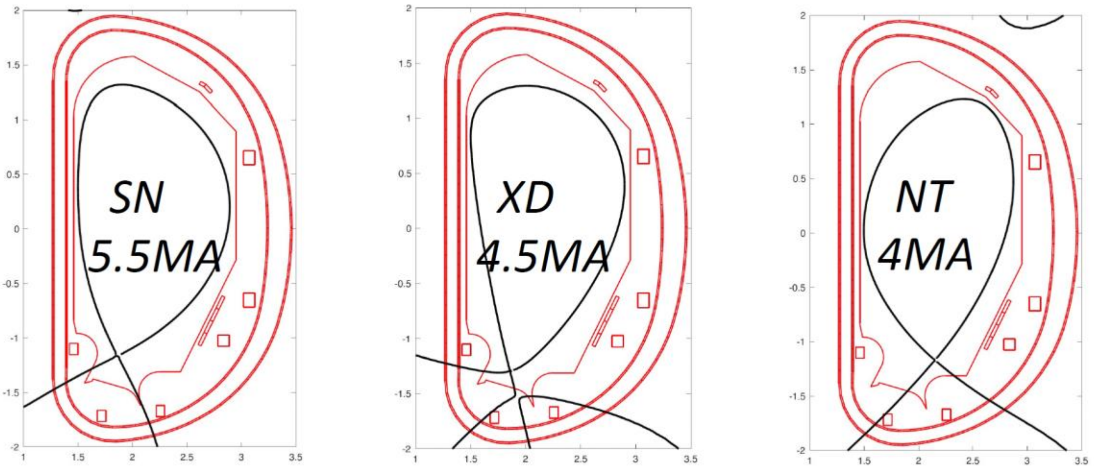

Fig. 1.4: DTT magnetic configurations, obtainable at different plasma currents: From left to right: SN, XD, NT

Therefore, since DTT will operate possibly before and certainly in parallel with ITER, it will have also the fundamental task to support ITER operations in several different aspects as, for instance, disruption avoidance and mitigation. Working at lower toroidal field and therefore at higher β, DTT could even partially explore advanced regimes of operation. With its tungsten PFC, it will be complementary to JT-60SA, which has started and will continue operation for several years with Carbon PFC. In order to accomplish all these tasks, DTT has some unique and reactor relevant features, i.e. high field, high current, low collisionality despite its high density, full W actively cooled divertor, long pulse, dominant electron heating, low torque.

These important features will allow DTT to give some unique contributions to the European and the international fusion programmes. Within the same device, quite different magnetic equilibrium configurations can be compared. In a priority order, Single Null (SN), X divertor (XD) and Negative Triangularity (NT) configurations can be explored (see Fig. 1.4), even within the same discharge. It has to be noted that what is depicted in Fig. 1.4 is not indicating an equilibrium, but a class of scenarios: for any of them, all the main divertor parameters can be varied and actively controlled, i.e. long or short duration, triangularity (up to -0.4 for NT), position of the second null, etc. DTT will explore an extensive parameter range with the aim of solving a crucial issue for power exhaust, in particular whether the Eich empirical scaling for the power energy decay length works in reactor-grade regimes or a more favorable behaviour could be expected. Note that this is not possible in present-day tokamaks. Other key issues for power exhaust will be extensively investigated, such as detachment control, X-point radiation and ELM-free regimes (see Chap. 3).

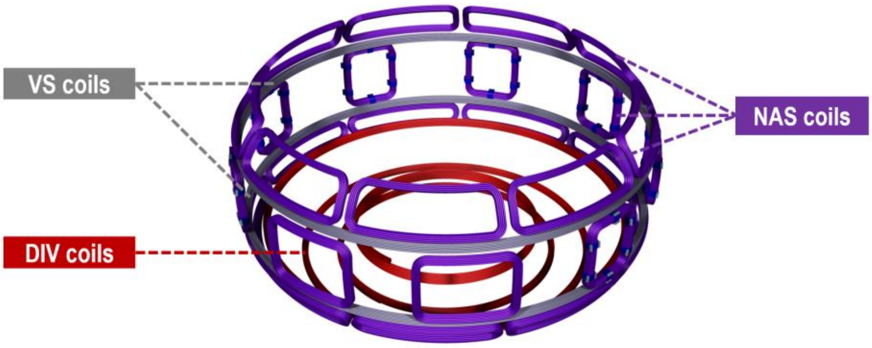

Fig. 1.5: DTT internal copper coil system. 4 divertor (DIV) coils, 2 vertical stability (VS) coils and 27 non-axisymmetric (NAS) coils

The actively cooled tungsten first wall and divertor, associated with the long discharge duration will allow understanding the impact of tungsten impurities and wall erosion/redeposition on plasma performance (see Chap. 3). DTT will have a dominant electron heating, similar to the heating produced by the alpha particles in a reactor. Moreover, the presence of energetic ion tails produced by NNBI and ICRH will allow studying the role played by Alfvénic instabilities in reactor relevant conditions (see Chap. 7). The flexibility of the first divertor design, the possibility to replace the divertor later on and mainly the presence of four divertor test modules will allow studying different materials for the divertor, such as tungsten sponges or liquid metals. DTT mechanical structures have been designed to survive fatigue up to several hundreds of various types of disruptions (including vertical displacement events) at the highest performances (I_p=5.5 MA and 45 MW power input). This will permit experimental disruption study campaigns that could be even finalized to help ITER in getting all the necessary licensing.

Fig. 1.6: DTT actively cooled divertor element

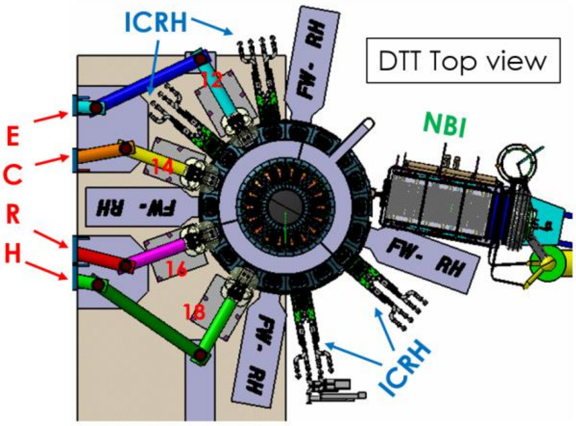

Fig. 1.7: Top view of the DTT tokamak with its heating systems: ECRH antennas (on the left side), ICRH antennas (top and bottom), NBI injector (right side)

1.4 DTT Research Phases and evolutions

The first plasma of DTT is presently expected by 2029. Four major phases are actually foreseen (Fig. 1.8). From now up to 2029, it is the **construction phase**. During this period, a strong cooperation between the Research Plan (RP) team and the construction team is mandatory and envisaged. The present issue of the RP has to be considered as the start of an activity that will continue during the next years, following the progress of both fusion physics and technology. As far as possible, the RP should be able to provide input to optimize the DTT construction by considering the above-mentioned knowledge evolutions. The first DTT plasma is intended to be a scientifically exploitable plasma, with reduced but still valuable parameters: B_T=3T, I_p= 2MA and P_{aux}= 8 MW of ECRH.

The DTT **first phase** will be dedicated to validating operation at all the initially available technical parameters (reduced plasma current, toroidal field and injected power). Since the very beginning, the divertor will consist of actively cooled W monoblocks, capable to sustain up to 20MW/m^2 of heat flux and compatible with all the magnetic configurations of Fig. 1.4. During this phase, the input power will progressively increase up to a coupled power of 14.5 MW of ECRH and 3 MW of ICRH. This will be the main goal of the DTT first phase. The power will be injected in all the three main configurations of Fig. 1.4 (SN, XD and NT) and the toroidal field and current will achieve the nominal values foreseen for this phase. Note that the level of heating power available during this first phase is already significant for a machine of the size of DTT. Disruption and runaway studies will start already in this phase and will be carried on in all phases. Mitigation experiments with SPI (Shattered Pellet Injection) in support of ITER will be carried out as early as possible, depending on the availability of the SPI system.

In the **second phase**, DTT will achieve higher performances, increasing the heating power by the injection of 9.5 MW of NNBI (neutral beams produced by acceleration of negative ions). This will allow testing the actively cooled tungsten divertor under a very large power flux (in particular conditions even up to 20 MWm^{-2}). The controlled injection of bulk and edge radiating impurities, together with the possibility to vary the average density by a factor close to two, will allow studying the role of plasma radiation in the three scenarios. The use of the divertor test modules will allow testing different PFC materials. All these experiments should allow the validation of a divertor concept to be proposed for DEMO, even if not yet fully optimized.

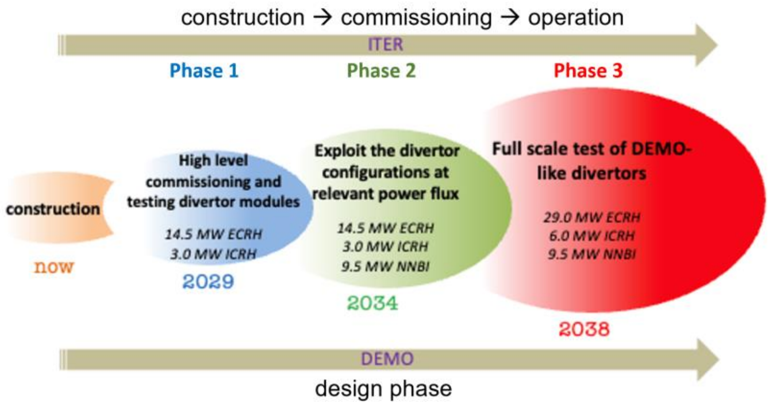

Fig. 1.8: planned DTT timeline, with respect to the ITER construction, commissioning and first operation phase and DEMO programme evolution.

In the **third phase**, the injected power will be increased to the nominal 45 MW, by adding 14.5 MW of ECRH and 3 MW of ICRH. During this phase, DTT will concentrate on its main target: the proposal of a complete solution (magnetic topology, divertor shape and material) for the DEMO divertor and possibly first wall, based on the experimental validation carried out on DTT. In this phase, DTT will be exploited in conditions (core, edge, EP) highly relevant for burning plasma physics. Of course, what described here for the different phases is just a general programmatic line: both the time phases and their contents will be carried out in strict correlation with the evolution of the ITER programme and of the DEMO design, as indicated in Fig. 1.8.

1.5 Headlines of the DTT Research Programme

Programme headlines correspond to primary objectives, attainable with the machine characteristics available in the different phases of the machine exploitation. They could be realized 1) when the machine has attained its nominal capabilities; 2) in intermediate phases (e.g., at lower heating power), or 3) in specific configurations, which are not in the baseline of the project (e.g., at half magnetic field; with liquid metal

PFCs). Moreover, some important headlines of the programme could not be necessarily related to the main mission of the machine. Within this Research Plan, it is important to address scientific and technical objectives that are considered as achievable along the various phases, in some cases not directly connected with the main mission of the DTT facility. Among the achievable objectives, a priority order and a time sequence should be elaborated.

Along the construction phase and the assembling phase, DTT can provide a fruitful contribution for the analogous phases of any complex future fusion device. As a large scale superconducting device, DTT will use some technologies also applied in ITER and could therefore encounter and tackle technical problems that would appear in ITER. Remote participation methods will be extensively employed and their efficiency tested. This role will be even more important in preparation of DEMO; close interaction with the design, engineering and scientific teams of both ITER and (European) DEMO will be suitable and has already started, to some extent. The same kind of help can clearly be given by DTT during the ITER commissioning phase. Along this phase, it will be fundamental to identify the most critical part of the machine components and the most robust tests to be performed. Along the first phase, DTT will definitely operate at reduced field and current, but with a sufficiently high power input, consequently it will be able to produce high β_N plasmas, in a complementary role to JT-60SA for the study of advanced scenarios (see Sec. 2.8.2).

Another very important point that could be explored starting from the first phase (following any necessity coming from ITER) is the disruption avoidance and mitigation of an unpredicted and casual disruption. A very important headline for the second phase will be to test many possible plasma scenarios, with the aim of selecting the safest ones with respect to disruptions and compatibility with PFCs. Understanding whether “exotic” configurations, such as NT and SN or XD with very long legs, could be viable at reactor grade parameters is fundamental. If one of these scenarios could be the key solution for the power exhaust and/or to obtain high performance plasmas without large ELMs, the finding would strongly constrain the DEMO project. In the third phase, DTT will achieve the highest performances. Under these conditions, a non-negligible fraction of Tritium will be produced by the D-D reactions and this Tritium fraction will cause D-T reactions, with a consequent production of 14 MeV neutrons. This neutron flux can roughly be evaluated of the order of 10^{11} m^{-2} and it could be used for some important functional studies for DEMO, such as, for instance, remote handling.

The main headlines for the various research subjects are described in the final sections of the corresponding chapters. A collection of these headlines is presented as a synoptic table in Appendix I.

High-level headlines, providing a synthetic view of the main objectives of the DTT research programme, are presented in Table 1.3.

Table 1.3. DTT programme high-level headlines. Expected relevance to ITER and/or DEMO is indicated by a *. Years are tentative.

Headline number	Headline contents	ITER	DEMO
Construction Phase 2022-2029			
C.1	Integrated modelling for prediction of baseline and alternative scenarios, including assessment of MHD stability and Energetic Particles (EP) properties		
C.2	Modelling for support to design of first wall, divertor, fuelling & pumping, DTM (divertor test modules), heating & current drive (H&CD) systems		
C.3	Definition of necessary and suitable diagnostic systems		
C.4	Set up IMAS infrastructure and dedicated workflows	*	

Phase 1 2029-2034			
1.1	ECRH and ICRH systems commissioning and optimization of basic functionalities	*	*
1.2	Commissioning and validation of fuelling & pumping systems and wall conditioning methods	*	*
1.3	Development of SN, NT and XD scenarios compatible with Phase 1 H&CD systems conditions	*	*
1.4	Development of half field/half current scenarios for initial high β_N studies		*
1.5	Optimization of ramp-up/ramp-down phases, in particular with respect to PFC conditions	*	*
1.6	Transport, MHD, EP initial studies, with validation of theory and modelling tools	*	*
1.7	Initial DTM testing activity	*	*
1.8	Extensive disruption and runaway electrons studies and mitigation, in support of ITER	*	
Phase 2 2034-2038			
2.1	NBI commissioning and combined operation with ECRH and ICRH systems	*	*
2.2	Scenario optimization at higher power level and with NBI	*	*
2.3	Detached regimes optimization and control by impurity seeding in various scenarios	*	*
2.4	Experimental assessment of edge transport at high plasma current and comparison with λ_q scalings and theory	*	*
2.5	Transport, MHD, EP physics studies for assessment of high β_N, hybrid and advanced scenarios, including NBI heating and associated EP	*	*
2.6	Development of small/no ELMs scenarios and their control with NAS (non-axisymmetric) coils and pellets. Assessment of compatibility with high plasma performance.	*	*
2.7	Extensive DTM testing at high power, in particular for new FW and divertor materials	*	*
Phase 3 2038-…			
3.1	Extension and optimisation of all scenarios at full heating power, in conditions of controlled core-edge integration	*	*
3.2	Wall erosion, W migration, D retention and removal studies and assessment in view of application to DEMO	*	*
3.3	Disruption prediction and mitigation studies, including SPI (shattered pellet injection), at full plasma performance	*	
3.4	Transport, MHD, EP physics studies for assessment of high β_N, hybrid and advanced scenarios in conditions of high power density, relevant for burning plasma physics		
3.5	Validation of advanced theoretical frameworks and reduced transport models in the presence of EP at full plasma performance	*	*
3.6	Integrated component testing at maximum power fluxes, in view of DEMO		*

1.6 Research Plan Outline

As already discussed, the DTT Research Plan should be considered as a living document, which will evolve all along the four DTT phases of Fig. 1.8. Therefore, the present version will just constitute a basis for future developments, which could spring out from the experiments and/or from the progress of theoretical knowledge. This first version of the Research Plan will be formed by nine Chapters (see Tab. 1.4), plus some Appendices shortly describing the present status of the DTT technical elements. An aspect explicitly missing in this Research Plan version is a chapter dedicated to diagnostics: at the present state of the project development, it has been considered that each chapter should treat the needs for diagnostics related to the topic of the chapter. In a later version, when the DTT diagnostic projects will be more advanced, a dedicated chapter could be added. Of course, also the Appendices must be intended as living documents that will evolve along the machine construction. Some overlap will naturally occur among the different chapters, but this should be considered as a positive aspect, which will integrate the various expert groups that have been working and that will elaborate future versions of the Research Plan.

Table 1.4. DTT Research Plan Chapters

Chapters	**Subject**
Foreword	*History, status and prospects of the DTT project*
Chapter 1: DTT power exhaust strategy	*DTT objectives, programme headlines, research phases*
Chapter 2: Plasma scenarios	*Reference scenarios in the various research phases*
Chapter 3: Divertor and SOL physics, plasma-wall interactions	*Divertor configurations, heat and particle exhaust*
Chapter 4: Transport physics & integrated modelling	*Plasma profiles and transport properties in the reference scenarios*
Chapter 5: MHD, disruptions and control	*Stability of reference scenarios, disruption studies*
Chapter 6: Physics of heating, current drive and fuelling	*Heating, current drive and fuelling sources*
Chapter 7: Energetic particle physics	*Energetic particle population and MHD in the reference scenarios*
Chapter 8: Theory and simulation	*Contribution of DTT to plasma theory for fusion research development*
Chapter 9: Fusion technology developments	*Opportunities for testing of fusion relevant components in DTT*
Appendices	*Main technical features*

1.7 References

[1.1] "Fusion Electricity – A roadmap to the realisation of fusion energy," https://www.euro-fusion.org/wpcms/wp-content/uploads/2013/01/JG12.356-web.pdf, November 2012.

[1.2] "European Research Roadmap to the Realisation of Fusion Energy," https://www.euro-fusion.org/fileadmin/user_upload/EUROfusion/Documents/2018_Research_roadmap_long_version_01.pdf, November 2018.

[1.3] *Special Section of Fusion Engineering and Design*, vol. **122**, pp. 253-294 and e1-e25, 2017.

[1.4] Siccinio M., et al., *Fusion Engineering and Design* **176** (2022) 113047

Chapter 2

PLASMA SCENARIOS

P. Mantica, C. Angioni,
F. Auriemma, N. Bonanomi, I. Casiraghi, A. Castaldo, M. Cavedon, A. Mariani, G. Rubino

This chapter discusses the plasma scenarios that are planned for DTT depending on the power level available in the different phases of the project. Time dependent simulations are shown, using both the METIS code and the ASTRA code with first principle transport models, to predict the plasma evolution throughout the duration of a plasma discharge for baseline scenarios at different B_T*,* I_p *and power. Alternative advanced scenarios and ELM-free scenarios are briefly discussed.*

2.1 Introduction

This chapter provides an overview of the plasma scenarios planned for DTT operations in the various phases of the heating capabilities. The chapter is structured as follows:

Sec. 2.2 provides a recall of heating phases foreseen in time during the power installation;

Sec. 2.3 provides a summary of the electromagnetic configurations achievable in DTT;

Sec. 2.4 provides a general overview of achievable plasma scenarios in the different heating phases;

Sec. 2.5 discusses the basic guidelines on pulse design (plasma current I_p ramp-up, flat-top, I_p ramp-down) and flux consumption optimization, using the 0.5-D METIS code;

Sec. 2.6 shows some examples of full pulse simulations obtained with 1.5 D ASTRA integrated modelling using first-principle transport models;

Sec. 2.7 discusses alternative scenarios to baseline: Hybrid, I-mode, Advanced Tokamak;

Sec. 2.8 discusses small ELMs/ELM free scenarios (EDA, QCE, QH, WPQH) and ELM mitigation strategies;

Sec. 2.9 discusses the possibility of scenarios with negative triangularity and the expected performance;

Sec. 2.10 presents a list of the research programme Headlines related to plasma scenario.

2.2 DTT heating phases

The DTT heating system [2.1 and Chapter 6] will provide up to 45 MW of coupled power by ECRH, ICRH and NBI systems. The NBI injector installation is planned for 2034. The ECRH and ICRH heating capabilities will be implemented in steps, as detailed in Table 2.1, which sets the terminology for naming the scenarios used throughout this Research Plan.

TABLE 2.1. SUMMARY OF DTT HEATING PHASES AND PLANNED SCENARIOS

Scenario	Ip (MA)	BT (T)	divertor	Power installed (MW)			
				EC	IC	NBI	
A	**2**	**3**	**SN/XD**	**8**	**0**	**0**	Phase 1 2029-2034
A NT	1.5	3	NT	8	0	0	
B	**2**	**3**	**SN/XD**	**16**	**4.75**	**0**	
B NT	1.5	3	NT	16	4.75	0	
C	**4**	**6**	**SN/XD**	**16**	**4.75**	**0**	
C NT	3	6	NT	16	4.75	0	
D	**5.5**	**6**	**SN**	**16**	**4.75**	**5-10**	Phase 2 2034-2038
D XD	4.5	6	XD	16	4.75	5-10	
D NT	4	6	NT	16	4.75	5-10	
D at low BT	2.75	3	SN	16	4.75	5-10	
E	**5.5**	**6**	**SN**	**32**	**9.5**	**10**	Phase 3 2038-onward
E XD	4.5	6	XD	32	9.5	10	
E NT	4	6	NT	32	9.5	10	
E at low BT	2.75	3	SN	32	9.5	10	

2.3 Electromagnetic configurations achievable in DTT

The flexibility of the DTT machine allows it to produce different alternative magnetic configurations [2.2], which increase divertor radiation without excessive core performance degradation, to study different solutions to the power exhaust problem. The DTT tokamak is in fact capable of realizing Single Null (SN), Negative Triangularity (NT) and X-Divertor (XD) configurations with a maximum flat-top plasma current of 5.5 MA, 4 MA and 4.5 MA respectively. In Figure 2.1 the flat-top plasma configurations designed by the CREATE-NL code [2.3] of E-SN, E-XD and E-NT are shown, while in Table 2.2 the main physics plasma parameters are reported (plasma current and toroidal field orientations are defined in Appendix A).

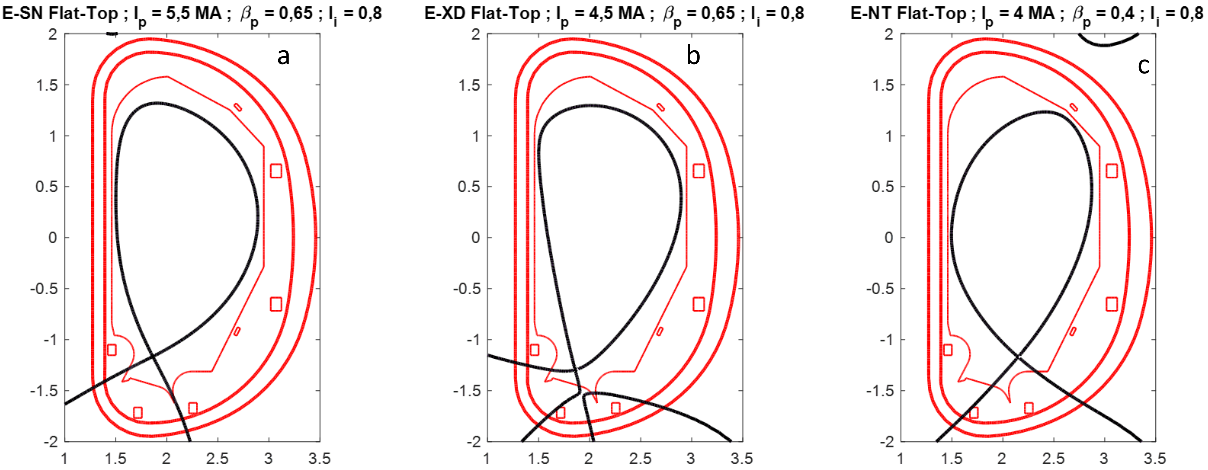

Figure 2.1: Flat-Top plasma configurations of SN (a), XD (b) and NT (c). For sake of simplicity only the E-SN configuration has been reported since for A-SN and C-SN the plasma electromagnetic configuration is similar from the geometrical point of view.

Table 2.2. DTT main geometry and plasma parameters for Flat-Top plasma configurations: E-SN, C-SN, A-SN, E-XD and E-NT.

Plasma Configuration	**E-SN**	**C-SN**	**A-SN**	**E-XD**	**E-NT**
I_p [MA]	5.50	4.00	2.00	4.50	4.00
β_p	0.65	0.60	0.30	0.65	0.40
l_i	0.80	0.90	0.90	0.80	0.80
R_{axis} [m]	2.28	2.27	2.25	2.31	2.26
Z_{axis} [m]	0.19	0.17	0.18	0.30	0.21
$R_{X-point}$ [m]	1.86	1.86	1.86	1.87	2.15
$Z_{X-point}$ [m]	-1.16	-1.16	-1.16	-1.29	-1.17
R [m]	2.20	2.20	2.20	2.20	2.18
a [m]	0.70	0.70	0.70	0.70	0.69
$B_{tor,tot}$ at Major Radius [T]	-5.96	-5.93	-3.00	-5.92	-6.01
$q_{95\%}$	-2.89	-3.93	-3.87	-3.66	-3.22
Elongation at separatrix (k)	1.78	1.79	1.78	1.85	1.75
$k_{95\%}$	1.65	1.64	1.64	1.67	1.62
Triangularity at separatrix (δ)	0.45	0.45	0.44	0.37	-0.14
$\delta_{95\%}$	0.33	0.33	0.31	0.25	-0.10
$\delta_{95\%,upper}$	0.37	0.36	0.32	0.24	-0.30
$\delta_{95\%,lower}$	0.29	0.30	0.29	0.25	0.09
Perimeter [m]	6.18	6.18	6.18	6.41	5.88
Volume [m^3]	34.19	34.29	34.32	34.39	31.84

2.4 Scenarios accessible in the different heating phases

Depending on the power level available in each phase, different types of scenarios or regimes will be achievable in DTT besides the standard H-mode baseline scenario. These are summarized in Table 2.3.

Table 2.3 . Scenarios achievable in DTT in the different heating phases

Scenario	B_T/Ip	Achievable types of scenarios/regimes
A **8 MW ECRH** **2029-30**	**3/2**	**L-mode, H-mode baseline SN , XD (β_N~1.7)**
	3/1.5	**NT L-mode**
	3/2	**Hybrid (β_N~tbd)**
B **16 MW ECRH** **+4.75 MW ICRH** **2031-32**	**3/2**	**H-mode baseline SN , XD (β_N~tbd)**
	3/1.5	**NT L-mode**
	3/1.5	**Hybrid (β_N~tbd)**
	3/1.5	**High β_N AT scenario**
C **16 MW ECRH** **+4.75 MW ICRH** **2033-34**	**6/4**	**H-mode baseline SN , XD (β_N~1.3)**
	6/3	**NT L-mode**
	6/4	**Hybrid**
	6/4	**I-mode**
	6/4	**EDA, QCE, QH, WPQH**
D **16 MW ECRH** **+4.75 MW ICRH** **+ 10 MW NBI** **2034-2038**	**6/5.5-4.5**	**H-mode baseline SN , XD (β_N~tbd)**
	6/4	**NT L-mode**
	6/4.5	**Hybrid**
	6/5.5	**I-mode (but NBI counter-current→ use reverse B_T/I_p and LSN no NBI)**
	6/5.5	**EDA, QCE, QH, WPQH**
D low BT	**3/2.75**	**H-mode baseline SN , XD at high β_N (β_N~tbd)**

16 MW ECRH +4.75 MW ICRH + 10 MW NBI 2034-2038	3/1.5	NT L-mode
	3/2	Hybrid
	3/1.8	High β_N AT scenario (β_N~tbd)

E 32 MW ECRH +9.5 MW ICRH + 10 MW NBI 2038-...	6/5.5-4.5	H-mode baseline SN , XD (β_N~1.6)
	6/4	NT L-mode
	6/4.5	Hybrid
	6/5.5	I-mode (but NBI counter-current using reverse BT/Ip and LSN)
	6/5.5	EDA, QCE, QH, WPQH
E low BT 32 MW ECRH +9.5 MW ICRH + 10 MW NBI 2038-...	3/2.75	H-mode baseline SN , XD at high β_N (β_N~2.1)
	3/1.5	NT L-mode
	3/2	Hybrid (β_N~tbd)
	3/1.8	High β_N AT scenario (β_N~tbd)

2.5 Designing the full time evolution of a DTT scenario

2.5.1 Available electromagnetic flux swing

Starting from the design of the Central Solenoid (CS), which provides an ideal solenoidal flux of 16.6Vs and a real pre-magnetization flux of 16.2Vs, the flux consumption in the different phases of the discharge is evaluated for the scenario E (full field, full current, full power). Under the pessimistic hypothesis of breakdown without ECRH, a flux loss of 0.8Vs is assumed for the breakdown and 0.75Vs for the creation of the first plasma at 0.1MA ($\Psi_{\mathrm{BD+}} = 14.65$ Vs). Concerning the ramp-up phase, the flux consumption has been estimated by means of the Ejima formula [2.4] achieving a start of flat-top (SOF) flux of:

$$\Psi_{\mathrm{SOF}} = \Psi_{\mathrm{BD+}} - \left(0.5\mu_0 \mathrm{R} l_i \mathrm{I_p} + \mathrm{C_{Ejima}}\mu_0 \mathrm{R I_p}\right) = 1.1\ \mathrm{Vs} \quad \text{(i.e. a flux consumption until SOF of 15.1 Vs)}$$

assuming $\mathrm{C_{Ejima}} = 0.45$, $\mathrm{R} = 2.19$ m, $\mathrm{I_p} = 5.5$ MA and $l_i = 0.8$. A plasma current ramp-up rate of 400kA/s has been assumed to make the resistive losses estimated by the Ejima formula compatible with the experimental data extracted by existing devices, such as JET.

During the flat top, a V_{loop}=0.18V is assumed to consider the resistive losses with a bootstrap fraction $I_{bs}/I_p = 0.22$. The duration of the flat-top is determined by the end of flat-top equilibrium having the reference flat-top plasma shape and minimum boundary flux, which is $\Psi_{EOF} = -3.55$ Vs. The limitation on EOF (end of flat-top) flux is due to:

- the possibility to perform an H-L transition in 1 s fulfilling the engineering constraints on maximum voltage and maximum vertical and separation forces on CS modules.
- the use of CS currents to control plasma shape, in particular to guarantee a minimum inner clearance of 4 cm between plasma column and inner wall.

This means that the flux consumption allowed until EOF is 19.75 Vs. This allows a flat-top duration of about 30s. A margin is also taken into account to perform the H-L transition.

The flux consumption during the ramp-down is estimated considering the opposite effect of the resistive flux losses and the inductive flux gain. Assuming a plasma current ramp-down rate of -250kA/s, the flux loss during ramp-down is approximately 4.5 Vs. It is worth mentioning that, since a new version of the DTT CS is currently under evaluation, a slight modification of the flux consumption during the whole scenario could be obtained. The flux consumption foreseen in the different discharge phases of scenario E is summarized in Table 2.4.

Table 2.4 . Summary of flux consumption in the different phases of DTT scenario E

	Plasma formation	Ramp-up	Flat-top	Ramp-down
Flux consumption	1.55Vs	13.55Vs	4.65Vs	4.5Vs

2.5.2 Breakdown

On DTT, a thorough evaluation of a robust and reliable breakdown scenario relies on the use of Electron Cyclotron Heating (ECH) power. To prepare for different scenarios, a series of simulations were conducted employing the codes BKD0 [2.5] and CREATE-BD [2.6] (Figure 2.2, left), alongside the GRAY code [2.7] for assessing Electron Cyclotron (EC) absorption. In DTT, the operational range includes a purely ohmic start-up with a toroidal electric field of 0.8 V/m and a stray field of 3 mT in a quite large region. Additionally, an EC sustained breakdown at 6 T, corresponding to the fundamental resonance frequency of 170 GHz used in the DTT ECH system, was explored. As depicted in Figure 2.2 (right), the comparison involves assessing the plasma current achieved after 150 milliseconds of simulation for various prefill pressures without impurities. The results indicate that in the ohmic scenario, the prefill pressure threshold for sustaining a breakdown is relatively low, about 2 mPa. By introducing Electron Cyclotron (EC) power - up to 5 MW of the initially available 8 MW for the DTT initial plasma - the pressure limit increases by a factor of 10, thereby significantly expanding the operational range for current start-up. Such a pressure window should be able to guarantee a successful breakdown also considering the presence of impurities. A more detailed investigation is planned, delving into various impurity mixtures and null quality. In any case, the large availability of EC power and its flexibility ensure the possibility to have a stable and reliable sustained plasma start-up. From a magnetic point of view, active voltage limits can support a large variety of scenarios. The availability of tools to automatically optimize the time evolution of magnetic fields allows the design and testing of alternative field null configuration breakdowns but also Trapped Particles Configurations, recently tested in tokamaks [2.8].

2.5.3 I_p ramp-up, flat-top and I_p ramp-down

The plasma discharge from the beginning of the current ramp-up (RU) to the end of the ramp-down (RD) has been studied by means of METIS [2.9], a fast numerical tool able to simulate the whole plasma discharge.

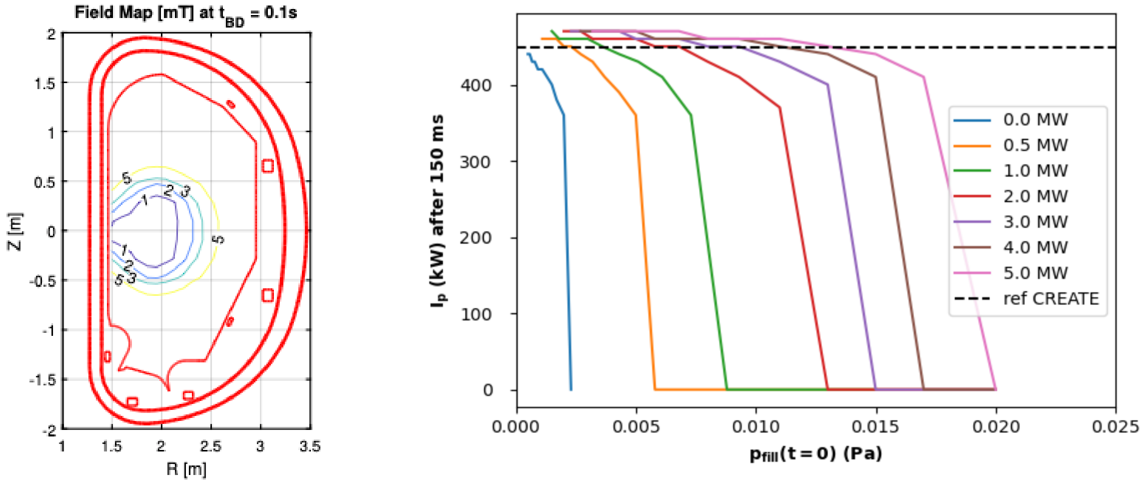

Figure 2.2: (Left) Reference breakdown conditions calculated by CREATE-BD. Iso-field lines obtained when the requested toroidal electric field is 0.8V/m for Ohmic scenarios. (Right) Plasma Current as calculated by BKD0-GRAY after 0.15 s of simulation for different prefilling pressure at different ECH power (6 T). The reference plasma current (dashed black line) is calculated by-CREATE-BD, assuming the plasma as a massive conductor with poloidal cross section that fills the breakdown region.

The electromagnetic equilibria at various times of the discharge have been provided by the CREATE-NL code and are shown in Figure 2.3. In the definition of the DTT scenario one has to bear in mind the main constraints to fulfil:

- maximum magnetic available flux from the CS, as defined in Sec. 2.5.1;
- maximum value of the internal inductance l_i, which means electromagnetic controllability of the system;
- compatibility with the Scrape-Off Layer and divertor conditions.

By considering the values used in the electromagnetic computation, we obtain that the limit for the maximum available magnetic flux is $\Psi_{max,sep}$. = 19.75 Vs at the End Of Flat-top (EOF). In addition, we take into account the constraints related to the SOL and divertor condition during the Flat-Top (FT) phase as in [2.10], which reflect on the value of the separatrix density $n_{e,sep} = 0.8\text{x}10^{20}$ m^{-3} and on the radiated power within the separatrix P_{rad}= 15 MW. Several waveforms have been defined to characterize the full plasma discharge from the RU to the end of the RD phase. They are plotted in Figure 2.4 for the Scenario E of DTT with Ne seeding and a current ramp-up rate of 400kA/s. As initial guess for the discharge duration, namely the reference case (Ref., solid lines), the FT duration (End Of Flat-top, EOF) is limited by the available magnetic flux $\Psi_{max,sep}$ to t(EOF) = 44s. By considering that the start of the stationary phase (Start Of Flat top, SOF) is foreseen at t~18s, the flat-top duration is Δt_{FT} = 26s.

The related waveforms in terms of power (P_{ECRH}=28.8 MW , P_{ICRH} = 6 MW , P_{NBI} = 10MW) and plasma quantities (Z_{eff}, I_p, $B(R_0)$, f_{GW}) are shown in Figure 2.4 a) and b). Auxiliary plasma heating during the RU phase is necessary in order to decrease the resistivity and to counteract the natural tendency of current density peaking with an off-axis deposition at ρ_{tor} = 0.6.

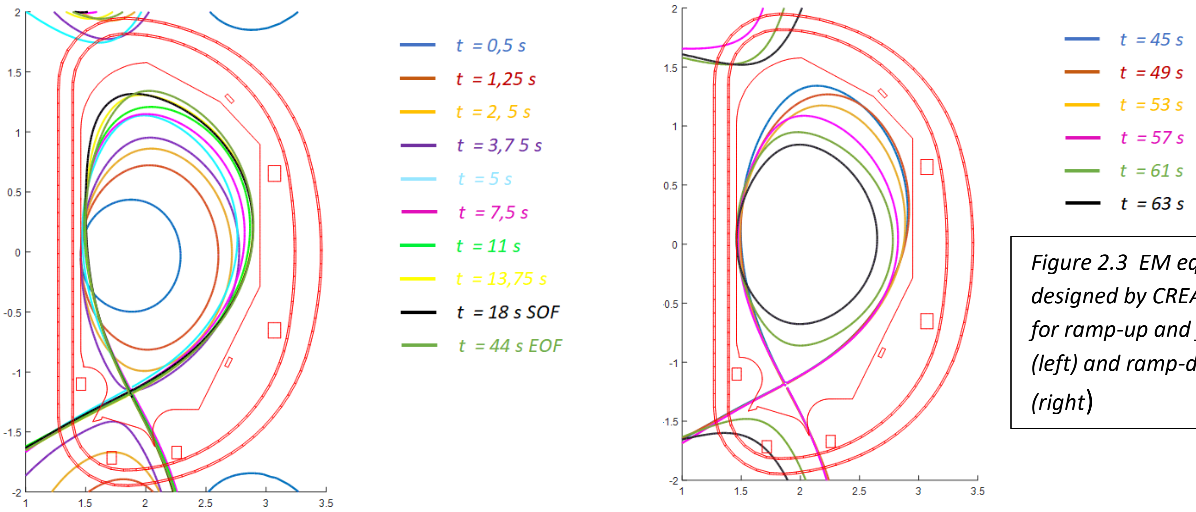

Figure 2.3 EM equilibria designed by CREATE-NL for ramp-up and flat-top (left) and ramp-down (right)

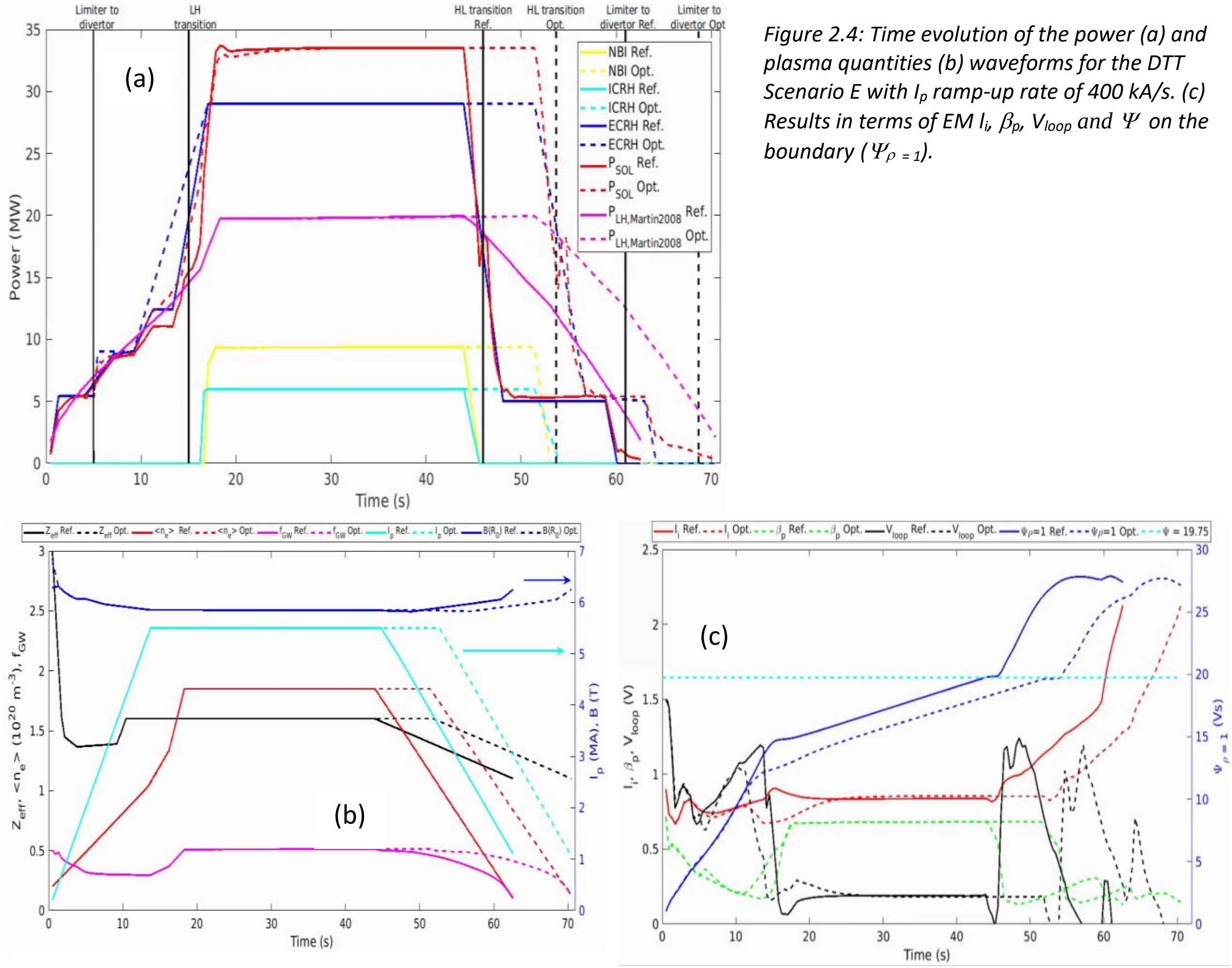

Figure 2.4: Time evolution of the power (a) and plasma quantities (b) waveforms for the DTT Scenario E with I_p ramp-up rate of 400 kA/s. (c) Results in terms of EM l_i, β_p, V_{loop} and Ψ on the boundary ($\Psi_{\rho=1}$).

In the reference case, the L-H transition is predicted to occur at t=15s, in line with the expectations, while during the RU phase the power crossing the separatrix is below the power predicted by the Martin 2008 [2.11] scaling, even though quite close to the threshold. The H-L transition is predicted to occur at t = 46s with a progressive decrease of the P_{ECRH} power from the full power value to a residual RD $P_{ECRH,RD}$ = 5 MW. The latter is necessary to control the fast increase of l_i during the RD phase when the plasma is still in divertor configuration. In terms of EM controllability, the goal is to keep l_i < 1.2. In the last part of the discharge, characterized by a small limited plasma, the external heating is turned off to limit the temperature of the ions ($T_{i,sep}$ < 50 eV) directly impinging on the limiter. Furthermore, a high value of the Z_{eff} is set at the beginning of the discharge, in line with current experimental observations [2.12] and to take into account possible resistive magnetic flux consumption (although the initial Z_{eff} is strongly related to the wall conditions and will be assessed only during the machine operation). The value of Z_{eff} during the FT is tuned to get the desired P_{rad}. In the terms of the line density evolution, the Greenwald fraction is kept above a certain value ($f_{GW}>0.3$). The scenario defined is compatible with both EM control ($l_i \approx 0.8$) and magnetic flux limitation.

However, a possible improvement can be obtained by acting on the EC heating during the RU phase. The comparison between the optimized (Opt., dashed line) and the reference case is depicted in Figure 2.4. The increase of the EC power ramp-up rate allows decreasing the plasma resistivity and saving a considerable amount of magnetic flux $\Delta\Psi$ = 2.5 Vs. This allows increasing the FT duration by 8s, with t(EOF) shifted to t=52s and Δt_{FT} = 34s. As a result, the time duration of the discharge is also longer in the final RD phase, but with the same features as in the Reference one. The aspect to highlight is the possibility to anticipate the L-H transition at t = 10s, that is during the RU current phase, as foreseen for example in ITER scenarios [2.13]. This condition can however lead to instability and its feasibility has to be assessed with more sophisticated tools.

A further increase of the flat-top duration can be reached by considering an acceleration of the current ramp-up by using an I_p ramp-up rate of 600kA/s. This allows saving magnetic flux $\Delta\Psi$ = 1.5 Vs by decreasing the resistive flux consumption during the RU phase. As a result, the flat-top duration increases from Δt_{FT} = 26s to Δt_{FT} = 32s.

2.6 ASTRA simulations of DTT baseline scenarios using IMEP and TGLF

2.6.1 Simulation methodology

The simulations presented in this section are carried out with the ASTRA [2.14, 2.15] transport code coupled with the TGLF-SAT2 [2.16] quasilinear model for the turbulent transport, the NCLASS [2.17] model for the neoclassical calculations, the FACIT [2.18] routines for the calculation of the neoclassical transport coefficients of the impurity densities and the IMEP [2.19] routines for the calculation of the H-mode pedestals. The simulations cover the whole confined plasma radius, up to the separatrix and are time-dependent. The evolution of the whole plasma discharge, from the early ohmic limiter phase up to the H-mode flat-top phase, is simulated. All the different phases (L-mode, L-H transition and H-mode) are treated in a single simulation, with the plasma parameters at the L-H transition determining the H-mode pedestals. The electron temperature T_e, the ion temperature T_i, the electron density n_e, the impurity densities, and the plasma current density j_p are predicted in these simulations. Details of the simulation methodology are presented in Appendix C.

In the following section, we will describe in detail the results obtained for the full power, full field and full current H-mode baseline scenario. Scenarios at reduced power, field and current are collected in Appendix C. Their main parameters are reported in Table 2.5.

2.6.2 Scenario E SN baseline

The DTT scenario E H-mode baseline SN is the main DTT reference scenario at full power, full field and full current. It will operate with a magnetic field B_T =5.85 T, plasma current $|I_p|$ =*5.5* MA and with a total auxiliary heating power $P_{heating} \approx$ *45* MW. It is the most challenging from a technical point of view, with two important open questions to be answered: 1) Will the total magnetic flux provided by the central solenoid be able to sustain the plasma current ramp-up and to maintain the H-mode phase at 5.5 MA for a few resistive times?

2) Will the plasma poloidal beta, β_{pol}, and internal inductance, l_i, be within the machine control capabilities? For these reasons, the DTT scenario E was studied in more detail with respect to the other scenarios, with scans in experimentally controllable plasma parameters such as $\overline{n}_e$, impurity content, heating power ramp and current ramp-up velocity.

Of the 45 MW of the total auxiliary heating power, 29 MW are given by ECRH, 6 MW by ICRH and 10 MW by NBI heating. In our simulations the ECRH heating is deposited both on-axis ($\rho_{tor} = 0.2$) and off axis ($\rho_{tor} = 0.6$) during the current ramp-up phase. This choice is adopted to maintain the internal inductance of the plasma below the machine limits: using only on-axis ECRH heating during the ramp-up phase would lead to values of l_i too high to be handled by the control systems. One pair of gyrotrons (each gyrotron delivers 0.9 MW of heating power) is turned on from the beginning of the simulation, during the limiter phase. Starting at *t=3* s, when the limiter phase ends and the plasma enters the divertor configuration, pairs of gyrotrons are switched on every two seconds (see Figure 2.7a). At *t=13.5* s, after the end of the current ramp-up phase, the ECRH power is moved fully on-axis. At *t=14.5* s, the remaining gyrotrons, the ICRH and the NBI power are switched on, reaching full heating power and triggering the L-H transition. We note that the use of ECRH only during the ramp-up/ramp-down was adopted for its flexibility, but the use of NBI or ICRH in these phases is not a priori excluded. This scheme for the ECRH heating is adopted in order to maintain the heating power just below the L-H power threshold predicted by the Martin scaling. In fact, in this phase we want to maximize the electron temperature in order to minimize the resistive flux consumption while still staying in L-mode. The ICRH power deposition on ions and electrons are calculated, in this case, using the PION code. The NBI power deposition on ions and electrons is calculated self-consistently within the simulation using RABBIT. The profiles of the power deposition of ECRH, ICRH and NBI are shown in Figure 2.8. The time waveforms of the heating powers and of the radiated power are shown in Figure 2.7a. The ratio between $\overline{n}_e$ and the Greenwald density during the ramp-up is kept at $\overline{n}_e/n_G \approx 0.35$.

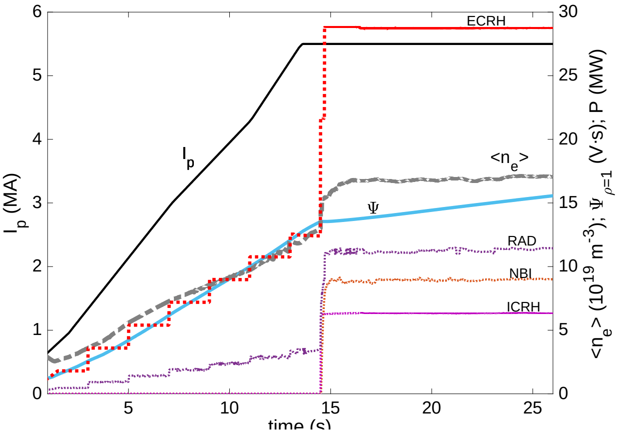

Figure 2.7a: Time evolution for scenario E of the plasma current (Ip), of the plasma auxiliary heating powers (ECRH, NBI, ICRH), of the power radiated within the separatrix (RAD), of the poloidal magnetic flux at the separatrix (Ψ) and of the line averaged electron density ($\overline{n}_e$). The jump in $\overline{n}_e$, following the strong increase in ECRH heating at t=14.6 s, marks the transition into H-mode.

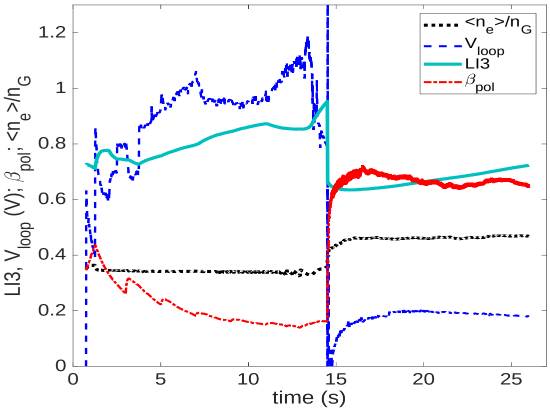

Figure 2.7b: Time evolution for scenario E of the plasma inductance (LI3), of the plasma loop voltage (V_{loop}), of the plasma poloidal beta (β_{pol}]) and of the ratio ($\overline{n}_e/n_G$). The jump in all of these parameters, at t=14.6 s, is due to the transition into H-mode.

The impurities used in modelling this scenario are the seeding gas (neon (Ne) in the L-mode phase and argon (Ar) in the H-mode phase) and tungsten (W). Ne and Ar will be puffed in order to regulate the radiated power, while W will mainly come from the DTT tungsten divertor and its concentration will be less controllable. In the simulations, a fixed ratio was kept between the lighter impurity and the W concentration at the separatrix $n_W/n_{Ne,Ar} = 0.03$. The imposed radiated power is the 25% of the total auxiliary heating power. The time-evolution of some plasma parameters of interest is shown in Figure 2.7b. The evolution of $\overline{n}_e$follows the current ramp, as desired, while the evolution of the temperatures follows the ramp in heating power. $\overline{n}$

shows a clear jump at the L-H transition around t=14.5 seconds. In this case, $\overline{n}_e/n_G$ goes from approximately 0.35 during the L-mode phase, to approximately 0.47 during the H-mode phase. Values of the internal inductance and of the poloidal beta are found to be within the level of acceptance for plasma control. The poloidal magnetic flux at the separatrix, Ψ_b, reaches a value of 14.6 Vs at the L-H transition. The loop voltage is around $V_{loop} = 0.2$ during the H-mode phase. Considering these two numbers and the fact that DTT will have a total magnetic flux of 19.7 V·s available before the ramp-down phase, the flat-top phase of the DTT scenario E is expected to last between 20 and 30 seconds. These numbers correspond to the reference value for the current ramp-up rate of 400 kAs^{-1}. A comparison between the flux consumption before the L-H transition with a current ramp of 600 kAs^{-1} has also been made: using a faster current ramp it will be possible to save 3 Vs, the flux consumption at the L-H transition passing from 14.5 Vs to 10.5 Vs. In this case, the flat-top phase of the DTT scenario E would last around 40 s.

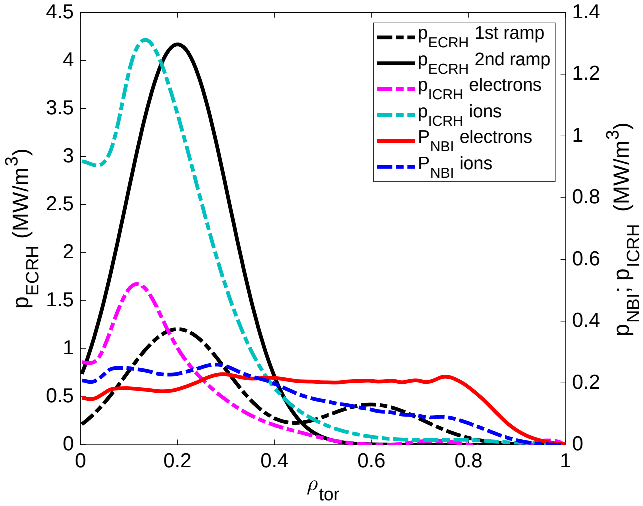

Figure 2.8 : Example of power deposition profiles of the auxiliary heatings obtained in the simulation of scenario E.

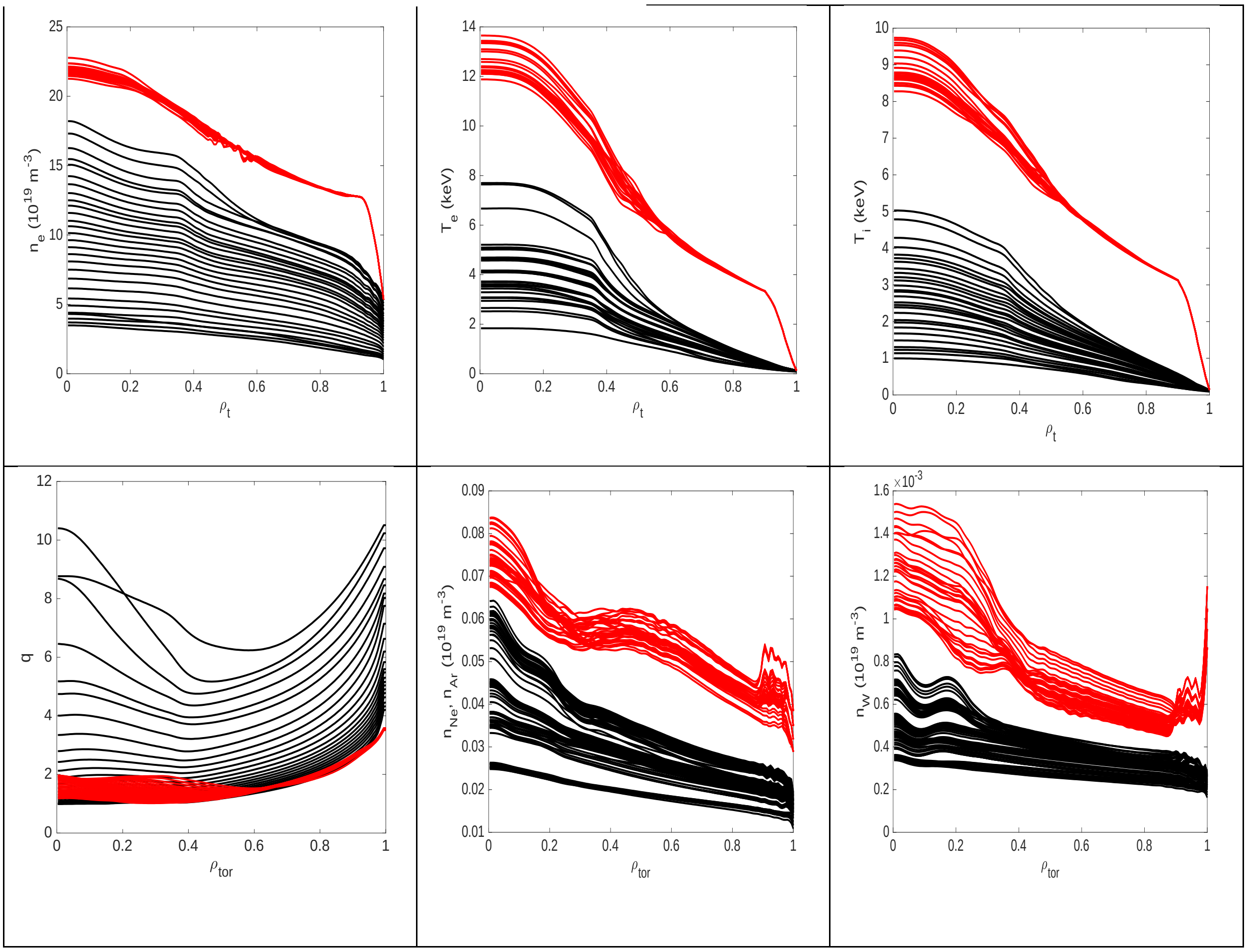

Figure 2.9: Time evolution for scenario E of the profiles of ne, Te, Ti, q, Ne/Ar and W density. The black lines indicate the L-mode phase of the plasma, with the electron temperature increasing with increasing power. The red lines indicate the H-mode phase of the plasma, with the profile fixed, outside ρ_{tor}=0.9, to the pedestal calculated by IMEP.

From a technical point of view, the faster current ramp is feasible, but how the plasma will react to such a fast ramp in terms of MHD stability remains to be understood. The time-evolution of the plasma profile of n_e, T_e, T_i is shown in Figure 2.9a-c. The evolution of the impurity densities, for the case where FACIT is used, are shown in Figure 2.9f-g. In Figure 2.9e the evolution of the profile of the effective charge, Z_{eff}, is shown. At t=13.2 s, towards the end of the current ramp, the ECRH power is moved fully on-axis. At the L-H transition, which in our case is expected, from the Martin scaling, around t=14.5 s and at a total power crossing the separatrix of $P_{LH} = 15.5$ MW, the IMEP routines are called for the calculation of the pedestals. A pedestal top in T_e and T_i of $T_{e,ped} = T_{i,ped} = 3.2$ keV is expected, with an n_e pedestal top of $n_{e,ped} = 12.3 \cdot 10^{19}$ m^{-3}. The boundary (at the separatrix) values of n_e and T_e during the H-mode phase are $T_{e,b} = 130$ eV and $n_{e,b} = 5.5 \cdot 10^{19}$ m^{-3}. The core value of T_e reaches $T_e = 12$ keV, while T_i arrives at 9 keV. n_e reaches high values of $n_e = 22 \cdot 10^{19}$ m^{-3}, with, as pointed before, a line-averaged density around 0.45 of the Greenwald density limit $n_G = 3.6 \cdot 10^{20}$ m^{-3}. The evolution of the plasma safety factor, q, is shown in figure 2.9d. The values of β_N, ν_e^*, ρ^* during the flat-top phase of scenario E are reported in table 2.5. An H factor $H_{98} \approx 0.9$ is expected in this case.

The current ramp down (RD) phase of the scenario E has also been simulated with the same ASTRA tools, in order to design a safe trajectory for the plasma termination. The main issue is to design the power waveform to drive the current from its maximum value I_p=5.5 MA to zero, avoiding an excessive increase of internal inductance that would lead to vertical instability and plasma disruption. As an additional result, the estimated flux consumption during the RD will provide a possible correction to the expected maximum flat-top length, given the magnetic flux available in the central solenoid.

The current ramp-down rate has been prescribed at 250 kA/s and two scenarios have been explored: a fast (1s) and a slow (5s) reduction of the auxiliary input power which allow respectively, an early or delayed H-L transition. In the slow case, the H-L transition occurs about 4 s after the end of flat-top (EOF) and hence the IMEP module is invoked to compute the pedestal evolution during the power ramp-down. In the fast case, it was found that a too fast reduction of the total input power leads to a too low plasma heating in the L-mode, which brings the current density profile to peak with consequent large increase of the internal inductance l_i leading to loss of control. To avoid this, the minimum auxiliary power to be left in the plasma turns out to be 10 MW from ECRH, 33% in the plasma core and 66% absorbed in the mid-radius region. In this way, the T_e profile remains sufficiently high and broad, keeping l_i close to the design value for optimal control. The flux consumption during the ramp-down in the slow case is 6.5Vs, which is about 2Vs higher than assumed in Table 2.4, determining a shortening of flat-top by about 10 s.

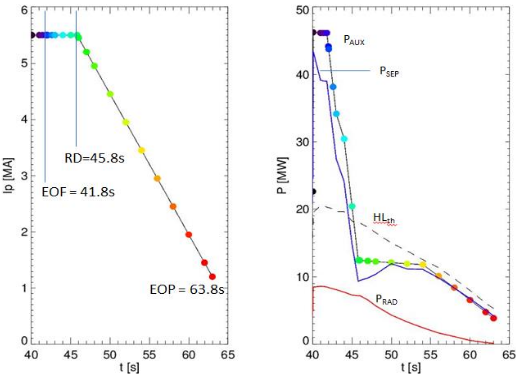

Figure 2.10: ASTRA simulation of the ramp down with the slow (5s) power ramp with prescribed impurities. The additional power (right panel) is reduced from 41.8s to 46s. The plasma enters the L mode at 45.2s (the H to L threshold is shown by the dashed line). The radiated power (solid red line) results well below the input power till the end of the plasma (EOP).

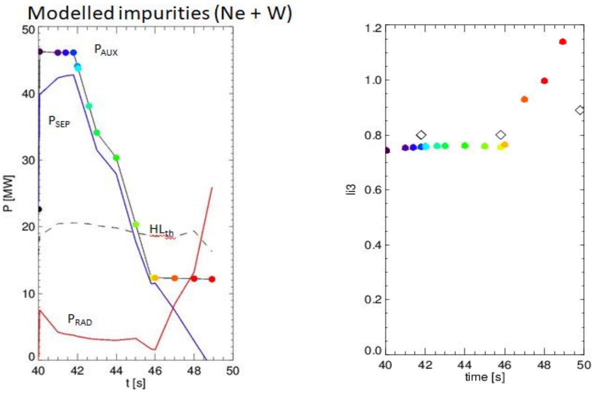

Figure 2.11: ASTRA simulation of the ramp down with the slow (5s) power ramp with modelled impurities. In this case the radiated power starts increasing at about 46s, leading to a shrinking of the current channel as shown but the l_i plot in the right panel. The empty diamonds represent the control system design value for the internal inductance.

It is important to note that the described tests have been carried out assuming prescribed impurity concentrations (Ar + W) and scaling their densities down to keep steady the Z effective profile. To have a more realistic description of the plasma behaviour, the FACIT code has been coupled to ASTRA to compute neoclassical impurities fluxes to be added to the turbulent fluxes computed by TGLF. Preliminary tests indicate that the 1s power ramp is too rapid and results in a chain of events that brings the plasma to a radiative collapse. Indeed the density profile, because of the sudden lack of the NBI source in the core, becomes deeply hollow, and a strong inward pinch brings the impurities to accumulate in the outer part of the plasma, with a large increase of the radiation power in particular from the outer region (ρ>0.6), an edge cooling and a consequent shrinking of the current channel. In the slow scenario, the density hollowness results less severe. Nevertheless, as shown in Figure 2.11, their accumulation is still present, and leads to a plasma disruption delayed by about 5s with respect to the fast ramp case. Optimization of the impurity mix and of their relative concentrations will be implemented in the future.

2.6.3 Comparison of DTT flat-top parameters with ITER and DEMO

In Table 2.5 the main parameters at flat-top for the four DTT scenarios described above and in Appendix C are summarized and compared with the corresponding parameters of ITER [2.20] and DEMO (version 2018 in [2.21]). In the table, the following definitions are used: $\nu_e^*=6.921\ 10^{-18}\ (q\ R\ n_e\ Z_{eff}\ \ln\Lambda_e)/(T_e^2\ \varepsilon^{3/2})$ with $\ln\Lambda_e=31.3-\ln(\sqrt{n_e}/T_e)$ and with $\varepsilon=(a/R)\sqrt{(1+k^2)/2}$, where a and R are the minor and major radii of the machine, k the elongation at the separatrix, while local values of q, Z_{eff}, n_e, and T_e are used. $\rho^*=\sqrt{2T_i m_i}/(e\ a\ B_{tor})$ with T_i in [J] and m_i in [kg].

Table 2.5. Comparison of DTT-ITER-DEMO parameters for baseline scenarios at flat-top

	DTT Sc A	DTT Sc C	DTT Sc E	DTT high-β_N	ITER	DEMO
R(m)/a(m)	2.19/0.70 = 3.1	2.19/0.70 = 3.1	2.19/0.70 = 3.1	2.19/0.70 = 3.1	6.2/2.0 = 3.1	9.07/2.92 =3.1
I_p/B_T (MA/T)	2/3	4/6	5.5/5.85	2.75/2.9	15/5.3	17.75/5.86
P_{tot} (MW)	7.2	20	45	45	150	450
P_{sep}/R_0 (MW/m)	2.6	6.4	15.5	15.5	14	18.9
Pulse length (s)	100	70	20-40	>100	400	7200
β_N (%)	1.7	1.3	1.6	2.7	2.1	2.5
τ_E (s)	0.52	0.64	0.42	0.2	2.9	6.9
$\rho^*_{\rho tor=0.5}$ (10^{-3})	4.6	3.2	3.8	4.7	2.0	1.5
$\nu^*_{\rho tor=0.5}$ (10^{-2})	6	2	1.2	2.5	0.3	0.3
$\rho^*_{ped.top}$ (10^{-3})	3.2	2.3	2.7	3.0	1.4	0.9
$\nu^*_{ped.top}$ (10^{-2})	35	10	5	7	2.2	4.4
q_{95}	4.4	4.1	3.0	3.0	3.2	3.9
n_G (10^{20} m^{-3})	1.3	2.6	3.6	3.6	1.2	0.66

2.7 ELMs in DTT scenarios, ELM mitigation strategies and small ELMs/ ELM-free scenarios

An important aspect of the DTT research is provided by the possibility of exploring the domain of existence and the performance of stationary regimes that feature sufficiently small or no ELMs. These regimes would be desirable in a reactor plasma, in which large type I ELMs cannot be tolerated [2.22]. This is of particular relevance considering the capability of DTT of concomitantly matching the collisionalities at both the separatrix and at the pedestal top that are expected in a future reactor, a critical element towards a complete and reliable core-edge integration. In this section, we first describe the characteristics of ELMs expected in the full power H-mode baseline scenario; then the main characteristics of a set of candidate regimes with small or no ELMs are reviewed, and the capabilities of DTT for the exploraiton of these regimes are discussed.

2.7.1 ELMs in DTT full power scenarios

Utilizing existing scalings [2.23] and the plasma profiles described in Section 2.6, the expected main characteristics of type-I ELMs in DTT full power scenarios are reported here.

Type-I ELMs decrease the plasma energy by typically $\Delta W_{ELM}/W_{ped}$ = 3–20 % in timescales of few hundred µs in present divertor tokamaks. A multi-machine scaling shows that $\Delta W_{ELM}/W_{ped}$ is a function of the normalized pedestal collisionality ν∗ (see figure 2.19, left-hand side). The reference full power scenario of DTT has a normalized pedestal collisionality (at ρ_{pol} = 0.97) of about ν∗ = 0.23 and hence $\Delta W_{ELM}/W_{ped}$ ≈ 9.6 %. Given W_{ped} = 3.56 MJ, ΔW_{ELM}= 0.34 MJ [2.10].

The relative energy loss during type-I ELMs is then used to determine the maximum energy fluence to the outer divertor ε_{peak} using the scaling proposed in [2.24] which results for DTT to be ε_{peak} = 2.10 MJ/m2 (figure 2.12, right hand side).

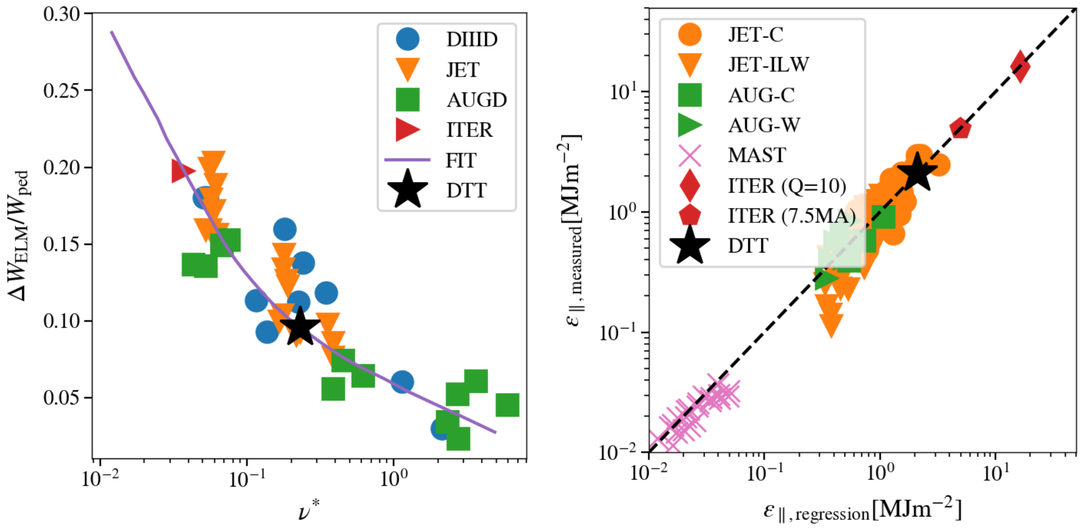

Figure 2.12: Left-hand side: Multi-machine scaling of the relative energy loss during type-I ELMs. Right-hand side: Multi-machine scaling of the maximum energy fluence during type-I ELMs [2.10].

The time scales of the ELM heat load is approximated by a triangular waveform with a decay time τ_{decay}= 2 τ_{ELM} in line with the free-streaming-particle models [2.25]. The rise time τ_{ELM} is well correlated with the time for the ion transport from the pedestal to the divertor $\tau = 2\pi R q_{95}(1+(3/2)^{0.5}\nu*)/C_{s,ped}$ where $C_{s,ped}$ is the ion sound speed. The results for DTT are τ = 250 µs and hence τ_{ELM} = 591 µs.

Finally, by performing time-dependent JETTO+QuaLiKiz simulations within the JINTRAC suite, the ELM frequency for the DTT full power scenario has been predicted. Employing a pedestal alpha critical α_{crit} model to trigger ELMs, their duration and intensity has been fine-tuned based on the previously discussed scaling outcomes. Setting a $\alpha_{crit} = 1.6$, i.e. just below the threshold required to replicate the pedestal profiles from EPED modelling, yielded an estimated ELM frequency of approximately 25 Hz for the DTT full power scenario. It is essential to note that this modelling approach does not account for any saturation effects of the pedestal, making the estimated frequency a maximal approximation of the possible ELM frequency.

2.7.2 EDA H-mode regime

The first regime that is considered is the enhanced D-alpha (EDA) H-mode [2.26]. It was first established in C-Mod with ICRH only. Later it has been also obtained in DIII-D [2.27], EAST [2.28] and ASDEX Upgrade [2.29]. This regime is mainly characterized by high fuelling, high density (and therefore usually also high collisionality in present devices) and features a quasi-coherent mode (QCM) at the plasma edge. The operational power window above the L-H power threshold is favored by a high triangularity of the plasma shape [2.29]. Typical edge safety factors are in the range between 4.5 and 7, but lower safety factors, although usually challenging, have been obtained in C-Mod and AUG, in the latter case using a combination of ICRH and NBI [2.30]. Usual operation is characterized by very high Greenwald fractions (0.9 – 1). EDA H-modes have been also obtained with a fraction of NBI heating and concomitant impurity seeding [2.31], where impurity seeding, also used as feedback actuator, can increase the operational window of the auxiliary power above the L-H within which the regime can be maintained without the occurrence of ELMs.

All of the characteristics of this regime are compatible with the operational capabilities of DTT, which therefore can be expected to be able to explore the domain of existence of this regime more closely approaching reactor relevant conditions, in particular low collisionality pedestal top concomitantly with low edge neutral penetration and reactor relevant densities. This can be considered a critical element in order to assess whether such a regime can be produced in a reactor, where in the pedestal region a much larger variation from high to low collisionality is achieved from the pedestal foot to the pedestal top. We note that the EDA H-mode regime is usually obtained in the ion grad-B drift direction towards the X-point, favorable for the transition to H-mode. In DTT at full field and current and at half the Greenwald density, the power threshold is about 20 MW, well below the total wave heating available on DTT, of 29 MW ECRH and 6 MW ICRH. In previous heating phases, with a total of 18 MW of wave heating only, the investigation of this regime might be limited to half magnetic field operation only. The impact of the inclusion of NBI on the robustness of this regime can therefore also be explored, in combination with high radiation fractions by impurity seeding.

2.7.4 QCE regime

Regimes that are characterized by small-ELMs are also of reactor relevance, since these regimes typically feature reduced ELM energy losses, with small ELM amplitudes and higher ELM frequency. A particularly interesting regime is that with type-II ELMs [2.32, 2.33], which has been recently reconsidered given its potential applicability to reactor conditions and dubbed quasi-continuous exhaust (QCE) regime [2.34, 2.35]. Indeed, while in present devices this regime is also characterized by very high plasma densities and consequent high collisionalities at the pedestal top, recent investigations have revealed that the requirements to enter this regime are specifically set by the separatrix conditions, and therefore are compatible with the plasma conditions which are present in reactor plasmas, such as those of ITER and DEMO [2.35]. The development of this regime relies on the destabilization of high frequency modes at the pedestal foot, producing quasi-continuous filamentary transport with broadened heat-flux footprint on the divertor plates. The consequent reduced pedestal width prevents the trigger of type I ELMs. These favorable conditions are observed to be particularly allowed by a long connection length between the low and the high field side of the plasma. Therefore, this regime is more easily obtained at high triangularity and sufficiently high safety factors [2.35, 2.36]. Operation with type-II ELMs is characterized by high fuelling, providing high density at the separatrix, and increased triangularity and elongation approaching double-null configurations. This regime has been recently also established at TCV [2.36] and reobtained at JET [2.37].

All of the conditions, which are currently observed to be required for the realization of this regime, are allowed by DTT operation. In this respect, while DTT would provide further confirmation of the relevance of the separatrix conditions with respect to the pedestal top collisionality for the establishment of this regime, it will also allow the documentation of the confinement performance of this regime when the pedestal collisionality is reduced to values which are reactor relevant and are not accessible in present devices at high separatrix density.

2.7.5 XPR-CRD scenarios

Impurity seeding is today routinely applied to reduce the heat fluxes to the divertor plates by producing large fractions of radiated power in the peripheral region and to also favor divertor detachment [2.38, 2.39]. Impurity seeding also affects the ELM behavior [2.40, 2.41], by reduction of the net heat fluxes across the pedestal and by local modifications of the profiles.

With very strong impurity seeding, the radiation is localized in a small region close to the X-point, inside the confined plasma [2.42, 2.43]. This poloidally and radially localized dense and cold portion of the plasma is highly radiating close to the X-point, effectively providing, as such, an X-point radiator (XPR). It is observed that, particularly with W walls, the localization of the X-point radiator can be controlled, preventing that it degenerates into a MARFE, a situation that is more difficult to prevent with carbon walls. By adopting measurements of the XPR by means of AXUV photodiodes (or soft X-rays), a control scheme can be established which uses impurity seeding and power as actuators and which allows one to maintain the XPR with very high radiating power fractions and complete detachment [2.43]. When the XPR is located sufficiently inside the plasma, ELMs are observed to disappear, allowing the plasma to naturally enter a stationary ELM-free regime [2.43]. In general, these conditions are still characterized by a relatively good confinement, without impurity accumulation.

It can be expected that an XPR will be routinely present in DTT operation with strong impurity seeding and high radiated powers. Therefore, DTT will have the possibility of exploring whether this regime of operation allows one to achieve high pressure values at the top of the pedestal when the plasma current and the auxiliary heating power are strongly increased. By developing an XPR with short divertor legs, so that the divertor target plates are located close to the magnetic X-point, the configuration of a compact radiative divertor (CRD) forms [2.44], a regime that can be expected to be regularly accessible by DTT.

2.7.6 I-mode regime

The improved energy confinement regime (I-mode) [2.45-47] is characterized by the presence of a pedestal in the temperature profiles and the absence of a strong pedestal in the density profile, leading to an alternative solution with respect to the H-mode. It features a practically H-mode like energy confinement but an L-mode like particle confinement, with also the favourable consequence of a short impurity confinement time [2.48]. It is regularly obtained in diverted configurations with the ion grad B drift directed away from the X-point and therefore unfavorable for the access to H-mode. It is characterized by the presence of a weakly coherent mode (WCM) in combination with the interesting property of the absence of ELMs [2.49], although it can exhibit periodic relaxation events that have some similarities with ELMs, when conditions approach those of the H-mode [2.50].

An unfavourable property is the fact that for its access it requires heating powers higher than those of an H-mode in favourable grad B drift configuration. An additional unfavourable aspect is that it has been found difficult to obtain plasmas that remain in the I-mode confinement regime while concomitantly obtaining complete divertor detachment [2.51]. An interesting property of the I-mode regime is the fact that the power required for the transition from L-mode to I-mode does not depend on the magnetic field [2.52,2.47]. This implies that the domain of existence of the I-mode regime increases with increasing magnetic field since, in contrast, the transition from I-mode to H-mode, requires a power that increases with increasing magnetic field. These properties imply that the I-mode operational power window broadens at high field and therefore can be expected to be large for DTT, whereas it is usually small in low field devices. Curves of the I-mode operational windows with different combinations of magnetic field and currents are presented in figure 4.3 in Chapter 4. In conclusion, it can be expected that DTT will be able to robustly access the I-mode confinement regime and will have the possibility to further explore the confinement properties of this regime, also with different divertor configurations, and to further investigate the possibilities of reaching detachment.

2.7.7 QH and WPQH regimes

In DTT a standard Quiescent H-mode (QH) regime [2.53] would be probably impossible to achieve, due to the required high rotation that is incompatible with the limited available NBI torque and with the relatively large DTT plasma mass. A Wide Pedestal Quiescent H-mode plasma (WPQH) [2.54,2.55,2.56] could be considered instead. This scenario was discovered at DIII-D, ramping down the NBI power, with corresponding torque, until a transition from standard QH to the WPQH occurs. At the transition, the coherent edge harmonic oscillations (EHO) that usually regulate the QH edge disappear and a rapid increase in the pedestal pressure height and width occurs. The key feature of this regime is that it is obtained at almost zero NBI torque, and thus could be compatible with DTT possibilities. In particular, in [2.57] it is reported that in DIII-D it was possible to sustain a full discharge in WPQH regime with zero net neutral beam torque, using non-axisymmetric magnetic perturbations to induce a neoclassical toroidal viscous (NTV) torque. A promising feature in view of a possible realization of the WPQH regime in DTT is that, as reported in [2.58], adding core ECRH improves the WPQH performance. Indeed, given the high available DTT ECRH power, this could help obtaining higher performance in this regime.

2.8 Alternative scenarios to H-mode baseline

2.8.1 Hybrid scenarios

Hybrid scenarios are a type of H-mode scenario which differs from the standard baseline because of a higher q_{95} ~ 4 but an improved core confinement (H factor ~ 1.2-1.4), which compensates the confinement loss due to lower plasma current. Hybrids are generally characterized by high β_N (>2.5) and increased bootstrap current fraction, and by a broad region of rather flat q profile in the plasma core. This can be obtained by suitable break-down and current ramp-up, e.g. with heating during ramp-up in ASDEX Upgrade [2.59] and DIII-D [2.60] or with a current overshoot in JET [2.61]. Such a q shape needs to be maintained in time by exploiting the bootstrap and the current drive sources. Different transport mechanisms can contribute to the improved core confinement, the main one is deemed to the non-linear electromagnetic stabilization described e.g. in [2.62].

The feasibility of Hybrid scenarios in DTT remains to be investigated. Better perspectives are likely at half B_T, where higher β_N values can be achieved. The capability to shape and maintain the q profile in the inner region also needs to be verified by integrated modelling, still to be performed.

2.8.2 Advanced scenarios

At an explorative level, 0-D calculations have been performed to investigate the possibility for DTT to also carry out research in the field of advanced tokamak scenarios, with high fractions of non-inductive current. Considering operation at half nominal magnetic field, 2.9 T, plasma currents between 1 MA and 2 MA are expected to allow operation with large fractions of bootstrap current and significant fraction of current drive at sufficiently high power. As an example, a summary of these results at 1.5 MA, q_{95} around 5.5, is shown in Fig. 2.13, with plots of β_N, β_{pol} and the non-inductive and bootstrap current fractions as a function of the heating power, for different values of the Greenwald fraction. These curves have been obtained conservatively assuming a confinement factor H = 1, with stored energy provided by the average between the IPB98(y,2) and the ITPA20-IL scaling laws. It can be noticed that, with heating power of 20 MW, respectively of 30 MW, at a Greenwald fraction of 0.5 (line averaged density of 5 10^{19} m^{-3}), the projected bootstrap fractions are 0.42 and 0.48. Moreover, conservatively assuming a current drive efficiency for the applied heating power, assumed to be ECRH, such that I_{CD} [kA] = 100 P_{CD} / n_{el} [MW, 10^{19} m^{-3}], about 400 kA and 600 kA of current are driven by ECCD at the same density. These relatively conservative calculations yield the expectation of non-inductive fractions of 0.7 and 0.9 respectively, thereby not excluding the possibility of fully non-inductive operation, if required at slightly reduced current with respect to 1.5 MA. These promising results have been confirmed by preliminary calculations with METIS, which also confirmed the possibility of reaching non-inductive current fractions above 80% at the same current and with densities at 0.9 the Greenwald density limit, thereby likely more compatible with the power exhaust requirements. Further and more complete 1-D calculations, with a complete model for the bootstrap current fraction and more accurate calculations of the driven current, are planned to verify these initial estimates. Studies are also required to assess the possibility of operating DTT at high power and relatively low density from the standpoint of the exhaust, in order to still keep the heat loads on the plasma facing components at a tolerable level.

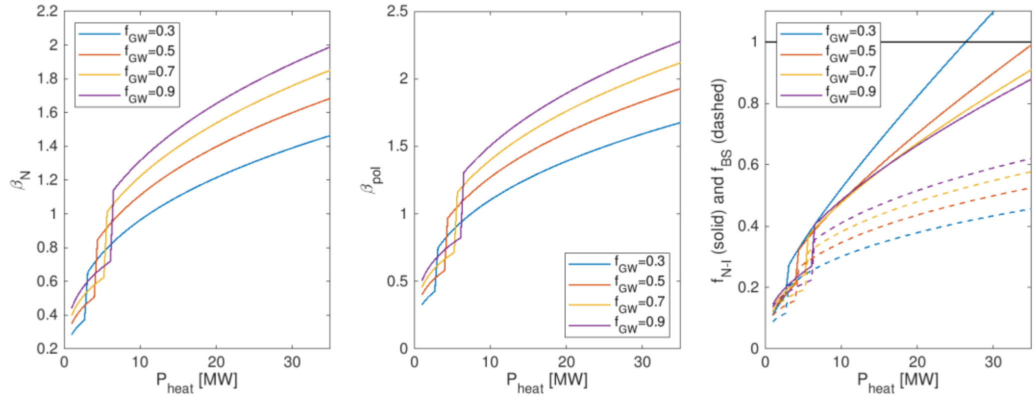

Figure 2.13: 0-D calculations of β_N, β_{pol}, and the bootstrap current (dashed) and total non-inductive current (solid) fractions for different densities as a function of the heating power at 1.5 MA. Fully non-inductive operation at high power is expected to be possible.

2.9 Negative triangularity scenarios

Negative triangularity (NT) options for the DTT full power scenario are under study. The design of the best plasma shape is under development. The reference NT separatrix is shown in Figure 2.1(c). The corresponding scenario would feature B_t = 5.85 T and I_p = 4 MA, with reduced plasma current compared with the positive triangularity (PT) counterpart, in order to have similar q_{95}. Due to the specific design of the DTT divertor (see Chapter 3), in NT scenarios the toroidal field can be reversed to operate in unfavourable grad B drift configuration and guarantee L-mode edge properties, whilst keeping the plasma current direction unchanged to allow full exploitation of the NBI power. A prediction of the heat transport properties for this scenario has been performed, running predictive ASTRA-TGLF SAT2 full radius simulations, compared with gyrokinetic flux-tube GENE [2.63] runs at selected radii [2.64]. The NT option has been compared with the PT SN reference full power scenario. Two additional shapes, here called NT-flipped and PT-flipped, have been also considered, which have been obtained by numerically flipping the PT and NT LCFS with respect to the $R=R_0$ cylinder, respectively, to single out the effect of changing the sign of the triangularity alone on transport.

The results of the predictive transport modelling, performed with boundary conditions at $\rho_{tor} = 0.94$, are summarized in Fig. 2.14. TGLF shows that the NT L-mode (blue) is not able to overcome the loss of the PT H-mode (red) pedestal and reach similar central temperatures. Flipping the shape does not affect the profiles for the L-mode, while it only affects the T_e profile for the H-mode. GENE flux-tube simulations have been performed at the two radial positions $\rho_{tor} = 0.7, 0.85$. An ITG dominant micro-instability regime has been found for all the four cases. A negligible heat flux reduction when inverting the triangularity from positive to negative has been observed for the L-mode, consistent with TGLF, while a strong linear and nonlinear stabilization of the fluxes has been found for the H-mode. However, the T_i profile is kept fixed at $\rho_{tor} = 0.7$ by its stiffness, while only a moderate gain in a/L_{Ti} is obtained at $\rho_{tor} = 0.85$ when inverting the triangularity. In particular, the nonlinear GENE ion heat fluxes at $\rho_{tor} = 0.85$ are shown in Fig. 2.15 versus a/L_{Ti} for the four considered cases. Even if GENE and TGLF do not find a sufficiently beneficial role of negative triangularity inside $\rho_{tor} \sim 0.9$, recent experiments performed at TCV [2.65] and ASDEX Upgrade [2.66] with DTT-like shapes indicate that, with the relatively small negative delta of the DTT NT reference scenario, a beneficial effect of negative triangularity mainly comes from the edge-SOL. This effect, however, has a very strong indirect impact on the core profiles, allowing TCV NT L-modes to overperform corresponding PT L-modes with the same NBI input power and reach similar central temperatures and pressures of double power PT H-modes. For ASDEX Upgrade, NT H-modes reach similar pressures to PT H-modes with the same input power, with much weaker ELMs. Therefore, these promising results indicate that for the DTT NT scenario there is still a chance of having central pressures comparable with the PT H-mode scenario without ELMs, if a stabilizing effect of NT would come from the edge-SOL. The further design of the DTT NT option will follow two strategies: 1) simulate the edge-SOL physics in a more consistent way, also taking into account the recent results of [2.67]; 2) find new NT shapes, with increased top triangularity and smaller volume, to increase the penetration depth of the beneficial effect of NT inside the plasma. Regarding the second option, a new shape has been proposed with almost double top negative triangularity, which will be tested in TCV experiments with similar geometry.

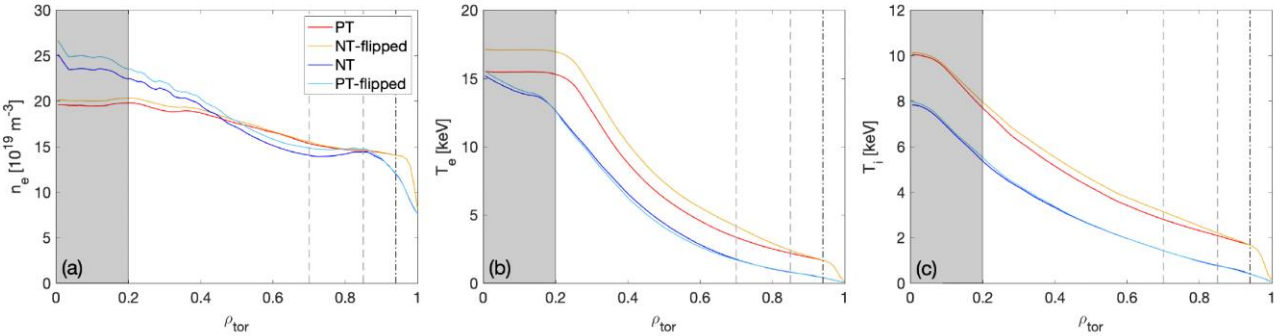

Figure 2.14: ASTRA-TGLF predicted density and temperature profiles. The electron density, electron temperature and ion temperature are shown in (a), (b) and (c). The radii of the gyrokinetic/quasi-linear analysis are shown by vertical dashed lines, while the upper radial boundary of the ASTRA predictive simulations is indicated by vertical dash-dotted lines. The gray band indicates the inner region, where TGLF predictions are not reliable (adapted from [2.64])

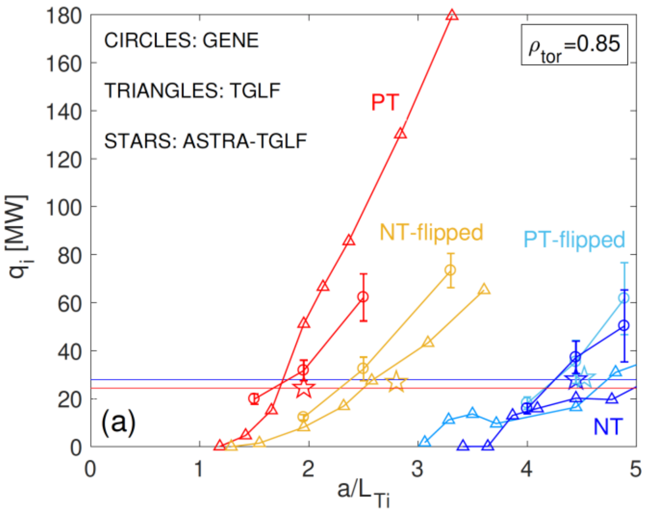

Figure 2.15: Ion temperature stiffness plot for the four considered cases at ptor = 0.85, comparing GENE with TGLF. The electron heat flux q_e is shown in versus a/L_{Ti}, which is the main drive of the ITG dominant micro-instability. The GENE results are indicated by circles (error bars represent the standard deviation of the fluxes time traces over the same time interval that has been considered to compute their averages), while the TGLF SAT2 stand-alone results by triangles. Finally, the stars represent the ASTRA-TGLF SAT2 fluxes (the ASTRA-TGLF q_e values for the reference DTT PT and NT scenarios are also indicated by horizontal lines). (adapted from [2.64])

2.10 Headlines of the research programme for plasma scenarios

In this section, we summarize the main headlines of the DTT research programme for plasma scenarios, according to the various phases of implementation of the DTT heating system and of plasma operations.

Headline number	**Headline contents**	**Priority (+, ++, +++)**	**ITER**	**DEMO**
Construction Phase 2022-2029				
C.2.1	Definition of the central solenoid desired capabilities	+++		
C.2.2	Carry out integrated modelling of baseline and alternative scenarios	++	*	*
Phase 1 2029-2034				
1.2.1	Development of baseline L-mode and H-mode scenarios A, B, C in SN or XD divertor configuration	+++	*	*
1.2.2	Development of Negative Triangularity scenarios	+++		*
1.2.3	Development of Hybrid scenarios at half power	++	*	*
1.2.4	Development of high β_N AT scenarios at half field, half power	++	*	*
1.2.5	First studies of small/no ELMs regimes	++	*	*
Phase 2 2034-2038				
2.2.1	Improvement of all phase 1 scenarios at higher power	+++	*	*
2.2.2	Development of small/no ELMs scenarios	+++	*	*

Phase 3 2038-…				
3.2.1	Optimisation of all phase 1 and 2 scenarios at full power	+++	*	*
3.2.2	Optimisation of small/no ELMs scenarios at full power	+++	*	*

2.11 References

[2.1] Granucci G., et al., Fusion Eng. Des. 122 (2017) 349
[2.2] Ambrosino R., et al., Fusion Engineering and Design 167 (2021) 112330
[2.3] Albanese R., et al., Fusion Eng.Des. 96–97 (2015) 664
[2.4] Ejima S. et al., Nuclear Fusion 22 (1982)
[2.5] Granucci G., et al., Nucl. Fusion 55 (2015) 093025
[2.6] Di Grazia L.E., et al, Fusion Engineering and Design 176 (2022)
[2.7] Farina D., Fusion Science and Technology, 52 (2007) 154
[2.8] Lee J et al 2017 Nucl. Fusion 57 126033
[2.9] Artaud J.F., et al., Nuclear Fusion 58 (2018)
[2.10] Casiraghi I., et , Plasma Phys. Control. Fusion 65 (2023) 035017
[2.11] Martin Y R , et al., J. Phys.: Conf. Ser. 123 (2008) 012033
[2.12] Sips A.C.C., et al., Nucl. Fusion 49 (2009) 085015
[2.13] Sips A.C.C., et al ., Phys. Plasmas 22 (2015)021804
[2.14] G. Pereverzev, P. N. Yushmanov, "ASTRA Automated System of TRansport Analysis in a Tokamak",Report of the Mak-Planck-Institut für Plasmaphysik, IPP 5/42 (Garching Germany, 1991)
[2.15] Fable e., et al., Nucl. Fusion 53 (2013) 033002
[2.16] Staebler G. M., et al., Nucl. Fusion 62 (2022) 0420
[2.17] Houlberg W.,et al, Phys. Plasmas 4 (1997) 3230
[2.18] Fajardo D., et al., Plasma Phys. Control. Fusion 64 (2022) 05501
[2.19] Luda T., et al., Plasma Phys. Control. Fusion 65 (2023) 034001
[2.20] Mantica P., et al., Plasma Phys. Control. Fusion 62 (2020) 014021
[2.21] Siccinio M., et al., Fusion Engineering and Design 176 (2022) 113047
[2.22] E. Viezzer et al. Nucl. Materials Energy 34 (2023) 101308.
[2.23] Igitkhanov Y. , et al. IEEE Transactions on Plasma Science 42.9 (2014), 2284
[2.24] Eich T., et al., Nuclear Materials and Energy 12 (2017), 22nd PSI, 84
[2.25] Eich T., et al. Journal of Nuclear Materials 390-391 (2009), 760
[2.26] M. Greenwald, et al. Phys. Plasmas 6 (1999) 1943.
[2.27] P. Mossessian, et al. Phys. Plasmas 10 (2003) 689.
[2.28] P.J. Sun, et al. Phys. Plasmas 26 (2019) 012304.
[2.29] L. Gil, et al. Nucl. Fusion 60 (2020) 054003.
[2.30] T. Puetterich private communication 2023
[2.31] A. Kallenbach, et al. Nucl. Fusion 61 (2021) 016002.
[2.32] J. Stober et al Nucl. Fusion 41 (2001) 1123.
[2.33] G. Saibene et al Nucl. Fusion 45 (2005) 297.
[2.34] E. Wolfrum et al PPCF 53 (2011) 085026.
[2.35] G. Harrer et al PRL 129 (2022) 165001
[2.36] B. Labit et al Nucl. Fusion 59 (2019) 086020
[2.37] M. Faitsch 2023 private communication
[2.38] A Kallenbach et al 2013 Plasma Phys. Control. Fusion 55 124041
[2.39] A. Kallenbach et al 2015 Nucl. Fusion 55 053026
[2.40] M.N.A. Beurskens, et al. Nucl. Fusion 48 (2008) 095004.
[2.41] M.G. Dunne 2017 Nucl. Fusion 57 025002
[2.42] M. Bernert, et al. Nucl. Mat. Energy 12 (2017) 111.
[2.43] M. Bernert Nucl. Fusion, 61 (2021), Article 024001].
[2.44] T. Lunt et al Phys. Rev. Letters 130 (2023) 145102
[2.45] D.-G. Whyte et al 2010 Nucl. Fusion 50 105005
[2.46] A.E. Hubbard et al 2017 Nucl. Fusion 57 126039
[2.47] T Happel et al 2017 Plasma Phys. Control. Fusion 59 014004
[2.48] J.E. Rice et al 2015 Nucl. Fusion 55 033014
[2.49] A. E. Hubbard et al 2011 Phys. Plasmas 18 056115
[2.50] D. Silvagni et al 2020 Nucl. Fusion 60 126028
[2.51] T. Happel et al 2021 Nucl. Fusion 61 036026
[2.52] A.E. Hubbard et al 2016 Nucl. Fusion 56 086003
[2.53] Burrell K.H., et al., Plasma Phys. Control. Fusion 44 (2002) A253
[2.54] Chen Xi, et al., Nucl. Fusion 57 (2017) 086008
[2.55] Chen Xi, et al., Nucl. Fusion 57 (2017) 022007
[2.56] Viezzer E., et al., Nuclear Materials and Energy 34 (2023) 101308
[2.57] Burrell K.H., et al., Nucl. Fusion 60 (2020) 086005
[2.58] Chen Xi, et al., Nucl. Fusion 60 (2020) 092006
[2.59] Gruber O et al 1999 Phys. Rev. Lett. 83 1787
[2.60] Luce T C et al 2004 Phys. Plasmas 11 2627
[2.61] J.Hobirk et al 2012 Plasma Phys. Control. Fusion 54 095001
[2.62] J Citrin and P Mantica 2023 Plasma Phys. Control. Fusion 65 033001
[2.63] Jenko F.,et al. Phys. Plasmas, 7 (2000) 1904
[2.64] Mariani A., et al., submitted to Nucl. Fusion
[2.65] Balestri A., et al., to be submitted to Plasma Phys. Control Fusion
[2.66] Aucone L., et al., to be submitted to Plasma Phys. Control Fusion
[2.67] Nelson A.O., et al., Phys. Rev. Lett. 131 (2023) 195101

Chapter 3

DIVERTOR AND SOL PHYSICS, PLASMA-WALL INTERACTIONS

P. Innocente, E. Tsitrone, M. Wischmeier,
S. Brezinsek, H. Bufferand, N. Carlevaro, M. Cavedon, G. Ciraolo, J.W. Coenen, Y. Corre, A. Gallo,
J. Gaspar, G. Nallo, R. Neu, F. Subba, C. Theiler, N. Vianello, S. Wiesen, M. Wirtz

This chapter discusses divertor scenarios, Scrape-off layer (SOL), far-SOL and plasma wall interaction studies that can be done in DTT. The main contributions that DTT can provide to ITER and DEMO are identified, together with the requirements in terms of diagnostics and auxiliary systems. The advised sequence of divertor operation has been defined based on the power available in the different DTT phases.

3.1 Introduction

As underlined in the EUROfusion roadmap, power exhaust is a major challenge for next step fusion devices. One of the main targets of DTT is to explore reactor relevant plasma exhaust solutions, while keeping an integrated approach to core-edge scenarios. DTT is meant to accompany ITER exploitation and set the basis for the DEMO design in this crucial area.

As far as plasma exhaust is concerned, the divertor is a key component, which will have to face unprecedented heat, particle and neutron loads compared to present-day devices (see [3.1] for ITER and [3.2] for DEMO). DTT has been specifically designed to provide new insights in this area, in particular:

- Testing whether the advanced divertor solutions (e.g., high radiative single null scenarios, alternative divertor configurations or liquid metals) can be technically integrated and are able to withstand the strong thermal loads foreseen in DEMO [3.3];
- Improving the experimental knowledge in the area of plasma exhaust and plasma wall interactions (PWI) for parameter ranges that cannot be addressed by present devices.

Table 3.1 lists the parameter range that DTT can reach, with relevant figures of merit for power exhaust, such as P_{SOL}/R and P_{SOL}B/R, which are related to the heat flux able to reach the divertor target. It shows that DTT in its final stage of operation at full power lies significantly above present day machines, and reaches parameters of interest for ITER [3.1] and DEMO [3.2] in terms of power exhaust. In addition to the normalized power crossing the separatrix, DTT can test SN and most alternative divertor configurations (ADC) in collisional regimes and magnetic configurations close to those of ITER/DEMO.

Table 3.1. Comparison of DTT with present-day machines and ITER/DEMO for parameters of relevance for plasma exhaust (Note that the values given here for DTT correspond to its final stage of operation at full power for a standard divertor single null configuration. Refined values for the various divertor configurations can be found in Table 3.5 in section 3.3.2).

	AUG	**JET**	**JT-60SA**	**DTT**	**ITER**	**DEMO**
R (m)	1.65	3.0	2.93	2.19	6.2	9
a(m)	0.5	1.0	1.14	0.70	2.0	2.9
I_p (MA)	1.4	4	4.6	5.5	15.0	17.75
B_T (T)	3.2	3.45	2.28	5.85	5.3	5.86
V_p (m^3)	13	80	122	28	853	2218
<n> (10^{20} m^{-3})	1.2	1	0.9	1.5	1.0	0.8
P_{Tot} (MW)	30	40	35	45	150	450
P_{SOL} (MW)	**24**	**32**	**25**	**32**	**100**	**170**
P_{SOL}/R (MW/m)	**14**	**11**	**9**	**15**	**16.13**	**18.9**
P_{SOL}B/R (MW*T/m)	**44**	**37**	**20**	**85**	**85**	**111**

The DTT divertor has been designed in a flexible way, so that a wide range of alternative divertor configurations, such as the X divertor (XD), the Super X divertor (SXD), the SnowFlake divertor (SF), the Double Null divertor (DN), can be accommodated for comparison with the Single Null (SN) reference divertor configuration. In addition, plasma shapes with negative triangularity (NT), which has recently been shown to be potentially attractive for a reactor, can also be accommodated. This is illustrated in Figure 3.1.

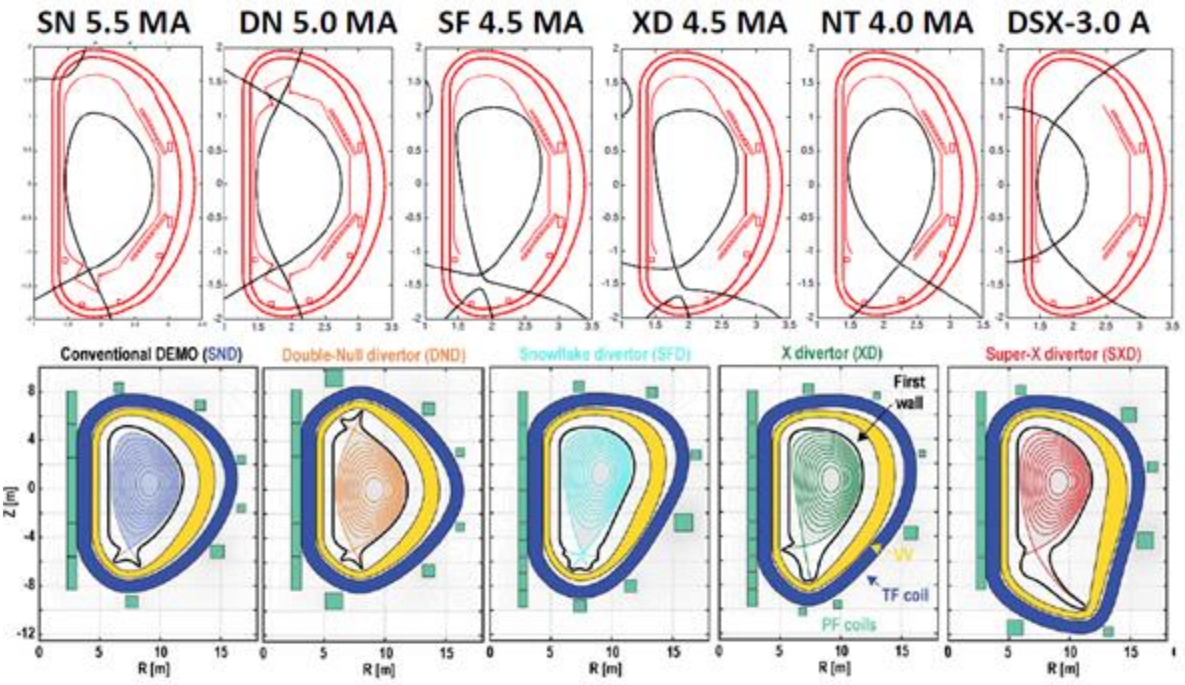

Figure 3.1: Example of DTT plasma shapes (upper row) and their counterparts presently studied for DEMO (lower row) (from reference [3.3])

In this chapter, the high priority research topics to be tackled by the DTT programme in the area of plasma exhaust and plasma wall interactions are listed. Section 3.2 gives a short description of the DTT plasma facing components as well as the main diagnostics relevant for divertor, SOL and PWI physics. Further details are summarised in Appendix D. Section 3.3 is focused on the divertor physics studies, presenting how the comparison between the reference SN configuration and ADC will be addressed. Section 3.4 is dedicated to far SOL and first wall physics, while section 3.5 describes the R&D programme in the field of PWI.

3.2 DTT plasma facing components and diagnostics relevant for divertor and SOL physics

The shape presently selected for the divertor is the so-called Wide Flat Divertor (WFD), composed by three sections: the inner vertical target (IVT), the flat central part (Dome) and the outer vertical target/horizontal target (OVT/OHT). The central Dome acts as a standard dome in terms of neutrals sub-divertor closure for SN configuration with strike points on IVT/OVT and as a target for XD, NT and SF configurations. The divertor accepts all previously described configurations and their long leg variants moving the inner strike point upward on the IVT. For the reference SN standard scenario at B_T = 5.85 T and I_p = 5.5 MA the grazing angle between magnetic field lines and the target surface at both IVT and OVT is 2° (see Table 3.2), which is smaller than the ITER one but similar to the one presently foreseen for DEMO. Based on power exhaust modelling done with the SOLEDGE2D and SOLPS-ITER edge codes [3.4], the WFD provides reasonable performance in terms of core impurity concentration ($Z_{eff} \approx 3$) required to operate in detached conditions by impurity seeding in the DTT full power (P_{add} = 45 MW, $n/n_G \approx 0.5$) scenario E in SN configuration at 5.5 MA and XD at 4.5 MA.

The divertor is composed by 54 divertor modules (see Figure 3.2), 3 for each 20° sector; out of these, 4 can be test modules. In the standard modules, the configuration is based on the ITER-grade bulk W monoblock concept (see Table 3.2). The standard modules can be cooled by water in the 30-130°C range (which allows replicating ITER conditions). The technology has been qualified up to 20 MW/m^2. As in ITER, the divertor monoblocks are shaped toroidally to protect leading edges.

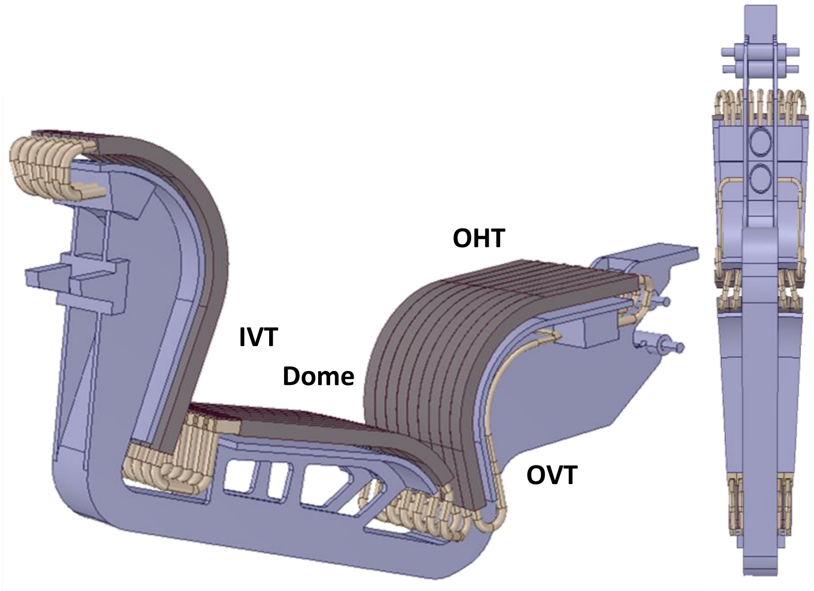

Figure 3.2: Side view and bottom view of the divertor module with 9 monoblocks row on the IVT and 7 monoblocks row on the dome and IVT.

Table 3.2. Monoblocks parameters on the different parts of divertor with: α the reference grazing angles for SN-PT (SN) and SN-NT (NT) configurations; l_{mb} monoblocks length in toroidal direction, g_{cas} distance between cassettes, q_{tot}^{bevel} monoblocks bevel

	α [°]	l_{mb}[mm]	g_{cas}[mm]	ϑ_{tot}^{bevel} [°]	shaping
IVT	2 (SN)	24	8	1.65	
OVT	2 (SN)	24.5	10	1.45	
Dome	5.2 (NT)	25.5	9.5	8.6	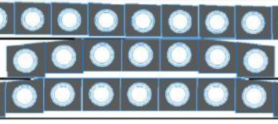
OHT	1.3 (NT)	27.5	12	4.6	

The first wall (FW) consists of three main components: the inboard (IFW), the outboard (OFW) and the top (TFW). All FW modules are actively cooled by water at 60°C. The OFW and TFW will be realized by plasma spray tungsten coating on Inconel panels and can stationary dissipate up to 0.5 MW/m^2. In the IFW 50% of the wall is realized by 18 W monoblocks limiters using the same technology of the divertor, allowing a maximum stationary toroidally averaged conductive heat flux of 7.5 MW/m^2. This higher limit can be useful during the initial limiter phase of discharges and for limiter experiments.

The PFCs (FW and divertor) can be cleaned and conditioned by heating up to 200 °C (up to 165 °C for ducts and bellows), Glow Discharge Cleaning (GDC) and boronization after maintenance activities operations (B_T off). GDC and boronization can be done also on weekends switching off the toroidal field but with heating at lower temperature (FW up to 130 °C, ducts and bellows up to 100 °C). Ion cyclotron wall cleaning (ICWC) will be available between pulse operations when B_T is on.

The following tables summarize the most relevant diagnostics for divertor and SOL physics studies available since the beginning of DTT operation (Table 3.3) and at the beginning of full power operation (Table 3.4).

Table 3.3. Phase 1 main PWI diagnostics

Diagnostic	**Measured parameter**	**Number/location**
Thomson scattering	n_e, T_e	*core/pedestal/SOL*
Charge exchange	*Ion temperature/rotation*	*core/pedestal/SOL*
Langmuir probes	T, n, J_{sat}	*divertor & FW*
Thermocouples	T_w	*divertor & FW*
Infrared cameras	T_w	*poloidal direction IVT, Dome, OHT and FW. Toroidally all PFCs*
Bolometer cameras	*Total radiation, tomography*	*core/divertor*
Visible D_α array	D_α *emission*	*divertor*
Visible/VUV spectrometers	*Impurities line emissions*	*divertor*
Visible Zeff Bremsstrahlung	Z_{eff}	*core/divertor*
Penning spectroscopy	*Neutral pressure and composition*	*divertor*
Fast Pressure Gauges	*Neutral Pressure*	*sub-divertor* *outer mid-plane*
RGA Neutrals Gas Analyzer	*Neutral Gas composition*	*sub-divertor* *outer mid-plane*
Microbalance/long term samples	*Deposition*	*divertor*

Table 3.4. Additional PHASE 2 PWI diagnostics

Diagnostic	**Measured parameter**	**Number/where**
Reflectometry	Density Profile Reconstruction	*Core/Pedestal/SOL*
Thomson scattering	n_e, T_e	*divertor*
Scanning infrared interferometer	n_e	*divertor*
Reciprocating Langmuir probe	n_e, T_e, J_{sat} *profile*	*outer mid-plane*
GPI	*Plasma fluctuations*	*outer mid-plane*
LIBS	*Surface Material composition*	*divertor*
Thermal helium beam	n_e & T_e *fluctuations*	*outer mid-plane*

3.3 Divertor and edge physics studies

Following basic Scrape-off Layer physics, which assumes that the heat transporting width of the SOL is inversely proportional to the plasma current, the parallel heat flux is proportional to $P_{SOL}B_T/R$, with P_{SOL} the total power entering the scrape-off layer. With its high heating power and therefore potentially large P_{SOL} combined with the high B_T, DTT will be able to explore power exhaust conditions that are relevant to ITER and DEMO.

DTT will serve to address several aspects of fundamental SOL physics for elaborating heat flux mitigation techniques and particle exhaust at parameters close to ITER and DEMO, such as e.g. SOL collisionality, neutrals opacity, plasma density, SOL connection length. The access to the various divertor topologies and configurations described in the introduction provides a wide range of parameters that can be modified to study the impact on the divertor solution, as well as the pedestal and core performance. Interpretative transport and turbulence studies will be crucial for identifying the dominating physics processes under varying conditions. One of the advantages of DTT will be that while the dimensions of the divertor will be certainly smaller than those of ITER or DEMO, the device has the potential of having neutral mean free path to divertor size ratios that are highly relevant for these larger devices. This is often an issue for identifying the relative weight of the individual physics processes in present-day machines in view of extrapolations. The expected high recycling fluxes and consequentially the high divertor neutral pressure, combined with the large volume of the divertor, will furthermore facilitate the validation of the role of neutral-neutral collisions with respect to the evaluation of the overall tokamak pumping efficiency. Certainly, the high neutral pressure, combined with the high recycling fluxes and plasma densities, provide a test-bed to scrutinize the role of atomic as well as molecular volumetric processes with respect to power, but especially to momentum removal and thereby addressing a highly disputed subject on the role of molecular physics. DTT with its size and the high toroidal field, as well as sufficiently long pulse durations, implying a constant recycling flux at the targets, will allow investigating the predicted role of B_T in facilitating the access to detachment. It is expected that the machine size and high B_T will favorably impact the compressibility of the impurity and thus its enrichment in the divertor. Such findings will need to be compared to experimental data from JT-60SA, JET, WEST, ASDEX Upgrade, as well as TCV and MAST-U.

With respect to SOL perpendicular particle and heat transport, a key element that DTT should be able to address is the role of the ion vs. the electron heat channel and thus the regimes in which the empirical Eich scaling [3.5] dominates over the numerical predictions from the turbulence code XCG1 for λ_q [3.6]. Furthermore, DTT will be able to provide further insights on enhanced transport at the H-L mode transition threshold regarding the normalized collisionality parameter α_t, defined in Refs. [3.7][3.8]. This will also allow testing scaling predictions for the density decay profile in ITER relevant scenarios and thereby provide further insights into the associated increase of first wall fluxes. The expected enhanced fluence per pulse to the main chamber wall during operation compared to present-day devices may also allow shedding additional light on the long-term storage effects and the dynamic balance of adsorption and implantation versus desorption, in view of particle balance issues relevant for long pulse operations. With a cryo-pump capable of actively pumping He, this enhanced fluence to the plasma facing components will allow providing more insight into the role of the first wall as intermediate storage in view of the overall fuel cycle and in particular the removal of He.

Overall, DTT will provide a highly ITER and DEMO relevant environment for benchmarking the numerical codes against experimental data and thereby bridge the existing gap for extrapolations to ITER and DEMO, thus addressing its main mission as a Divertor Test Tokamak.

3.3.1 Divertor scenario development

Naturally, experimental work is expected to start with single null operation as this is the current reference for ITER as well as DEMO and the most accessible in terms of control after commissioning of the device. Further on, alternative divertor configurations will be used for parameter studies to access the various physics dependences (e.g. B_T, B_p ρ_i, α_t → related perpendicular transport). The documentation of well diagnosed experimental results will allow the characterization of divertor, pedestal and core parameters in order to validate integrated core-edge codes independently of the magnetic configuration. Generally, the overall aim will be to establish a reliable operation of the device with low levels of W, with impurity seeding and at high performance in H-mode. The scientific community has not yet established a unique set of parameters along which to qualify the performance of any particular divertor configuration. In this respect, once such criteria have been settled, DTT has the potential to provide data for a sufficiently informed assessment of the most performing divertor configuration, while providing the physics basis to extrapolate to the appropriate configuration for DEMO.

In its course of operation, DTT shall attain the following milestones to achieve the before mentioned goals:

- Investigate heat flux mitigation techniques by strike point sweeping for machine protection, in line with establishing detachment control as the performance of the device is increased in terms of current, field and heating power;

- Assess the accessibility to the detachment by variations of fueling and impurity seeding for various magnetic configurations as these become available for operations;
- Investigate various degrees of detachment from partial to full detachment and impact on the choice of impurity levels and mixes on plasma performance;
- Investigate the performance of various fueling methods (SMBI, pellets, regular gas valves) and the impact of their poloidal variation;
- Investigate the parallel heat flux to the two divertor targets as a function of the magnetic configuration and topology;
- Develop and establish reliable real time control methods for power and particle exhaust;
- Access and retain detachment across the various phases of the discharge independently of the magnetic configuration, to assess the dynamic resilience towards a loss of power exhaust control;
- A priority of DTT will be the study of small and no ELM regimes compatible with exhaust solutions, as these are currently believed to be the most DEMO relevant regimes (see Chap. 2, Sec. 2.8). Such operational scenarios include the EDA H-mode, the QCE as well as the X-point radiating regime. Furthermore, the use of RMPs (3D effects) is foreseen in connection with expected small λ_q to address ITER/DEMO related issues of detachment under non toroidally symmetric conditions.

3.3.2 Alternative divertor configurations

DTT has been specifically designed to study the capability of a large set of alternative divertor magnetic configurations in order to develop acceptable conditions at the divertor targets while maintaining good core performance. The magnetic system of DTT can realize the most promising alternative divertor configurations [3.3]: the flux flaring towards the target (XD), the increasing of the outer target radius (Super-X) and the movement of a secondary X-point inside the vessel (X-point target) as well as the entire range of SnowFlake (SF) configurations and the Double Null (DN). Among these, the ADC with highest priority will be the XD, which is expected to provide some advantage with respect to the SN, without requiring highly increased engendering constraints and costs. Although L-mode negative triangularity (NT) is not considered as such to be an alternative divertor configuration, it presents at least one major advantage in power exhaust, the absence of ELMs. They can be avoided, even at high input power, in the reversed toroidal field configuration, still retaining a good global energy confinement thanks to the lower transport in the $0.5 \leq \rho \leq 0.9$ region. As a possible second advantage, the L-mode operation can provide a longer heat flux decay length, making power exhaust dissipation by the divertor easier. Furthermore, NT might ease the restrictions on how much power may at most be dissipated in an XPR, as retaining sufficient power crossing the separatrix to be above the H-L back transition would not be a requirement *per se*. The device will also allow investigating the compatibility of plasma performance in NT with power and particle exhaust requirements. To this end, NT experiments will be performed in reversed field configuration, which provides the easiest access to the L-mode no-ELMs regime. This has the additional advantage to be compatible with a unidirectional toroidal shaping of the monoblocks of the dome (and of the OHT). In fact, for the same direction of the plasma current, the inner strike point of NT in reversed B_t and the outer strike point of XD (or SN and SXD) in forward B_t will share the same direction of the magnetic pitch angle. Note that NT experiments in forward B_t are not relevant for the assessment of the configuration performance, since they are more prone to the L-H transition and consequently to the presence of ELMs, whose removal is the possible main advantage of the configuration.

Due to limitations based on the maximum forces to the poloidal coils, on the divertor shape and the lack of a second divertor on the top of the vessel, not all the previously mentioned configurations can be realized or exploited at the maximum plasma current or additional power (see Table 3.5). The shapes of some of these configurations are shown in Figure 3.1 and compared with proposed SN and ADCs configurations in DEMO.

Table 3.5. Maximum plasma current and additional power for the SN and alternative configurations.

Configuration	**Max I_p (MA)**	**Max P_{add} (MW)**
SN-PT	*5.5*	*45*
XD	*4.5*	*45*
SFP/SFN	*4.5*	*45*
SN-NT	*4.0*	*45*
SN long leg	*5.5*	*45*
SXD	*4.5*	*45*
DN	*3.8*	*8(*)*
DN-long leg	*3*	*8(*)*
DXD long leg	*2.5*	*8(*)*

(*) The value depends on the final definition of the top first wall

3.4 Far SOL physics and first wall loads

While the divertor is the most heavily loaded component in terms of plasma exhaust, the first wall is also a key player for PWI, in particular during plasma ramp-up and ramp-down phases. As it represents a large surface with a poorer impurity screening efficiency compared to the divertor, it can also be a significant source for impurity core contamination during the flat-top part of the discharge, depending on the local plasma conditions. Those plasma conditions (in particular incident wall fluxes and energy) are not well defined at present, as the far SOL physics is complex and needs further investigation. Finally, the first wall also has to withstand transient loads due to off-normal events, such as disruptions or Vertical Displacement Events (VDE).

This section lists the contribution of DTT in this area, which is of particular relevance since DTT features a full tungsten environment, as foreseen for DEMO but also under discussion for ITER at the time of writing.

It should be noted that adequate diagnostic coverage of the first wall is necessary to progress in this area: far SOL plasma profiles, first wall heat and particle loads (particle fluxes and energy), W erosion and deposition …, as well as plasma edge modelling tools with grids extended up to the walls.

3.4.1 Optimizing plasma ramp-up and ramp-down

Optimizing the plasma ramp-up and ramp-down will be done in close connection with scenario development (see Chapter 2, Section 5.3), taking into account the following constraints:

- Minimizing flux consumption in the ramp-up phase to ensure a sufficient duration for the flat-top;
- Avoiding MHD, in particular linked to the complex interplay with W transport and subsequent impact on plasma core profiles;

- Avoiding plasma control issues (restricted l_i and β range).

As was shown in full W devices, restricting the limiter phase to a duration as short as possible and applying ECRH early in the discharge should be key to ensure that the right target in terms of plasma conditions can be reached for the subsequent phase of the discharge. The following points are of particular interest from the point of view of plasma exhaust and PWI:

- Minimize W influx from the first wall to the plasma core during ramp-up/ramp-down and characterize first wall erosion and material migration during this phase;
- Ensure acceptable heat loads on the first wall during ramp-up/ramp-down.

The impact of boronization on the W influx from the first wall should in particular be investigated.

3.4.2 Assessing far SOL transport and first wall fluxes

Next step fusion devices are expected to operate at high separatrix density / divertor neutral pressure in order to ensure plasma partial (or even full) detachment and stay within tolerable heat loads on the divertor. In present-day devices, a progressive broadening of the SOL density profile, the so called “density shoulder formation” is observed when increasing fueling to reach those conditions [3.9][3.10]. This can impact first wall heat and particle loads, as well as first wall erosion. Characterizing the first wall loads under conditions relevant for divertor detachment and understanding the underlying physics (turbulent transport in the far SOL region) is therefore key for predicting the lifetime of the first wall in next step fusion devices.

DTT will also have to stay in this regime (high density/partial divertor detachment) when operating at high power and will therefore contribute to progress in the understanding of far SOL transport in relevant conditions. In addition to the first wall diagnostics quoted in the previous section, turbulence imaging diagnostics, as well as measurements of the divertor pressure and of the upstream and target plasma profiles, would bring additional value for the subsequent modelling effort. State-of-the-art edge turbulence codes would be required for interpreting the experimental results obtained.

The main items to be investigated include:

- Characterization of the wall loads (from plasma, charge-exchange neutrals, radiation) and associated W erosion/migration during all phases of the discharge for the reference SN configuration (including the impact of ELMs) and overall in-vessel power and energy balance;
- Characterization of the far SOL plasma and turbulent SOL transport at high separatrix density / divertor pressure for different scenarios (reference type I ELMy H mode, mitigated and ELM-free regimes), varying in particular the turbulent parameter α_t (defined in Ref. [3.6]), the fueling method (gas vs pellets);
- Impact of the divertor configurations (reference SN configuration versus ADC) on far SOL plasma and wall loads, as well as associated W erosion/migration.

In addition, 3D effects (such as impact of RF systems, discrete limiters etc. and tile shaping with associated local shadowing from the plasma) should be taken into account for the wall loads and the associated material migration (see also Section 3.5.2).

3.4.3 Impact of off-normal events on the first wall

Finally, the wall loads due to off-normal events (unmitigated/mitigated disruptions, VDE, runaway electrons impact …) should be characterized. As DTT can operate at high field/high current, the disruptions loads are

of particular interest for comparison with scalings derived from present-day devices. Fast thermal loads diagnostics would be required for that purpose.
Possible first wall damage following off-normal events should be documented in situ (regular visual inspection) and ex situ after retrieving the damaged components (W recrystallization, surface topology change, melt layer, etc.). This will provide data to validate the codes assessing material cracking and melting for next step fusion devices, provided the associated thermal loads can be specified accurately enough.

3.5 Plasma Wall Interactions in a full tungsten environment

Controlling Plasma Wall Interactions (PWI) is key for operating a future reactor successfully. Indeed, PWI can affect plasma performance (as it provides the source of impurities potentially penetrating to the core, and governs the plasma recycling regime), reactor maintenance (as net erosion of the vessel components will determine their lifetime before a change is required) and safety (as fuel retention and dust production stemming from PWI should be minimized).

Tungsten is presently considered as the most promising plasma facing material for DEMO and a future reactor. Discussions are also ongoing at the time of writing to shift to a full tungsten environment for ITER.

DTT therefore offers an outstanding opportunity to study PWI in a full W environment under relevant high power operation and investigate the behaviour of ADCs in this regard. In addition, DTT will contribute to the validation of PWI codes for extrapolation to next step devices (such as simulation tools for local and global W migration or fuel retention). Finally, DTT is equipped with test divertor modules, allowing dedicated PWI studies as well as test of advanced materials and cooling schemes for PFC.

This section will deal with the following items:

- Wall conditioning;
- W erosion and subsequent material migration;
- Fuel retention and recovery; dust production and removal;
- W morphology changes under plasma loading;
- PWI impact on machine protection.

Finally, future PFC testing and diagnostics enhancements are briefly discussed, but the reader is referred to Chapter 9 for more details.

3.5.1 Wall conditioning

Wall conditioning was shown to be key for plasma performance in high Z metallic devices (most high Z machines such as ASDEX Upgrade, Alcator C Mod, EAST or WEST perform regular low Z conditioning, using boronization or lithium coatings) [3.11][3.12][3.13]. Wall conditioning is of particular importance for starting a device after a vent or during an experimental campaign to perform specific high performance programmes (for instance low density/collisionality in ASDEX Upgrade). Boronization is presently contemplated for ITER, should the device be shifted to a full W configuration. Wall conditioning for DEMO is still an open issue, given the extremely high duty cycle foreseen.

DTT is equipped with a variety of wall conditioning techniques of relevance for ITER: baking, glow discharge cleaning (GDC), standard boronization, Ion Cyclotron Wall Conditioning (ICWC). It should be noted that only ICWC can be performed between plasma discharges, while GDC/boronization can be performed over a weekend with the toroidal field off, as is the case for all superconducting devices.

The following items should be tackled:

- Optimizing the wall conditioning sequence after a vent (baking / GDC / boronization);
- Monitoring the impact of GDC/boronization on plasma recycling (main fuel) and intrinsic impurities (tungsten and oxygen level in particular) during a campaign and defining the optimized boronization parameters / frequency. In particular, assessing the oxygen source and how it evolves following boronizations would bring valuable input for ITER/DEMO;
- Investigating the boron deposited layers (structure, thickness, uniformity, stability, fuel trapping …) as a function of the boronization parameters.

As this has been lacking on present-day devices, it would be worth adapting a number of diagnostics to be able to take measurements during the conditioning phases (density, temperature, spectroscopy … during GDC/boronization), if technically feasible. Adding an impurity powder dropper could also be considered, in order to be able to perform real time conditioning, as presently considered as a mitigation plan for ITER.

Finally, the relevance of trying to start DTT for a short period without a boronization in order to get reference shots in a boron free machine should be discussed, in terms of risks (increased operational time and complexity of start-up / reduced operational domain) versus scientific output for ITER/DEMO.

3.5.2 W erosion and material migration

Controlling W core contamination will be key for plasma performance. This section will focus on the W erosion sources and how W is screened in the SOL, while subsequent W transport in the pedestal/core and resulting W core concentration is dealt with in Chapter 4.

The following items should be addressed as a function of plasma regimes (from attached to detached divertor conditions, in L and H modes, with and without impurity seeding, ELMing or ELM free plasmas) and divertor configurations (comparing SN with ADC):

- Quantitative evaluation of W gross erosion sources from main chamber and divertor. The contribution of inter-ELMs versus intra-ELMs should be assessed;
- Evaluation of W screening efficiency for the different W sources in the divertor and main chamber (looking in particular at the prompt W redeposition fraction as a function of plasma conditions / divertor configuration).

The main contributors to the W core contamination (divertor versus main chamber components) should be identified in close connection with the W edge/core transport part of the programme, so that integrated scenarios minimizing W impact on plasma performance can be developed. This requires an extensive coverage of the vessel in terms of line of sights for the visible spectroscopy, viewing all components of interest in the divertor region as well as in the main chamber. The time resolution of this diagnostic should allow ELM resolved measurements. It would also be very valuable to provide WI and WII line intensity measurements, to gain insight on the prompt W redeposition processes.

In addition, material migration (defined as wall material transport from a surface to another) should be investigated. This will allow assessing PFC erosion and lifetime, as well as the location of material deposition, useful to optimize fuel removal methods (see Section 3.5.3). Regarding deposited layers, it will be of interest to check whether DTT, expected to run relatively long pulses, will form unstable layers generating UFO and impurity ingress in the plasma, as was observed in other long pulses devices operating with actively cooled PFC. The following points should be investigated:

- Global net erosion/deposition pattern to be assessed, in order to assess PFC lifetime both for the divertor and the main chamber components;

- Structure of the deposited layers : layer thickness, layer stability during operation/vents, composition (W, impurities (B, O …), fuel trapping …);
- Local erosion/deposition pattern, such as in the gaps of castellated structures, shadowed areas in shaped structures.

In addition to visible spectroscopy, giving access to gross W erosion, this research area will require specific diagnostics, such as quartz microbalance (QMB) giving results on erosion/deposition during / after a shot) or components (such as specific samples or erosion marker tiles giving campaign integrated results). It would also greatly benefit from a divertor manipulator. It will involve a dedicated post mortem analysis program, which should be planned well ahead, to optimize the components installation and retrieval for analysis. The interpretation of the results will rely on using state-of-the-art material migration codes, if possible in 3D given the discrete limiter structures foreseen for the DTT first wall.

3.5.3 Fuel retention and recovery; dust production

Fuel retention should be minimized in next step fusion devices, for safety (in-vessel inventory Tritium limit) as well as for maximizing the Tritium (T) breeding ratio. Dust production should also be minimized for safety and operational issues.

In full W devices using boronization as conditioning technique, as potentially contemplated for ITER, fuel retention is expected to be dominated by codeposition with boron (B). DTT will complement the scarce database from present-day full W devices on this topic. Both particle balance, allowing assessment of fuel retention on a shot-to-shot basis, and post mortem analysis, providing campaign integrated results, should be performed.

In addition, DTT can contribute to optimizing the cleaning sequence for ITER by assessing the efficiency of fuel removal in a W/B environment.

The following items should be investigated:

- Assessment of fuel retention in a full W environment (long pulse / high fluence required for particle balance accuracy) as a function of plasma regimes (attached / detached divertor conditions) and divertor configuration. Investigating the impact of plasma composition in reactor relevant conditions (D, traces of He, seeding impurities) is also an important issue;
- Comparison of fuel recovery efficiency for the various techniques contemplated for ITER: baking / GDC / Ion Cyclotron Wall Conditioning (ICWC) (and potentially ECWC if technically feasible, although ICWC is considered as more efficient);
- Assessment of dust production and characterization of the dust collected;
- Impact of boronization on all the points mentioned above (fuel retention / removal / dust production).

Given the low fraction of gas expected to be retained in a full W environment, the particle balance diagnostic should be designed in order to achieve an accuracy better than 1% in measuring the amount of injected and extracted gas.

In situ fuel retention measurements should also be implemented to complement the post mortem analysis programme. DTT offers an integrated test-bed for the laser based diagnostics foreseen for ITER, such as LID-QMS (laser induced desorption – quadrupole mass spectrometer) and LIBS (laser induced breakdown spectroscopy). It is recommended to assess which option (LID QMS, LIBS or both) would be the most relevant to assess fuel retention and layer composition in DTT (presently, only LIBS is foreseen as Phase 2 diagnostic in the baseline, see Table 3.4).

3.5.4 W morphology changes under plasma loading

W morphology is known to be modified under plasma loading, potentially leading to enhanced W erosion or degraded heat exhaust capability. DTT will provide an integrated test of components under relevant combined heat/particle plasma loads. The following points should be investigated:

- Assessment of W material properties changes under D plasma loading (blistering ...) and He operation (nanostructures, W fuzz ...) and potential impact on PFC power handling performance/ W erosion.
- Assessment of W material properties changes under high power loading (W recrystallization, cracking, local melting…) and potential impact on PFC power handling performance/ W erosion

Finally, although DTT will reach a significantly lower neutron fluence compared to ITER/DEMO, the impact of neutrons on PWI should be monitored, as some effects (such as enhanced fuel trapping in W) appear at moderate fluence (~0.1 dpa).

3.5.5 Wall monitoring system

As DTT will be operated with actively cooled components, having a reliable wall monitoring system is key to protect the integrity of PFC and avoid long shutdown periods in case of water leaks.

The full W environment of DTT will be prone to reflections and, as it was shown in other W devices, erosion/redeposition on the PFC, leading to strong local W emissivity changes. All of the above makes infrared data interpretation challenging both for physics and for machine protection.

It is therefore recommended to allocate experimental time for testing machine protection schemes in the early phase of operation of DTT, as well as to set up a procedure to monitor W emissivity changes during operation.

3.5.6 Future PFC and edge diagnostics enhancements: using DTT divertor test modules

DTT will be equipped with a set of four divertor test modules (DTM), which can be more easily removed for inspection/modifications than other divertor sectors. It is recommended to establish a dedicated program taking advantage of this feature, well ahead of the start of operation. In particular, these sectors could be equipped with high risk of failure diagnostics (like Langmuir probes/Quartz Micro Balances ...) for a faster replacement.

The reader is referred to Chapter 9 for a detailed description of the issues to be investigated with those modular divertor sectors, but a first list of items that could be investigated is given below, first in terms of PWI related studies:

- Markers for dedicated erosion/redeposition studies;
- Dedicated components for D-retention measurements;
- Dedicated set-up to expose pre-damaged components or perform melting studies;
- Testing of new diagnostics (mainly) for detachment control and heat flux measurement.

In addition, options for advanced components could be tested, such as for instance:

- Testing of advanced W materials (W alloys ...) and components (DEMO like …)
- Preparing a divertor technology upgrade (optimized tile shaping, non-monoblock technology, such as flat tiles …)
- Running dedicated experiments, associated to modelling, for testing a new divertor shape

- Performing exploratory experiments on liquid metals, should the DTM sectors be suitable for such tests.

All of the above should come in support to the optimization of the divertor shape towards a specific reactor relevant ADC solution on a longer term. The installation of an upper divertor consistent with the lower ADC could also be envisaged.

3.6 Headlines of the research programme for Divertor, SOL and PWI

In this section, we summarize the main headlines of the DTT research programme on divertor, SOL and PWI, according to the various phases of implementation of the DTT heating system and of plasma operations.

Headline number	Headline contents	Priority (+, ++, +++)	ITER	DEMO
Construction Phase 2022-2029				
C.3.1	Definition of first wall shape and parameters	+++		
C.3.2	Definition of markers types and position in FW	++		
C.3.3	Definition of optimal diagnostics requirements for PEX/PWI analysis	++	*	*
Phase 1 2029-2034				
1.3.1	Developments and characterization study of plasma start-up and ramp-up scenarios with boronization	+++	*	
1.3.2	Developments and characterization of plasma start-up and ramp-up scenarios without boronization	+	*	*
1.3.3	Development and characterization of strike point sweeping method	+++	*	*
1.3.4	Development and characterization of SN detached configuration in L-mode	+	*	
1.3.5	Development and characterization of SN detached configuration in H-mode	+++	*	*
1.3.6	Development and characterization of XD divertor configuration	+++		*
1.3.7	Development and characterization of NT divertor configuration	+++		*
1.3.8	Optimization and characterization of boronization	++	*	

1.3.9	Quantification and characterization of D retention in clean W	+++	*	*
1.3.10	Quantification of the impact of boronization on D retention	++	*	
Phase 2 2034-2038				
2.3.1	Experimental assessment of edge transport at high plasma current and comparison with λ_q scalings and theory	+++	*	*
2.3.2	Evaluation of transport parameters in limiter phase and in the far-SOL	+++	*	*
2.3.3	Optimization and characterization of detachment by seeding	+++	*	*
2.3.4	Development and characterization of methods to control detachment	+++	*	*
2.3.5	Development and characterization of ELM control methods by gas-puffing, pellet RMP	++	+	
2.3.6	Development, control and characterization of XPR low-ELMs scenarios	++	+	*
2.3.7	Optimization and characterization of XD configuration with seeding	+++		*
2.3.8	Test new FW and divertor materials	++		*
Phase 3 2038-…				
3.3.1	Optimization of detachment in SN with different seeding	+++	*	*
3.3.2	Optimization and characterization of XD configuration	+++		*
3.3.3	Optimization and characterization of NT configuration	+++		*
3.3.4	Comparison of SN to XD and NT configurations	++		*
3.3.5	Estimation of wall erosion and W migration and validation of codes	+++	*	*
3.3.6	Evaluation of D retention after erosion/redeposition and W surface modification	+++	*	*
3.3.7	Development and characterization of methods for D removal	++	*	*

3.7 References

[3.1] R.A. Pitts et al., “Physics basis for the first ITER tungsten divertor”, Nuclear Materials and Energy 20 (2019) 100696, https://doi.org/10.1016/j.nme.2019.100696

[3.2] F. Maviglia et al., “Impact of plasma-wall interaction and exhaust on the EU-DEMO design” Nuclear Materials and Energy 26 2021) 100897, https://doi.org/10.1016/j.nme.2020.100897

[3.3] H. Reimerdes et al., “Assessment of alternative divertor configurations as an exhaust solution for DEMO”, Nucl. Fusion 60 (2020) 066030, https://doi.org/10.1088/1741-4326/ab8a6a

[3.4] P. Innocente et al., “Design of a multi-configurations divertor for the DTT facility” Nuclear Materials and Energy 33 (2022) 101276, https://doi.org/10.1016/j.nme.2022.101276

[3.5] T. Eich et al, “Scaling of the tokamak near the scrape-off layer H-mode power width and implications for ITER” Nucl. Fusion 53 (2013) 093031; https://doi.org/10.1088/0029-5515/53/9/093031

[3.6] C. S. Chang et al., “Constructing a new predictive scaling formula for ITER’s divertor heat-load width informed by a simulation-anchored machine learning” Phys. Plasmas 28 (2021) 022501; https://doi.org/10.1063/5.0027637

[3.7] T. Eich et al, “Turbulence driven widening of the near-SOL power width in ASDEX Upgrade H-Mode discharges” Nucl. Fusion 60 (2020) 056016; https://doi.org/10.1088/1741-4326/ab7a66

[3.8] T. Eich and P. Manz and the ASDEX Upgrade team “The separatrix operational space of ASDEX Upgrade due to interchange-drift-Alfven turbulence” Nucl. Fusion 61 (2021) 086017; https://doi.org/10.1088/1741-4326/ac0412

[3.9] D. Carralero et al.,”Study on the density shoulder formation in the SOL of H-mode plasmas” Nuclear Materials and Energy 12 (2017) 1189–11 93 http://dx.doi.org/10.1016/j.nme.2016.11.016

[3.10] N. Vianello et al “Scrape-off layer transport and filament characteristics in high-density tokamak regimes” Nucl. Fusion 60 (2020) 016001; https://doi.org/10.1088/1741-4326/ab423e

[3.11] J. Winter “Wall conditioning in fusion devices and its influence on plasma performance” Plasma Phys. Control. Fusion 38 (1996) 1503;

[3.12] T. Wauters et al. “Wall conditioning in fusion devices with superconducting coils” Plasma Phys. Control. Fusion 62 (2020) 034002; https://doi.org/10.1088/1361-6587/ab5ad0

[3.13] D. Douai et al ”Recent results on Ion Cyclotron Wall Conditioning in mid and large size tokamaks” Journal of Nuclear Materials 415 (2011) S1021; https://doi.org/0.1016/j.jnucmat.2010.11.083

Chapter 4

TRANSPORT PHYSICS AND INTEGRATED MODELLING

C. Angioni, P. Mantica, I. Casiraghi

In this chapter, the main elements of the DTT contribution to the research on tokamak transport and confinement are described, with particular emphasis on the progress towards ITER operation and the definition of a DEMO tokamak reactor. The domains of dimensionless parameters, which are achievable in the different phases of the DTT operation, are identified based on general scaling laws, and their high (unique) relevance in addressing the challenges of core-edge integration in a fusion reactor from the transport physics standpoint is underlined. The main missions in this topical area are described; possible experiments on transport and confinement are organized in four main groups, and outlined in the different phases of operation of DTT. Finally, plasma profiles from theory-based transport modelling predictions are shown as examples of reference conditions that can be obtained in DTT experiments. The chapter is concluded with basic lists of essential diagnostics and headlines of the research programme.

4.1 Introduction

In this chapter, the main properties of DTT to address critical questions in the field of tokamak transport and confinement are presented, related possible experimental research is outlined and applications of integrated modelling with specific emphasis on scenarios are described. The connection of the experimental research with the different phases of operation of DTT is highlighted, with particular emphasis on the foreseen achievable values of magnetic field and current and the progressive availability of heating systems. In particular, this chapter is closely connected with Chapter 2, in what concerns the timeline of the scenario development and the related integrated modelling activities.

The chapter is structured as follows:

Section 4.2 describes the characteristics of DTT that are particularly relevant for transport studies.

Section 4.3 provides an overview of the expected operational windows in both engineering and dimensionless parameters at half field and full field, making use of available scaling laws.

Section 4.4 identifies the main missions of DTT from the standpoint of the research on tokamak transport and confinement.

Section 4.5 outlines the corresponding research organized in four main topical areas.

1. General confinement properties
2. Core-edge integration
3. L-H transition and H-mode pedestal
4. Core transport physics

These four areas are also related to the different phases of operation.

Section 4.6 provides examples of the current flat-top temperature and density profiles, which are predicted to be achieved in the different phases of the DTT operation.

Section 4.7 provides a general description of the diagnostics requirements for the outlined experimental research plan on transport and confinement in the various phases of operation.

Section 4.8 presents a list of the research programme headlines related to transport and confinement.

4.2 DTT characteristics relevant for confinement and transport studies

The main characteristics of the DTT device from a tokamak confinement standpoint are provided by the high magnetic field and high total auxiliary heating power with respect to the plasma size. With a minor and major radius of 0.7 and 2.2 meters respectively, and a plasma volume up to about 35 cubic meters, DTT plasmas can reach currents in excess of 5 MA thanks to the very high magnetic field, up to ~6 T. These properties imply that DTT plasmas can be considered to cover a complementary domain of parameters with respect to tokamaks which, for a given similar plasma size, are more limited in maximum current due to a lower value of the magnetic field. In this respect, an extremely interesting feature of DTT is the possibility of operating the highly powered ECRH system (up to 32 MW) both at full field in 1st harmonic ordinary propagation (O1) mode and at half field in the 2nd harmonic extraordinary propagation (X2) mode. Operation at half field (~3T) and half current allows DTT to also produce plasma discharges that become directly comparable to those obtained in low field tokamaks, which have a lower capability of reaching high current through high magnetic field, but providing the possibility of achieving operation at high plasma beta. Operation at high beta, in contrast, will be limited at full magnetic field.

Due to DTT high magnetic field, the combination of high current (5.5 MA) at low plasma size (minor radius of 0.7m) provides very high Greenwald density limit (3.57 10^{20} m^{-3}) [4.1]. The Greenwald density limit is matched by the ECRH O1 density cut-off at 5.85 T, which is at 3.58 10^{20} m^{-3}, allowing DTT operation not to be limited by the density cut-off. Correspondingly, with operation at about half magnetic field (~3 T), the ECRH X2 density cut-off is at 1.79 10^{20} m^{-3}, consistently matching the Greenwald density limit at 2.75 MA. Of course, in conditions in which plasma operation is pushed up to high plasma densities, i.e. at the density limit at the pedestal top, central densities can exceed the cut-off for ECRH absorption. In these extreme conditions, the possibility of applying ECRH has to be carefully examined during the DTT operation.

As will be demonstrated in a set of plots, which show expected achievable dimensionless parameters, the combination of high current (allowing high confinement) and high power (allowing the achievement of high temperatures) yields that DTT plasmas can combine high density with low collisionality in the pedestal region. This feature provides the possibility of achieving combinations of parameters that, differently from present low magnetic field / low current tokamaks, manage to match the conditions that are expected to occur in a fusion tokamak reactor, i.e., low collisionality at the pedestal top with high density and high collisionality at the separatrix. In combination with the full tungsten walls, as currently planned for both ITER and DEMO, these properties put DTT in a unique condition in order to address critical open questions on the integration among core, edge (pedestal) and SOL, the big challenge towards the definition of the operational point of a fusion reactor. High core confinement, sufficiently high pedestal pressure, without large edge localized modes (ELMs), and tolerable exhaust conditions in the plasma-wall interaction have to be concomitantly achieved by tokamak confinement regimes and related discharge scenarios to be considered reactor relevant. The relevance of the studies dedicated to core-edge integration, which are allowed by the DTT experimental capabilities, is augmented by the high edge opacity to neutral penetration at DTT high densities. This will allow DTT edge pedestal conditions to closely resemble those of a reactor plasma. Of particular interest is the aspect of investigating the properties of the DTT reactor-like pedestal with the particle source provided by pellet fueling inside the pedestal top, while concomitantly the neutral penetration from the SOL to inside the separatrix is limited.

Regarding the confinement regimes of operation, the high field of DTT naturally provides a relatively large operational window for L-mode operation at full field, although significantly more limited at half field. From the Martin scaling for the L-H transition power [4.2], the L-H power threshold at half the Greenwald density limit is only 6 MW at 3T, whereas it is 20 MW at 5.8T (14 MW at the line averaged density of 10^{20} m^{-3}). According to the Ryter scaling for the density at which the L-H power threshold is minimum [4.3], this minimum density is 3.9 10^{19} m^{-3} and 8 .2 10^{19} m^{-3} at 3T / 2 MA and 5.8T / 5.5 MA respectively, corresponding to 0.30 and 0.23 Greenwald fractions respectively. Clearly, normal DTT operation will regularly be above these relatively low densities. It remains that the experimental determination of the density for minimum L-H power threshold is still an interesting experimental goal for the validation of the model and related scaling, particularly given the DTT flexibility of operating at different fields and currents while keeping high heating powers. Equally important is the role that DTT can have in assessing the impact of a W wall on the L-H power threshold at high magnetic field, in comparison with the extrapolations from present devices. Moreover, as already described in Chapter 2, the possibility of operating with both favourable (grad B drift towards the X-point) and unfavourable (grad B drift away from the X-point) configurations for H-mode access broadens the L-mode operational window. In particular, this is expected to provide a wide operational domain for the I-mode regime [4.4] at high magnetic field, especially at not too high current. Moreover, plasma shape flexibility in reaching high positive triangularity allows DTT to explore ELM-free scenarios like the EDA H-mode [4.5, 4.6] and the quasi-continuum exhaust regime (type II ELMs) [4.7, 4.8], within the interesting operational conditions of core-edge integration which have been previously introduced. Plasma conditions able to also produce operation with a stable X-point radiator [4.9, 4.10] are naturally offered by DTT. In fact, it can be expected that this will be the most regular condition of operation of DTT plasmas with high impurity seeding. Therefore, DTT directly offers the possibility of also exploring compact radiative divertor solutions [4.11].

Finally, some limitations have to be highlighted. Somewhat unavoidably connected with the capability of reaching reactor relevant plasma conditions in terms of density, collisionality and powers per unit surface at the boundary, DTT heating systems mainly deliver auxiliary electron heating, with limited capabilities of direct ion heating (direct auxiliary ion heating fraction does not exceed the 25% of the total auxiliary heating power [4.12, 4.13]). While this feature can be considered to be similar to that of a fusion reactor, at high power DTT plasmas can be expected to also obtain reactor relevant ratios of electron to ion thermal exchange time (τ_{ei}) to the thermal energy confinement time (τ_{th}) only at high current and sufficiently high density (at least around half the Greenwald density limit). This implies that not all regimes of operation of DTT can produce plasmas with electron to ion temperature ratios that approach one. Figure 4.1 shows the expected ratio of τ_{ei}/τ_{th} at 2.9T and 30 MW of heating (left) and 5.8T and 40 MW of heating (right) as a function of the Greenwald fraction, compared to ITER and DEMO reference values in their high power, high current baseline phases. The confinement times have been computed with the ITPA20-IL scaling law, which is also used to obtain the corresponding volume-averaged values of the electron temperature, which enter the electron to ion energy exchange time.

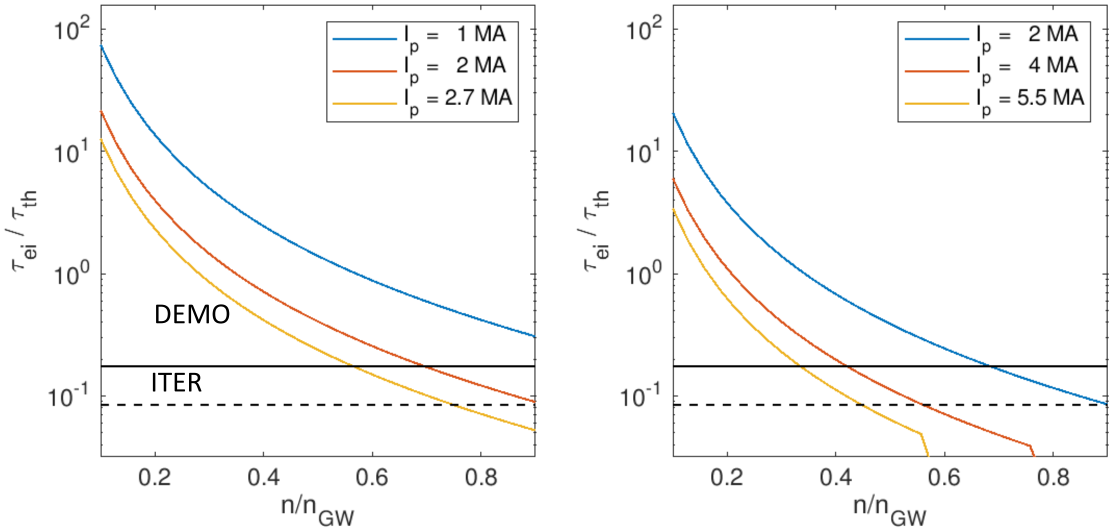

Fig. 4.1: Volume-averaged values of the electron to ion energy exchange time divided by the confinement time at 2.9 T, 30 MW (left) and at 5.8T, 40 MW (right), as a function of the Greenwald fraction for three values of the plasma current. Horizontal lines identify the ITER (dashed) and DEMO (solid) reference values at full current and full power, as well as at foreseen high Greenwald fraction (0.9).

An additional limitation is provided by the relatively modest current drive capabilities at full current and full field, as described in Chapter 6. Finally, while in principle DTT plasmas can be operated and heated up to the Greenwald limit at full field and current, at those extremely high densities it can be expected that the pulse length will be significantly shortened.

For convenience of the reader, the main points described in this section have been summarized in the list of bullets here below.

- High field, high current, high heating power, dominant electron heating, flexibility in heating at both full field / full current and half field / half current
- ECRH density cut-off at Greenwald density limit, edge opacity to neutral penetration
- High density and low collisionality
- Full W walls like ITER and DEMO
- Small L-mode operational window at half field, broader L-mode operational window at full field
- Capability of operating with favourable and unfavourable grad B configuration for H-mode access
- Limitations: limited auxiliary ion heating, limited length of flat-top at maximum current and density (close to the Greenwald limit), modest current drive capabilities at full field and full current

4.3 DTT operational windows from engineering to dimensionless parameters at half field and full field

In this section, a set of plots will show the DTT expected achievable domains of parameters connecting engineering parameters with volume-averaged dimensionless plasma parameters. These plots are obtained by making use of available scaling laws. In particular, L- and H-mode operational windows are determined according to the Martin's scaling law for the L-H transition, at both half and full magnetic field. It is important to recall that in the presence of metallic walls, a reduction of the L-H power threshold has been observed in comparison with results with carbon facing components [4.14, 4.15]. This reduction is of about 25% and has been included in these calculations. The plasma confinement is described with the IPB98 scaling laws for L-mode confinement [4.16] and with the ITPA20 ITER like [4.17] for DTT H-mode confinement (the latter is deemed more appropriate for high density H-mode prediction as compared to the IPB98 H(y,2) scaling law [4.16]). The derived dimensionless parameters can be interpreted to reflect volume-averaged values, obtained from the thermal stored energies, which are computed with the global confinement scaling laws.

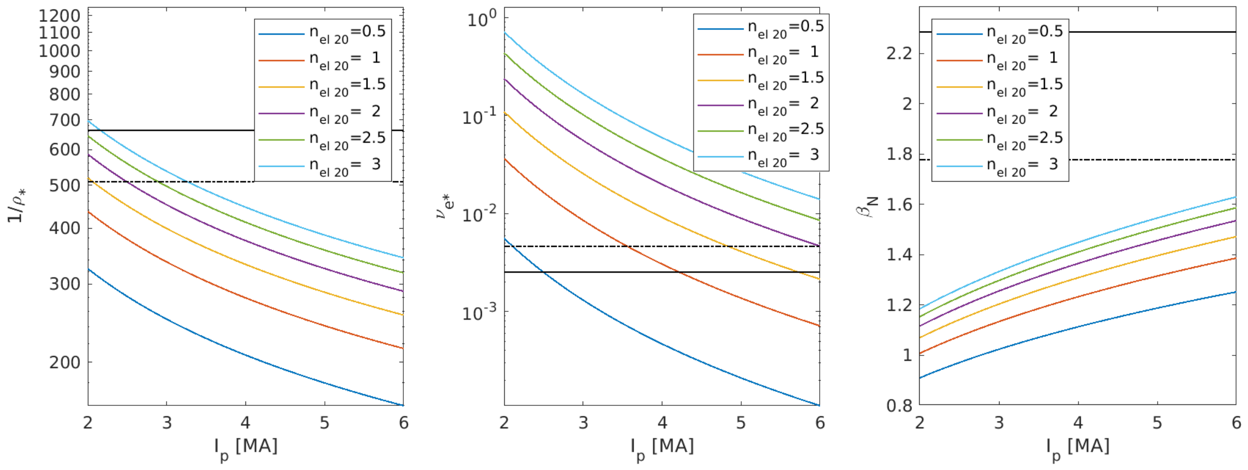

Fig. 4.2: Dimensionless plasma parameters (from left to right: volume-averaged values of $1/\rho_*$, ν_{e*} and β_N) as a function of the plasma current in MA, for different values of the line-averaged density at 5.8 T, with 40MW of auxiliary heating. We recall that at 5 MA, a line-averaged density of 1.5 10^{20} m^{-3} corresponds to a Greenwald fraction of 0.42. Horizontal lines give DEMO (solid) and ITER (dashed) reference values. From the application of the scaling laws, the thermal stored energy is computed and then used to compute the dimensionless parameters. This is also used for the calculation of β_N. The expression of ν_{e*} used in these plots is $\nu_{e*} = 5\ 10^{-5}\ \ln\Lambda\ Z_{eff}\ R\ q\ n_e / (T_e^2\ (r/R)^{1.5})$, with lengths in meters, density in 10^{19} m^{-3} and temperature in keV.

Figure 4.2 shows an example with 40 MW of auxiliary heating at 5.8T; dimensionless parameters are plotted as a function of the plasma current for different values of the electron density (dashed horizontal line is the ITER baseline reference, solid line is a DEMO-like reference).

This plot exemplifies the capability of DTT plasmas to cover ITER and DEMO volume-averaged (almost pedestal top) collisionalities at the same densities foreseen for reactor operation, of about 10^{20} m^{-3}. At the same time, it can be observed that even with 40 MW of auxiliary heating, DTT has limited capabilities of reaching reactor relevant values of β_N. An additional interesting aspect is that, like reactor plasmas and differently from usual high power operation in present devices, DTT plasmas are solidly within the theoretically expected local limit in terms of achieved ρ_* values.

The limitations in reaching high values of β_N at full magnetic field can be overcome by allowed operation at half magnetic field, where the ECRH can be operated in X2 mode. This is demonstrated in Fig. 4.3, where plasmas at 2.9 T and 2.7 MA have been considered with increasing heating power, again at different line-averaged electron densities. Here, at low power, the L-mode operational window can be identified.

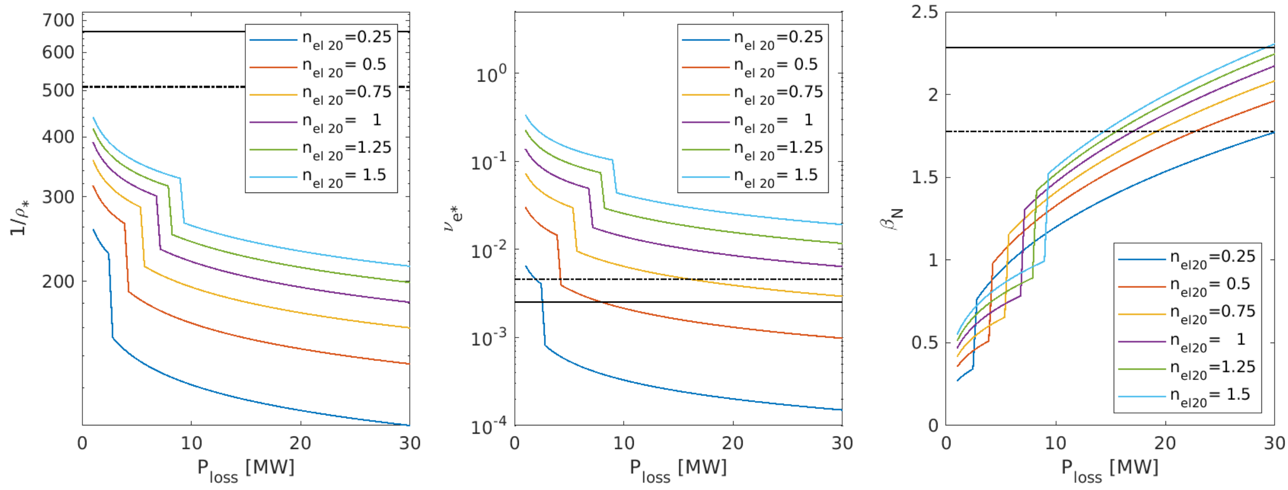

Fig. 4.3: Dimensionless plasma parameters (from left to right volume averaged values of $1/\rho_*$, ν_{e*} and β_N) as a function of the heating power in MW, for different values of the line averaged density at 2.9 T and 2.7 MA. We recall that at 2.7 MA, a line-averaged density of 10^{20} m^{-3} corresponds to a Greenwald fraction of 0.57. Horizontal lines give DEMO (solid) and ITER (dashed) reference values.

Figure 4.3 demonstrates the capability of DTT operation at half magnetic field of combining reactor relevant β_N above 2 with reactor relevant volume-averaged collisionalities of $\nu_{e*} < 10^{-2}$ at reactor densities around 10^{20} m^{-3}, with applied heating powers around 30 MW. This feature is unique in combination with full W walls.

4.4 DTT main missions from the standpoint of transport and confinement research in tokamaks

In this section a list of missions and related research areas are identified for DTT, with particular emphasis from the standpoint of confinement and transport studies. To this end, first the main general missions of DTT are recalled from Chapter 1:

- Validation of optimum power exhaust strategy for DEMO and related plasma scenarios, with full core-edge integration at high performance
- Support to the various phases of ITER exploitation

From these general statements, a set of specific missions are listed here below, which are of particular relevance for transport and confinement studies. As already mentioned, an overarching general element is that DTT naturally allows parameter decorrelation in comparison to low field devices.

DTT main missions from a confinement and transport standpoint

- Explore compatibility of power exhaust strategies with the existence of high confinement regimes (particular relevance to be given to stationary ELM-free and small ELM regimes with high confinement)
- Achieve ELM-free scenarios (I-mode, EDA H-mode, seeded no ELM regimes (XPR – CRD), QH, small ELMs (QCE = type II ELMs). *(Note: EDA: Enhanced D-alpha. XPR: X Point Radiator. CRD: Compact Radiative Divertor. QH: Quiescent H-mode. QCE: Quasi Continuous Exhaust).*
- Explore and possibly demonstrate the capability to reach detachment in each of these regimes
- Explore impact of ELM control techniques
- Document role of radiation from required impurity seeding on confinement, accessibility of confinement regimes and performance
- Demonstrate control of profiles of impurity densities and radiated power density, impact of reactor-like pedestal on peripheral impurity screening and on seeding scenarios
- Characterize the access to high confinement regimes (in particular H-mode) with dominant electron heating, high radiation fractions and limited edge neutral penetration, particularly important in combination with W wall and high B_T.
- Document the confinement (core and pedestal) properties over the large variations of parameters allowed by the DTT design (field, current, power and density)
- Perform comparisons of confinement and transport properties at low and high field (and correspondingly low and high current) in the same device
- Improve existing scaling laws, particularly concerning the dependences on plasma current and magnetic field
- Explore plasma rotation (intrinsic and with external torque) at low collisionality and low ρ_*

4.5 DTT research areas on transport and confinement and related experimental phases

The research missions identified in the previous section are planned to be achieved by a set of research topics that, in this research plan, are organized in four main research areas. These are described here below.

1. **General confinement properties**
   - Ohmic and L-mode properties of confinement (including positive and negative triangularity δ, scaling of confinement / transport vs I_p, B_T, n_e in electron heated conditions, ρ^* scaling, isotope studies)
   - Properties of H-mode confinement (note that DTT should be able to access H-mode with ECRH (+ICRH) only) (B_T vs q_{95}, and B_T vs R (low vs high field), opaque edge and fueling, isotope studies)
   - Negative vs positive triangularity (in principle also possible from relatively early phases). Requires sufficient fraction of ion heating for complete investigations.
2. **Core – edge integration physics**
   - Regimes with no ELMs or small ELMs, EDA, QCE, (QH), I-mode, negative δ
   - Impurity seeded detached scenarios at ITER- and DEMO-relevant values of ν^*, ρ^* and β with ITER- and DEMO-like plasma shape
   - Impact of Greenwald fraction on edge and core transport, density limit studies (Giacomin scaling [4.18] in comparison to Greenwald scaling)
   - Plasmas with high density but low collisionality

- Impurity control, particularly in the presence of a reactor-like pedestal
- Study of Advanced Tokamak and Hybrid scenarios and of their compatibility with power exhaust solutions. Comparison high/low B_T.

3. L-H transition and H-mode pedestal

- L-H transition physics with W-wall from low to high magnetic field and plasma current, impact of divertor configurations and exhaust requirements (impact of impurity seeding and of separatrix density, opaque edge, isotope studies) as well as impact on pedestal performance in H-mode.
- Pedestal physics, role of ideal and resistive MHD in limiting pedestal top pressure, role of transport (collisionality, high density decorrelation)
- Physics of fuelling by gas puff and pellet injection (impact on L-H transition, pedestal and confinement)
- High density and low collisionality
- Effects of shaping (from high positive δ~0.5 to negative δ)

4. Specific on core and edge transport physics

- Transport in plasmas with dominant electron heating and low torque
- Confirm & further assess ITG / TEM / ETG (high density) paradigm (n/n_{GW} vs ν^*)
- Ion stiffness mitigation strategies
- Density peaking at negligible core NBI particle sources, impact of electron heating
- Impurity transport, including impact of a reactor-like pedestal
- Properties of intrinsic rotation / residual stress (profile shearing, ρ^* scaling, edge residual stress dependences) in L- & H-mode
- Turbulence diagnostics, model validation

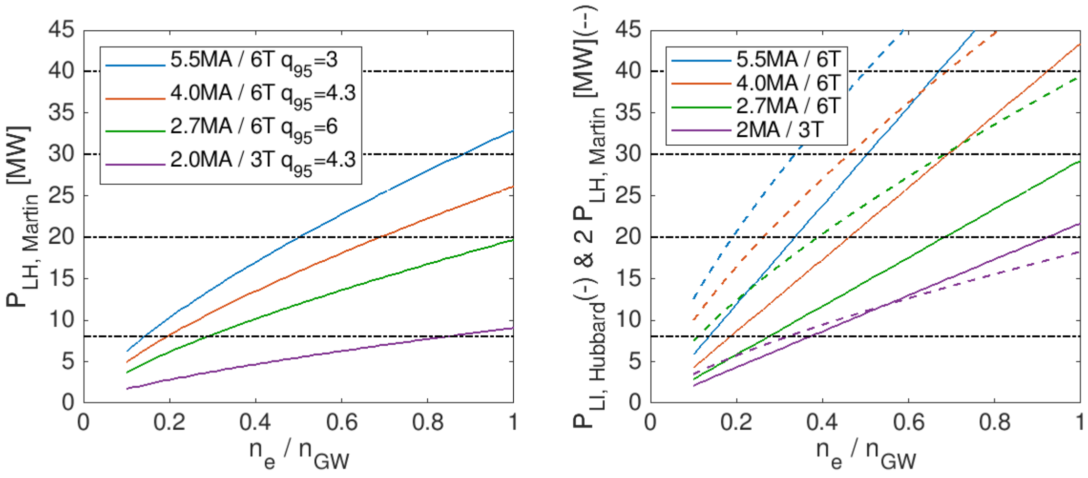

Fig. 4.4: Heating power for H-mode access (left) and for I-mode access (right) for different combinations of current and magnetic fields, foreseen in the different DTT phases, as a function of the corresponding Greenwald fraction. Horizontal dashed lines identify maximum heating power in the different DTT heating phases (8 MW for phase A, 20 MW for phases B and C, 30 MW for phase D, 40 MW for phase E. In phase A (8 MW), access to H-mode is only possible at low Greenwald fraction and with limited power window above the threshold. The same situation is present in phase C (20 MW, 6T and 4 MA). A large operational window for the I-mode regime should be particularly possible at 6T with reduced current.

Experiments in these research areas can be performed in the different phases of DTT operation, in connection with Table 2.1 presented in Chapter 2 and related Table 2.3 of the corresponding heating phases. In this perspective, it is of interest to consider the power windows for H-mode as well as I-mode access in the different heating phases. These are presented in Figure 4.4. It is worth mentioning that in these plots the actual Martin scaling has been applied, and thereby a reduction of about 25% of the L-H power threshold can be expected as a consequence of the W wall [4.14], this however, for conservative purposes, has not been included in these plots. For the I-mode access, a multi-device scaling has been applied [4.19]. It is also important to underline that, for I-mode operation, reversed magnetic field configuration (H-mode unfavourable grad B drift direction) also requires reversed plasma current, with consequent restricted availability of NBI heating, as NBI becomes counter-current.

The analysis of the power windows, which allow the access of the different confinement regimes in the different DTT heating phases, provides guidelines to outline the possible transport and confinement experiments in the different DTT phases. These are presented here below.

- **Commissioning** (including actively cooled W PFCs)
  Initial operation with reduced field and current and reduced power.
- **Phase 1, heating phase A** (8 MW ECRH, 3T, 2 MA)
  Initial phase in L-mode. With a maximum power of 8 MW, access to H-mode is in principle possible, but available power window above the L-H threshold is relatively limited (expected operation is below 1.5 P_{LH}). Initial operation in hydrogen will allow first isotope experiments. Isotope studies, based on deuterium - hydrogen comparisons, will also be possible in later phases of the DTT operation, following the development of the research interests.
- **Phase 1, heating phase B** (16 MW ECRH, 4.75 MW ICRH, 3T, 2 MA)
  A large number of transport experiments can be performed, particularly in connection with research areas 3 and 4. These experimental results can be also planned for future direct comparisons with corresponding experiments in later phases at maximum field and current. Operational window above P_{LH} is large; the exploration of I-mode in reversed B_T configuration is also possible with sufficient excess in heating power.
  Moreover, at 2.5-2.7MA/3T there is already the possibility of exploring the ITER Baseline Scenario (less than 20 MW required, with a combination of ECRH and ICRH).
  High beta operation is potentially possible, but still limited in this phase by the maximum available power. In contrast, accessibility to small ELMs and ELM-free stationary regimes can start to be investigated.
- **Phase 1, heating phase C** (16 MW ECRH, 4.75 MW ICRH, 6T, 4 MA)
  While this phase is of relatively limited interest from the standpoint of scenario development, given the combination of high magnetic field and current and low power, from the standpoint of transport studies this phase is of high potential interest. With an L-H power threshold of 16.5 MW at half of the Greenwald limit at 4 MA, the available power for robust H-mode operation at maximum allowed current and magnetic field of this phase is limited. In contrast, a large operational window becomes available for L-mode transport studies, L-H transition studies and L-I transition studies (in unfavorable grad B configuration), comparing plasmas at different magnetic fields and currents.This is also of high interest for the characterization of global confinement properties.
- **Phase 2, heating phase D** (16 MW ECRH, 4.75 MW ICRH, 5-10 MW NBI, 6T, 5.5 MA)
  The availability of the NBI heating power opens the possibility of robust operation in H-mode reaching a maximum current of 5.5 MA. Confinement and transport studies can compare different currents and fields also in H-mode operation. Accessibility to small ELM and stationary ELM-free regimes at high magnetic field and current can also be explored. I-mode operational window at 6T can also be determined (upper boundary in power likely still limited by available power).
  Hybrid / advanced tokamak (e.g. at 2 – 2.5 MA/ 3T) scenarios also becomes possible (likely require up to 10 MW NBI to reach sufficiently high beta operation) with ITER and DEMO W walls. Capabilities of heating and current drive can be investigated and exploited, diagnostics and control capabilities can be assessed. These capabilities provide an additional DTT mission in developing DEMO relevant scenarios with DEMO-like wall and compatibility with exhaust at DEMO relevant beta (note that at full field DTT scenarios will not have DEMO relevant beta values, but can marginally reach those of

the ITER baseline. In contrast, at maximum current and field, DTT can reach DEMO relevant values of ρ* and collisionality)

- **Long term: Phase 3, heating phase E** (32 MW ECRH, 9.5 MW ICRH, 10 MW NBI, 6T, 5.5 MA)

  All experiments and foreseen scenarios become possible at the maximum nominal heating power levels, allowing full exploitation, also with different divertors.

4.6 Predictions of plasma profiles during current flat-top phases

Physics–based multi–channel simulations of the main DTT baseline operational scenarios during stationary current flat-top phases have been performed to more solidly document the plasma parameter domains that will be achieved during DTT operation. This integrated modelling activity has both guided and followed the machine design evolution in the last years, leading to a sequence of updates described in [4.12] and [4.13]. Following the recent decision to move upwards the plasma by about 12 cm with respect to the magnetic equilibria used in [4.13], in order to accommodate a new divertor design, the simulations were updated further.
The up-to-date plasma profile predictions for the main baseline scenarios with the SN configuration with positive triangularity during stationary current flat-top phases are presented in this section.

4.6.1 Description of simulation methodology

The core integrated simulations predict radial profiles of the electron and ion temperatures, density (both main species and impurity), toroidal rotation, and current density, calculating consistently the magnetic equilibrium, the heating profiles, and the non-linear interactions between the different transport channels and between heating and plasma. The simulations were performed using the JINTRAC [4.20] modelling suite with its core plasma transport code JETTO [4.21] or employing the transport solver ASTRA [4.22, 4.23] within a mixed iterative ASTRA-JINTRAC approach thoroughly discussed in [4.12]. The turbulent transport is calculated either by the TGLF-SAT2 model [4.24, 4.25] or by the QuaLiKiz (QLK) model [4.26, 4.27]. In particular, the JETTO transport solver was used for full physics DTT simulations using the QLK model, while the TGLF runs were performed adopting the ASTRA-JINTRAC scheme. The neoclassical heat and particle transport are calculated by the NCLASS module [4.28] for all plasma species in the JINTRAC runs, while the ASTRA runs use the NCLASS model for the main species and the FACIT analytic model [4.29] for all other ion species (with Z>6). The simulation domain covers the region inside the separatrix, but the transport equations for heat, particle, and momentum are only solved from the top of the pedestal inward. In the pedestal region, the kinetic profiles of the two main species are kept fixed, and $T_e = T_i$ is assumed. The pedestal profiles were previously determined by specific runs of the Europed code [4.30] using the EPED1 model [4.31], for each scenario. Two impurities are always included: a seeding impurity (argon, neon, or nitrogen) used to increase the radiative dissipation, reducing the divertor power load, and tungsten coming from the first wall and the divertor.

The treatment of impurity density profiles is performed in multiple steps. First, the impurity charge profiles, and the contributions to impurity densities and radiation up to the separatrix of each ionisation state of impurities (treated separately), are obtained using the SANCO code [4.32] in the JINTRAC suite. These JINTRAC calculations use the recycling factor, the escape velocity, and the neutral influx equal to zero to conserve the particle number. A radially constant effective charge Z_{eff} and an impurity density ratio

$n_W/n_{seed.imp}$ are tuned to be compatible with typical values in tokamaks operating in full detachment and with SOL modelling predictions and are set as SANCO initial conditions. These entail certain concentrations of the seeding impurity and tungsten during these simulations. Then, in the ASTRA runs, impurity densities and radiation are calculated, with fixed ionisation profiles taken from the JINTRAC runs, since ASTRA includes the physically more comprehensive FACIT model (not included in JINTRAC) for the impurity neoclassical transport, yielding more realistic predictions of the impurity density profiles. Thus, a further JINTRAC modelling step was performed, with fixed profiles of impurity densities and radiation taken from ASTRA. The toroidal rotation is predicted by the application of a theory-driven empirical model [4.33, 4.34] (details in [4.13]).

During the JINTRAC and ASTRA simulations, the MHD equilibrium is recalculated by equilibrium solvers ESCO and SPIDER [4.35] respectively, keeping the plasma boundary fixed to the reference shape provided by the free boundary solver CREATE–NL [4.36]. Simulations do not include sawteeth and hence their profiles have to be mainly interpreted as related to the transport-saturated pre-crash condition, except for a case described at the end of section 4.6.2, which was carried out using the Porcelli model [4.37] to predict sawteeth of the full power scenario. ELMs are not included in the modelling yet, but first estimations of their impact on the full power scenario predictions through suitable scalings are discussed in Chapter 2, section 2.7.1. The heating systems are modelled self-consistently by specific codes during the JINTRAC simulations, while for the ASTRA cases heating and current densities are predicted within the JINTRAC-ASTRA loop. The ECRH power deposition and the EC current drive are calculated by the GRAY code [4.38], the NBI sources are modelled by the PENCIL code [4.39]. As described in [4.40], the sum of prompt and ripple NBI fast particle losses is around 2% only and therefore have been neglected in this modelling activity. The ICRH power deposition and the synergy effects with NBI are computed by the PION code [4.41]. In the simulations presented here, an ICRH frequency of 90 MHz and a concentration of 5% hydrogen as minority species are always set. For each scenario, also the 2.5 MeV DD neutron rates (including both thermal-thermal and thermal-fast nuclear reactions) are calculated, in order to verify the compatibility with the presently foreseen neutron shielding.

4.6.2 Scenario E SN baseline

The E scenario with SN configuration works at full current and full field (B_{tor}=5.85T, $|I_p|$=5.5MA), with the complete installed external power of 48 MW (with 32 MW by ECRH in O-mode, 9.5 MW by ICRH, and 10 MW by NBI at 510 kV). In the E SN modelling, the transport equations are solved within ρ_{tor} = 0.94. The core integrated modelling of the E SN scenario is performed using both TGLF-SAT2 (in ASTRA runs) and QLK (in JINTRAC runs) as turbulent transport models. Argon is used as seeding impurity (Z_{eff}=1.75 and n_W/n_{Ar} = 0.01 as initial conditions). The pedestal pressure was obtained repeating the Europed modelling, using in input a temperature at the separatrix of T_{sep} = 200 eV, a pedestal top electron density of n_{ped} = 1.4x10^{20}/m^3 to have an electron density at the separatrix of about n_{sep} ~0.8x10^{20}/m^3, a value of β_{pol} = 0.55, and a relative shift of (T_{pos}–n_{pos}) = 0.012ψ_N. The radial profiles of electron temperature T_e, ion temperature T_i, electron density n_e, toroidal angular velocity ω_{tor}, safety factor absolute value |q|, seeding impurity density $n_{seed.imp.}$, tungsten density n_W, effective charge Z_{eff}, radiative power density Q_{rad}, and radiative power P_{rad} are shown in Figure 4.5. The corresponding heating profiles are shown in Fig. 4.6. Figure 4.5 shows that the two transport models provide temperature and density profiles in good agreement. Values of T_{e0} ≈ (12.4-14.2) keV, T_{i0} ≈ (8.9-9.8) keV, and n_{e0} ≈ (2.1-2.3)x10^{20}m^3 are reached at the plasma centre. In the power balance, the Ohmic power P_{Ohm} ≈ (1.3-1.8)MW is relatively negligible, the core radiated power P_{rad} ≈ 13 MW is around the 30% of the total power, and a collisional power of P_{ei} ≈ (15-21)MW flows from electrons to ions. The radial profiles of current densities are shown in Fig. 4.7 (negative values indicate a current density flowing in the opposite direction with respect to the toroidal magnetic field). They refer to the run with QLK, but the TGLF case exhibits alike profiles. The total current density J is mainly due to the inductive contribution and its profile is very similar to the inductive one, except for an edge peak due to bootstrap current. The total DD neutron rate for scenario E is predicted ~ 0.95x10^{17} neutrons s^{-1}. Neutron loads of this order of magnitude can be easily withstood by the neutron shields currently planned for DTT.

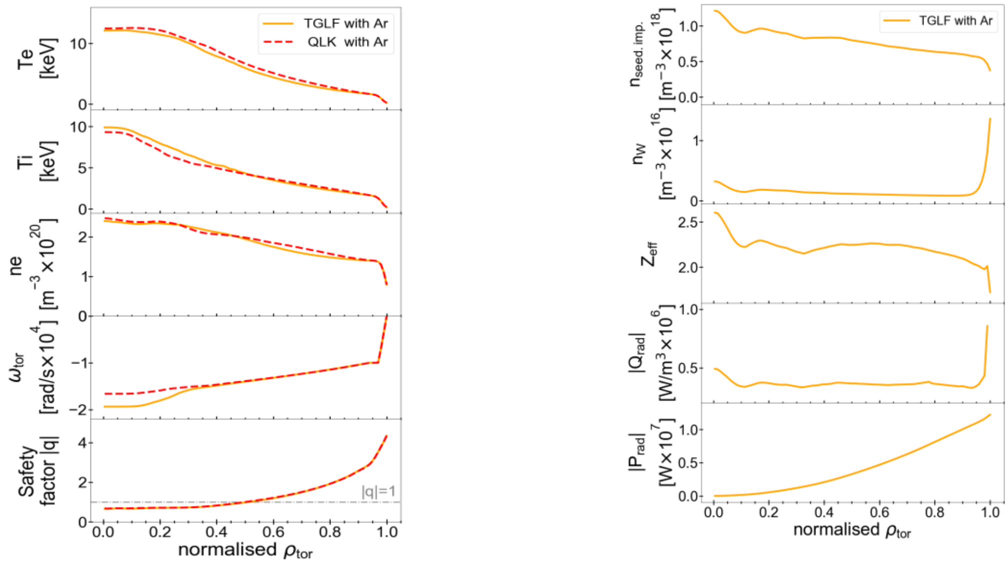

Fig. 4.5: Radial profiles for the E SN scenario flat-top phase: (a) of the electron and ion temperatures, electron density, toroidal rotation, and safety factor absolute value, with turbulent transport calculated by TGLF SAT2 (solid orange lines) or by QLK (dashed red lines) with argon; (b) profiles of the seeding impurity and tungsten densities, effective charge, radiative power density, and radiative power, calculated by TGLF and FACIT.

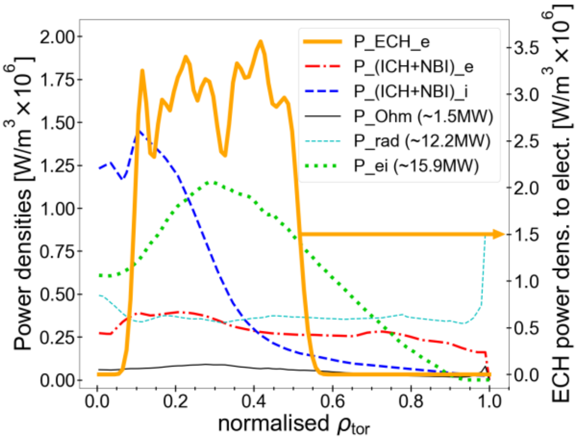

Fig. 4.6: Radial profiles of power densities for the E SN scenario: ECRH power deposited to electrons P_{ECRHe}, NBI and ICRH power deposited to electrons $P_{(ICRH+NBI)e}$, NBI and ICRH power deposited to ions $P_{(ICRH+NBI)i}$, Ohmic power P_{Ohm}, radiative power Prad, and thermal exchange power between electrons and ions P_{ei} (from the TGLF-SAT2 simulation).

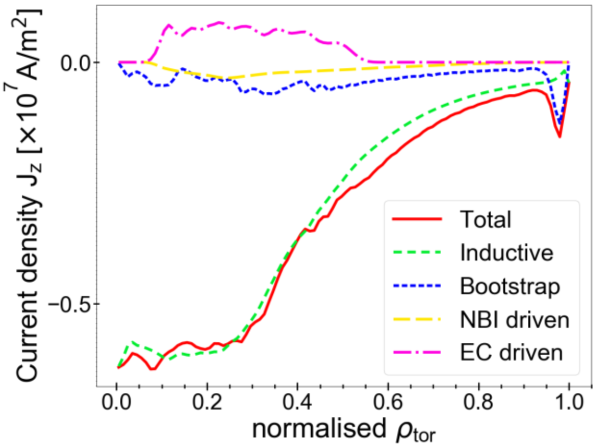

Fig. 4.7: Radial profiles of current densities in the SN E scenario: total current J, inductive current J_{ind}, bootstrap current J_{BS}, NBI drive current J_{NB}, and EC drive current J_{EC}.

The first analysis of the sawtooth impact on the E SN scenario kinetic profiles and on the safety factor in DTT was presented in [4.13]. Specifically, sawteeth were included into a JINTRAC simulation with QLK as turbulent transport model and with argon as seeding gas, using the Porcelli sawtooth crash trigger model and the Kadomtsev complete reconnection model [4.42]. This analysis has been updated with the new E SN equilibrium. The electron temperature evolution at the plasma centre, displayed in Figure 4.8, clearly shows a typical sawtooth oscillation, with a relatively long period of about half a second, produced by the stabilising effect of the ICRH and NBI driven fast particles, and the remarkable variation of the central electron temperature of about 7.5 keV, practically 50% of the central temperature.

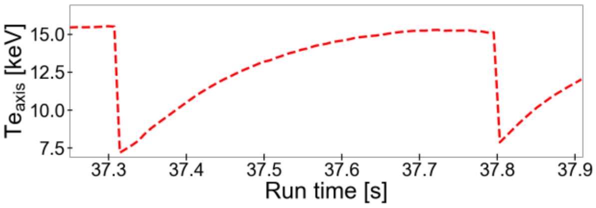

Fig. 4.8: Time evolution of the electron temperature at the plasma centre during a sawtooth, computed by JINTRAC.

The mixing radius is as large as $\rho_{mix} \approx 0.55$ (ρ_{mix} describes the portion of of plasma involved in the reconnection process), a bit larger than the $|q|=1$ radial location $\rho_1 \approx 0.5$. It is known that the complete flattening of the q profile described by the basic Kadomtsev complete reconnection model does not always occur experimentally, and q_0 can remain below 1 after the crash. The large q = 1 radius predicted for the E scenario is an indication that the same large sawteeth could occur experimentally in DTT [4.43, 4.44]. The mixing radius larger than half radius also suggests that an incomplete reconnection is likely to take place as relaxation process. The incomplete reconnection changes the sawtooth impact, increasing its frequency, therefore plasma scenarios are expected less prone to the onset of MHD instabilities as the neoclassical tearing modes, which can lead to loss of confinement [4.45]. The description of the incomplete reconnection relaxation by a more accurate reconnection model, as the one discussed in [4.37], is presently planned for future work.

4.6.3 Scenario C SN baseline

The C scenario with SN configuration works at full vacuum toroidal magnetic field (B_{tor} = 5.85T), but with reduced plasma current ($|I_p|$ = 4.0 MA) and with an installed external power ~ 20 MW (with 16 MW by ECRH in O-mode and 4.75 MW by ICRH). This power is very marginal to enter H-mode, depending on the amount of radiated power. In the following, we keep radiation low enough to get above L-H threshold, but an

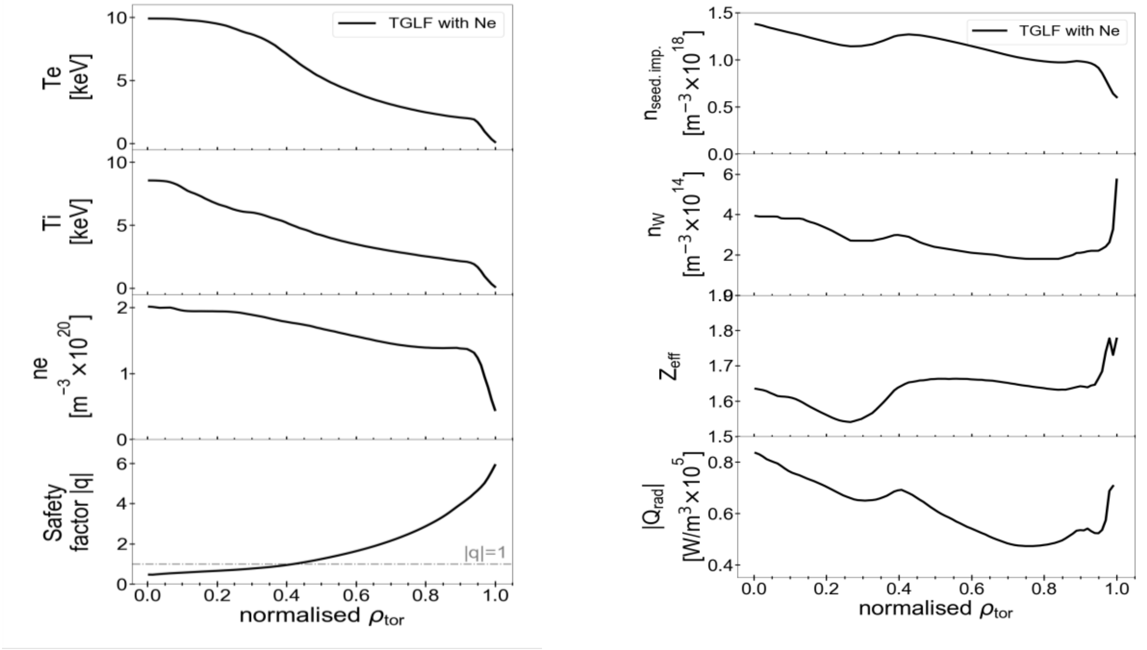

Fig. 4.9: Radial profiles for the C SN scenario flat-top phase (a) of the electron and ion temperatures, electron density and safety factor absolute value and (b) of the seeding impurity (Neon) and tungsten densities, effective charge and radiative power density, with turbulent transport calculated by TGLF and neoclassical by FACIT.

alternative simulation would be possible with more radiation and L-mode. The core integrated modelling of the C SN scenario was performed using TGLF-SAT2 as turbulent transport model within an ASTRA simulation. The transport equations were solved within ρ_{tor} = 0.89. Neon was used as seeding impurity (Z_{eff} =1.4 and n_W/n_{Ne} = 0.003 as initial conditions). The pedestal pressure was calculated by the Europed modelling, using in input a temperature at the separatrix of T_{sep} = 100 eV, a pedestal top electron density of $n_{ped} = 1.4\text{x}10^{20}/\text{m}^3$ to have an electron density at the separatrix of about $n_{sep} \sim 0.45\text{x}10^{20}/\text{m}^3$, a value of β_{pol} = 0.65, and a relative shift of (T_{pos}–n_{pos}) = 0.006ψ_N. The radial profiles of electron temperature T_e, ion temperature T_i, electron density n_e, safety factor absolute value |q|, seeding impurity density $n_{seed.imp.}$, tungsten density n_W, effective charge Z_{eff}, radiative power density Q_{rad} are shown in Figure 4.9. Toroidal rotation was set to zero due to the lack of NBI. For the C scenario, a DD neutron rate of about $2.6\text{x}10^{16}$ neutrons s^{-1} is predicted.

4.6.4 Scenario A SN baseline

The modelling update to the present equilibrium of the A SN scenario during stationary current flat–top phase has not been completed yet. Thus, also in this case simulations based on the previous magnetic equilibrium configuration are presented in this subsection [4.13].

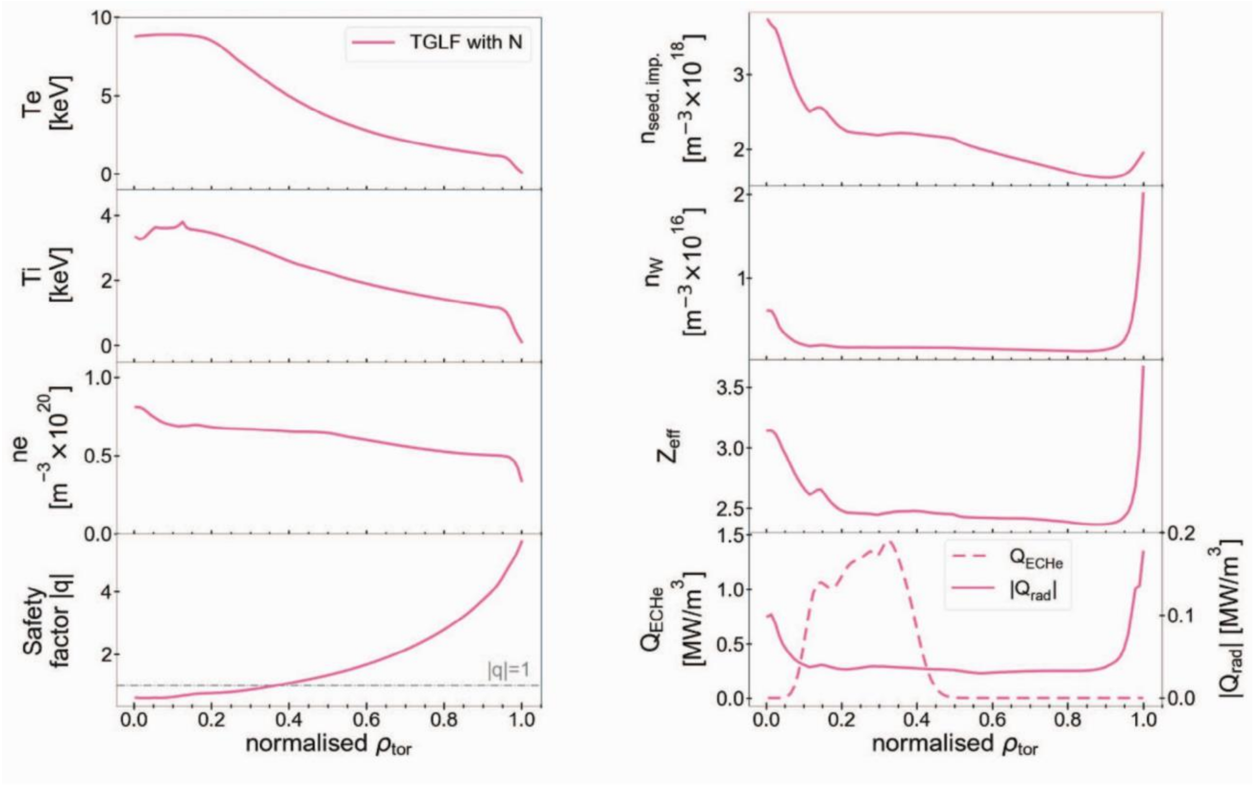

(a) (b)

Fig. 4.10: Radial profiles for the A SN scenario flat-top phase (a) of the electron and ion temperatures, electron density and safety factor absolute value and (b) of the seeding impurity (nitrogen) and tungsten densities, effective charge, radiative power density, and radiative power, with turbulent transport calculated by TGLF and neoclassical by FACIT. It is underlined that these results refer to the previous magnetic equilibrium configuration, and have not been updated yet to the new upshifted magnetic equilibrium.

The A scenario with SN configuration works at half magnetic field (B_{tor} = 3T) and further reduced plasma current (|I_p| = 2.0 MA) and with an installed external power of 8 MW (entirely supplied by ECRH in X-mode). The core integrated modelling of the A SN scenario was performed using TGLF-SAT2 as turbulent transport model within an ASTRA simulation. The transport equations were solved within ρ_{tor} = 0.92. Nitrogen was used as seeding impurity (Z_{eff} =2.5 and n_W/n_N = 0.001 as initial conditions). The pedestal pressure was calculated by the Europed modelling, using in input a temperature at the separatrix of T_{sep} = 100 eV, a pedestal top electron density of n_{ped} = 0.5x10^{20}/m^3 to have an electron density at the separatrix of about n_{sep} ~0.34x10^{20}/m^3, a value of β_{pol} = 0.25, and a relative shift of $(T_{pos}-n_{pos}) = 0.020\psi_N$.

The radial profiles of electron temperature T_e, ion temperature T_i, electron density n_e, safety factor absolute value |q|, seeding impurity density $n_{seed.imp.}$, tungsten density n_W, effective charge Z_{eff}, radiative power density Q_{rad}, and radiative power P_{rad} are shown in Figure 4.10. For the A scenario, a DD neutron rate of about 2x10^{14} neutrons s^{-1} is predicted.

4.7 Basic description of diagnostic requirements for transport studies

In the table below, a short description of the foreseen diagnostic systems for transport and confinement studies is provided, organized for different measured quantities in the first column, with the corresponding diagnostics as scheduled in Phase 1 (central column) and Phase 2 (right column).

Measured Parameters	**Diagnostics, Phase 1**	**Diagnostics, Phase 2**
Electron Density, and density profiles	Interferometers (vertical and tangential), Thomson Scattering (core-edge)	Thomson Scattering (edge-divertor), Reflectometry, He-Beam
Electron Temperature profiles	ECE Radiometer, Thomson Scattering (core-edge)	Thomson Scattering (edge-divertor)
Ion Temperature profiles	CXRS, core - edge – SOL (diagnostic NBI)	
Rotation profiles	CXRS, toroidal and poloidal (diagnostic NBI)	
Safety factor	MSE (diagnostic NBI) and polarimetry	
Impurities	CXRS, Bolometry, SXR Crystal and XUV spectrometry, Visible spectrometry, Visible Z_{eff} Bremsstrahlung, VUV Spectrometry	SXR and Bolometry tomography, Laser Blow Off, Tracer encapsulated Solid Pellet,
Density fluctuations		Phase Contrast Imaging, Beam Emission Spectroscopy, Thermal He Beam, Reflectometry
T_e fluctuations		Correlation ECE
Fast Ions		Fast Ion Loss Detectors, Fast Ion Deuterium Alpha charge exchange

4.8 Headlines of the research programme for transport and confinement physics

In this section, we summarize the main headlines of the DTT research programme on transport and confinement physics, according to the various phases of implementation of the DTT heating system and of plasma operations.

Headline number	Headline contents	Priority (+, ++, +++)	ITER	DEMO
Construction Phase 2022-2029				
C.4.1	Additional integrated modelling of baseline and alternative scenarios, assessment of MHD stability and Energetic Particles (EP) properties.	+++		
C.4.2	Diagnostics for plasma operation, essential profiles measurements (temperatures, densities, rotation), bolometry, SXR spectroscopy	+++		
Phase 1 2029-2034				
1.4.1	Ohmic and L-mode transport properties at half field and half current (Scen. A,B), and full field full current (C)	+++	*	*
1.4.2	H-mode access at half (A,B) and full field (C) with P_{ext}<20 MW and dominant electron heating	+++		
1.4.3	First studies of effects of impurity seeding on confinement for edge-core integrated scenarios (B, C)	+++	*	*
1.4.4	Characterize transport in edge and core in different scenarios, compare full and half field	+++	*	*
1.4.5	Transport properties in presence of 3D ELM control, in no ELM regimes and in negative triangularity plasmas	+++	*	*
Phase 2 2034-2038				
2.4.1	Extend all studies of Phase 1 to higher power, with increased emphasis on transport aspects of core-edge integration	+++	*	*
2.4.2	Characterize transport in high beta hybrid / advanced scenarios at high power and half field and current	+++	*	*
Phase 3 2038-…				
3.4.1	Extend all studies of Phase 1 and 2 to full experimental capabilities, with emphasis on transport properties with energetic particles	+++	*	*

4.9 References

[4.1] M. Greenwald et al 2002 *Plasma Phys. Control. Fusion* **44** R27
[4.2] Y.R. Martin et al 2008 J. Phys.: Conf. Ser. 123 012033
[4.3] F. Ryter et al 2014 Nucl. Fusion 54 083003
[4.4] D.G. Whyte et al 2010 Nucl. Fusion 50 105005
[4.5] M Greenwald *et al* 2000 *Plasma Phys. Control. Fusion* **42** A263
[4.6] L. Gil *et al* 2020 *Nucl. Fusion* **60** 054003
[4.7] J. Stober *et al* 2001 *Nucl. Fusion* **41** 1123
[4.8] G.F. Harrer et al 2022 Phys. Rev. Lett. 129 165001
[4.9] M. Bernert *et al* 2017 *Nucl. Materials Energy* **12** 111-118
[4.10] M. Bernert *et al* 2021 *Nucl. Fusion* **61** 024001
[4.11] T. Lunt et al 2023 Phys. Rev. Lett. 130, 145102
[4.12] I. Casiraghi *et al* 2021 *Nucl. Fusion* **61** 116068
[4.13] I. Casiraghi et al 2023 Plasma Phys. Control. Fusion **65** 035017
[4.14] F. Ryter *et al* 2013 Nucl. Fusion **53** 113003
[4.15] C.F. Maggi *et al* 2014 Nucl. Fusion **54** 023007
[4.16] *ITER Physics Basis Editors et al 1999 Nucl. Fusion **39** 2175*
[4.17] G. Verdoolaege *et al* 2021 *Nucl. Fusion* **61** 076006
[4.18] M. Giacomin et al 2022 Phys. Rev. Lett. 128 185003
[4.19] A.E. Hubbard *et al* 2016 *Nucl. Fusion* **56** 086003
[4.20] M. Romanelli *et al* 2014 *Plasma and Fus. Res.* **9** 3403023
[4.21] G. Cenacchi and A. Taroni 1988 *Report ENEA-RT-TIB* 88-5
[4.22] G.V. Pereverzev and P.N. Yushmanov 2002 *IPP Report* 5/98 (Max-Planck-Institut für Plasmaphysik)
[4.23] E. Fable et al 2013 Plasma Phys. Control. Fusion **55** 124028
[4.24] G.M. Staebler *et al* 2016 *Phys. Plasmas* **23** 062518
[4.25] G.M. Staebler *et al* 2021 *Plasma Phys. Control. Fusion* **63** 015013
[4.26] C. Bourdelle *et al* 2016 *Plasma Phys. Control. Fusion* **58** 014036
[4.27] C.D. Stephens *et al* 2021 *J. Plasma Phys.* **87** 905870409
[4.28] W.A. Houlberg *et al* 1997 Phys. Plasmas **4** 3230–42
[4.29] D. Fajardo *et al* 2022 *Plasma Phys. Control. Fusion* **64** 055017
[4.30] S. Saarelma *et al* 2018 Plasma Phys. Control. Fusion **60** 014042
[4.31] P.B. Snyder *et al* 2011 *Nucl. Fusion* **51** 103016
[4.32] L. Taroni 1994 *21st EPS Conf. Contr. Fus. Plas. Phys.* (Montpellier) vol **102**
[4.33] A. Peeters *et al* 2009 *Phys. Plasmas* **16** 062311
[4.34] A. Peeters *et al* 2011 *Nucl. Fusion* **51** 094027
[4.35] A.A. Ivanov 2005 *32nd EPS Conf. on Plasma Physics*—Terragona **29C** (ECA), P-5.063
[4.36] R. Albanese, R. Ambrosino and M. Mattei 2015 *Fusion Eng. Des.* **96–97** 664–7
[4.37] F. Porcelli *et al* 1996 *Plasma Phys. Control. Fusion* **38** 2163–86
[4.38] D. Farina 2007 *Fusion Sci. Technol.* **52** 154–60
[4.39] C.D. Challis *et al* 1989 *Nucl. Fusion* **29** 563
[4.40] C. De Piccoi *et al* 2023 European Fusion Theory Conference, to be submitted to J. Plasma Phys.
[4.41] L-G. Eriksson *et al* 1993 *Nucl. Fusion* **33** 1037
[4.42] B.B. Kadomtsev 1975 *Fiz. Plazmy* **1** 710
[4.43] J. O’Rourke 1991 *Plasma Phys. Control. Fusion* **33** 289
[4.44] F.M. Levinton *et al* 1993 *Phys. Fluids B* **5** 2554
[4.45] O. Sauter *et al* 2002 *Phys. Rev. Lett.* **88** 105001

Chapter 5

MHD, DISRUPTIONS AND CONTROL

E. Nardon, G. Vlad, M. Falessi,
E. Alessi, R. Ambrosino, B. Baiocchi, D. Bonfiglio, I. Casiraghi, L. Frassinetti, M. Gobbin, Y. Kominis,
P. Maget, M. Nocente, S. Nowak, L. Pigatto, L. Piron, F. Porcelli, G. Ramogida, D. Testa,
N. Vianello, F. Zonca

This chapter discusses MHD instabilities expected in DTT scenarios and means for their control, as well as plans concerning disruptions, their avoidance and mitigation. The expected MHD instabilities comprise internal kink modes (sawteeth), Neoclassical Tearing Modes (NTMs), Edge Localized Modes (ELMs), as well as infernal modes. MHD instabilities associated to a high β_N *such as NTMs may be addressed at reduced* I_p *and* B_t *in the early operation of DTT. A set of non-axisymmetric coils will be used mainly to compensate error fields and control ELMs, but also possibly to control NTMs in conjunction with electron cyclotron heating and current drive. Disruption (and runaway electrons) avoidance and mitigation will be an important research topic on DTT. For disruption mitigation, a shattered pellet injection system is planned. Altogether, the DTT programme described in this chapter is very relevant to future large tokamaks and in particular to ITER, especially in the field of disruption avoidance and mitigation.*

5.1 Important features of DTT

Some features of DTT should be kept in mind when considering MHD, Disruptions and Control (MDC):

1. The large nominal B_t and I_p tend to make β_N relatively modest (see Chapter 2) while they potentially imply large disruption loads. Operation at reduced B_t and I_p but relatively high input power is however planned for the first phase (high level commissioning) of the DTT programme (see Chapter 1), in which larger β_N values may be reached (see Chapter 2). This may allow investigating advanced scenarios, with DTT playing a complementary role to JT-60SA.
2. While reference scenarios in single null configuration with $q_{95}=3$ are rather standard from an MDC point of view, other scenarios (e.g. negative triangularity, double null, X divertor, etc.) will explore less well known territory.
3. DTT will be equipped with two key actuators for MHD control: a powerful Electron Cyclotron Resonance Heating (ECRH) system (see Chapter 6) and a set of in-vessel Non-AxiSymmetric (NAS) coils (see Fig. 5.4).

5.2 MHD stability and control

5.2.1 Assessment of 'basic' MHD stability for DTT scenarios

Ideal and (classical) low-n resistive MHD stability studies have been performed for the E (full power, single null) and A (single null) scenarios (see Chapter 2), in the positive triangularity configuration, using the CHEASE equilibrium solver combined with the MARS code, which solves the full MHD linear, resistive equations [5.1, 5.2]. When sawteeth are not included in the model, the q=1 radius predicted by integrated modelling with JINTRAC [5.3] is quite large and the q profile is flat in the core with a low value. For example, $\rho_{tor}(q=1)\approx0.55$ (where ρ_{tor} is the square root of the normalized toroidal flux) and $q_0\approx0.5$ in the E scenario, as shown in Fig. 5.1. This q profile results in a large, dominantly m/n=1/1, internal kink mode being unstable. At higher n values, infernal modes are found in the E scenario, which may limit the achievable plasma performance. These are low-n to medium-n instabilities excited by the large pressure gradient combined with the low shear in the core. In the A scenario, infernal modes are stable due to the lower pressure gradient. For the E scenario, a sensitivity study with respect to q_0 and β was performed [5.1, 5.2]. Unstable external kink modes were found, but only at values of q_0 or β far above what is expected from the integrated modelling, indicating that this scenario is not expected to suffer from Resistive Wall Modes (RWMs) (note that in their present design, the NAS coils would be too slow for RWM control).

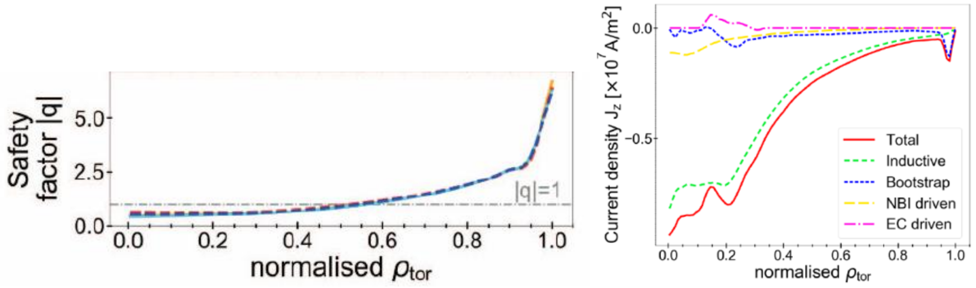

Fig. 5.1: q (left) and current density (right) profiles from JINTRAC simulations of the E scenario (from Figs. 2 and 6 of [5.3])

5.2.2 Sawteeth and their control

A sawtooth model was included in some JINTRAC simulations [5.3]. With a Kadomtsev complete reconnection model, a long sawtooth period (0.72 s) and large crashes ($\Delta T_e \approx 5.1$ keV) were found for the E scenario, as shown in Fig. 5.2 (left). An incomplete reconnection model [5.4] could however be more realistic based on the following arguments. Kadomtsev reconnection assumes single m/n=1 helicity during the non-linear growth of the m/n=1 magnetic island. The single helicity assumption however becomes questionable in two circumstances: 1) when poloidal mode coupling, due to the poloidal modulation of the equilibrium magnetic field, becomes important. This coupling depends on the local r/R parameter; 2) when secondary instabilities are excited during the m/n=1 island growth. These instabilities are expected to become more virulent if the primary m/n=1 island grows rapidly, as they are likely driven by pressure and current density gradients across the reconnection region. Therefore, although there is no conclusive theoretical or experimental evidence, it appears that the relatively large values of the q=1 radius and the relatively large growth rate of unstable internal kink modes that are associated with the DTT E scenario are likely to lead to a violation of Kadomtsev's single-helicity assumption and hence to incomplete reconnection. Preliminary JINTRAC simulations including an incomplete reconnection model suggest that this will result in somewhat smaller sawtooth period and crash size, as shown in Fig. 5.2 (right). Predicting the sawtooth period is important because it has been found empirically to be related to the β_N value above which sawteeth trigger Neoclassical Tearing Modes (NTMs) (which are discussed in section 5.2.3) [5.5].

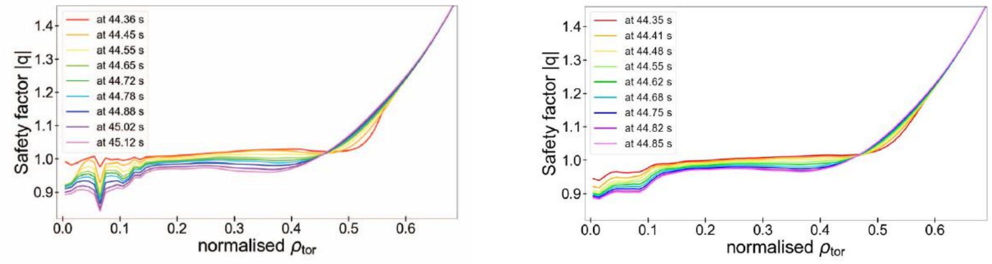

(a) Relaxation of the $|q|$ profile. (a) Relaxation of the $|q|$ profile.

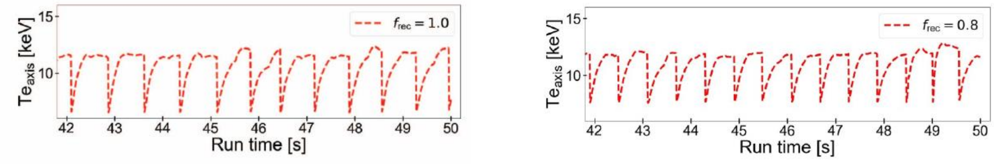

(b) Time evolution of T_{e0}. (b) Time evolution of T_{e0}.

Fig. 5.2: Evolution of the q profile (top) and electron temperature at the magnetic axis (bottom) in JINTRAC simulations of the E scenario with a Kadomtsev complete reconnection model (left) and incomplete reconnection model with f_{rec}=0.8 (right) (Figs. 9 and 10 of [5.3])

Even though it is too early to tell, the risk exists that sawteeth trigger NTMs in some DTT scenarios. It is thus important to consider sawtooth control methods. One possibility is to modify the current density profile in the core using Electron Cyclotron Current Drive (ECCD) in order to limit the q=1 radius to perhaps 30-40% of the minor radius. JINTRAC simulations however find a small effect of ECCD on the q profile in the E scenario, which is consistent with the fact that the EC-driven current is small compared with the inductive current [5.3][5.6]. Sawtooth pacing may thus be needed in order to avoid NTMs, which would be a similar situation to the one foreseen for the EU DEMO [5.7]. Sawtooth pacing in DTT may *a priori* be done with ICRH (like, e.g., in JET [5.8]), ECCD (like, e.g., in TCV [5.9]) or even possibly NBI (as observed in JET from non-intentional drops of the NBI power). However, there has been no modelling so far on these topics. The efficiency of sawtooth pacing, as well as the impact of fast ion populations on sawteeth, may be hindered in view of the relatively large poloidal β if the q=1 radius is allowed to expand to 50% of the plasma minor radius. This is supported by preliminary analytical estimates of fast ion effects in DTT. More accurate simulations of ICRH-produced fast ions and fusion α particles effects on internal kink modes in DTT remain to be done.

5.2.3 Tearing modes (including NTMs)

Tearing Modes (TMs) and Neoclassical Tearing Modes (NTMs) – together designated as (N)TMs – are a concern for future tokamaks because they may reduce plasma performance and modify impurity transport. Furthermore, (N)TMs may grow and lock, producing large magnetic islands capable of triggering a disruption. DTT will allow investigating (N)TMs and their control in a wide range of magnetic configurations.

5.2.3.a (N)TM stability and dynamics

In order to assess the stability and impact of (N)TMs in DTT scenarios and to evaluate the ECH&CD power required for their stabilization or suppression, the (N)TM module developed by ISTP-CNR and SPC-EPFL, already integrated in JINTRAC and in the European Transport Solver (ETS), has been used. The (N)TM module solves the generalized Rutherford and torque balance equations to evaluate the (N)TM evolution in terms of its amplitude, frequency and phase. It could be extended to take into account the effects of error fields and externally applied NAS magnetic perturbations.

At nominal B_t (5.85 T), β_N is expected to remain moderate in DTT scenarios (see Chapter 2), suggesting that NTMs should not be a critical issue. However, as discussed in Section 5.2.2, large sawteeth with a long period are predicted in the E scenario, which may potentially trigger NTMs. A useful modelling task would be to estimate the risk of triggering NTMs for each scenario based on the predicted sawtooth period and β_N value, using the empirical scaling described in [5.5].

For the E scenario, the evolution of m/n=3/2 and 2/1 NTMs, assuming that these are destabilized by sawteeth, has been evaluated with both JINTRAC and ETS [5.10], indicating that the island width would saturate at moderate size (~10% of the minor radius). On the other hand, an influx of impurities or a loss of density control could modify the current density profile towards TM-unstable conditions ($\Delta'_0>0$) and lead to a 2/1 island width of up to ~20% of the minor radius, potentially leading to a disruption [5.10].

Hybrid and advanced tokamak scenarios at reduced B_t (typically 3 T) are in preparation (see Chapter 2) and should allow complementary studies to those that will be carried out in JT-60SA with its carbon wall. These scenarios achieve high β_N (up to 2.5), implying more unstable conditions for NTMs. In some conditions (flux pumping), moderate 3/2 modes may in fact be beneficial in controlling the core pressure and safety factor profile.

Finally, it is important to evaluate the risk of (N)TM locking in DTT scenarios. Mode locking has for example been found to be an issue during investigations of the ITER Baseline scenario in ASDEX Upgrade [5.11]. Even though the larger electron density in DTT is a favourable factor against mode locking, the risk clearly exists due to the low predicted plasma rotation. As a matter of fact, preliminary studies indicate that in the D scenario, locking of the 3/2 NTM could happen [5.12]. The risk of mode locking is partly connected to the quality of error field correction (see Section 5.2.5).

5.2.3.b (N)TM avoidance and control

The avoidance of NTMs in DTT will rely on the flexible heating system, delivering up to 45 MW into the plasma. More than 20 MW of ECH&CD will be installed on equatorial Real Time (RT) -steerable launchers capable of changing the profile of beam power deposition from narrow to wide regions in the core plasma [5.13], thus enabling the optimization of the current and pressure profiles.

NTMs can be controlled/suppressed by raising the current inside the island via ECH&CD. In DTT, upper EC launchers delivering up to 7.2 MW at 170 GHz with good current drive efficiency at the 3/2 and 2/1 surfaces will be available for NTM control. These launchers will be RT-steerable and thus in principle able to track the NTM position. Efforts are ongoing to enhance the speed of the GRAY beam-tracing code for RT implementation. In this context, fast RT equilibrium reconstruction constrained by motional Stark effect measurements could be useful. The development of NTM control schemes in DTT can be of support to ITER and JT-60SA exploitation. They could also help bring to higher technological readiness levels those control schemes eligible for applications in DEMO, for instance those based on the use of a (quasi-) in-line ECE diagnostic. The latter would require integrating an ECE diagnostic in the ECH&CD upper launchers and/or installing additional ECE antennas in free upper ports, possibly RT-steerable.

As shown in Figure 5.3 [5.10], JINTRAC simulations for the E scenario find that a full suppression of the 2/1 NTM can be obtained by early intervention of the ECH system or using modulated ECCD in phase with the island O-point. Such early intervention is however extremely demanding for the control system, which should be sensitive to islands as small as 2-3 cm and able to provide phase detection for proper power modulation (feasible up to 5 kHz). This calls for an intense effort to develop the control system.

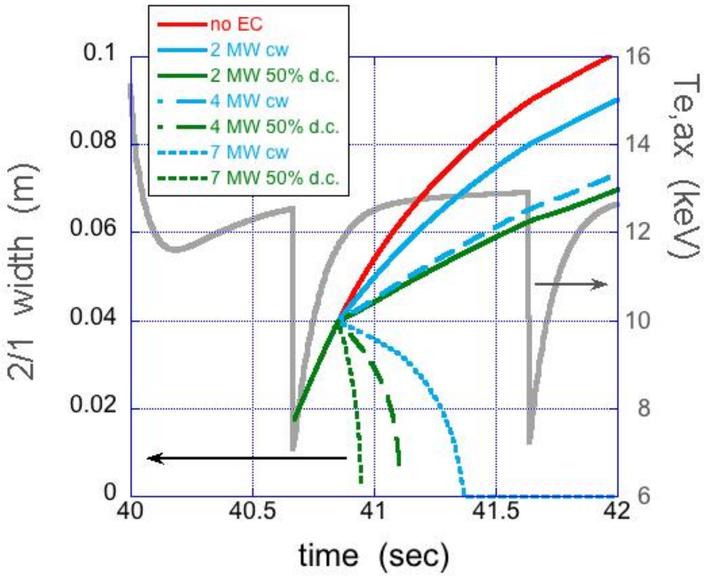

Figure 5.3: Prediction with JETTO/JINTRAC + NTM module of the 2/1 island width evolution for different EC power levels (either steady [blue] or modulated [green] in phase with the O-point) in the E (full power) scenario. In gray line, the central electron temperature shows sawtooth activity with a period of around 1 s.

In case of (N)TM locking, dedicated control techniques could be used. For instance: 1) for NTMs, the phase of the mode could be controlled with the NAS coils and set in such a way to allow ECCD in the O-point region to suppress the mode, as described in [5.14]; 2) (N)TMs could be forced to rotate by producing an adequate rotating field with the NAS coils, as proposed in [5.15]. It would be helpful to plan preparatory modelling work on these topics.

5.2.4 Pedestal and edge localized modes

The pedestal height and width used as boundary conditions in the integrated modelling of DTT scenarios discussed in Chapter 2 have been obtained [5.16, 5.3] using the Europed code [5.17]. Europed uses the EPED1 model [5.18], which is based on combining the stability constraints for peeling-ballooning modes and kinetic ballooning modes. Sensitivity studies have been performed, in particular with respect to the density at the separatrix, and a moderate effect on pedestal properties and global profiles was found [5.16]. In relation to peeling-ballooning modes, it is also noteworthy that the JALPHA workflow [5.19] was recently adopted at the ENEA Laboratories to assess MHD stability. It has been applied to the E (full power) scenario, confirming the equilibrium's stability with respect to modifications in pedestal pressure and current density (j-α diagram).

The size and duration of hypothetical Type I Edge Localized Modes (ELMs) have been estimated for the E scenario based on existing scalings [5.3]. However, it is to be noted that, given the high density at the separatrix, the E scenario might be in a Type II or small ELM regime. This question requires further modelling.

ELM control can be a critical aspect of scenario development. It has been found, e.g. in the development of both the Baseline [5.20] and Hybrid [5.21] scenarios for the JET DTE2 campaign, that too frequent ELMs (associated to high gas dosing) degrade confinement, while too infrequent ELMs can lead to core impurity accumulation issues, resulting in the existence of a sharp maximum for the neutron rate as a function of the ELM frequency. ELM control could also be required to avoid damage to Plasma Facing Components (PFCs).

ELM control with Resonant Magnetic Perturbations (RMPs) may be used in DTT, with strong relevance to ITER and future reactors. The RMPs will be produced by a set of three rows of nine NAS coils (a configuration close to the ITER one), shown in Figure 5.4. The MARS-F code has been used to compute, in toroidal geometry and including flow, the resistive plasma response to different vacuum fields with toroidal mode numbers n=1, 2 or 3 [5.22]. The resonant components of external fields are found to be significantly screened in DTT reference full power scenarios, as shown in Figure 5.5, with n=2, 3 being the most useful to trigger edge response. Conversely, n=1 perturbations have stronger coupling with the plasma core and are likely less useful for ELM control. From this study, optimal current distributions in the NAS coils for ELM suppression, according to criteria based on empirical evidence (e.g. using the normal plasma displacement in the X-point region, shown in Fig. 5.6), have been calculated. Depending on the number of active coils and scenario, coil currents between 20 and 40 kAt are predicted to be effective for ELM mitigation. The development of ELM control with RMPs during the operation of DTT will be part of the general development of H-mode scenarios discussed in Chapter 2.

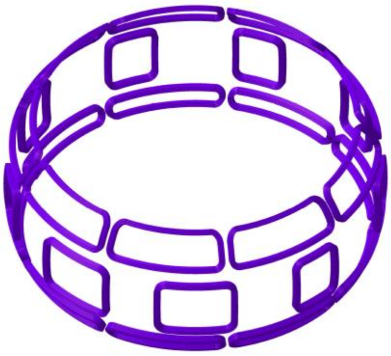

Figure 5.4: Simplified view of Non-AxiSymmetric (NAS) coils

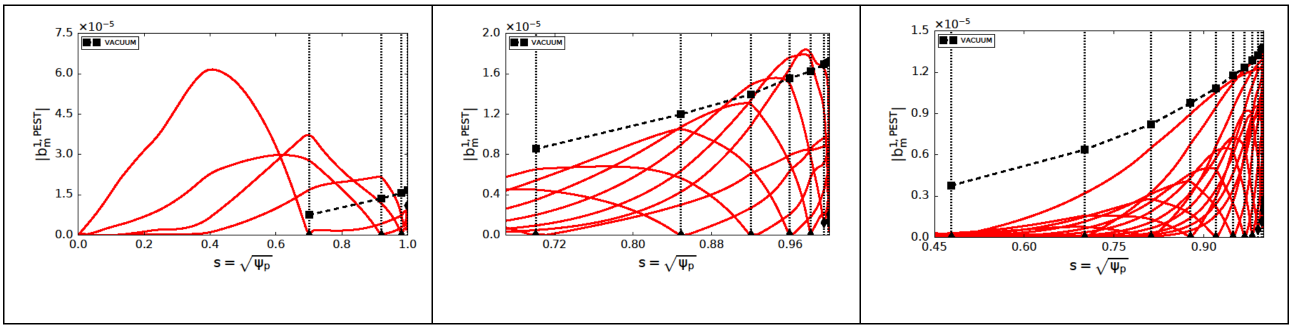

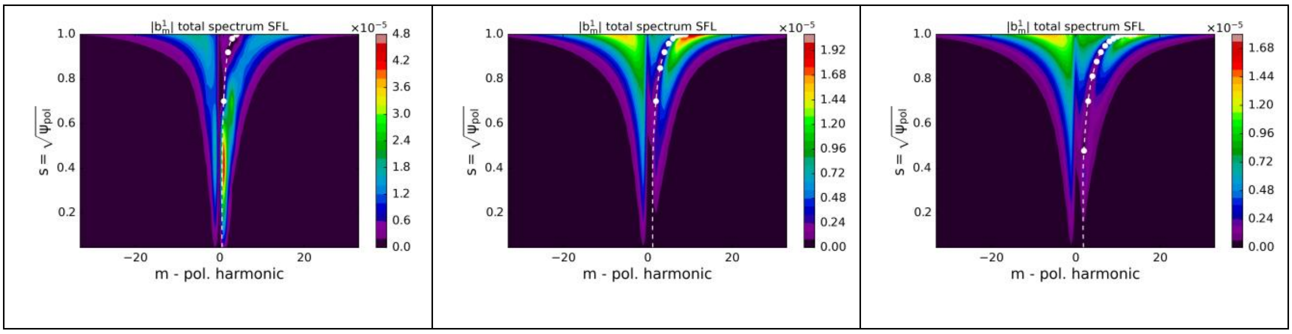

Figure 5.5: (Top) Radial profiles of plasma response harmonics for the first (i.e. radial) contravariant component of the perturbed field, compared to the vacuum field value at rational surfaces marked by black squares. (Bottom) From left to right, poloidal spectra of n=1, 2, 3 unit-current perturbations from mid-plane coils.

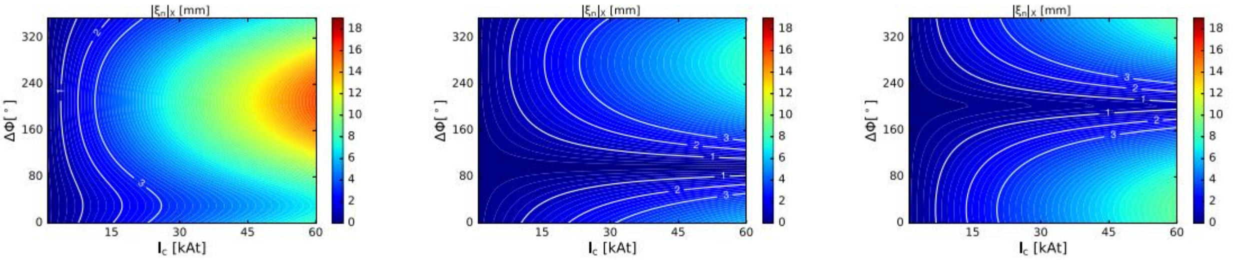

Figure 5.6: MARS-F-predicted normal plasma displacement in the X-point region produced by the off-mid-plane NAS coils as a function of their current and of the toroidal phasing between the upper and lower coils, for the E scenario and for (from left to right) n=1, 2 and 3 configurations (from Fig 9 of [5.22]).

ELM pacing by pellet injection may also be an option in DTT, although the design of the pellet injection system is at a preliminary stage (see Chapter 6).

Besides active ELM control, an important research topic in DTT will be the development and study of small ELMs and ELM-free regimes, as discussed in Chapter 2.

5.2.5 Error fields

Error Fields (EFs), i.e. spurious magnetic field perturbations, shall be minimized in the phase of coil design and installation, as well as during plasma operation due to their detrimental effect on plasma performance. The NAS coils will be used for this purpose, thus acting both as ELM control coils and EF correction coils. Depending on the scenario, these tasks could be performed simultaneously by all NAS coils or with different dedicated subsets of NAS coils. EFs expected from manufacturing and assembly errors of DTT superconducting coils have been calculated using a stochastic procedure based on a linearized model and it has been estimated that NAS coils currents of 50 kAt will be sufficient to correct the so-called ‘three-mode error index’ under 50 ppm with a 95% probability [5.23].

The importance of plasma response to EFs has been recognized in both modelling studies and experimental applications. Thus, metrics that include this response, such as the so-called ‘overlap’ criterion adopted in ITER [5.24], shall be applied to DTT. Repeating the above-mentioned stochastic procedure using the overlap criterion instead of the three-mode error index before the assembly of DTT would allow defining assembly accuracy requirements in the same way as done for ITER [5.25]. This task, which may be at the same time beneficial for DTT and of high interest to ITER, is under consideration.

The presence of EFs will be assessed performing dedicated vacuum discharges and identification studies with plasma during the early operation of DTT. The main method that will be used is the novel non-disruptive compass scan method [5.26], which is supported by the ITPA MDC group. Experimental results will be complemented with plasma response modelling with MARS-F and GPEC. Both codes, although with different approaches, allow the evaluation of plasma response to NAS perturbations and are routinely used in modelling workflows for calculating EF correction recipes.

5.3 Disruptions

5.3.1 Disruption budget and monitoring

DTT will be a relatively large machine with large B_t and I_p in which disruptions will be a serious matter. The DTT mechanical structures were designed to withstand ~1000 full performance disruptions, assuming that half of them could be Vertical Displacement Events (VDEs) in the worst conditions [5.2]. The global disruptivity (including minor and mitigated disruptions) expected in DTT, based on experience from present machines such as JET and ASDEX Upgrade, has been estimated to 30 %, with unmitigated disruptions at full performance representing 20 % of all disruptions, i.e. ~1000 events over the life of DTT. Thus, disruption mitigation is in principle not required in DTT as far as the mechanical integrity of the machine is concerned.

The Thermal Quench (TQ) and Current Quench (CQ) characteristic times have been estimated according to scalings defined in [5.27]. This led to a minimum linear CQ duration of 4 ms. Much longer CQ durations (40 ms) have also been considered based on observations of unmitigated disruptions in tokamaks with a metallic wall. These could imply larger ElectroMagnetic (EM) and thermal loads due to larger and longer lasting halo currents.

The reference EM loads for the structural assessment have been calculated by performing a full set of simulations in various conditions (including major disruptions and VDEs) with the 2D axisymmetric MAXFEA code and the 3D CarMa0NL code. The forces and paths of induced currents in 3D structures have been calculated also with the ANSYS code using as input the plasma evolution calculated by MAXFEA. A further benchmark of the plasma evolution calculated by these codes will be carried out with the non-linear MHD code JOREK.

During the operation of DTT, disruptions will be monitored, in particular in terms of their TQ and CQ timescales, as well as induced and halo currents (measured by Rogowski coils and shunts) and mechanical loads (measured by strain gauges, possibly including optical ones). Experimental disruptions will be compared to the above-mentioned dimensioning simulations with MAXFEA and other codes. If discrepancies are found, simulations will be run again with more realistic parameters and the disruption budget will be updated.

5.3.2 Disruption prevention and avoidance

Disruption prevention and avoidance is a key topic for future machines, such as ITER and DEMO, in which disruptions will have to be exceptional events or even completely absent. Thanks to its resilience to disruptions, DTT may act as a test-bed for disruption prevention and avoidance algorithms and strategies, in particular those in development for ITER.

‘Disruption prevention’ means controlling the plasma in such a way that no critical limits are overcome. This will be addressed with the help of a Matlab simulation platform aimed at closed loop plasma scenario simulations, including a modelling of the Plasma Control System (PCS). In DTT, the development of disruption prevention schemes may concern in particular the ramp-up phase and involve tailoring the current density profile by additional heating [5.28], as well as the ramp-down phase, possibly attempting to delay the H-L back transition as recently tested at JET [5.29].

'Disruption avoidance' means Exception Handling (EH), i.e. being able to react adequately in case a critical limit is overcome (in spite of disruption prevention attempts) or an unforeseen event destabilizes the plasma. The DTT PCS will include EH, following the guidelines used for ITER, but with reduced complexity. Furthermore, DTT will present similarities with ITER in terms of its actuators (in particular ECH&CD and the NAS coils) and of the metallic wall, making it a good test-bed for ITER disruption avoidance strategies. For example, DTT will be able to test strategies to react to an excess of impurities or to a breach of H- or L-mode density limits [5.30, 5.31], and to test the joint use of ECH&CD and NAS coils in case of mode locking, as described in Section 5.2.3.b. In addition, the above-mentioned Matlab simulation platform may be used to develop fast plasma shutdown strategies.

The principal guidelines to feed the DTT PCS with information from a wide set of diagnostics in real time, allowing the implementation of disruption prevention and avoidance (as well as prediction, discussed below), are defined.

5.3.3 Disruption mitigation and disruption physics

Like ITER, DTT will be equipped with a Disruption Mitigation System (DMS) based on the Shattered Pellet Injection (SPI) technique. Also in this area, DTT may act as a companion to ITER on which the tools pre-selected for ITER could be deployed and tested.

The DMS will be triggered when an unavoidable disruption is predicted. This will require implementing a disruption prediction algorithm. The development of such algorithms is an active research topic, in particular in relation with ITER [5.32].

The DTT SPI system will comprise two (optionally four) multi-barrel injectors in two toroidally opposite upper oblique ports. From the maximum total plasma thermal energy of around 14 MJ (including fast ions), it has been estimated that 10^{23} atoms per pellet are appropriate, corresponding to cylindrical pellets of diameter ≈12 mm and length ≈18 mm. The injection velocity is foreseen to be greater than 300 m/s, leading to a flight time well below 10 ms. The option of an additional Massive Gas Injection (MGI) system is considered for operation before the commissioning of the SPI system.

Several tokamaks have performed SPI experiments in recent years, but none has used SPI as a routine DMS, in contrast to what is planned for DTT and ITER. It is important to stress, however, that disruption mitigation is less critical in DTT than in ITER: as mentioned above, the structural integrity of DTT is ensured by design considering the worst expected disruptions as possible events in the life of the machine. The use of the DMS in DTT merely aims at minimizing risks related to mechanical fatigue as well as a possible degradation of the PFCs. Joint efforts between DTT and ITER on the modelling and operation of their SPI systems appear nonetheless clearly justified. This is already ongoing on the modelling side, where for example JOREK is being used to model both machines. Work is indeed underway to simulate with JOREK SPI-mitigated as well as MGI-mitigated DTT disruptions. One aim of these simulations is to assess whether the baseline design with two SPIs is appropriate or whether two additional SPIs are required.

Concerning the general physics of disruptions, with its high I_p and B_t relatively to its size (which, among other effects, results in a high Greenwald density limit), DTT will produce valuable data to test disruption models in an unusual range of parameters. DTT will also allow investigating the physics of disruptions in Negative

Triangularity (NT) configurations, which may receive interest in relation with possible NT reactor design studies. Last but not least, DTT may allow assessing how liquid metal divertors cope with TQ heat loads. Such divertors might indeed prove much more resilient than solid divertors, which would relax the requirement of mitigating TQ heat loads.

5.3.4 Runaway electrons

Runaway Electrons (REs) are probably the most concerning disruption-related issue for future large tokamaks, such as ITER and DEMO. Once these machines are activated, unavoidable RE 'nuclear' seeds combined with an avalanche amplification by many orders of magnitude may produce multi-MA RE beams even in mitigated disruptions, which present a large risk of causing important damage [5.33].

5.3.4.a RE generation and avoidance

It is not clear if natural disruptions will produce RE beams in DTT. The use of a full W wall may lead to rather slow CQs, which tends not to promote RE generation, as observed at JET [5.34]. On the other hand, DTT will operate at higher I_p and B_t than JET, which promotes RE generation. JOREK simulations are planned in order to assess RE generation in natural DTT disruptions. In the frame of this activity, JOREK will be benchmarked against theory-verified results from the SCOPE3D code regarding the interaction between REs and magnetic islands.

If RE beams turn out to occur in natural disruptions, it is likely that they may be avoided in SPI- or MGI-mitigated DTT disruptions. This will also be assessed with JOREK. In addition, recent experiments in several devices (e.g. ASDEX Upgrade [5.35], COMPASS, DIII-D) have shown that the application of NAS fields may reduce the RE current, which can be of interest to ITER as a complement to SPI. Use of NAS coils is considered in order to study this topic on DTT.

On the other hand, if natural disruptions do not produce RE beams in DTT, a recipe to produce such beams will need to be developed as a pre-requisite to experiments on RE mitigation (discussed in the next section). This recipe would typically involve the massive injection of impurities (e.g. Ne or Ar) in the form of either gas or shattered pellets. JOREK simulations would be helpful in order to prepare this recipe.

5.3.4.b RE beam mitigation

Since the generation of multi-MA RE beams seems very difficult to avoid in ITER and DEMO (during the nuclear phase of operations, at least), mitigation of and/or resilience to RE beam impacts is a crucial topic for these machines. Concerning ITER, it is hoped that H_2 SPI into RE beams will lead to a benign termination, as observed in present machines [5.36]. DTT will offer the possibility to further test this key strategy and it would be of high interest to ITER if this could be done during Phase 1 (2029-2034) of the DTT operation, especially at high I_p. This would require having the SPI system operational during this phase. Concerning EU DEMO, the current strategy for resilience to RE beam impacts is based on sacrificial limiters. Design studies regarding possible sacrificial limiters in DTT are ongoing. This may be an area for collaboration between the DTT and EU DEMO teams. JOREK simulations are ongoing or planned to study the dynamics of RE beams and their termination in both machines [5.37].

5.4 Relevant diagnostics

In order to measure magnetic fluctuations, DTT will be equipped with an extensive poloidally and toroidally distributed set of in-vessel mineral-insulated-cables pick-up coils and low-temperature co-fired ceramics sensors with a sensitive band expanding above 1 MHz.

An equatorial ECE system will be available, with adequate spatial (1 cm in X2 mode) and temporal (5 µs) resolution to diagnose NTMs and a broad coverage from the HFS to LFS (in O1 mode) allowing diagnosing sawteeth.

SXR and bolometer tomography systems will allow investigating the interplay between MHD activity and impurities.

Measurements of plasma rotation by Charge Exchange Recombination Spectroscopy (CXRS) will allow, e.g., cross-checking the identification of NTMs with equilibrium reconstruction.

Two diagnostic systems are planned to measure bremsstrahlung radiation from REs in the hard X-ray/gamma-ray (HXR/GR) energy range, meant to be available respectively for Phase 1 and Phase 2. The Phase 1 system is a set of four HXR/GR detectors using BC-509 liquid scintillator at different toroidal positions in the torus hall (see Figure 5.7 left). These will be complemented, at each position, with one neutron monitor using NE213 liquid scintillator and one GR monitor using sodium iodide NaI(Tl) inorganic scintillator, designed based on experience from the FTU tokamak. In DTT scenarios where REs are generated, differences in the temporal patterns of the signals from BC-509, NE213 and NaI(Tl) will allow determining the neutron/HXR/GR admixture of the radiation field in the DTT torus hall and identifying, in real time, the signature from the RE bremsstrahlung radiation. The primary goal of the HXR/GR detectors is machine protection. The Phase 2 system is instead a set of GR detectors to be installed together with neutron detectors in the horizontal neutron camera of DTT (see Figure 5.7 right). The detectors are cylindrical $LaBr_3$(Ce) crystals as those used at JET [5.38], observing the plasma through 9 collimated lines of sight and equipped with neutron attenuators to enable measurements of the energy spectrum of the bremsstrahlung radiation emitted by confined REs. They are meant to support physics investigations by providing information on the RE energy spectrum and spatial distribution.

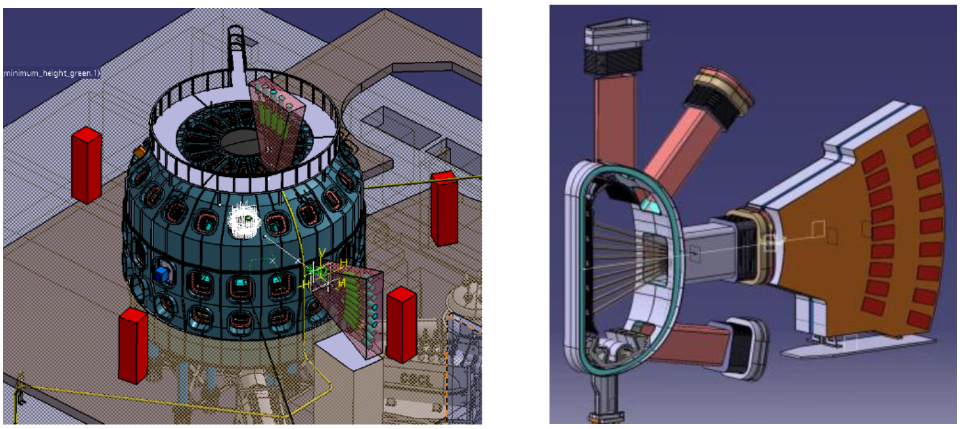

Figure 5.7: Left: Planned positions of the HXR/GR monitors (indicated by red boxes) in the DTT torus hall. Right: Sketch of the DTT horizontal neutron camera. The red boxes in the front row are neutron detectors, with gamma-ray detectors represented by the red boxes behind them.

5.5 Headlines of the research programme for MHD, disruptions and control

In this section, we summarize the main headlines of the DTT research programme regarding MHD, disruptions and control, according to the various operation phases of DTT.

Headline number	**Headline contents**	**Priority (+, ++, +++)**	**ITER**	**DEMO**
Construction Phase 2022-2029				
C.5.1	Preparatory modelling of the main DTT scenarios focused in particular on basic MHD stability (ideal/resistive low-n modes and high-n peeling-ballooning modes) and NTM avoidance and control	++		
C.5.2	Error field modelling including plasma response in order to provide accuracy criteria for machine assembly	++	*	
Phase 1 2029-2034				
1.5.1	Development of error field correction	+++	*	*
1.5.2	NTM control studies (exploiting high β_N scenarios at reduced I_p and B_t)	++	*	*
1.5.3	Development of disruption prevention and avoidance (continuing in later phases)	++	*	*
1.5.4	RE studies (in particular, RE impacts on the wall / sacrificial limiters and, as soon as the SPI system is available, RE beam mitigation by H_2 or D_2 SPI) (continuing in later phases)	+++	*	*
Phase 2 2034-2038				
2.5.1	Development of sawtooth pacing method (especially if needed for NTM avoidance)	++(+)	*	*
2.5.2	Development of ELM control with the NAS coils	++	*	
Phase 3 2038-...				
3.5.1	Studies on disruption prediction and mitigation with SPI at full performance (prepared already in previous phases)	+++	*	

5.6 References

[5.1] Fusco V., et al., ‘Stability analysis of low-n modes for the Divertor Tokamak Test facility Single Null Scenario’, 47th EPS Conference on Plasma Physics, 2022, http://ocs.ciemat.es/EPS2022PAP/pdf/P2a.125.pdf.

[5.2] Crisanti F., et al., ‘Physics basis for the Divertor Tokamak Test facility’, 29th IAEA Fusion Energy Conference, London, 2023.

[5.3] Casiraghi I., et al., ‘Core integrated simulations for the Divertor Tokamak Test facility scenarios towards consistent core-pedestal-SOL modelling’, Plasma Phys. Control. Fusion 65 (2023) 035017.

[5.4] Porcelli F., et al., ‘Model for the sawtooth period and amplitude’, Plasma Phys. Control. Fusion 38 (1996) 2163.

[5.5] Chapman I., et al., ‘Empirical scaling of sawtooth period for onset of neoclassical tearing modes’, Nucl. Fusion 50 (2010) 102001.

[5.6] Baiocchi B., et al., ‘ECH in DTT: system capabilities and applications in plasma scenarios’, 22nd joint workshop on electron cyclotron emission and electron cyclotron resonance heating, Daejeon, 2024.

[5.7] Siccinio M., et al., ‘DEMO physics challenges beyond ITER’, Fusion Eng. Des. 156 (2020) 111603.

[5.8] Lerche E., et al., ‘Sawtooth control with modulated ICRH in JET-ILW H-mode plasmas’, Nucl. Fusion 60 (2020) 126037.

[5.9] Goodman T.P., ‘Individual Sawtooth Pacing by Synchronized ECCD in TCV’, AIP Conf. Proc. 1406 (2011) 505–508, https://doi.org/10.1063/1.3665024.

[5.10] Granucci G., et al., ‘Roles of ECH system in DTT plasma operations’, 29th IAEA Fusion Energy Conference, London, 2023.

[5.11] Pütterich T., et al., ‘The ITER Baseline Scenario at ASDEX Upgrade and TCV’, 47th EPS Conference on Plasma Physics, online, 2021.

[5.12] Nowak S., private communication, 2023.

[5.13] Baiocchi B., et al., ‘Core transport modelling of the DTT full power scenario using different fuelling strategies’, Nucl. Fusion 63 (2023) 106009.

[5.14] Volpe F., et al., ‘Avoiding Tokamak Disruptions by Applying Static Magnetic Fields That Align Locked Modes with Stabilizing Wave-Driven Currents’, Phys. Rev. Lett. 115 (2015) 175002.

[5.15] Zohm H., et al., ‘Forced Rotation of Tearing Modes by Time Varying RMP Fields’, IPP internal report, 2022.

[5.16] Casiraghi I., et al., ‘First principle-based multi-channel integrated modelling in support of the design of the Divertor Tokamak Test facility’, Nucl. Fusion 61 (2021) 116068.

[5.17] Saarelma S., et al., 'Integrated modelling of H-mode pedestal and confinement in JET-ILW', Plasma Phys. Control. Fusion 60 (2018) 014042.

[5.18] Snyder P.B., et al., 'A first-principles predictive model of the pedestal height and width: development, testing and ITER optimization with the EPED model', Nucl. Fusion 51 (2011) 103016.

[5.19] JALPHA workflow, R. Coelho, ITM/WPCD EUROfusion Work Packages.

[5.20] Garzotti L., et al., ‘Development of high-current baseline scenario for deuterium-tritium high fusion performance at JET’, 29th IAEA Fusion Energy Conference, London, 2023.

[5.21] Lerche E., et al., ‘Development of a hybrid plasma scenario for D-T experiments in JET-ILW’, 6th Asia Pacific Conference on Plasma Physics (AAPPS-DPP2022), online.

[5.22] Pigatto L., et al., ‘Numerical investigation of toroidal plasma response for ELM control via magnetic perturbations in the DTT Tokamak’, to be published in Nucl. Fusion (https://iopscience.iop.org/article/10.1088/1741-4326/ad0c09).

[5.23] Albanese R., et al., ‘Error field and correction coils in DTT: A preliminary analysis’, Fusion Eng. Des. 189 (2023) 113437.

[5.24] Park J.K., et al., ‘Error field correction in ITER’, Nucl. Fusion 48 (2008) 045006.

[5.25] McIntosh S., et al., ‘Translating Physics Limits to Millimeters’, SOFE 2023.

[5.26] Piron L., et al, ‘Error field detection and correction studies towards ITER operation’, 29th IAEA Fusion Energy Conference, London, 2023.

[5.27] Hender T., et al., ‘Chapter 3: MHD stability, operational limits and disruptions’, Nucl. Fusion 47 (2007) S28.

[5.28] Vincenzi P., et al., ‘Exploring Divertor Test Tokamak (DTT) operation space and plasma scenarios through time-dependent 0.5D integrated modelling’, 47th EPS Conference on Plasma Physics, online, 2021.

[5.29] Sozzi C., et al., ‘Termination of discharges in high performance scenarios in JET’, 28th IAEA Fusion Energy Conference (FEC 2020), online, 2021.

[5.30] Maraschek M., et al., ‘Path-oriented early reaction to approaching disruptions in ASDEX Upgrade and TCV in view of the future needs for ITER and DEMO’, Plasma Phys. Control. Fusion 60 (2018) 014047.

[5.31] Esposito B., et al., ‘Disruption avoidance by means of electron cyclotron waves’, Plasma Phys. Control. Fusion 53 124035 (2011).

[5.32] Pautasso G., et al., ‘The ITER disruption mitigation trigger: developing its preliminary design’, Nucl. Fusion 58 (2018) 036011.

[5.33] Nardon E., et al., ‘Modelling of Runaway Electron Dynamics in Tokamak Disruptions’, 29th IAEA Fusion Energy Conference, London, 2023.

[5.34] de Vries P., et al., ‘The impact of the ITER-like wall at JET on disruptions’, Plasma Phys. Control. Fusion 54 (2012) 124032.

[5.35] Gobbin M., et al., ‘Runaway electron mitigation by 3D fields in the ASDEX-Upgrade experiment’, Plasma Phys. Control. Fusion 60 (2018) 014036.

[5.36] Paz-Soldan C., et al., ‘A novel path to runaway electron mitigation via deuterium injection and current-driven MHD instability’, Nucl. Fusion 61 (2021) 116058.

[5.37] Vannini F., et al., ‘Runaway electrons beam termination and wall loads in DEMO’, 65th Annual Meeting of the APS Division of Plasma Physics, Denver, 2023.

[5.38] Nocente M., et al., ‘MeV range particle physics studies in tokamak plasmas using gamma-ray spectroscopy’, Plasma Phys. Control. Fusion 62 (2020) 014015.

Chapter 6

PHYSICS OF HEATING, CURRENT DRIVE & FUELLING

C. Sozzi, D. Van Eester, P. Vincenzi, D. Terranova,
L. Aucone, B. Baiocchi, A. Cardinali, C. Castaldo, S. Ceccuzzi, C. De Piccoli, L. Figini, J. Hillairet,
C. Hopf, P. Innocente, P. Jacquet, D. King, P. Mantica, C. Tsironis

A powerful and diversified heating and fuelling system is envisaged in DTT in order to contribute to its main mission: investigating a heat-exhaust system capable to withstand the power load of a fusion reactor, in an environment that allows to integrate all the main physics elements occurring in a burning plasma. It includes Electron Cyclotron Resonance Heating (ECRH), Ion Cyclotron Resonance Heating (ICRH) and Negative Neutral Beam Injection (NNBI) with 45 MW in total at its full development. The physics of the electron heating will have a primary importance in DTT in an unprecedented range of physics and engineering parameters. The ICRH and NNBI systems will extend the range of attainable heating schemes allowing mimicking reactor relevant conditions, in particular by producing energetic ion populations. Plasma fuelling at high density will be provided by an advanced matter injection system.

6.1 Introduction

The DTT tokamak is primarily designed to contribute to the demonstration of a heat-exhaust system capable to withstand the power load of a fusion reactor, in an environment that allows integrating all the main physics elements occurring in a burning plasma. For this mission, a powerful and diversified heating and fuelling system is required, capable of delivering to plasma 20 MW in the first phase and 45 MW at its full development, with a plasma central density in the range of 2.5×10^{20} m^{-3}. The main characteristics, lines of development and items of the experimental work to be implemented in order to bring such systems to full performance, subject to the functional requirements, are summarized in this chapter.

In the following sections, simple descriptions are given of the various systems delivering particles and/or energy to the DTT plasma. To allow easy comparison while keeping the information of each system grouped, a similar structure for all the subsystems will be followed: first, a brief description will be provided and the relevance of the DTT project in the context of ITER and DEMO will be sketched. Second, a brief summary of the specific power/fuelling source will be provided and the tasks it will fulfil in DTT. Table 6.1 provides a summary to illustrate how the various systems can contribute. Then, the procedure for the systems commissioning is briefly described, together with a list of the plasma diagnostics which are important to exploit the systems at full performance and to accomplish their tasks in the experiments. Finally, a mention of the modelling required to guide optimal operation is given.

Table 6.1. Functional requirements of the heating and fuelling systems. For each system and task, a categorization is given: *** essential, ** useful, *usable, - not applicable. (1) Indirect ion heating via collisions at high plasma density. (2) Combined use of heating systems and pellet should be considered since operations with pellet will require at least a minimum amount of additional heating

Task in DTT	ECRH	ICRH	NNBI	Pellet
Preionization, Breakdown and Start-up	**/***	*/**	-	-
Plasma current ramp-up and ramp down	**	**	*	-
H-mode access and exit	**	**	**	**
Electron heating	***	**	***	-
Ion heating	*(1)	***	**	-
Current drive	***	*	**	-
Core MHD control (NTM, ST)	***	*/**	*	-
Fast ions generation	-	***	***	-
Kinetic profiles control	**	**	*	**
Impurity access/accumulation control	**	**	**	**
Momentum injection and control	-	-	**	-
Transport studies	**	**	**	**
Isotopic studies	-	**	**	**
Wall cleaning	*/**	**/***	-	-
Fuelling (2)	*	*	*	***
Elm pacing	*	*	*	**

6.2 The DTT ECRH system

Electron Cyclotron Resonance Heating (ECRH) will be the primary heating system in DTT. Electromagnetic waves in the ECR range are very effectively coupled to the plasma up to the density cut-off of about 3.5 10^{20} m^{-3} in O1 propagation (fundamental Ordinary mode, wave electric field parallel to the static magnetic field of the tokamak) at 5.85 T and up to 1.7 10^{20} m^{-3} in X2 mode (second harmonic eXtraordinary mode, wave electric field perpendicular to the static magnetic field) at half field operation of 2.9 T. They transfer their power to the electron population, with an extreme capability of localization of the absorption in a wide range of radial positions, also thanks to the possibility of using quasi-optical techniques to redirect the waves in the desired direction. These peculiar characteristics allow a variety of applications besides plasma heating.

6.2.1 System description and ITER/DEMO relevance

DTT will be equipped with the most powerful ECRH system ever before ITER, incorporating several cutting-edge technical innovations. Basic components of the systems are 32 gyrotron sources at 170 GHz of 1 MW each, delivered in two stages, arranged in clusters of 8 units fed by 4 main high voltage power supplies. The ECRH power can be modulated up to 5 kHz frequency. The 8 microwave beams of each cluster are transmitted by a first-of-a-kind multi-beam, evacuated quasi-optical transmission line to one of the 4 DTT sectors dedicated to the ECRH launching systems. Each ECRH sector is equipped with 6 independent, plasma-facing launching mirrors located in the equatorial port and 2 in the corresponding upper port (Figure 6.1). Each launching mirror is steerable in both poloidal and toroidal directions (Figure 6.2) providing access and optimal absorption to the whole plasma core for power deposition and current drive [6.1]. The upper launcher has favourable access to the 2/1 and 3/2 rational surfaces and is mainly dedicated to the control of the MHD activity while the equatorial launcher is dedicated to heating and current drive for scenario access and the other tasks. The achievable steering range and the corresponding current drive efficiency are summarized in Figure 6.3.

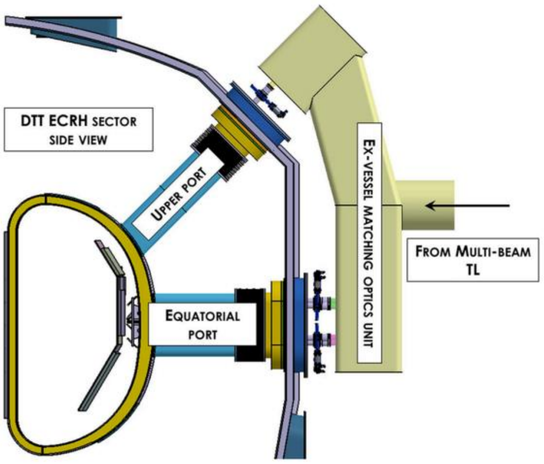

Figure 6.1. Side-view of a DTT sector housing the ECRH antennas [6.1]

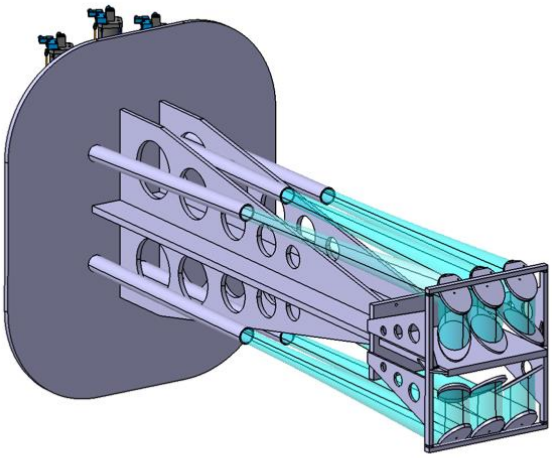

Figure 6.2. The ECRH equatorial antenna

As for Table 6.1, the flexibility of the ECRH allows a wide range of applications, assisting the implementation of plasma scenarios along the whole discharge duration from start-up to termination and also for machine walls conditioning (ECWC). The whole process of bringing to maturity the use of ECRH for the various, to some extent competing tasks is valuable for the preparation of the ECRH operation in ITER given the similarities of the two systems.

DTT, as ITER and DEMO, will be predominantly an electron-heated device. One specific contribution that DTT can develop is the study of the indirect ion heating through the interaction with the electron channel at reactor relevant density. This is a key point in particular in the transients entering and leaving the phase of the discharge in which a significant amount of fusion power is expected in ITER and DEMO. The role of ECRH in a number of operational conditions and physics tasks is summarized next.

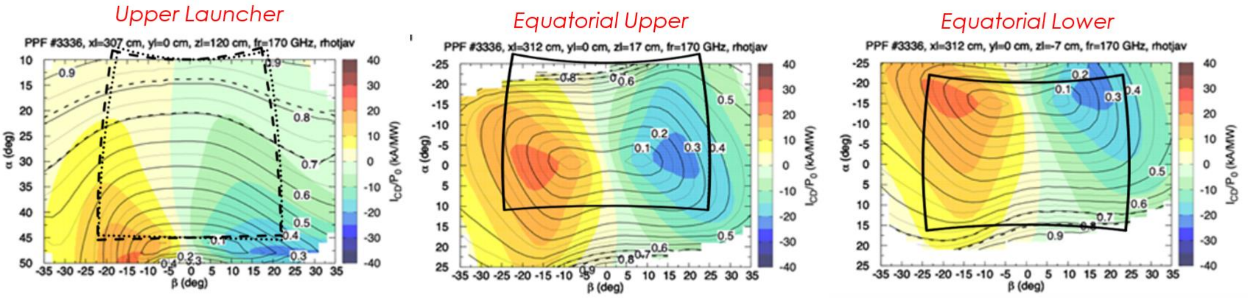

Figure 6.3. Current drive [kA/MW] efficiency for the DTT reference scenario E. Black curves represent the ρ_{tor} normalized radius, dashed lines the 2,1 and 3,2 magnetic surfaces. The mechanically accessible steering range of the ECRH beams is enclosed in the ~rectangular area. α, β are respectively the poloidal and toroidal injection angles.

6.2.2 Heating and current drive source and system-specific tasks

Electron Cyclotron Wall Cleaning (ECWC). The standard requirements for the ECRH system rely on the possibility for short pulse He or D_2 plasma, typically a few hundreds of ms per pulse; the polarizations considered are the ordinary for fundamental or extraordinary for second electron cyclotron harmonic operation. In the first case, a significant toroidal component (~20°) of the injection angle is beneficial, while in the second case perpendicular injection is essential. Optimal pre-fill pressure varies in the range of 10^{-4}-10^{-3} mbar. The optimization of the poloidal magnetic field components - typically with vertical component of B_v ~ 0.2-2% B_t - is important for compensating the vertical B**x**gradB drift by a vertical pitch angle. Different patterns have been tested: purely vertical, or quadrupole and barrel-shaped Trapped Particle Configuration (TPC) combining a radial component. Preliminary evaluations of the vacuum magnetic configurations candidates for ECWC and of the needed active current settings in the coil systems have been performed with CREATE-L [6.2].

EC assisted breakdown. Both the O1 and X2 absorption schemes for EC assisted breakdown can be adopted for the plasma start-up in DTT. In the first case, toroidally oblique launch favours the conversion of the unabsorbed EC wave at the fundamental harmonic, O1 polarized, to X1 by an oblique reflection on the metallic surface of the inner wall. This conversion enhances the absorption efficiency by a large factor in the magnetic null region, provided that this is crossed by the EC resonance layer. Use of such a configuration in DTT will require further analysis due to the non-uniform layout of the inner wall (alternate tungsten monoblocks/tungsten coated cooling pipes). The diagnostics set for EC wall cleaning and assisted breakdown include a Fast camera, Thomson scattering, Interferometry, SPRED (survey, poor resolution, extended domain spectrometer in the vacuum ultra-violet range), Passive CXRS (Charge-Exchange Recombination Spectroscopy, in the visible range), RGA (Residual Gas Analyzer), EC stray radiation detector, pressure gauges, mass spectrometry, spectroscopy, Langmuir probes and magnetic probes.

EC assisted ramp-up. Simulations have shown that balancing the ECRH on-axis and off-axis components of the deposition profile in the phase in which the current is ramped up (while the plasma density is rising) reduces the plasma internal inductance favourably, limiting the flux consumption. This optimization is also applicable for the plasma termination, counteracting the peaking of the current density profile [6.3].

EC heating and current drive in flat-top. The reference DTT Single Null full power scenario is characterized by B_t=5.85T, I_p=5.5 MA, R=2.19 m, a=0.7 m and by additional auxiliary power coupled to the plasma P_{aux}=45 MW (28.8 MW from the EC system). Analysis of the flat-top phase of this scenario has confirmed that the allowed range of angles of the launchers permits to reach the whole plasma volume, from central (ρ~0.1; ρ is the normalised minor radius) to peripheral core plasma (ρ~0.7-0.8), with complete absorption. This will ensure bulk heating and core current drive (CD) for profile tailoring, and NTM mitigation in correspondence of the main rational surfaces. The maximum value of driven co-current is about 25 kA/MW at (ρ_{tor}~0.1). [6.3]

Sawteeth control. The DTT reference scenario E (I_p=5.5MA, B_t=5.85T, 32MW ECRH, 9.5MW ICRH, 10MW NNBI installed power) has a safety factor profile with q_0~0.5 and q=1 at $\rho_{tor}\approx$0.55, such that a wide plasma region is expected to be affected by sawtooth activity. In general, in such a scenario the EC and the other non-inductive currents at the plasma centre are significantly lower than the total current. Despite the wide flexibility of the ECRH system, which allows selection of injection angles that optimize power deposition across a wide range of ρ_{tor}, scenario simulations indicate little margin for reducing the size of the region affected by the sawteeth. The analysis performed shows a moderate positive effect in broadening the ECRH deposition region from $\rho_{tor} \leqslant 0.2$ to $0.05 \leqslant \rho_{tor} \leqslant 0.7$ in scenario E [6.5][6.6].

EC beam control at high density. The reference DTT full power scenario is characterized by high density plasma (n_{e0} ~$2.5x10^{20}m^{-3}$). The density perturbations related to pellet fuelling have been considered to estimate the potential impact on the EC propagation and consequently the need of beam realignment to compensate the radial displacement due to the deflection caused by the variation of refraction around the 2/1 magnetic surface (ρ~0.8). For the pellet size and frequency required for plasma fuelling (<1mm, 16 Hz), no significant adjustments are required. Manageable adjustments of the EC beam aiming (~2°) are required for larger pellet size [6.6].

NTM control. NTMs can easily be triggered by the sawtooth crashes. Generalized Rutherford Equation (GRE) analysis shows that the uncontrolled 2,1 mode can grow up to ~0.15m, likely leading to disruption. Preliminary evaluations show that the mode growth can be controlled and even suppressed with 4-7 MW of ECCD, depending on the control approach (modulated or cw) and on the promptness of the actuator application [6.8].

Impurity control. The beneficial role of core electron heating, particularly ECRH, in reducing the central accumulation of heavy impurities (W) has been experimentally demonstrated [6.8] and is widely used as a tool to complement the control of the plasma scenario. A systematic evaluation of the amount of ECRH power needed for impurity control in all the DTT scenarios is not yet available. However, scenario simulations are giving initial indications. The effect on impurity accumulation of the ECRH deposition broadening mentioned above results in a tolerable but yet visible increase in the core tungsten concentration [6.6]. Also the simulation of scenario A (B_t = 3 T,$|I_p|$ = 2.0 MA and 7.2 MW of ECRH coupled in X2 mode at $0.03 \leqslant \rho_{tor} \leqslant 0.47$) shows a tendency to tungsten core accumulation, while scenario C (B_t = 5.85 T, $|I_p|$ =4.0 MA, 14.4 of coupled ECRH, central deposition, 3 MW of RF) does not. The assessment of the core heating power needed for impurity control is a key contribution in preparation of the operations of ITER and DEMO.

6.2.3 System commissioning, required diagnostics and dedicated modelling

Some of the key tasks of the ECRH system will mainly be fulfilled in a specific and pre-determined phase of the discharge (pre-ionization, breakdown, ramp-up or ramp-down) or between plasma pulses (ECWC). For those tasks, the development path for the baseline application is relatively straightforward, based on the optimization of the characteristic parameters as suggested by previous experiments and by modelling. Likely, such applications will be developed during the initial phase of the ECRH operations in DTT, as they support very basic machine operations.

Other tasks of the ECRH system, such as the control of kinetic profiles, of sawteeth, NTMs, and impurities will be developed at a later stage since they support the access and control of the plasma scenarios, in particular for the optimization of the performance in terms of plasma pressure, purity, confinement and stability. The development of such applications is of critical importance for reaching and maintaining the target plasma scenario. In principle, the fulfilment of those tasks may require competing specifications in the allocation of the ECRH power and launching parameters. An essential step will be the evaluation of the amount of power to be reserved for each task, keeping into account potential mutual coupling effects. For example, the radial distribution of power requested for tailoring the q-profile might contribute, either positively or negatively, to the control of impurity transport. Priorities need to be defined for the ECRH actuator for each plasma scenario. Such priorities will likely depend on the plasma discharge phase, on the proximity of operational limits and on the main purpose of the ongoing experiment.

Simulation codes for beam propagation, power absorption and non-inductive current drive are well developed and validated tools, applicable in many plasma conditions relevant for most of the above-described tasks. For some peculiar situations, operationally important in a fusion reactor perspective (for example gas pre-ionization and density fluctuations), both the theory and the associated numerical tools are active research topics.

The exploitation of the ECRH capabilities implies the development of control schemes involving several diagnostics, including at least: equatorial ECE (fast radiometer and a wide-band spectrometer) and fast density measurement for the control of the kinetic profiles, EC stray detectors for the optimization of the injection settings, magnetic probes for MHD control, and bolometers in the visible range for impurity control.

The various applications will be detailed and developed as part of the DTT commissioning programme. A good part of the commissioning of the main components of the ECRH system can be conducted with reduced interference with the DTT vacuum vessel and in general with the torus hall. The gyrotron sources, including their power supplies and cryomagnets can be brought to performance using local dummy loads to dump the output wave power. Each beam routing through the transmission line up to the launching system can be commissioned by using a dummy load in the torus hall. Multi-beam operation of the transmission line and the commissioning of the launching systems require a target plasma with sufficient absorption of the ECRH power. A key diagnostic for all the commissioning phases with plasma is the EC stray detector.

6.3 The DTT ICRH system

Ion Cyclotron Resonance Heating (ICRH) - making use of radio frequency (RF) waves - is a key heating method in many magnetic confinement devices, and will also be installed on DTT. Its main assets are its ability to directly affect the ion population and its good spatial localisation in the plasma. Its flexibility offers targeting various species and adjusting the power deposition location at will. Aside from its primary role as a heating technique, the coupled RF power can be exploited for a wide variety of purposes such as to create high-energy populations and hence to affect MHD, turbulence and transport.

6.3.1 System description and ITER/DEMO relevance

At the end of an in-depth study, the optimal design for the DTT ICRH launcher was found to be a 3-strap antenna with lateral folded straps and an end-fed centre-grounded central strap (see e.g. [6.10],[6.11]). Figure 6.4 provides an idea of the launcher. The antenna front-end has to be installed and maintained via a remote handling system because its toroidal extension exceeds the width of the port duct. Optimized coupling is ensured through a (largely external) matching circuit with 3dB hybrid couplers and impedance transformers, allowing to catch changes in the plasma load so that the power reflected to the generator remains modest at all times. The antenna box as well as the straps are poloidally curved but not specifically tailored to any particular configuration. The mean antenna-plasma distance can be adjusted to enhance coupling both by moving the launcher radially and by modifying the plasma shape. An alternative, innovative, and promising antenna design, based on a self-matching mechanism, has been preliminarily assessed and may be considered for the second pair of antennas. Active cooling is mandatory to withstand the heat loads during entire full-performance plasma pulses. Up to 9.5MW of RF power is intended to be installed by the end of the DTT experimental phase. The foreseen frequency range extends from 60 to 90MHz.

Operation at high currents and fields is naturally associated with high densities. The thus enhanced resistance and collisionality reduces the energies that sub-populations can reach. On the other hand, DTT will have - in particular at the full development phase of its life - a massive amount of auxiliary heating installed. The wide range of parameters that can be covered makes DTT a unique machine to explore widely differing regimes, from quiet plasmas (as currently foreseen for future fusion power plants and thus – until further notice - the intended regime for DEMO) to discharges that are extremely vulnerable to the tiniest change in settings because of the presence of energetic particle populations. The fate and role of these populations can yield drastic bifurcations in the plasma response, which can be exploited to enhance performance, provided experimental testing shows steerability through changing the engineering parameters, while making use of state-of-the-art diagnostics and real-time control. More specifically, DTT will provide valuable input for ITER on various fronts. Studying and optimising the coupling of RF waves for the wide variety of plasma shapes intended to be explored in DTT is one evident example.

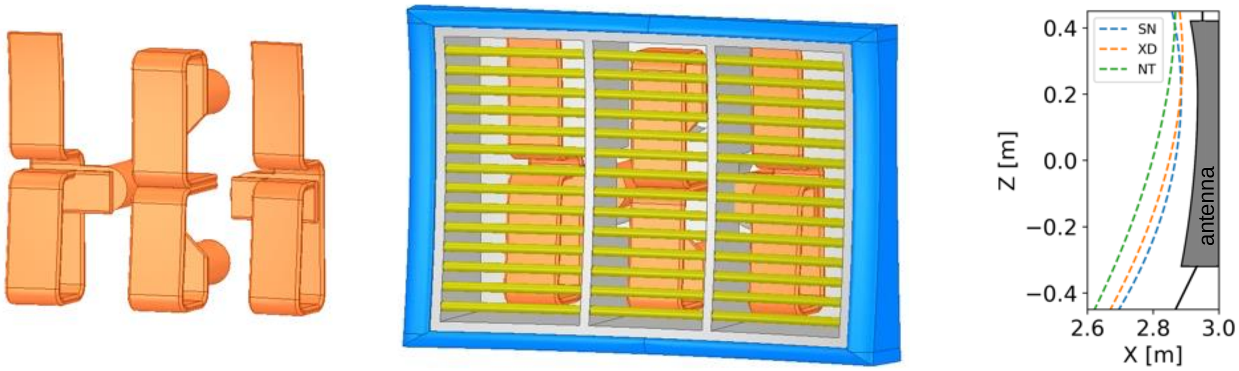

Figure 6.4. Present DTT ICRH antenna design: 3-strap structure (left), 3D view of the antenna in its antenna box with Faraday screen (middle) and qualitative side view of the front end of the antenna box with last closed flux surface for various foreseen plasma shapes (right).

6.3.2 Heating and current drive source and system-specific tasks

Due to its flexibility, ICRH will be able to contribute to the DTT programme in a wide variety of ways. It can provide wall conditioning in between pulses and can be of help at the plasma start-up as well as plasma “landing” (real-time controlled exit of H-mode of high-performance discharges). Exploiting antenna phasing not only allows coupling power but also transferring - modest - momentum into the plasma, which locally can impact the current density (current drive), MHD stability (pacing) or confinement (turbulence). Fundamental cyclotron heating remains powerful at low temperatures while harmonic heating is best suited for the high-temperature flat top phase; both can be optimised depending on specific needs. For gaining insight into the role fast ions populations play in influencing and steering MHD and turbulence, minority and trace-ion 3-ion heating schemes offer options. Harmonic heating of majority ions or fast ion beams can also be exploited in the foreseen range of frequencies and fields.

A proper understanding of the physics underlying wave heating requires in-depth modelling on various fronts: on the fastest (RF) time-scale, the direct transfer of externally coupled wave power to the plasma constituents requires solving the relevant wave equation, itself leaning on an assessment of the antenna-plasma coupling in a sufficiently realistic model of the actual geometry. The Coulomb collisional interaction of the various types of charged particles requires solving the bounce-averaged Fokker-Planck equation, ideally accounting for the deviations of guiding centres from magnetic surfaces under the influence of drift effects. On the slowest (transport) time scale, the ultimate fate of the discharge under the influence of heating power needs to be determined. Closely related but often somewhat isolated from the former, MHD phenomena associated with bursty rather than smooth diffusive/convective behaviour require dedicated attention as well. Detailed modelling tools exist for studying these various aspects.

Figure 6.5 illustrates key scenarios at full B_t-field. The left subplot provides the directly absorbed power fraction as computed by the 2D wave solver TORIC [6.12] for the standard minority heating scheme either involving a H or a ^{3}He minority at concentrations around 4%. The right subplot provides the single pass absorption for the 3-ion scheme using a 0.1% ^{3}He trace as the third ion type immersed in an H+D mix, as obtained from a 1D wave equation solver TOMCAT [6.12]. In the early testing phase at reduced magnetic field and before the full installation of all systems, H minority and D majority central heating are available adopting 60MHz and B_t~4T. Off-axis – and hence less optimal - heating can be achieved if operating at half field. RF heating relying on ^{3}He is not possible in that early phase. Via the gas injection system and relying on real-time techniques making use of diagnostic data, the concentrations of the plasma constituents are monitored and steered to ensure optimal desired operating conditions, either maximising the impact on the bulk plasma temperature - and in particular that of the ions - or seeking the creation of very high energy tails in the context of MHD studies or when seeking to influence turbulence. The adopted RF frequency range equally offers options to directly as well as indirectly heat majority or beam populations, profiting from effects arising from the simultaneous use of the various available heating techniques (see e.g. [6.14], [6.15]).

At full field and operating at the high densities and temperatures foreseen for DTT, synergistic effects boost the plasma performance when keeping the minority concentration modest. For example, operating at H concentrations of 1-2% allows simultaneous heating of the minority at its fundamental cyclotron frequency (N=1) and harmonic heating (N=2) of the bulk D as well as the beam. Combining beam and wave heating provides RF waves with a less collisional target to further heat the plasma (reaching a steady state is only possible when wave power absorbed by a population is transferred to other populations or evacuated from the heat source location), making RF heating more efficient than it is when acting in isolation. The creation of high-energy tails can also indirectly be of benefit for the ions: since RF waves primarily accelerate charged ions to high energies (unless purposely avoiding this effect), electrons benefit from fast ions slowing down via Coulomb collisions. Enhancing the electron temperature increases the critical energy and thus favours more of the beam energy flowing to the ion population.

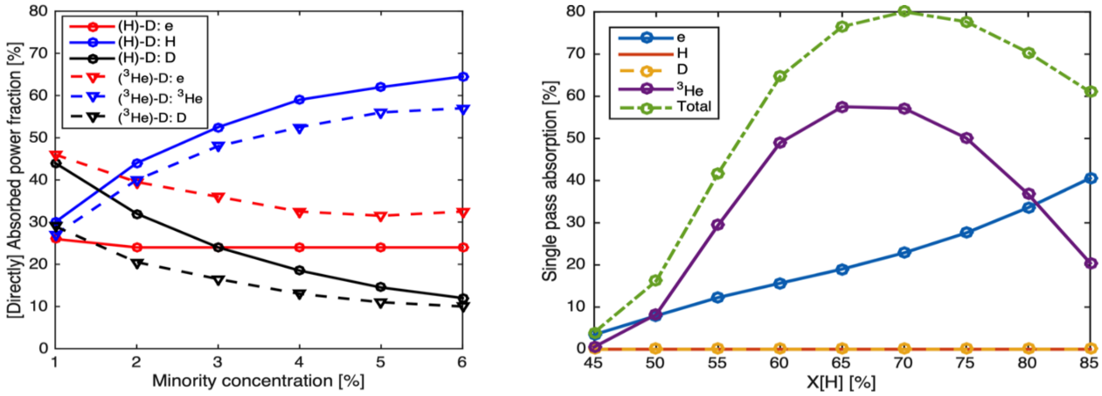

Figure 6.5. Example of the directly absorbed power fraction as a function of the H or 3He minority concentration in a D plasma for the standard minority heating scheme with minority concentrations of a few percent (left) and single transit absorption for the 3-ion scheme involving 0.1% of 3He as the trace ion in a H+D plasma (right).

Aside from its main role as a plasma heating technique, ICRH is instrumental in getting insight into the interplay between fast ion populations and plasma instabilities. As it requires a resonance condition to be satisfied, ion heating by RF waves is necessarily well localized, an effect that is routinely exploited experimentally. In particular to avoid the undesired excitation of neoclassical tearing modes by the violent crashes following fast particle stabilization of sawteeth: these crashes can be forced prematurely by pacing the RF power. RF power modulation is also routinely used to determine the experimental power deposition profiles (for a JET example, see e.g. [6.16]).

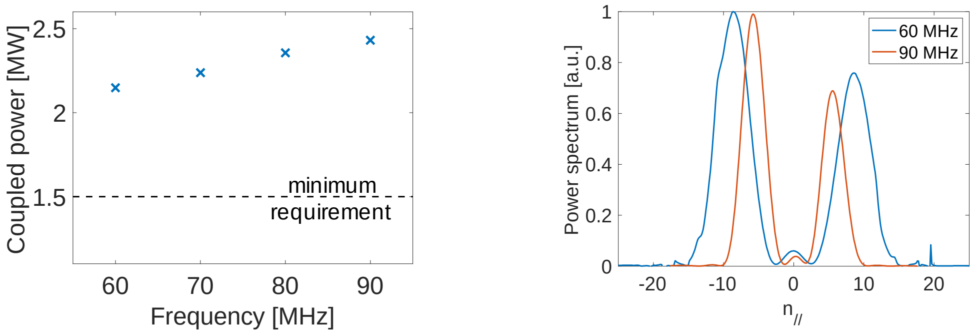

Figure 6.6. Coupled power as a function of the generator frequency for a distance of 30 mm between the antenna and the plasma (left) and corresponding antenna spectrum (right).

ICRH coupling critically depends on the ability of the launched waves to tunnel through the low-density edge evanescence region. The power that can be coupled at various frequencies for a typical edge density profile expected to be relevant for DTT is shown in Figure 6.6 (left subplot). The here predicted potential of ICRH to heat the plasma will be updated at a later stage, the antenna design still being in progress. The corresponding antenna power spectra in terms of $n_{//}=k_{//}/k_o$ (where $k_{//}$ is the wave vector component parallel to the static magnetic field and k_o is the wave number in vacuum) are shown in the right subplot of that same figure. The spectra have two main peaks that are slightly asymmetrical w.r.t. $n_{//}=0$, offering possibilities to drive a modest non-inductive current.

6.3.3 System commissioning, required diagnostics and dedicated modelling

Commissioning of the ICRH system will be done in steps, first on test banks in vacuum, then inside the machine in presence of plasma, while gradually increasing the power. L-mode conditions are ideal for such commissioning, but ultimately the system needs to be capable to operate in H-mode under a variety of plasma conditions. Since the available installed power will increase during DTT's lifetime, earlier experience will guide upgrades and optimisation of steering tools.

Given DTT's focus on exploring various plasma configurations to study divertor loads (see e.g. [6.17]), ensuring optimal coupling will require closely monitoring the edge density (adopting e.g. a Li beam or reflectometry) and having means to actively or indirectly adjust it. Protection cameras should monitor hot spots and arc detection for safe operations. Ways to explore how impurity generation, due to the RF sheath effects, can be kept minimal will inherently be a sub-aspect of the DTT experimental programme; providing detailed insight requires the proper diagnostic tools (e.g. spectroscopy). The fact that RF waves boost the perpendicular energy of specifically targeted ion sub-populations requires dedicated fast particle diagnostics (see the more detailed description of such diagnostics in Sec. 6.4.3), but equally offers opportunities for learning how to harness or even control fast-particle-induced phenomena. Dedicated RF-earmarked experiments will explore the potential of the technique while finding solutions for potential issues and providing data to benchmark and improve models.

6.4 The DTT NBI system

Neutral Beam Injection (NBI) is a widely used system to heat fusion plasmas, in most of the current fusion devices. NBI is also used to efficiently induce current in the plasma, it can inject torque and the generation of a high-energy tail in the ion population is of great interest for energetic particle studies. NBI is a robust H&CD method, independent of any resonance condition. However, for an efficient use, beam energetic particles must be well confined in the plasma: this is taken into account in the design phase of the NBI system, when system objectives are defined and system parameters are consequently decided. NBI will be installed in DTT, with characteristics, objectives and timing described in the next subsections.

6.4.1 System description and ITER/DEMO relevance

DTT will be equipped with a state-of-the-art Neutral Beam Injection (NBI) system, based on negative-ion acceleration up to 510 keV particle energy. It will be the NBI system with the second-highest injection energy after ITER NBI, and the only other negative-ion based beam in a high-magnetic-field device with full metal wall. The high injection energy is required for proper beam absorption at high plasma density, e.g. as foreseen in DTT reference scenario E SN (see Chapter 2), and to study super-Alfvénic energetic particles (EPs) (see Chapter 7). The system [6.18][6.19], sketched in Fig. 6.7, is designed to inject ~10 MW at full energy, with horizontal, tangential injection (average tangency radius R_{tang} ~ 1.95 m) in the same direction as the plasma current I_p - i.e. opposite to the toroidal magnetic field B_t direction, to minimize trapped particle population and first-orbit losses. The presence of stray fields in the injector area will result in beam duct losses with a consequent slight reduction of the injected power to the plasma, and in the movement of NBI shine-through footprint on the DTT first wall [6.21] [6.22]. In DTT there is also the option to switch I_p/B_t directions, leading to counter-current NBI, which, due to expected larger power losses, may face operational restrictions. The beam can accelerate H or D ions and originates from a single injector featuring a single, negative-ion, source. The overall beam geometry presents a focus at the NBI first wall port, resulting in a positive finite beam divergence when passing through the plasma. To have an efficient coupling to the variety of plasmas that will be tested in DTT, especially in terms of density and shapes, DTT NBI will be capable of varying its injection energy in the range 10-100% of the nominal value, with the associated injected power varying approximately linearly with energy in the range E_{NBI} ≈ 250:510 keV. DTT NBI will be available from Phase 2 of the machine (see Chapter 1 and Chapter 2, Table 2.3), after a commissioning phase discussed in sub-section 6.4.3.

The recent re-scheduling of ITER operation phases confirmed the relevant role of NBI in ITER plasmas, with the option of a future machine upgrade by the installation of a third injector. ITER NBI operations will start with H and then D injection, close in time with the currently foreseen DTT NBI installation and first operations. Although DTT does not envisage D-T operations, high energy NBI will contribute to ITER-relevant EP physics in fusion operation phases, which will likely take place after the first DTT NBI operations. Synergy for NBI commissioning of high-energy, negative-ion based NBI system and first beam operations is also foreseen between ITER and DTT, exploiting the experience of JT-60SA. This synergy is particularly relevant due to several DTT NBI design solutions that are similar to those of the ITER injectors.

NBI-heated scenarios with dominant electron heating and low plasma rotation are relevant for studies of ITER/DEMO heating conditions. The DTT range of magnetic field and plasma current, and the high-energy NBI enable the exploration of EP physics similar to those expected for ITER alphas, as discussed in Chapter 7. Significant contributions to ITER/DEMO are expected also for ionization cross section validation at high-energy, both in D and H. DTT is also an ideal framework to use, test and validate EP modelling tools, with the ongoing effort to implement the IMAS suite in DTT modelling activities. The installation in DTT of several EP-related diagnostics will also serve to the development of measurement techniques relevant for MeV-class ions in future reactors.

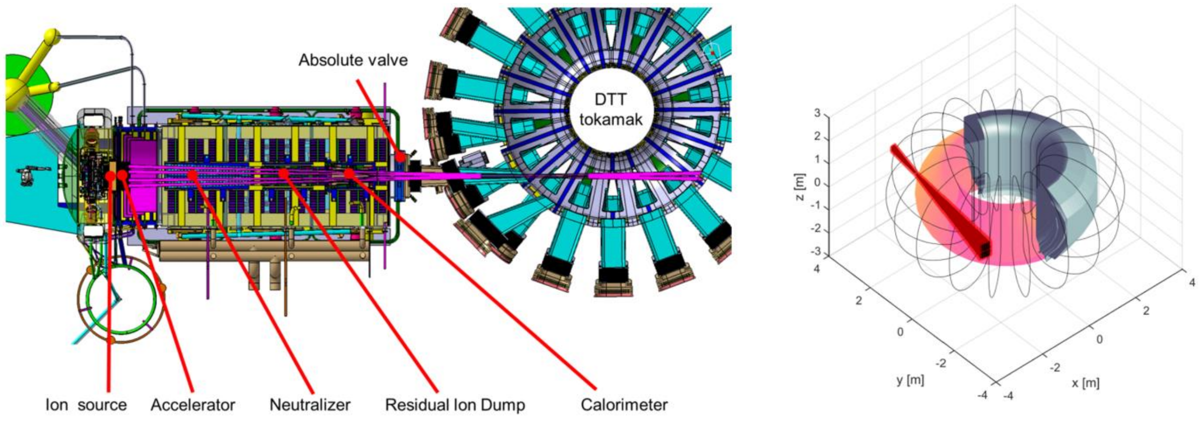

Figure 6.7. DTT neutral beam sketch. Adapted from [6.18] and [6.19].

6.4.2 Heating and current drive source and system-specific tasks

The NBI system designed for DTT will be capable of contributing to plasma performance via effective plasma heating to both electrons and ions, current-drive, and small torque injection and particle flux. As described in Chapter 2, DTT NBI will be used for a large variety of plasmas, in scenarios labelled as “D” and “E”, which include H-mode baseline (in SN and DN magnetic configurations), hybrid, negative-triangularity, I-mode by counter-current injection, if feasible, no/small ELM regimes and reduced B_t/I_p plasmas. DTT NBI will be able to contribute to all these scenarios characterized by different plasma conditions thanks to E_{NBI}/P_{NBI} modulation capabilities. Depending on injection parameters, heating schemes and plasma conditions, electron/ion heating ratio and current-drive can be adjusted, and different EP distributions can be obtained. The numerical prediction of NBI energetic particle (EP) behaviour, confinement and interaction with DTT plasmas presented in this section mainly regards the reference SN plasma scenario “E”, which sets most of the DTT NBI design parameters. However, work is ongoing to determine NBI source terms for different DTT plasma scenarios and configurations [6.20][6.21]. The presence of three different heating systems increases DTT operation flexibility, and will result in synergies, such as NBI-ICRH synergy, to be further investigated. ECRH will indirectly affect NBI EP slowing down by its role in determining the plasma electron temperature.

Efficient NBI ionization in DTT plasmas. Efficient neutral beam ionization in the plasma is essential to avoid the shine-through losses, which can harm the first wall and set boundaries for NBI operations. Shine-through typically increases with injection energy and decreases with plasma density. NBI in the reference, Single-Null (SN), plasma scenario "E" is characterized by a negligible shine-through fraction [6.19][6.21], with relevant beam ionization in the outer part of the plasma (see Fig. 6.8: (a) and (b) show the ionization flux in top and poloidal views; (c) illustrates the dependence of the shine-through loss fraction on plasma density and injection energy). At nominal injection energy in SN plasmas, shine-through losses exceed 1% when plasma density is decreased below $1{\cdot}10^{20}$ m^{-3}. A decrease of injection energy (at the cost of injection power reduction) lowers the fraction of shine-through losses, as shown in Figure 6.8(c).

A first investigation in case of 1% of NBI shine-through (at nominal NBI injection power and energy) resulted in a peak heat flux of ~0.5 MW/m^2 on the first wall [6.22]. The peak heat flux results significantly decreased in case of NBI energy/power reduction or in case of a de-focusing of the NBI beamlets: if the nominal beamlet divergence is doubled, the heat flux peak is more than halved. The shine-through density limit for safe NBI operation is strictly related to the allowed heat flux on the first wall components and has not yet been defined: the design of plasma-facing components is currently in progress, in particular in the area of the NBI shine-through footprint.

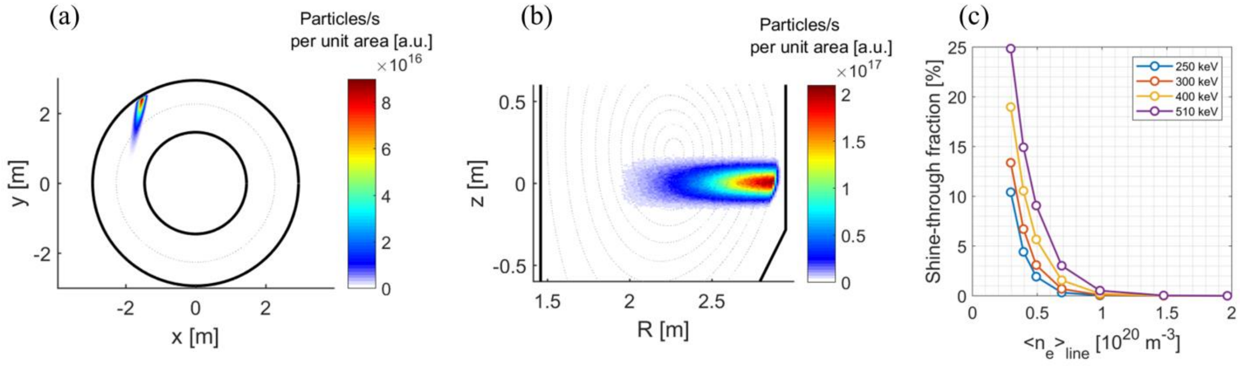

Figure 6.8. DTT NBI ionization in reference SN plasma scenario "E". Figures (a) and (b) show the ionization flux in top and poloidal views, Fig. (c) illustrates the dependence of shine-through loss fraction on plasma density and injection energy. Adapted from [6.20].

NBI heating, current drive and energetic particles features. For DTT's reference scenario "E" SN plasma, the population of beam EPs is formed mainly by confined passing particles (~84 %), with a small fraction of trapped orbits (~15 %). Stagnation EP orbits are found close to the magnetic axis (~1 %). By decreasing the beam injection energy or increasing plasma density (and hence moving ionization position towards the edge), the fraction of passing EP orbits decreases and EP orbit losses, though rare, increase [6.20][6.21]. Even considering the presence of magnetic field ripple, orbit losses remain negligible for the reference scenario (see Chapter 7 and [6.23], [6.24]).

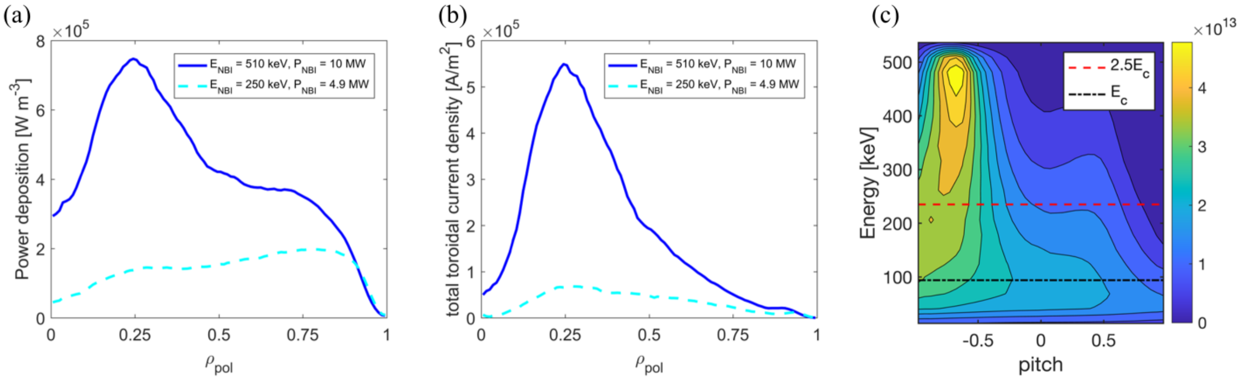

Figure 6.9. NBI deposited power (a) and driven current density (b) profiles in DTT's SN plasma scenario "E" for two different NBI configurations. Fig. (c) shows the volume-integrated, steady-state, EP distribution function at nominal injection parameters for scenario "E", with lines representing the average critical energy "E_c" and 2.5·E_c. Adapted from [6.21].

The electron/ion heating ratio is approximately 60:40% for scenario "E", with a current drive in the order of 0.2 MA (~ 20 kA/MW, i.e. ~ $0.1 \cdot 10^{20}$ A/Wm^2). Lowering the injection energy to 250 keV, the driven current strongly decreases to ~0.05 MA (also due to injection power reduction) and the power ratio to plasma ions increases up to almost 55% [6.20]. Figure 6.9 (a) and (b) show typical power and driven current density profiles expected in the DTT SN-type plasma "E", for two NBI configurations at different injection energy and power. The relevant ion heating ratio is due to the relatively high electron temperature, which determines a significant contribution of EP-plasma ion collisions during the slowing down. This is seen in Figure 6.9 (c), which represents the NBI EP distribution function for scenario "E": the newly born fast ions, characterized by an almost tangential pitch, are rapidly subject to pitch-angle scattering at lower energies due to ion collisions. The possibility of variations in DTT of E_{NBI}/P_{NBI}, plasma density (and temperature due to different heating schemes) and synergy with ICRH open the possibility of studying a variety of NBI EP population distributions. Further details on NBI EP confinement and stability are reported in Chapter 7.

6.4.3 System commissioning, required diagnostics and dedicated modelling

After the installation of the NBI system in the Phase 2, a commissioning phase will be dedicated to prepare NBI operations in the plasma [6.25]. The initial commission phase will be done without coupling the beam with the plasma: the beam will be collected on the calorimeter, and the valve connecting the beam to the torus will be shut (see Figure 6.7). This phase will include several steps. Gas flows and the operative pressure in the beamline components will be verified. The high-voltage commissioning of the NBI will follow, to be tested with gas pressure before tests with the beam. The extraction of the beam from the negative ion source will be tested and diagnosed, increasing beam current density, energy and pulse length by steps. The conditioning phase of a negative ion source is complex due to the presence of Caesium. Initially, the beam extraction will be carried out without gas in the neutralizer; afterwards the beam neutralization will be tested. During NBI commissioning, the residual ion dump will be tested. A second commissioning phase foresees the beam coupled to the plasma: this phase will require stable plasma operations above minimum shine-through limit density, and the correct operation of machine-protection diagnostics. First NBI operation in the plasma will start with short pulses, to be extended by steps if tolerable heat loads will be confirmed in the beamline components. Once in operation, daily NBI conditioning routines will be required before experiments. NBI operation at reduced energy may require specific conditioning. Duration and details of the NBI commissioning phase and ion source conditioning routines are under definition.

Diagnostics are necessary to allow correct NBI system operations, guaranteeing at the same the machine protection. These diagnostics are being currently designed. A description of the main diagnostics that are normally used for machine protection and NBI operations is provided next. First of all, fast and accurate data from NBI power supplies are necessary for beam setting optimization and to find faults. In the NBI box, a calorimeter is used to measure NBI power and beam alignment, while thermocouples on exposed components and visible/infra-red (IR) cameras are needed for heat load detection and quantification. Pressure gauges and residual gas analysers provide measurements on pressure, vacuum monitoring and leak detection. Along the path towards the torus, the beam can be characterized via Beam-Emission-Spectroscopy (BES) diagnostic. To prevent damages in the NBI duct due to heat loads from re-ionization events, a specific diagnostic system is being studied for DTT. Other tokamaks, e.g. ASDEX Upgrade and JET, make use of measurements based on H-alpha light emission (Doppler shifted), on fast duct pressure measurements (penning gauge) or cameras for hot-spot detection.

In the torus, excessive beam shine-through can damage the first wall components. To generally detect hot spots, not only due to shine-through losses, DTT will be equipped with IR cameras. ASDEX Upgrade and W7-X devices make also use of pyrometries, to be investigated for DTT. The quantitative measurement of shine-through through thermocouples embedded in first wall panels may result too slow for machine protection, but would give precious information on beam ionization, useful e.g. for the validation of beam ionization cross sections in a range of beam energy (~100:500 keV) which is unique among existing experiments. This validation is of uttermost interest for ITER operations. Further investigation on DTT diagnostic systems able to characterize the beam shape and attenuation inside the plasma are ongoing.

To scientifically exploit DTT NBI from the operational/physics point of view, several diagnostics are being designed, as also mentioned in Sec. 7.4. These include FIDA (Fast-Ion D Alpha) for fast ion energy and density characterization, FILD (Fast Ion Loss Detector) and NPA (Neutral Particle Analyser) for the characterization of fast ion losses and a Time-Of-Flight (TOF) spectrometer for fast ion (and neutron) energy spectrum measurements. The current driven by NBI can be inferred combing measurements of FIDA and MSE (Motional Stark Effect), which is currently not foreseen for DTT. A diagnostic beam for Charge-eXchange (CX) process measurement (for T_i measurement) is under study.

The design and realization of the DTT NBI system will benefit from the experimental campaigns of the ITER Neutral Beam Test Facility, since several NBI design solutions are similar, often improved, with respect to the ITER NBI system. Collaboration on negative-ion based NBI systems and EP physics with high-energy NBI devices (LHD, JT-60SA) is desirable and to be planned.

Modelling activities are currently ongoing to support NBI and DTT design. In the medium-long term, a deeper integration of accurate NBI-plasma interaction modelling is envisaged on integrated modelling suites of codes (e.g. JETTO+ASCOT simulations) and to study NBI-ICRH synergy. We aim to exploit the ITER-relevant IMAS environment, which could help in DTT modelling goals. We mention in particular the study of an EP modelling workflow to assess EP stability starting from NBI EP distribution functions (see Chapter 8 for more details).

6.5 Plasma fuelling

The particle (gas or pellet) injection systems in DTT serves various purposes. Among these: achieving the desired density and assisting in tailoring its profile, injection of noble gas impurities for creating a radiative mantle protecting the divertor and massive gas injection for disruption mitigation. Particle fuelling is not only important to ensure that the desired core and pedestal parameters are reached. The efficiency with which RF waves can be coupled to the plasma is critically dependent on the density profile faced by the antenna. Different tasks require different matter injection features, therefore the compatibility of all requirements is a study in its own right. Opting for independent pellet injectors for gas fuelling and ELM-pacing allows in principle a better coverage of the requirements for each task.

6.5.1 System description and ITER/DEMO relevance

The main gas injection system is positioned in the mid-plane in port 5. As is the case for most tokamaks, the DTT objectives put particular emphasis on both central fuelling and divertor fuelling. The gas injection required for both main ion and impurity injection, excluding the massive gas injection case for the purpose of mitigating the consequences of a disruption, is about 200 Pa m^3/s [6.26]. Mass spectrometer stations are used to monitor the residual gas and to detect vacuum leaks. The number of pumps needed for evacuating the DTT vacuum chamber depends on its total area - including ports and ICRH antennas – and has to be defined. By allowing for the specific INCONEL 625 vacuum vessel and first wall outgassing rate of $6.7\ 10^{-9}$ Pa $m^3/s/m^2$ at 100 ◦C, after all cleaning procedures, the effective pumping speed needed for pumping the torus down to $P = 1.33\ 10^{-7}$ Pa is about $10 m^3/s$.

The pellet injection system is critical for the DTT experiment and therefore specific modelling is required in order to identify the design characteristics of the system and its flexibility (not only mass, speed and injection rate but also injection position and direction). Fuelling pellets need deep plasma penetration and mass deposition, while ELM pacing pellets require shallow penetration and smaller mass. In this respect, first analyses [6.27] indicate that adequate fuelling (see Fig. 6.10) is only guaranteed for high field side (HFS) injection, exploiting the ∇B-drift motion for technically acceptable injection speed. On the other hand, ELM pacing pellets can be injected both from the HFS and LFS (Low Field Side) of the machine, given the very small penetration required, but injection frequencies are critical in order to limit the energy due to stimulated ELMs. Note that injection frequencies are also important for the fuelling pellets in order to sustain the desired operation density profile.

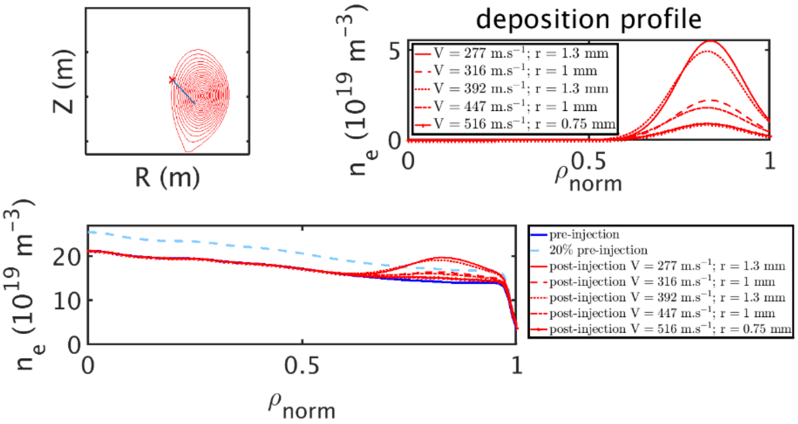

Figure 6.10. (a) Injection geometry, (b) deposition profile and (c) pre- and post-injection densities for a pellet injection.

In this respect, modelling of DTT scenarios can only be realistic if the actual particle injection is accounted for. A theory-based integrated modelling effort of the plasma response to deuterium fuelling in the full power scenario E of DTT was performed using the 1.5D transport code JETTO with the quasilinear anomalous transport model QuaLiKiz for the core region [6.7]. It was found that the amount of neutral flux at the separatrix needed in order to sustain the desired pedestal density level with gas puffing is so large that the feasibility limits of the foreseen pumping system are exceeded, regardless of the type of impurity introduced, thus making the use of pellets mandatory. The simulations performed with pellet injection as fuelling method predict that the pedestal density is well sustained with realistic parameters for the DTT injector. The sustainment of the core density depends strongly on the electron cyclotron (EC) power deposition width: a very peaked EC power deposition profile does not allow high density plasmas, which are required for the full power scenario (see Fig. 6.11). Broadening the EC power deposition profile permits to achieve the expected density (see Fig. 6.12). Negligible modifications of the EC deposition are found during a single pellet cycle and after several pellet cycles, indicating full compatibility between the EC system and the pellet injection system for the full power scenario.

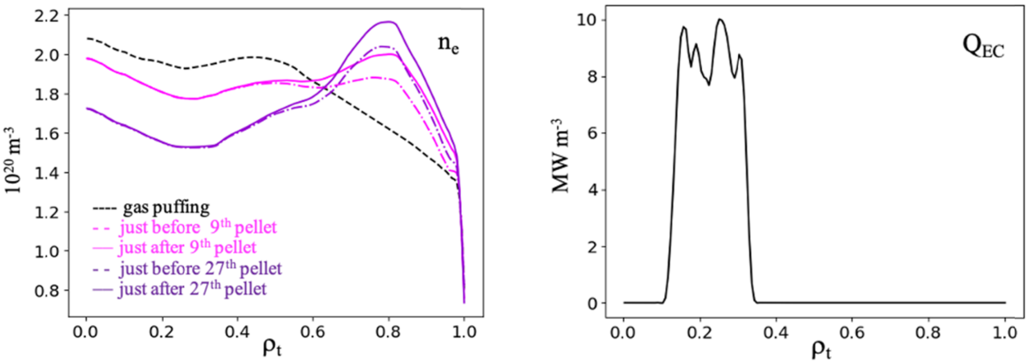

Figure 6.11. Left: electron density profiles as calculated by the simulations of the DTT full power scenario E with transport model QuaLiKiz, solving the transport equations up to the separatrix with pellet injection as fuelling method and with Ne as seeding gas. The temporal slices of the density profile just before (dashed line) and just after (solid line) the 9th (magenta) and the 27th (violet) pellet are represented. The density profile obtained by the corresponding gas puffing simulation is shown with the black dashed line. Right: the relative peaked EC power deposition profile, as used in the reference DTT full power scenario E.

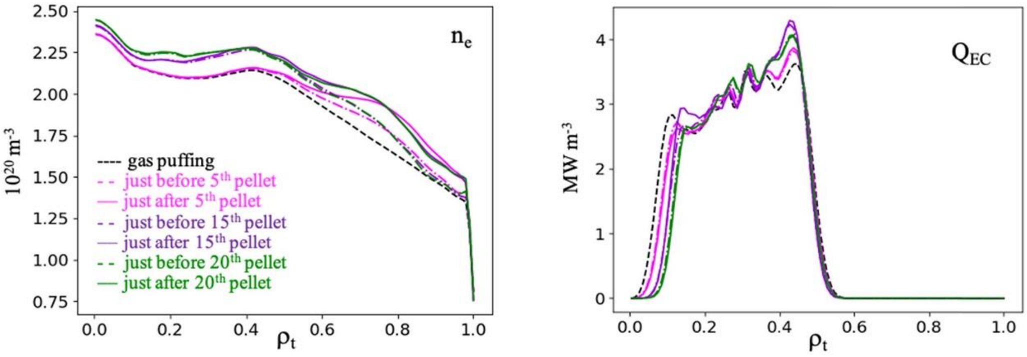

Figure 6.12. Left: electron density profiles as calculated by the simulations of the DTT full power scenario E1 with transport model QuaLiKiz, solving the transport equations up to the separatrix with pellet injection as fuelling method and with Ne as seeding gas. The temporal slices of the density profile just before (dashed line) and just after (solid line) the 5th (magenta), the 15th (violet) and the 20th (green) pellet are represented. The density profile obtained by the relative gas puffing simulation is shown with the black dashed line. Right: the relative self-consistently calculated EC power deposition profile.

6.5.2 Modelling needs

Modelling of ELM regimes and the effect of pellet injection in DTT is still to be addressed, but it is mandatory in order to infer required frequencies for ELM pacing, but also considering recent results [6.28] that show how on larger machines ELM control by pellet injection cannot be considered from the HFS as it would require massive pellets (with consequence on both plasma performance and pumping system). On large machines ELMs can be triggered in a manageable way only with LFS injection and in particular far from the peeling boundary, preferring the ballooning boundary (since the collisionality regime plays an important role and is more critical at low collisionality and thus in peeling-limited regimes for edge pressure). This may not be the case for DTT that is a much smaller machine (though modelling shows it to be important in DIII-D as well, see [6.28]), but the study has to be addressed since the requirement of two injection lines has important consequences on the design of the system. In this respect adequate modelling (e.g. with JOREK) and future experiments should also address the synergy between RMP and pellet injection for ELM control as this may provide valuable options also in view of ITER.

6.5.3 System specifications and diagnostics

The design of the injection line from a technical point of view was addressed considering all viable options, given the limited available space to enter the vacuum vessel (see Fig. 6.13), but it has also to comply with physics requirements in order for the system to be effective. Given the fact that HFS injection is mandatory (for fuelling), the present design of the pellet injector assumes an injection line entering from port 3 and going around the vacuum vessel and then down the central column. This poses limits on the maximum sustainable injection speed to be around 500 m/s (or less, given the curvature of the line) and therefore either a centrifuge or a pneumatic injector are technically viable options. A more detailed assessment of the required injection frequencies may still discriminate between the two solutions. A centrifuge system similar to what is chosen for JT-60SA likely offers more flexibility in the combined use of fuelling and ELM-pacing pellets (total pellet mass can be better accounted for and synchronized), although the extruding system still has critical technical issues.

Supersonic molecular beam injection (SMBI) systems are also being considered for fuelling, although operation at high density does not show significant improvement with respect to standard puffing systems, differently from low-density operation where they provide a valuable option.

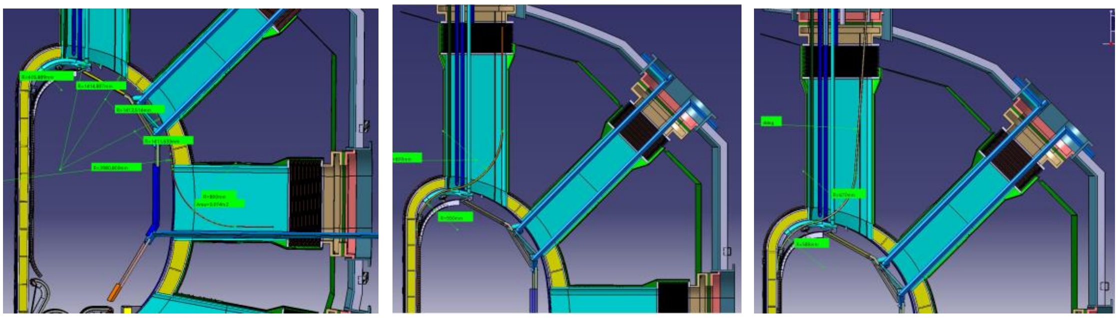

Figure 6.13. Panels from the left: injection from port 3, from port 1 vertical, from port 1 tilted.

The fuelling system being complex and crucial, it requires a suitable laboratory environment in order to ensure the execution of an appropriate campaign of tests - both of the plants and on the tokamak with plasma - can be done to optimise the system prior to the actual installation on the machine. A first design of the HFS injection line for DTT is available and will be tested experimentally to characterize the entire process, from pellet formation to the actual injection. Specific aspects looked into will be mass reduction, fragmentation, reproducibility, achieved speed and residual gas that enters the vacuum vessel in the wake of the pellet. The latter is a critical aspect as space is very limited in DTT and the injection line has to be installed along with the machine assembly (the only viable option being the one described above entering from port 3 to reach HFS).

Diagnostics requirements for fuelling systems have to be considered already in the design phase and can be split into two main aspects: pellet diagnostics and neutral gas diagnostics.

As for the first one, apart from the standard systems used to measure pellet mass (microwave cavity), velocity and fragmentation (optical barrier detectors), it will be fundamental to have fast cameras in order to detect the ablation cloud evolution and possibly Position Sensitive Detectors (PSD) to reconstruct the 3D pellet trajectory as well as the time evolution of the ablation cloud.

As for neutral gas measurements, it will be important to measure neutrals pressure as an indication of gas recycling and plasma-wall interactions. To this end, pressure gauges such as those used on ASDEX Upgrade [6.29] would be necessary. These measurements will be also important to assess the performance of the divertor system and in this respect a Neutral Gas Analyzer (NGA) system will be installed to measure the evacuated gas under the divertor.

The DTT research programme will contain dedicated experiments to assess the specific role of the particle fuelling systems.

6.6 Headlines of the research programme for heating, current drive and fuelling

In this section, we summarize the main headlines of the DTT research programme for the heating, current drive and fuelling subjects, according to the various operation phases of DTT.

Headline number	**Headline contents**	**Priority (+, ++, +++)**	**ITER**	**DEMO**
Construction Phase 2022-2029				
C.6.1	Assessment of ECRH, ICRH, NBI, matter injection performance (modelling) in connection with respective high priority tasks	+++	*	*
C.6.2	Assessment of interfaces with diagnostics and control system	++	*	*
Phase 1 2029-2034				
1.6.1	ECRH, ICRH initial system commissioning, asynchronous and with plasma, including optimization of coupling	+++	*	*
1.6.2	ECRH and ICRH commissioning of functionalities supporting basic machine operations: wall cleaning, assisted start-up, current ramp-up and ramp-down at half and full magnetic field	+++	*	*
1.6.3	ECRH and ICRH basic control functionalities: sawteeth, NTMs, impurities, density and ELM pacing at half and full magnetic field	+++	*	*
1.6.4	Access to H-mode Baseline and Hybrid scenarios	++		
Phase 2 2034-2038				
2.6.1	NBI system commissioning (asynchronous and with plasma)	+++		

2.6.2	Verification of NBI power losses (in particular duct and shine-through losses) and optimization of parameters with respect to density	+++		
2.6.3	Combined use and optimization of parameters of the heating and fuelling systems for scenario access and control	+++	*	*
2.6.4	Control of kinetic and impurities profiles	++	*	*
Phase 3 2038-…				
3.6.1	H-mode operation at full power	+++		*

6.7 References

[6.1] F. Fanale et al., Fusion Engineering and Design Volume 192, July 2023, 113797 https://doi.org/10.1016/j.fusengdes.2023.113797
[6.2] DTT Report [https://www.dtt-dms.enea.it/share/page/site/dtt/document-details?nodeRef=workspace://SpacesStore/22b9d745-2441-4f26-81ce-bdc097de0859]
[6.3] Bonanomi N. et al., "Full radius time-dependent simulations of the DTT tokamak plasmas" https://tr-236-3142.teamresa.net/shared/tr_236_3142/medias/Files/Monday_PosterSessionI_BookAbstracts.pdf
[6.4] Baiocchi, B. et al., EC-21 Workshop, 2023 [https://doi.org/10.1051/epjconf/202327701006]
[6.5] I. Casiraghi et al 2021 Nucl. Fusion **61** 116068
[6.6] I. Casiraghi et al 2023 Plasma Phys. Contr. Fusion **65** 035017
[6.7] B. Baiocchi et al. (2023) Nucl. Fusion **63**, 106009
[6.8] S. Nowak et al., report 2023-MHD-MSS NTM Stability Studies –Sub Task 03 - DTT ID: MSS-TEC-04054_A2
[6.9] J. Stober et al 2003 Nucl. Fusion **43** 1265
[6.10] S. Ceccuzzi et al. (2023) AIP Conf. Proc. 2984, 03001
[6.11] D. Milanesio et al. 2024 Nucl. Fusion **64** 016015
[6.12] M. Brambilla (1999) Plasma Phys. Contr. Fusion **41**, 1
[6.13] D. Van Eester et al. (1998) Plasma Phys. Contr. Fusion **40**, 1949
[6.14] A Cardinali et al (2020) Plasma Phys. Control. Fusion **62**, 044001
[6.15] A. Cardinali et al 2022 J. Phys.: Conf. Ser. 2397, 012017
[6.16] P. Mantica et al. (2011) Plasma Phys. Contr. Fusion **53**, 124033
[6.17] A. Castaldo et al (2022) MDPI Energies 15, 1702. https://doi.org/10.3390/en15051702
[6.18] P. Agostinetti, et al., "Innovative concepts in the DTT Neutral Beam Injector", presented at the 30th IEEE Symposium on Fusion Engineering (SOFE 2023), submitted to IEEE Trans. on Plasma Science.
[6.19] P. Vincenzi et al., Fusion Engineering and Design **189** (2023) 113436
[6.20] C. De Piccoli et al., "NBI energetic particle confinement and orbit characterization for Divertor Tokamak Test plasma scenarios", EFTC conference 2023.
[6.21] C. De Piccoli et al., "Impact of NBI shine-through and beam-plasma interaction on the Divertor Tokamak Test facility", 2024, submitted to Nucl. Fusion.
[6.22] F. Veronese et al., "Report on the beam simulations for DTT NBI with updated duct and improved modeling of vacuum and shine-through", 2023, DTT report ID:NIP-TEC-54041
[6.23] G. Spizzo et al., Nucl. Fusion **61** (2021) 116016
[6.24] M. Gobbin et al., Plasma Phys. Control. Fusion **65** (2023) 075013
[6.25] P. Agostinetti et al. "Rationale for the updated cooling requirements of DTT NBI", 2023, DTT report ID: DTT-TEC-54007
[6.26] G. Mazzitelli et al. (2017) Fus. Eng. & Design, **122**, 375
[6.27] B. Pégourié, Final Report EXTRA-Common milestones PEX/DTT, Topic 4: CEA-01 Neutrals and impurities model and pumping, Deliverable-ID PMI-2.3-T011-D001, 15/09/2020
[6.28] A. Wingen et al., "Prediction of pellet mass thresholds for ELM triggering in low-collisionality, ITER-like discharges", 29th IAEA Fusion Energy Conference (2023) IAEA-CN-316/1605.
[6.29] A. Scarabosio and G. Haas, AIP Conference Proceedings **988** (2008) 238, https://doi.org/10.1063/1.2905075

Chapter 7

ENERGETIC PARTICLE PHYSICS

G. Vlad, M. Falessi, E. Nardon,
A. Dal Molin, M. Gobbin, Y. Kominis, M. Nocente, F. Porcelli, G. Spizzo, D. Testa, F. Zonca, M. Zuin

This chapter discusses the role that DTT can play in studying the energetic particle physics in the frame of "core-edge integration" while considering different plasma shapes at ITER and DEMO relevant plasma parameters. The peculiar role of energetic particles as mediators of cross-scale couplings in reactor relevant burning plasmas is briefly introduced. A section related to the NNBI and test particle transport is presented, in which prompt and ripple losses of energetic particles are discussed, together with the effects of the presence of RMP coils. Details on the simulation activity for Energetic Particle Physics is also considered, with a short review on past and recent activity performed and future envisaged work. Next follows a section related to DTT as a test-bed for energetic particle diagnostics relevant either to future reactors or in relation to turbulence and instabilities.

7.1 Introduction

One of the main focuses of the DTT research mission is studying "core-edge integration" with different plasma shapes at ITER and DEMO relevant parameters. In these conditions, DTT is expected to generate energetic ions through various methods, such as NNBI (Negative Neutral Beam Injection) and ICRH (Ion Cyclotron Resonance Heating). These energetic ions are anticipated to interact with Alfvén waves, including Toroidal Alfvén Eigenmodes (TAEs) and Energetic Particle Modes (EPMs), among others.

Because of the weak Kadomtsev scaling approach considered in designing the device (see Chapter 1 and Chapter 8), the supra-thermal ions in DTT are characterized by typical dimensionless orbit widths, which are expected to be similar to those of burning fusion plasmas and are generally smaller than in present-day devices (the dimensionless orbit width of the supra-thermal ions is defined as the characteristic Larmor radius or magnetic drift orbit size normalized to the machine size). Furthermore, the ratio of supra-thermal ion speed to the Alfvén speed in DTT is similar to what is expected in ITER/DEMO, ensuring that the strength of Energetic Particle (EP) drive of Alfvénic fluctuations via wave-EP resonant interactions is preserved. Furthermore, the spatiotemporal cross-scale coupling between core turbulence and Alfvénic fluctuations is preserved thanks to preservation of the thermal plasma dimensionless orbits and the plasma β (the ratio of kinetic to magnetic energy densities). Due to these similarities in dimensionless parameters and plasma behavior, the integrated physics behaviors of DTT plasmas are expected to be similar to those anticipated in ITER/DEMO.

Because of what stated above, the Alfvénic fluctuation spectrum in DTT, resonantly excited by EPs, is expected to be characterized by toroidal mode numbers (n) of the order of 10, which is similar to what is expected in foreseen ignited plasmas.

The peculiar role of energetic particles as mediators of cross-scale couplings in reactor relevant burning plasmas is explained in Refs. [7.1, 7.2], where the possibility of achieving core-edge integrated plasma regimes that are reactor relevant is discussed in detail. Briefly, the DTT high performance plasmas can be divided in an inner core region, characterized by weak magnetic shear and low-frequency Alfvénic activity, and an outer core region, with typically finite magnetic shear and dominated by radially extended TAEs, as discussed in [7.3, 7.4], where a reference model equilibrium is adopted in order to study the linear and nonlinear dynamics of EP driven Alfvénic fluctuations and corresponding EP transport. It has to be noted that, as predicted by theory and numerically verified, the interlink of these two regions is crucially affected by the q-profile. The q-profile not only controls the linear stability and structure of the fluctuation spectrum but also influences the nonlinear saturation mechanisms and ensuing transport.

7.2 NNBI and test particle transport

Regarding the Energetic Particles produced by Negative Neutral Beam Injection (NNBI), detailed analyses were presented in [7.5, 7.6] (see also Chap. 6), where prompt losses and ripple induced losses for a beam at 510 keV and injection angle with respect to the first wall of 40° were estimated to be, respectively, ~0.01% and ~0.07% [7.5, 7.6]. To deal with a significant statistics and improve the accuracy in the heat flux determination at the wall, an algorithm has been implemented to obtain from the initial distribution by TRANSP a new one having the same features but with the desired number of particles. Such a procedure has allowed dealing with 10^6 fast ions in numerical simulations [7.6]. The vast majority of the losses are due to a ripple-resonant mechanism for particles with pitch (defined by $v_{/\!/}/v$ with $v_{/\!/}$ the parallel velocity of the particle with respect to the magnetic field and v the module of the velocity) $\lambda = 0.6$ and 0.65; such a behaviour is consistent with the theory of ripple-precession resonance (see Fig.7.1).

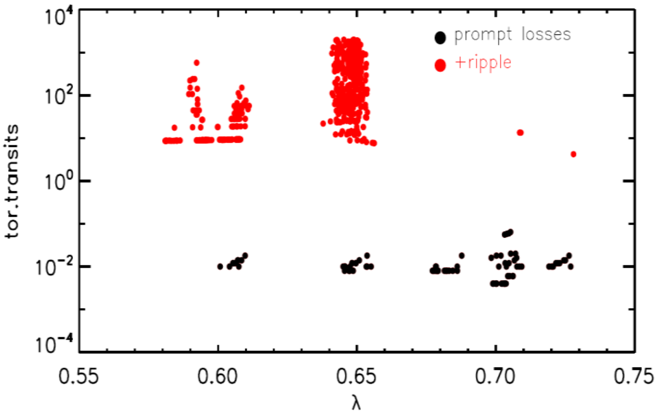

Fig.7.1: Loss times of ions with 510 keV energy as a function of pitch $\lambda = v_{/\!/}/v$. Run with $N_p = 10^6$ particles and toroidal turns $N_{tor} = 2000$. Red dots are losses occurring only in simulations with ripple, black dots also in those without ripple (prompt losses).

Resonant losses are distributed in the toroidal angle while they are instead more localized in the poloidal angle θ, just under the mid-plane, $-11° < \theta < 0$, with θ the Boozer angle. This distribution corresponds to a band ∼ 50 cm wide along the separatrix towards the X-point. This is reasonable, since lost ions are banana orbits whose tips drift radially of a step Δr at each bounce until the banana orbit intercepts the separatrix. Given the direction of the current and magnetic field in DTT, this happens at $\theta < 0$.

It should be noted that both the prompt and resonant losses scale with the orbit width of the considered particles ($\Delta \sim q\,\rho_L$ for the far passing beam ions, and $\Delta \sim \mathrm{sqrt}(2R/r)\, q\,\rho_L$ for the banana-trapped fast ions, with q the safety factor, ρ_L the Larmor gyroradius of the fast ion, R the major radius and r the minor radius). Thus, because of the safety factor dependence, both losses are reduced when plasma current is increased (see, e.g., Ref. [7.7]), although a precise evaluation would require detailed calculations.

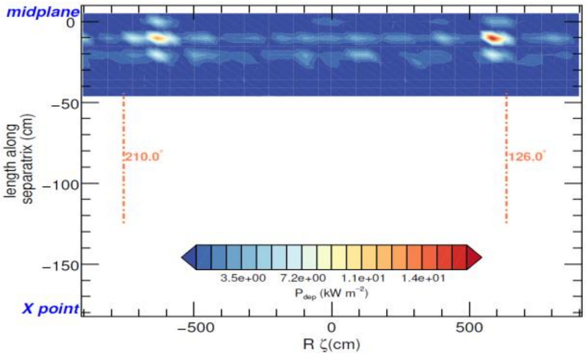

Fig.7.2: Map of the power load (in kW/m²) calculated with a 40 × 10 binning. In panel (b) the two vertical, dashed lines mark the injection and exit angles, $\zeta_{inj} = 126°$ and $\zeta_{out} = 210°$.

The final positions in poloidal (θ) and toroidal (ζ) angle of lost particles are projected on the separatrix surface (Rζ, L) where L is the distance along the separatrix from the mid-plane towards the X-point and $R = R_0 + r$, r being the radius of the LCFS. In this way, Rζ is the distance in cm along the toroidal direction on the equatorial plane. Then the plane (Rζ, L) is cut into bins to obtain a 2D histogram of the losses distribution that is used to evaluate the associated heat flux. The map of power loads, $P_{dep}(R\zeta,L)$ is shown in Fig. 7.2 in the case of a 40×10 binning. The statistics is sufficient to reveal toroidal inhomogeneities: heat loads display a toroidal periodicity that is approximately that of the TF ripple N = 18. There are also two "hot spots" in P_{dep}, with the maximum power load $P_{max} = 19.1$ kW/m² being reached in the hot spot placed at Rζ ∼ 600 cm. By comparing Fig. 7.2 with the toroidal distribution of initial positions, it can be deduced that the hot spots correspond approximately to the injection and exit angles, ζ_{inj} = 126° and ζ_{out} = 210°, the maximum power load being reached at the injection angle. Since the maximum power load is reached in a hot spot that coincides with the injection angle, it is reasonable to check the dependence of this value on the binning. For this reason, a sensitivity scan has been performed by varying the number of bins both in the vertical and horizontal directions in the (Rζ,L) plane. The maximum power load P_{max} in the hot spot is thus estimated to saturate at a value of $P_{max} = 63 \pm 7$ kW/m^2 which is within the tolerance of PFC of the first wall and negligible compared to the power flux of thermal particles on ICRH antennas, designed to withstand 2.5 MW/m^2.

The calculations presented so far describe fast ions that are lost under the action of the magnetic equilibrium and ripple, only. Toroidal Alfvén Eigenmodes (TAE) can interact with the ripple, and could in principle enhance fast ion losses in future DTT experiments, in a way similar to what was reported on TFTR in the past [7.8]. For this reason, further numerical simulations including both ripple and TAE effects on the fast ion population are on schedule. The spectrum and radial profiles of TAE have been determined by DAEPS/FALCON, MARS and HYMAGYC codes and first tests have concerned toroidal wave number with *n=1* and *n=10*. The work to implement the perturbation fields in the ORBIT code is currently ongoing [7.9]: to this end, an algorithm has been written to convert the main quantities provided by the tools cited above in Boozer coordinates, which are required for ORBIT runs. The new simulations will provide important hints about the effect of these modes on the confinement of high-energy ions from NBI for the future operations in DTT.

In the future, in order to prepare experimental campaigns with more detail, further activities will be required on:

- Studying the resonance structures created by NNBI ions in the DTT plasma on the various scenarios considered.
- Test particle transport: this includes investigating prompt and ripple losses of energetic particles and understanding the effects of Resonant Magnetic Perturbation (RMP) coils. Ripple losses have been found to have a strong dependence on the energy and injection angle of NNBI. Simulations also including electromagnetic perturbations generated by the energetic particles themselves (EP driven modes) are envisaged.

Simulation codes to be utilized for supporting experimental efforts and data interpretation include mainly CHEASE (for high-resolution equilibrium), ORBIT, ASCOT, METIS, FAFNER, TRANSP, JINTRAC, MARS, and HYMAGYC (see Appendix H for simulation codes).

7.3 Simulation activity for EP physics

As a general comment on fast particle physics in DTT, preserving the super-Alfvénicity of the neutral beam will be necessary to mimic the energetic particle physics of ITER. Roughly speaking, this would require that the ratio between the transit frequency of the energetic particles $\omega_{t,EP}$ and the Alfvén frequency ω_A, which scales as $\omega_{t,EP}/\omega_A \sim v_{th,EP}/v_A$, lies within the TAE and EAE (elliptical Alfvén eigenmodes) gaps (here $v_{th,EP}$ and v_A are, respectively, the thermal velocity of the EPs and the Alfvén velocity). The present choice of 510 keV NNBI is marginally super-Alfvénic, and interesting operation for DTT from this point of view will require full exploitation of the machine performances (full plasma current and core plasma density, e.g., at fixed Greenwald fraction, and full magnetic field in order to maintain constant ρ_*, the dimensionless orbits).

Preliminary studies of linear stability of Alfvénic modes driven by a population of EPs have been carried out for the full power scenario using a *model* SN equilibrium: a Maxwellian distribution function has been assumed, with constant EPs temperature (450 keV, somewhat lower than the nominal 510 keV), ITER-like EP density profile, major radius R_0=2.09m and B_0=6T [7.10].

The study uses the HYMAGYC (HYbrid MAgnetohydrodynamics GYrokinetic Code) suitable to analyze EP-driven Alfvénic modes in general high-β axisymmetric equilibria, with perturbed electromagnetic fields fully accounted for. Several EP-driven modes have been found. In Fig.7.3 the growth-rate and frequency (both normalized to the on-axis Alfvén frequency ω_{A0}) vs the toroidal mode number n, in the range n=1-20, are shown. Results for purely ideal MHD modes are also given using light blue open circles, infernal-like modes driven by EPs are shown using black full circles, and EP-driven Alfvénic modes are shown using red diamonds. The growth-rate for the EP-driven modes looks to have its maximum for n≥17. In Fig. 7.4 an example of the power spectra for a simulation considering the toroidal mode number n=10 is shown in the plane (s, ω) (s is the normalized radial-like coordinate, and ω is the frequency). In the left frame an EP-driven mode (EPM) is observed (early simulation phase, $t\omega_{A0}$ =72), whereas the right frame shows the appearance of an infernal-like mode driven by EPs, with a frequency smaller (in absolute value) than the EPM (which, by the way, is still observable; later simulation phase, $t\omega_{A0}$ =100). The Shear Alfvén and magneto/acoustic continua, as calculated by the FALCON code [7.11, 7.12] are superimposed: larger and darker symbols refer to Alfvénic oscillations, while smaller and lighter ones to ion sound waves.

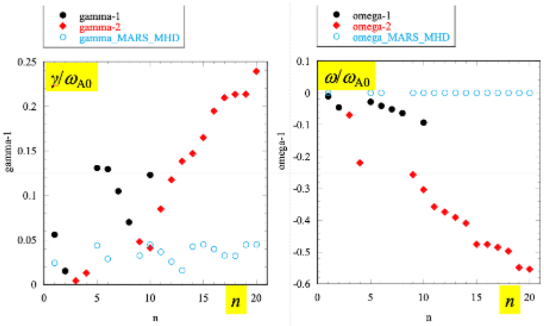

Fig.7.3: MARS and HYMAGYC results for a model Full Power DTT SN equilibrium: growth-rate (left) and frequency (right).

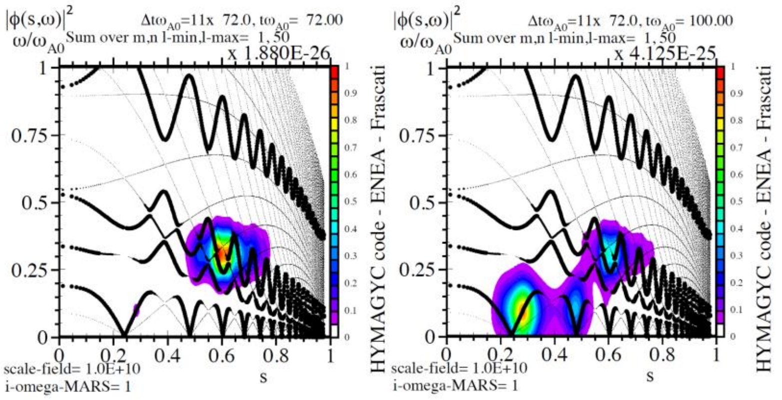

Fig. 7.4: Frequency spectra of the electrostatic potential in the plane (s,ω) as obtained by a linear HYMAGYC simulation with mode number n=10. Coloured structures refer to an energetic particle driven mode (left, $t\omega_{A0}$ =72) and to the appearance of the infernal-like mode (right, $t\omega_{A0}$ =100). Dots refer to Shear Alfvén and magneto/acoustic continua, as calculated by the FALCON code; larger and darker symbols refer to Alfvénic oscillations, while smaller and lighter ones to ion sound waves.

To properly simulate EP physics in DTT, it is essential to have realistic scenarios with on-axis q values that are not unrealistically low. Moreover, it would be desirable to have equilibria optimized with respect to medium to high-n ballooning modes stability. Additionally, the availability of realistic EP distribution functions generated by ICRH and NNBI is crucial for accurate simulations, the behaviour of the EP-driven Alfvénic modes possibly being strongly dependent on the details of the EP distribution function in phase space. Thus, numerical tools to compute auxiliary heating deposition (ICRH, NNBI) will be crucial, as well as experimentally obtained EP distribution functions (see Section 7.4).

Recently, moderate-n simulations were performed for a realistic, up-to-date full-power DTT equilibrium. The study encompassed both linear and nonlinear EP-driven mode dynamics, considering a slowing-down distribution function for the EPs and an off-axis peaked EP radial density profile [7.13]. Indeed, the considered equilibrium has a plasma cross-section vertically shifted with respect to the equatorial plane, resulting in a configuration in which the NNBI deposited EPs are peaked off-axis. Preliminary single-n simulations of such equilibrium indicate the destabilization of a first mode, situated radially close to the magnetic axis in the region where the EP density radial gradient is positive. As this mode saturates, typically inducing a local flattening of the EP density profile, a second, weaker mode emerges in the external region of the discharge, where the EP density radial gradient is negative. A similar phenomenology has indeed been observed in simulations considering the AUG-NLED benchmark case equilibrium with a comparable off-axis peaked EP density profile [7.14]. The potential interplay between these two modes, and the associated enhanced EP radial transport if the radial regions of the discharge involved in the two modes overlap, is quite interesting and deserves further investigation.

One important impact on the EP physics and the control of plasma operation could occur because of the effect of applied Resonant Magnetic Perturbations (RMPs) on EP losses [7.15]. In ASDEX Upgrade experiments, it has been demonstrated that an edge transport layer is formed and controlled by changing RMP coil perturbation amplitude and phasing. This essentially occurs because of the overlap of EP nonlinear resonances [7.16], with the effect of either enhancing or decreasing the EP losses. The recent configuration of RMPs in DTT should have the possibility to consider such effects in detail.

Performing scans while varying the EP parameters, such as the ratio of the velocity of the EPs to the Alfvén speed ($v_{th,EP}/v_A$), the normalized Larmor radius (ρ_{EP}/a), the ratio of the EP density to the thermal ion density (n_{EP}/n_i), and radial profiles of safety factor, bulk, and energetic particle density profiles will be required to illustrate the overall stability of the EP-driven Alfvénic modes in the different proposed DTT scenarios. Note that, however, such scans can be computationally very demanding and will require access to high-performance computing (HPC) resources. As an example, simulation codes described in the present and in the following chapter deal with the description of one (EP population) or all of the components (EP plus bulk populations) of the DTT plasma using a gyrokinetic description for the distribution functions, in its phase-space and time evolution, to keep tracks of the mutual interaction of the plasma species with electromagnetic oscillations of the plasma itself, and ultimately describing the associate anomalous transport. Particle-In-Cell (PIC) techniques are typically used, which require a large number of simulation markers ($10^6 – 10^9$) to describe the distribution function in phase-space with sufficiently low numerical noise. Each nonlinear gyrokinetic simulation would easily require elapsed time execution of few days using typically from 10 to 100 computational nodes (each of one equipped with 48 CPU) on a highly parallel computer of the size of the MARCONI EUROfusion machine. Note also that the space resolution required for burning plasmas is typically higher (typical toroidal mode number $n \approx 20$-30) than the one used for simulating present-day devices ($n \approx 1$-10), the space resolution typically scaling as n^3. The tremendous resources required for these tasks, both in memory and computation nodes, are then evident. Several HPC centers have already been used so far for the simulation activities described in the present Research Plan, e.g., ENEA CRESCO at Portici, ENI HPC5, MARCONI EUROfusion at Cineca: the first two being HPC centers linked to two of the DTT stakeholders (ENEA and ENI), the third one being a HPC EUROfusion facility which yearly launches Calls for Proposals.

At present, EP studies in DTT have been focused only on full power scenarios, considering an EP population generated by NNBI . On the other hand, it would be highly desirable to consider also the stability on EP driven modes in scenarios that will be obtained in earlier phases of DTT, in which a moderate ICRH would be already present (e.g., scenario B during Phase 1, at half current and half toroidal field, $I_p(MA)/B_T(T)=2/3$ and $P_{ECRH}(MW)/P_{ICRH}(MW)=16/4.75$), see Table 2.1). Indeed, considering a high-β scenario during the initial phases of DTT operation at a low toroidal magnetic field could provide valuable insights for the future full power scenarios. Additionally, comparing DTT results with existing results from other devices, such as JT-60SA (which also has NNBI at 500 keV) may offer further validation and understanding.

Current transport models typically do not include the effects of EP-driven Alfvénic modes, such as nonlinear saturation and mutual interaction between Alfvén waves and EPs. Including these effects in transport models will be essential for predicting and understanding radial transport of EPs in the plasma (see Chapter 8). Determining the typical spectrum of oscillations driven by EPs in the range of Alfvénic modes is also necessary for computing nonlinear fluxes in phase space: this is a valuable input that can be provided by the simulation activities developed within this Research Plan section. The Phase Space Zonal Structures (PSZS) theory can provide valuable insights into the implications on transport (see Chapter 8).

Several EUROfusion initiatives related to theory and simulation efforts in the field of EP physics and burning plasma physics are of interest for the development of this Chapter of the DTT Research Plan:

- CfP-FSD-AWP21-ENR-03 (ATEP: Advanced Energetic Particle Transport Models) - this initiative focuses on developing advanced models for understanding the transport of energetic particles in fusion plasmas. The DTT reference scenario is available for benchmarking and testing, but it requires updating with more recent parameters;
- TSVV Task 10: Physics of Burning Plasmas;
- TSVV Task 2: Physics Properties of Strongly Shaped Configurations (in particular, Negative Triangularity (NT)) - in the activities considered in this task, DTT equilibria have been specifically considered;
- other EUROfusion initiatives (e.g., WPs (WPTE, WPSA, WPPrIO, etc.) and International Collaborations, e.g., China, the Center for Nonlinear Plasma Science (CNPS), etc.).

7.4 DTT as a test-bed for reactor-relevant EP diagnostics

DTT is expected to have a diverse population of energetic ions in a broad energy range, from hundred keV to a few MeV. One source of fast ions is the neutral beam, which is made of a heating beam and a diagnostics beam, albeit a final decision of the implementation of the latter is still pending. With the primary goal to provide plasma heating and current drive, the heating beam will inject deuterons that start at the energy of 500 keV and reach the thermal range via slowing down. The diagnostics beam, instead, is predominantly meant to facilitate the application of the diagnostic systems based on charge-exchange emission. Another source of energetic ions is the ICRH system that, depending on the heating scheme adopted, can accelerate protons, deuterons or ^{3}He ions in the energy range of a few MeV.

The diagnostics of such a diverse mix of energetic ions is experimentally challenging and different from the experience of current devices, in which there is a relatively sharp distinction between systems for mid-size (such as ASDEX Upgrade) and large-size (such as JET) devices. In the former case, the machine is not designed to confine MeV range ions, which are predominantly lost. The energies of the confined fast ions are, typically, up to few hundreds of keV or less. A very powerful method to study ions in this range comes from the application of charge-exchange based reactions, for example by means of neutral particle analyzers or the fast ion Dα diagnostics. Large size devices can confine MeV range ions, which are responsible for the fast ion instabilities observed. In this case, diagnostics that exploit spontaneous nuclear reactions that involve the MeV range fast ions are predominantly used.

For the first time, DTT will combine a mix of diagnostics based on both charge exchange and nuclear reactions. The present plan for the DTT EP diagnostic systems comprises a fast ion loss detector (FILD), a fast-ion Dα (FIDA) system, a scintillator based neutral particle analyzer (NPA), a time of flight neutron spectrometer (TOF) and gamma-ray spectrometers (GRS) [7.17]. The design of these systems has just started and their actual capabilities are not known at the time of writing. Here we can list the goals and challenges that have been identified so far.

The FILD will be the only system aimed at measuring unconfined fast ions. The design target is primarily to measure beam deuterons born at 500 keV, but the system is also expected to have measurements capabilities for ions accelerated by the RF system in the MeV range. Specific DTT challenges concern the heat loads on the probe, which may limit the measurement time as well as the probe insertion position, which in turn defines the fraction of phase space that is accessed with the system.

Confined particles will be measured by the combination of the other systems. Currently, FIDA and NPA are meant to measure deuterons from the heating beam and preliminary synthetic signals are under evaluation. One anticipated challenge is due to the decrease by about one order of magnitude of the charge-exchange cross-sections at deuterons energies in the range of some hundreds keV, which may limit the signal to noise ratio and effectively constrain these systems to probing deuterons in the 100-200 keV range.

The TOF is expected to provide measurements over a broad deuteron energy range, from thermal to the MeV range, but with a presumably coarser phase space resolution. MeV range ions other than deuterons will be primarily probed by gamma-ray spectroscopy, as demonstrated mostly at JET [7.18]. Most of the systems provide partial and/or indirect information on the fast ions, for example in terms of the visible or nuclear emission they induce. Therefore, an important modelling task will be to merge the information provided by the different systems and translate it into areas of the fast ion phase space, or orbits, than can or cannot be probed by the envisaged set of systems. As DTT is a relatively compact, superconducting device, engineering constraints are more severe than in presently available mid-size tokamaks and dictate the geometry and position of the diagnostics in the machine. An anticipated consequence is that the fast ion phase space will likely not be fully covered. A second task of theory and modelling will thus be to bridge the unmeasured regions. Both tasks will benefit from the development of synthetic diagnostics, i.e. a diagnostic specific framework that, starting from theoretical predictions of the fast ion phase space in the different DTT scenarios, can translate this information into expected diagnostics signals for direct comparison with measurements.

Two further opportunities in the area of fast ion diagnostics development and tests are worth mentioning. The first one is the possibility to test alpha particle diagnostics. Although DTT is not designed to operate with deuterium-tritium plasmas, alpha particles can be generated by the D+^{3}He fusion reaction in plasmas of deuterium that also contain ^{3}He in the mixture. Effective alpha particle generation is possible due to reactions involving thermal ^{3}He and fast components of the deuterium population that can be generated either from the heating beam or by coupling RF heating to the beam population as a way to drive deuterons to the MeV range [7.19]. The scenarios are also relevant for studies on the interplay between fast ions and thermal transport (more details are given in Chapter 8). The possibility to test alpha particle diagnostics in plasmas without 14 MeV neutron emission from the D+T reaction is, experimentally, an advantage, as it provides simpler environment conditions, for example in view of determining the detailed fast ion phase space sensitivity of a specific technique before the system is exposed to the challenging radiation background of a DT plasma.

A second opportunity comes from the triton burn-up component of the neutron emission (TBN) in deuterium plasmas. As it is well known, deuterium plasmas generate 2.5 MeV neutrons via the $D+D \rightarrow n+^3He$ reaction, but also 1 MeV tritons via the $D+D \rightarrow p+T$. The fast triton population can react with thermal deuterium during its slowing down path, leading to 14 MeV neutron emission. Calculations for DTT parameters [7.20] show that, mostly due to the higher core electron temperature of DTT compared with present machines, the TBN emission is about 5% of the total neutron emission and up to 7% of the local neutron emission in the core, which can be compared with a typical value of ≈1% in present-day tokamaks. This observation has motivated the development of a TOF system than can also measure TBN. From a fast ion physics point of view, the interest in 1 MeV tritons comes from the fact that they are a proxy of 3.5 MeV alpha particles from D+T fusion reactions, as the triton speed is ≈2/3 of that of the alpha particles. Hence, by measuring triton confinement in MHD active deuterium plasmas, through measurement of the TBN component by the DTT TOF, we will be able to study the effect that the instabilities would have on alpha particles in DT-equivalent plasmas for the various scenarios envisaged.

7.5 Diagnostics for Fast Ions vs instabilities & turbulence

In addition to diagnostics specifically designed to measure the fast ion velocity/energy/spatial distribution and losses, DTT should/could be equipped with diagnostics specifically designed for measuring the interaction between fast ions and coherent (Eigenmode-like) instabilities and incoherent (broadband) fluctuations. These diagnostics are then ideal to complement the more standard fast ion diagnostics discussed previously. Some examples/ideas are presented here with a brief description.

- High-frequency magnetic sensors, possibly 3D (HF-MAG): this is essentially the standard diagnostic capable of measuring coherent (Eigenmode-like) instabilities and incoherent (broadband) fluctuations, with the major caveat however that the magnetic sensors are mounted on the in-vessel side of the wall and therefore do NOT provide a localised measurement of these fluctuations. Development of magnetic sensors for DTT is well advanced using different technologies (Low Temperature Co-fired Ceramic (LTCC), photo-lithography process, standard Mirnov): all of them would be in principle capable of providing 3D measurements (δB_{POL}, δB_{RAD}, δB_{TOR}) up to frequencies well into the MHz range, if the ex-vessel cabling is sufficiently short and the data acquisition (DAQ) is correctly set up. Development of the positioning of the (3D) magnetic sensors is also well advanced, with several possible configurations suitable for providing measurements of toroidal $|n|\leq 20$ and poloidal mode numbers $|m|\leq 30$. Relevant references are [7.21, 7.22, 7.23].

- Beam Emission Spectroscopy (BES): this diagnostic allows the measurement of fluctuations with moderate to long wavelengths ($k\rho_i \leq 1$) in the density profile of the background plasma, due to the effect of such fluctuations on the photon spectrum emitted by the halo of an injected neutral beam. These fluctuation spectra can then be used to monitor the background plasma regimes (ITB formation due to increased shear-flow) and to provide information on the scattering of the injected beam ions. Relevant references are [7.24, 7.25].

- Laser Induced Fluorescence (LIF): this diagnostic uses selective optical tagging through resonant fluorescence to determine the multi-D velocity and spatial distribution function of the selected (fast) ion species. Scatter of the fast particles induced by fluctuations will directly manifest itself through changes in the detected LIF spectrum, as scattered particles cannot be tagged any longer with the same resonant fluorescent beam. Additionally, the same system can provide measurements of the q-profile, hence allowing multiple usage for the same diagnostic. Relevant references are [7.26, 7.27, 7.28].

- Experiments on the interplay between fast particles and thermal transport: The interpretation of measurements and simulations linking the alpha-particle distribution function to the onset and suppression of ITG and TEM turbulence has first been presented in 2012, for the analyses of the sawtoothing DTE1 alpha-heating experiment at JET. In these experiments a much-larger than expected ion temperature (T_i) was measured, by far exceeding the prediction of a classical slowing-down and energy transfer from the alphas (αs), while the electron temperature (T_e) was in excellent agreement with such predictions. An explanation was presented in 2012, linking the larger T_i increase to the suppression of ITG turbulence by the fusion-born αs, with the assumption that sawteeth would only moderately affect the phase-space αs distribution (this assumption being essentially due to lack of suitably detailed measurements of the αs radial diffusion).

These simulations (see Fig.7.5) corroborate the analysis of the ion-drift-wave turbulence measurements. The observed reduction in the linearly calculated ITG growth rate γ_{ITG}, together with the experimental evidence that the amplitude of ITG turbulence reduces to below measurable levels in the presence of enough αs close to their birth energy, suggests a weaker turbulent transport, in line with the χ_i reduction implied by the earlier TRANSP analyses.

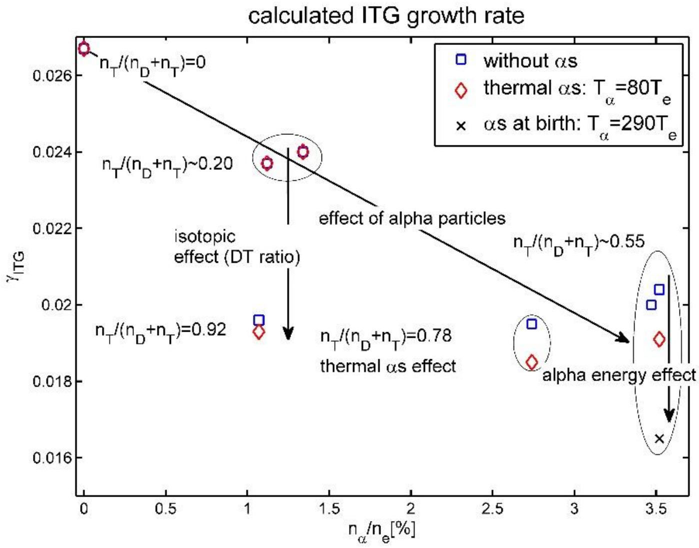

Fig. 7.5: The maximum ITG growth rate as a function of the concentration of αs. The calculation uses the value of $n_T/(n_D+n_T)$ and the actual background plasma data at R=3.5m for all the discharges in the JET DTE1 alpha-heating experiment.

An experiment was proposed at JET for the DTE2 and again for the DTE3 campaign to precisely assess the role of sawteeth in this phenomenon of ITG suppression by the α particles. However, the experiment could not be realised due to lack of steady-state performance (requirement: 1MW of fusion α-power steady over at least 5sec, i.e. a few sawtooth periods to allow for pacing via ICRH/ECRH). DTT would be well suited for such experiments, which could provide a convincing explanation of the role of sawteeth-induced radial diffusion vs ITG turbulence suppression by fast ions. Relevant references are [7.29, 7.30].

- Direct observation of phase-space transport: The direct observation of phase-space transport induced by energetic ions has been recently illustrated using a technique named Imaging Neutral Particle Analyzer (INPA) [7.31, 7.32]: this kind of diagnostic would be precious in DTT for analysing flows induced by Alfvén instabilities (see Chapter 8 for further comments).

7.6 Headlines of the research programme for energetic particles

In this section, we summarize the main headlines of the DTT research programme for the EP subject, according to the various operation phases of DTT.

Headline number	**Headline contents**	**Priority (+, ++, +++)**	**ITER**	**DEMO**
	Construction Phase 2022-2029			
C.7.1	Verification of linear stability of EP driven modes on available scenarios with NNBI and ICRH using global gyrokinetic codes	++	*	*
C.7.2	Nonlinear simulations of EP driven modes on available scenarios with NNBI and ICRH using global gyrokinetic codes	++	*	*
C.7.3	Numerical study of the EP distribution function in phase space (NNBI, ICRH, NNBI & ICRH)	++	*	
C.7.4	Numerical study of EP test particle losses induced by magnetic field ripple and in presence of global Alfvén eigenmodes.	++	*	*
C.7.5	Set up IMAS infrastructure and dedicated workflows	+++		
	Phase 1 2029-2034			
1.7.1	Optimization of experimental scenarios to observe EP driven modes on Phase 1 scenarios	++	*	*
1.7.2	Validation of linear and nonlinear EP dynamics simulation on Phase1 experiments.	++	*	*
1.7.3	Validation of EP distribution function experimental reconstruction on Phase1 experiments.	++	*	*
1.7.4	Validation of EP test particle losses simulations with experimental observations.	++	*	*
	Phase 2 2034-2038			
2.7.1-2.7.4	Same as Headlines 1.7.1-1.7.4, but on Phase 2 scenarios	++	*	*
	Phase 3 2038-…			
3.7.1-3.7.4	Same as Headlines 2.7.1-2.7.4, but on Phase 3 scenarios, taking full advantage of the relevance of DTT regarding burning plasma regimes.	+++	*	*

7.7 References

[7.1] F. Zonca and L. Chen, *Reviews of Modern Physics,* vol. 88, p. 015008, 2016.

[7.2] F. Zonca and et al., *Plasma Physics and Controlled Fusion,* vol. 57, p. 014024, 2015.

[7.3] T. Wang and et al, *Physics of Plasmas,* vol. 26, p. 012504, 2019.

[7.4] T. Wang and et al, *Physics of Plasmas,* vol. 25, p. 062509, 2018.

[7.5] G. Spizzo and et al, *Nuclear Fusion,* vol. 61, p. 116016, 2021.

[7.6] M. Gobbin and G. Spizzo, *Plasma Physics and Controlled Fusion,* vol. 65, p. 075013, 2023.

[7.7] B. Wu and et al, *Plasma Physics and Controlled Fusion,* vol. 59, p. 025004, 2017.

[7.8] R. B. White and et al, *Physics of Plasmas,* vol. 2, p. 2871, 1995.

[7.9] M. Gobbin, G. Spizzo, M. V. Falessi, V. Fusco, G. Vlad and F. Zonca, in *49th EPS Conference on Plasma Physics, poster Mo MCF9*, Bordeaux, France: European Physical Society (Petit Lancy).

[7.10] G. Vlad and et al, “Preliminary studies of Energetic Particle driven Alfvénic modes for a model DTT equilibrium using HYMAGYC,” in *MET-ENR final Workshop*, 2021.

[7.11] M. V. Falessi and et al, *Journal of Plasma Physics*, vol. 86, p. 845860501, 2020.

[7.12] M. V. Falessi and et al, *Physics of Plasmas*, vol. 26, p. 082502, 2019.

[7.13] P. Vincenzi and et al, *Fusion Engineering and Design,* vol. 189, p. 113436, 2023.

[7.14] G. Vlad and et al, “Non-linear benchmark between HYMAGYC, MEGA, ORB5 and XTOR-K codes using the NLED-AUG test case to study Alfvénic modes driven by energetic particles,” in *IAEA FEC, 1701 TH-W/P3-25*, London, 2023.

[7.15] M. Garcia Munoz and et al, *Plasma Physics and Controlled Fusion,* vol. 61, p. 054007, 2019.

[7.16] L. Sanchis and et al, *Plasma Physics and Controlled Fusion,* vol. 61, p. 014038, 2019.

[7.17] D. Moseev and et al, *Reviews of Modern Plasma Physics,* vol. 2, p. 7, 2018.

[7.18] M. Nocente and et al, *Plasma Physics and Controlled Fusion,* vol. 62, p. 014015, 2020.

[7.19] M. Nocente and et al, *Nuclear Fusion,* vol. 60, p. 124006, 2020.

[7.20] M. Nocente, “CALCOLI NEUTRONICI,” SLE-SPT-40003, 2021.

[7.21] D. Testa and et al, “First Developments towards Producing Inductive Magnetic Sensors using State-of-the-Art Photolithography Techniques,” *Journal of Instrumentation,* vol. 18, p. C06002, 2023.

[7.22] D. Testa and et al, “Development of algorithms for the end-end system simulation and performance analysis for a high-frequency magnetic diagnostic system: application to TCV, JET and ITER,” *Fusion Engeenering and Design,* vol. 188, p. 113406, 2023.

[7.23] D. Testa, “Manufacturing, Installation, Commissioning and First Results with the 3D Low-Temperature Co-fired Ceramic High- Frequency Magnetic Sensors on the Tokamak à Configuration Variable, Tutorial Paper,” *Review of Scientific Instruments,* vol. 91, p. 081401, 2020.

[7.24] R. Fonck, “Plasma fluctuation measurements in tokamaks using beam-plasma interactions,” *Review of Scientific Instruments,* vol. 61, p. 3487, 1990.

[7.25] M. W. Shafer and et al, “Localized turbulence suppression and increased flow shear near the q=2 surface during internal transport barrier formation,” *Physical Review Letters,* vol. 103, p. 075004, 2009.

[7.26] R. A. Stern, “Plasma ion diagnostic using resonant fluorescence,” *Physical Review Letters,* vol. 34, p. 1548, 1975.

[7.27] A. Fasoli and et al, “Direct measurement of ion phase-space orbits in an electrostatic field,” *Physical Review Letters,* vol. 63, p. 2052, 1989.

[7.28] E. Foley, “Measurements with magnetic field in the National Spherical Torus Experiment using the motional Stark effect with laser induced fluorescence diagnostic,” *Review of Scientific Instruments,* vol. 84, p. 043110, 2013.

[7.29] D. Testa and M. Albergante, “A phenomenological explanation for the anomalous ion heating observed in the JET alpha heating experiment of 1997,” *Nuclear Fusion,* vol. 52, no. 8, p. 083010, 2012.

[7.30] D. Testa and M. Albergante, “Evidence for a new path to the self-sustainment of thermonuclear fusion in magnetically confined plasmas,” *Europhysics Letters,* vol. 97, p. 35003, 2012.

[7.31] X. Du and et al, “Visualization of Fast Ion Phase-Space Flow Driven by Alfvén Instabilities,” *Physical Review Letters,* vol. 127, p. 235002, 2021.

[7.32] J. Rueda-Rueda and et al, “Phase-space measurements of MHD-induced fast-ion transport in the ASDEX Upgrade tokamak,” in *29th Fusion Energy Conference, Oct.16-21 (2023), London, UK*, London, 2023.

Chapter 8

THEORY AND SIMULATION

M. Falessi, G. Vlad, E. Nardon,
G. Brochard, C. De Piccoli, G. Falchetto, M. Gobbin, Y. Kominis, P. Lauber, M. Nocente, M. Salewski,
G. Spizzo, P. Vincenzi, F. Zonca, M. Zuin

This chapter aims at summarizing the main challenges that theoretical plasma physics must address in reactor-relevant fusion plasmas. Giving a complete list is beyond the present scope and, for this reason, the focus will be on those physics problems that will play a crucial role in the DTT research program. At the same time, the general and fundamental physics aspects discussed below are not limited to DTT. They are analysed here because they are general and will be relevant for ITER and DEMO. In this respect, the role of theory in the DTT conceptual design phase has been to identify machine parameters that could allow addressing those general and fundamental physics issues. Similarly, in the present preparatory phase, theory assumes a key role to make predictions beyond the capability of present physics models. Following verification, these predictions can guide the conceptual design of experiments that will provide a relevant test-bed for validation.

The contents of this chapter are the result of ongoing international collaborations, within EUROfusion, particularly the ENR-ATEP [8.1] and the TSVV10 [8.2], with the Center for Nonlinear Plasma Science (CNPS) collaboration network [8.3], also supported by the Natural National Science Foundation of China and the Italian Ministry for Foreign Affairs and International Cooperation.

8.1 Weak similarity scaling & DTT

The impact of the weak similarity scaling argument [8.4], as highlighted in Chap. 1, is one example of the significant role that theory and simulations have played in shaping the key features of DTT. This approach enables the exploration of the integration between core and edge physics in reactor relevant conditions, notably those relevant for ITER/DEMO. Consequently, DTT is characterized by a dimensionless parameter range close to those machines, enabling the exploration of operational issues and testing innovative technical solutions. This, in particular, allows the investigation of cross-scale couplings between various spatiotemporal scales in reactor relevant plasma conditions, which characterize fluctuations around equilibrium profiles and the equilibrium state itself. Notably, the normalized energetic particle Larmor radius and kinetic pressure in DTT closely resemble those in ITER, as illustrated in Figure 1.1 of Chapter 1. This equivalence is crucial for the scientific exploitation of DTT, as the dynamics of energetic particles heavily influence the interplay between different spatiotemporal scales. Therefore, one of the goals of the DTT research programme, and in particular of the theory part, is to investigate this complex interaction and provide insights that would support ITER operations. This is of fundamental importance for the scientific programme also because DTT will have an overlapping timeline with ITER and, therefore, DTT support to ITER will be a key element.

The possibility of investigating DTT specific aspects that are peculiar to burning plasmas relies on the similarity argument based on the existence of three dimensionless parameters in the equations governing quasi-neutral, collisional, finite-β plasmas, i.e., ρ^*, β and ν^* [8.5]. This similarity argument is the theoretical foundation of the concept of dimensionless similarity experiments [8.6]. In the original formulation and for fixed equilibrium geometry and profiles, the similarity argument corresponds to having one free quantity to choose among B (magnetic field), R (major radius), n (density) and T (temperature). One therefore can fix nR^2, $BR^{5/4}$ (or $I_pR^{1/4}$ for fixed safety factor profile, with I_p the plasma current) and $TR^{1/2}$ as "engineering quantities" corresponding to maintaining an identical set of ρ^*, β and ν^* with R free to vary [8.7]. However, already extending the similarity argument to the plasma edge, as required by the DTT mission, where atomic physics effects are expected to play a key role, challenges the description of plasmas in terms of ρ^*, β and ν^* only and suggests the introduction of T as a further "dimensionless" parameter [8.7]. Using the collection of ρ^*, β, ν^* and T, on the other hand, makes it impossible to define a non-trivial set of similarity experiments. A thorough discussion of this point is given by Lackner et al. [8.6]. Similar issues and challenges to extending the similarity argument arise with burning plasmas [8.5, 8.7, 8.8], since dominant α particle heating brings in additional physics beside those of quasi-neutral, collisional, and finite-β plasma, exactly as plasma edge behaviours reflect atomic physics.

Thus, the attempt of extending the conventional similarity argument [8.5] to burning plasma relevant experiments yields the apparent paradox that only the trivial solution exists, for which ITER relevant burning plasma physics issues can be addressed in ITER only. This problem may be solved only relaxing the idea of maintaining identical ρ^*, β, ν^* while identifying crucial physics aspects, which allow us to investigate the broadest possible range of dynamics that are peculiar to burning plasmas in an integrated fashion [8.7, 8.8]. This allows us to construct a "weak" similarity argument and suitably rescale plasma parameters with respect to those of ITER, while still addressing the relevant integrated physics. "Weak" here is to be intended as in its rigorous mathematical definition, i.e., as an argument reproducing a general result under less stringent assumptions, which are relaxed in a controlled way and yield the original "strong" result in the appropriate limit. This can be done in two ways: one is based on introducing an additional *ad hoc* dimensionless parameter ε and assuming that ρ^*R^ε, β and ν^* are fixed (to those in ITER) and appropriately rescaling T with respect to the ITER reference value; the other assumes that ρ^*R^ε, β and τ_{SD}/τ_E are fixed and, as in the former case, appropriately rescales T with respect to the ITER reference value. The usefulness of the "weak" similarity approach is that it introduces an "order relation" in the 4-dimensional tokamak operation space at fixed profiles, geometry etc. (e.g., plasma facing components), based on the choice of integrated physics to be investigated and parameterized by T(R). In other words, the value of ε controls the physics, while T(R) controls the performance once the physics is fixed. Therefore, machines with lower ε are closer to ITER because they are closer to the original similarity argument, while – for fixed ε – machines with higher T(R) have better performance by the established "order relation". In fact, the requirement that T(R) is a monotonically increasing function restricts the accessible values of ε. The strength of this approach is that one can generate classes of plasma equilibria for which the hierarchy of spatiotemporal scales and, thus, plasma self-organization properties are preserved. Corresponding equilibria, obtained by rescaling T and/or R, however, are distinct by the achievable plasma performance, which is an increasing function of T and/or R and, ultimately, plasma current.

It can be shown that the two proposed scalings give very similar results; however, while the first approach is aimed at preserving core-edge nonlinear plasma couplings, the second one is justified in terms of focus on the physics of plasmas with predominant fusion alpha particle self-heating. For this reason, we will refer to the first case as the "weak" Kadomtsev scaling and to the second one as the "weak similarity" scaling for fusion plasmas. It is also interesting to note that these similarity arguments relax spatial scale constraints, since this still allows maintaining unaltered cross-scale couplings between meso- and micro-scale fluctuations at ITER relevant values of ρ^*, provided the ratio of supra-thermal ion energies is chosen to scale linearly with thermal plasma temperature at fixed electron heating fraction. This condition, in fact, ensures a clear link of supra-thermal with thermal ion energies, which reflects the predominant power density transfer of fusion alpha particles to thermal electrons while slowing down by drag due to Coulomb collisions. On the contrary, relaxing β would alter the cross-scale coupling in frequency space between drift-waves and Alfvénic fluctuations; meanwhile, this would also alter equilibrium similarity, e.g., due to different Shafranov shifts, and the free energy density available to drive instabilities by both thermal and supra-thermal plasma components. This latter argument is also the key reason why, when dealing with physics integration of burning fusion plasmas, preserving τ_{SD}/τ_E is a more appropriate choice than fixing ν^*. In fact, this allows preserving the ratio of the supra-thermal ion free energy density to that of thermal ions, for in a burning plasma of fusion interest, where the local power balance is dominated by thermal plasma heating due to supra-thermal ions, $(\tau_{SD}/\tau_E) \approx (\beta_H/\beta)$. Note, however, that the differences between the "weak" Kadomtsev and "weak similarity" scalings, obtained by the present arguments, are not substantial, as shown below, which is suggestive that both these 0-D arguments are robust and largely consistent in identifying the relevant parameters in the plasma operation space that allow addressing burning plasma relevant physics. In fact, both scalings are to be taken as indicative 0-dimensional scalings that help identifying the potentially interesting region of the tokamak operation space, where more detailed analyses are to be performed. Furthermore, in both cases, one can identify a minimum value of ε above which the "weak" scaling argument is "physically meaningful": this value is fixed by the condition that the plasma temperature is either constant or increasing with R within the same ε–ordered set.

The "weak" Kadomtsev scaling, i.e., the one based on the invariance of $\rho^* R^\varepsilon$, β and ν^*, is readily obtained. In particular, the first two conditions impose $n \approx R^{2\varepsilon-2}$ and $I_p \approx T^{1/2} R^\varepsilon$, while ν^* invariance implies $T \approx R^{\varepsilon-1/2}$, i.e.,for $\varepsilon=0$, the invariance of the "engineering quantities" introduced in [8.5]. Summarizing, the "weak" Kadomtsev scaling gives $n \approx R^{2\varepsilon-2}$, $T \approx R^{\varepsilon-1/2}$, $I_p \approx R^{3\varepsilon/2-1/4}$, $\tau_{SD} \approx R^{5/4-\varepsilon/2}$ and $\tau_R \approx R^{3\varepsilon/2+5/4}$. From this, one recognizes that values of $\varepsilon \leq 1/2$ are not "physically meaningful", for smaller devices would need to operate at higher temperatures. Meanwhile, for estimating the size-scaling of the energy confinement time, we need to assume some empirical confinement scaling law for the triple product $N=nT\tau_E$. Using a confinement scaling such as

ITER98y2, for which $N \propto (I_p/R^{1/3})^{5/2}$ [8.7, 8.8], one can estimate $(\tau_E/\tau_{SD}) \approx (I_p/R^{1/3}T)^{5/2}$ and, thus, $\nu^* \approx (\beta/I_p)(I_p/R^{1/3}T)^3 \approx (\beta/I_p)(\tau_E/\tau_{SD})^{6/5}$; therefore, at constant β and ν*, $(\tau_E/\tau_{SD}) \approx I_p^{5/6}$ and $\tau_E \approx R^{3\varepsilon/4+25/24}$ with the total power input $P \approx R^{9\varepsilon/4-13/24}$. Given the “weak” Kadomtsev scaling, it is straightforward to derive the “weak similarity scaling” for fusion plasmas, i.e., assuming that $\rho^* R^{\varepsilon}$, β and τ_{SD}/τ_E are fixed (to those in ITER). As before, the first two conditions impose $n \approx R^{2\varepsilon-2}$ and $I_p \approx T^{1/2} R^{\varepsilon}$, while – for fixed β and τ_{SD}/τ_E – the ITER98y2 confinement scaling implies $\nu^* \approx (1/I_p)$, i.e., $n \approx R^{2\varepsilon-2}$, $T \approx R^{2\varepsilon-2/3}$, $I_p \approx R^{2\varepsilon-1/3}$, $\tau_E \approx \tau_{SD} \approx R^{\varepsilon+1}$ and $\tau_R \approx R^{3\varepsilon+1}$. From this, one recognizes that “physically meaningful” values of the scaling exclude $\varepsilon \leq 1/3$. Finally, for the total power input one obtains $P \approx R^{3\varepsilon-2/3}$. It is worthwhile noting that both weak Kadomtsev and weak similarity scalings emphasize the important role of high plasma current in order to operate at low collisionality in reactor relevant conditions. This is one of the fundamental differences that will characterize next generation plasma devices with respect to present ones.

For the main mission of DTT, the choice of preserving the collisionality parameter ν* is more appropriate, since it importantly affects the edge physics and plasma-wall interaction as well as power and particle exhaust. Due to the nature of a reactor-relevant plasma, which is a complex, self-organized system in which diverse elements are tightly linked and necessitate appropriate description, the preservation of these physics with the corresponding spatiotemporal scales stands as a matter of paramount importance. Having fixed the class of plasma equilibria that is most properly representative of the physics addressed by the main DTT mission, targeted plasma operations are determined based on the choice of ε and machine size. These criteria are ultimately tight to cost and performance, since $\tau_E \approx R^{3\varepsilon/4+25/24}$ and the magnetic energy, which is a good proxy for the machine cost [8.4], is $\approx B^2R^3 \approx R^{3\varepsilon+1/2}$. In the case of DTT, these criteria led to the optimal choice of $\varepsilon = 0.75$ choice and R=0.35 (normalized to ITER major radius). In terms of ITER reference values, application of the weak Kadomtsev scaling to performance and cost would yield an estimate of the energy confinement time in DTT about 19% of the corresponding ITER value and a cost of about 6%.

8.2 Plasma as a complex system: nonlinear equilibria and self-organization

A reactor-relevant plasma represents a complex self-organized system, in which the fluctuation spectrum and the radial profiles represent evolving self-consistent nonlinear equilibria [8.9, 8.10, 8.11] capable of developing a wide range of different spatiotemporal scales. Taming this complexity and self-organization is crucial for achieving stationary conditions necessary for efficient power production through fusion reactions. In these nonlinear equilibria, the various elements behave as a whole and changing one of them implies the modification of all the others, highlighting the intricate interplay between fluctuation spectrum, radial profiles, plasma instabilities, and fusion performance. Moreover, in D-T plasmas, most of the power density required to compensate for losses will be provided by heating from fusion alphas. Additionally, MeV-range energetic particles (EPs), primarily produced by ICRH and negative NBI will play a key role, by heating and fueling the thermal plasma and driving current (see Chap. 7 for details). EPs will interact with plasma instabilities and crucially influence turbulent transport, since they are responsible of mediating strong nonlinear coupling, significantly impacting fusion reactivity profiles, pressure-driven currents, MHD stability, transport, and plasma boundary interactions; thus, impacting fusion performance, stability, and control. In such a complex system, EPs play a unique role as mediators between different spatiotemporal scales [8.10], driving instabilities on meso-scales, of the order of EP Larmor and/or magnetic drift orbit width, intermediate between the microscopic thermal ion Larmor radius and the macroscopic plasma equilibrium scale length. These Alfvénic instabilities, in turn, provide nonlinear feedback onto the macroscales, exciting microscopic radial mode structures at Shear Alfvén Wave (SAW) continuum resonances that propagate and get absorbed elsewhere, challenging usual local analyses. These processes, in turn, may be mediated by formation of zonal flows and fields and radial spreading of soliton-like structures [8.10, 8.11]. It becomes of crucial importance for understanding burning plasmas and predicting their behaviors that these processes, whose features are affected by realistic equilibrium geometries and plasma non-uniformities [8.11], preserve the proper hierarchy of spatiotemporal scales, thereby supporting the arguments upon which the weak similarity scaling is constructed, as presented in the previous section.

These factors make the study of reactor-relevant plasmas challenging in present-day experiments and necessitate a conceptual change in the adopted approach. In particular, the power density profiles and characteristic wavelengths of collective modes in DTT are expected to strongly differ from those currently observed and will be shifted towards higher mode numbers. Furthermore, the dominant electron heating will introduce a different weighing of the electron-driven microturbulence. Another important novelty that will be a characteristic feature of DTT plasma operations is the presence of a non-perturbative EP population with characteristic energies larger than the critical energy, above which the collisional drag by thermal electrons on EP exceeds the pitch-angle scattering rate off thermal ions. In those conditions, both linear and nonlinear interaction of EPs with core plasma turbulence will be modified and predominantly affected by EP resonant and non-resonant diamagnetic response rather than by the dilution effect due to mildly supra-thermal ion contribution to the quasi-neutrality condition [8.11]. Determining how the power repartition between electrons and ions (ultimately expressed by the T_e/T_i ratio), depends on the heating mix, particularly as fast ions are introduced in the plasma, is a key area of investigation.

In DTT there exists the unique opportunity to compare electron heated plasmas without fast ions (when only the ECRH system is used) and with fast ions, with the additional possibility of varying their energy range and density. A simpler scenario is obtained when NBI at different power levels is added to EC heated plasmas. A more intricate scenario is obtained when ICRH is used to generate MeV range ions. A large variety of heating schemes could be adopted, for example the more standard hydrogen and ^{3}He minority heating, heating of the NBI deuterons at the second and third harmonic of the ion cyclotron resonance frequency or the three ions scenario. In all these cases, it will be necessary to characterize and understand the fast ion driven modes that are observed, the corresponding fast ion transport and the overall impact on turbulence. Understanding the mechanisms behind the impact of different energetic ion populations on turbulence must be aimed at finding what is the best mix of auxiliary heating systems to ensure that heating is effectively channeled from the electrons to the ions and, ultimately, the fusion neutron yield per MW of auxiliary heating power is maximized. Plasma operation scenarios (see Chap. 2 for more details) will also reflect different plasma edge conditions and plasma wall interactions at high density and low collisionality. These conditions must be addressed to improve our understanding of reactor-relevant plasmas. For these reasons, predictive capabilities based on numerical simulations as well as fundamental theories for constructing relevant reduced models will play crucial roles, and provide the necessary insights.

In the next sections, we will tackle some of these issues by presenting a comprehensive IMAS-based workflow to study transport processes in the presence of EPs [8.12, 8.13, 8.14]. This approach leverages the results of a recent EUROfusion Enabling Research project mentioned in the introduction of the chapter, which has the potential to facilitate verification and validation against experiments. Such advancements are of utmost importance for the DTT scientific exploitation since they may play a pioneering role in verification and validation of reduced models describing the physics of reactor-relevant plasmas. This synergistic collaboration among experiments, numerical simulation, and theory will therefore be essential.

The complex nature of reactor-relevant plasmas requires particular attention to the accurate characterization of Zonal flows and more generally Zonal Fields (ZFs) [8.15, 8.16, 8.17, 8.18]. ZFs can be generated by various nonlinear processes, such as thermal plasma instabilities, EPs driven instabilities, and geodesic acoustic mode (GAM) interactions. The understanding and characterization of these zonal flows/fields is essential for predicting and controlling the performance of the plasma due to their role in regulating plasma turbulent transport. This requires an analysis that accounts for multiple spatiotemporal scales in a self-consistent manner, considering realistic conditions such as equilibrium geometry, spatial non-uniformity, and kinetic effects [8.11]. Numerical simulations and experimental studies must be conducted in DTT to address these issues and provide insights into the complex behavior of ZFs and their impact on reactor relevant plasmas. The interaction between various time scales and structures in the plasma can lead to nonlocal behaviors, driven by EPs and other instabilities. Theoretical descriptions based on first principles are imperative to capture the complexity of these interactions. Meanwhile, numerical simulations, either gyrokinetic or hybrid/kinetic, must be global and fully electromagnetic to properly consider the expected nonlocal behaviours and corresponding equilibrium modifications. In fact, flux tube numerical simulation approaches have already revealed to be inadequate in this respect.

8.3 Gyrokinetic transport theory: general approach

As described in the previous sections, reactor relevant fusion plasmas behave as complex systems necessitating, in the general case, a global electromagnetic first principle-based approach. In particular, the crucial role of EPs, due to their characteristic energies, requires the description of transport processes occurring on completely different spatiotemporal scales compared to background transport. Furthermore, EP transport will be dominated by resonant processes with distinctive features in the EP phase space. Consequently, current research on EP-driven instabilities and transport in such plasmas, including DTT, is recognized to be limited by the costly and time-consuming high-fidelity numerical frameworks used, such as global MHD hybrid-kinetic or fully gyrokinetic codes (see Chap. 5 and Chap. 7 for more details). Although these simulations provide valuable insight into fundamental physics processes, they typically cover only a limited time range of the dynamics or rely on the separation of various time scales and, thus, have limited predictive capability of transport processes in realistic conditions. To reduce the numerical cost of gyrokinetic simulations of turbulent transport, the “local” flux-tube approximation is often adopted. However, the predictivity of turbulent transport in reactor-relevant fusion plasmas from nonlinear gyrokinetic simulations based on this reduced approach is often questioned, as anticipated in the previous section, since they cannot address the nonlocal behaviours connected, e.g., with the formation of zonal fields structures (ZFs) and EP physics in general.

To address this challenge, recently, the phase space zonal structures (PSZS) transport theory has been developed [8.22]. PSZS represent slowly evolving (on the transport time scale) structures in the phase space that are unaffected by collisionless dissipation, providing a suitable definition of plasma nonlinear equilibrium distribution functions [8.21]. They are therefore characterized by being “slowly evolving” and are not affected, e.g., by Landau damping. To satisfy this criterion, PSZS must be calculated by adopting a two-step averaging procedure. More precisely: first, an average along guiding center equilibrium orbits is applied; second, a filter is used, on the axisymmetric particle response, to remove the fast spatiotemporal variations on the characteristic particle orbit length-scale and/or the hydrodynamic time-scale. Consequently, PSZS depend solely on the equilibrium invariants of motion, such as the particle energy (per unit mass) $\mathcal{E} = \frac{v^2}{2}$, the magnetic moment $\mu = \frac{v_\perp^2}{2B}$, and the toroidal component of the canonical angular momentum P_ϕ.

The evolution of PSZS is described by the following equation [8.24]:

$$\frac{\partial}{\partial t}\overline{F_0}^{(\mathrm{O})}+\frac{1}{\tau_b}\left[\frac{\partial}{\partial P_\phi}\overline{\left(\tau_b\delta\dot{P}_\phi\delta F\right)_z}^{(\mathrm{O})}+\frac{\partial}{\partial\mathcal{E}}\overline{\left(\tau_b\delta\dot{\mathcal{E}}\delta F\right)_z}^{(\mathrm{O})}\right]_S=\overline{C^g}_S^{(\mathrm{O})}+\overline{S}_S^{(\mathrm{O})}$$

where $[\dots]_S$ denotes an appropriate spatiotemporal averaging [8.24], the bar indicates an average along (unperturbed) equilibrium orbits, $\tau_b$is the bounce time characterizing particle motion in the self-consistently evolving equilibrium magnetic field, $\delta\dot{P}_\phi$ and $\delta\dot{\mathcal{E}}$ represent respectively the variation of canonical angular momentum and particle energy per unit mass due to the interaction with the fluctuating electromagnetic fields.

The evolution of the PSZS component of the distribution function, i.e. $\overline{F_0}^{(O)}$, extends the concept of plasma transport processes to the phase space in the presence of collisions and sources (on the RHS of the equation already introduced), making it particularly relevant for weakly collisional plasmas with possible significant deviations from local thermodynamic equilibrium, e.g., the state described by Maxwellian distribution functions. Importantly, the PSZS theoretical framework allows the derivation of the usual plasma transport equations as a specific limiting case when the deviation from the local Maxwellian is small [8.22]. However, in the most general case, PSZS will not be associated with a reference Maxwellian since they will be the result of the competition between resonantly induced nonlinear transport, sources, and only weakly collisional effects, thus requiring a phase-space description [8.21, 8.22, 8.23, 8.27]. The importance of the deviation from the local thermodynamic equilibrium could be understood since the plasma on long times can evolve into a state that may still be close to some local Maxwellian but with significantly different plasma profiles with respect to those that would be achieved if the deviation from the local thermodynamic equilibrium was ignored [8.24].

The PSZS transport theory is of crucial importance for DTT. In fact, DTT plasmas will combine high density and low collisionality operations and will provide an ideal test-bed for validating the predictions based on this novel theoretical framework. In fact, peculiar features in DTT are the additional heating with both ICRH minority scheme as well as 510 keV NNBI for the generation of EP populations significantly above the critical energy. As an illustrative example, Fig. 8.1 shows a distribution function for NBI newly born fast ions obtained for DTT reference scenario E [8.39].

Thus, in DTT it will be crucial to develop advanced diagnostics techniques for the measurement and reconstruction of the EP distribution function, which will be dominated by the peculiar features of PSZS because of the underlying kinetic nature of wave-particle interactions and excitations of fluctuation spectra.

By solving PSZS transport equations through a hierarchy of transport models ranging from global gyrokinetic to quasilinear theories, we can develop and validate advanced reduced EP transport descriptions capable of capturing the long-time scale evolution of burning plasmas and provide insights into the non-locality of the underlying processes. Due to the limitations of standard gyrokinetic transport analysis discussed in the previous sections, it is of crucial importance for DTT to develop and validate predictive reduced transport models including all the essential physics elements.

One approach relies on exploiting the characteristic spatiotemporal scales of the fluctuation spectrum. Shear Alfvén wave fluctuations excited by EPs as well as drift waves, can be decomposed in Fourier series in the toroidal direction. For each toroidal mode number n, the fluctuation can be further described as a parallel (to the equilibrium magnetic field) mode structure, and a radial envelope. Correspondingly, nonlinear interactions can take the following three forms [8.10, 8.11]: mode coupling between two toroidal mode numbers, modulation of the radial envelope, and distortion of the parallel mode structure.

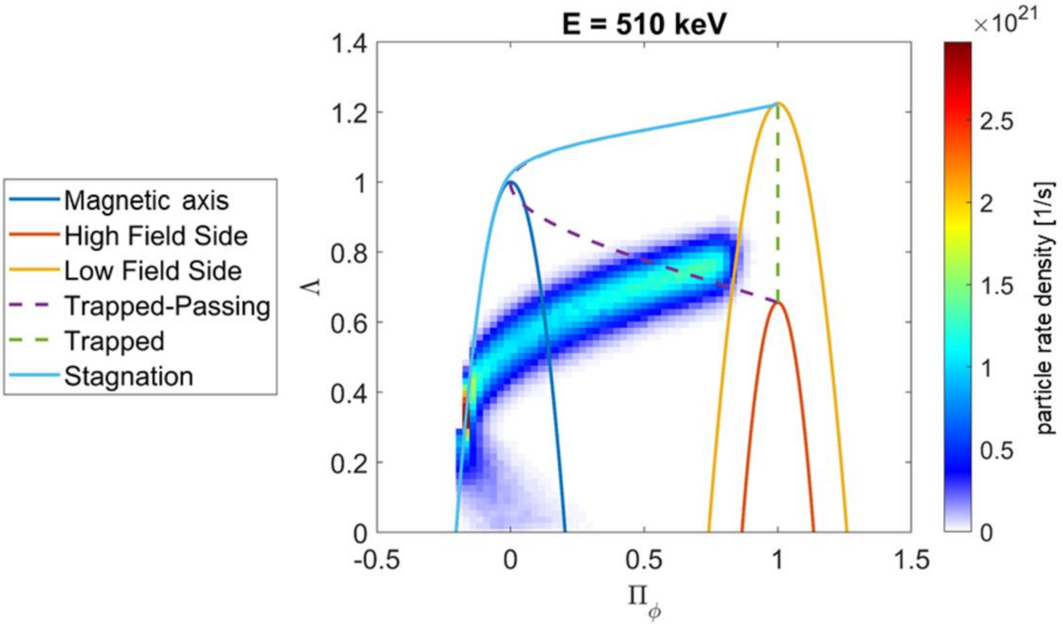

Fig. 8.1: Distribution function of newly born fast ions in DTT reference scenario at E = 510 keV in a space described by the normalized canonical angular momentum and the pitch angle. These results have been obtained using the BBNBI code [8.40].

Each of these processes exhibits distinct characteristic spatiotemporal scales. The parallel mode structure typically emerges on a time scale proportional to the inverse characteristic frequency ω^{-1}. Meanwhile, distortion of the radial envelope and coupling between two ns takes place on a nonlinear time scale $\tau_{NL} \gg \omega^{-1}$, which, for Alfvénic fluctuations, can be assumed of the order of the inverse linear growth rate of the considered instability, γ^{-1}. The existence of these different characteristic time scales suggests investigating plasma transport processes with three levels of approximation, using the PSZS transport equation [8.23, 8.24]. Phase space fluxes can be re-written formally separating the nonlinear radial envelope dependences from parallel mode structures. In this way, it is possible to clarify the interlink between fully nonlinear global gyrokinetic analysis and PSZS transport theory. In other words, at the lowest (zeroth) level of approximation, the PSZS transport theory describes phase space transport processes that are fully consistent with nonlinear gyrokinetics; suggesting, thus, that a viable route exists for implementing a comprehensive gyrokinetic analysis of turbulent transport in phase space [8.24]. The first level of approximation, meanwhile, assumes a weak amplitude expansion. Since, typically, $\tau_{\mathrm{NL}} \sim \gamma^{-1} \gg |\omega|^{-1}$, the parallel mode structure remains unmodified on the shortest time scale. At this level of approximation, the parallel mode structure is thus set by the linear theory, while nonlinear dynamics can be understood as coupling of the remaining relevant degrees of freedom n and amplitude of the radial envelope on a time scale τ_{NL}. Within this level of approximation, it is possible to address phase-locking and phase-bunching, which are important processes in the nonlinear dynamics of Alfvénic fluctuations and EP transport. In the second level of approximation, the fluctuation spectrum evolves without considering the coupling among different toroidal mode numbers; thus, describing nonlinearity solely through the EP transport processes in the phase space. In cases of multiple overlapping resonances and short de/auto-correlation time, this approach converges to the usual quasi-linear description [8.23].

8.4 Integration of theory, simulation and experiments

The success of the DTT research programme depends critically on the ongoing comparison of global numerical simulations, experimental observations, and reduced nonlinear theoretical models. This comparison is necessary to develop a robust predictive capability for reactor-relevant fusion plasmas and gain new insights on the underlying physics. Current theoretical understanding has indicated the crucial importance of accurately describing equilibrium geometry, plasma non-uniformities, radial mode structures, and kinetic processes [8.11]. On the other hand, well-diagnosed experiments play a key role in providing evidence for theoretical model verification and validation. The self-organisation of reactor-relevant plasmas is crucially influenced and determined by the behaviour of EPs [8.10]. Therefore, it is extremely important for the scientific exploitation of DTT to have an automated workflow, based on the Integrated Modeling and Analysis System (IMAS), to analyze the time-dependent stability of EP-driven modes in general tokamak geometry. This automated workflow must leverage efficient computational methods and theory-based reduced models to deliver fast and reproducible results. Such an approach represents a pivotal step towards creating tools for analyzing transport phenomena and optimizing the performance of any future fusion device such as DTT. Evaluating the phase space fluxes described in the previous section necessitates multiple linear computations at various time slices of a given scenario, i.e., ramp-up, flat-top, and ramp-down, requiring therefore a high degree of automatization.

Notably, a proof of principle tool capable of performing this kind of analysis has recently been made available by Popa et al [8.25]. This instrument offers valuable insights into the stability of Alfvén Eigenmodes in different scenarios and during the whole discharge, i.e., see Fig. 8.2 for a simple example. It is built on a hierarchical usage of the linear gyrokinetic eigenvalue code LIGKA [8.30], which is made possible using a centralized IMAS database that connects the different components of the workflow and guarantees the reproducibility and consistent interpretation of the different steps of the analysis.

Additionally, in line with the hierarchy of reduced descriptions outlined in the previous section, a suite of codes describing the parallel mode structure of the Alfvén Eigenmodes using the mode structure decomposition [8.35] named PEANUTS, based on Ref. [8.33, 8.34], has been included in the workflow. Figure 8.3(a) illustrates the radial structure of the DTT continuous spectrum for toroidal mode number n=20. The frequency normalized to the on-axis Alfvén frequency and radial location at ρ_{tor}=0.702 of an n=20 TAE mode is also indicated. The corresponding normalized parallel mode structure of the magnetic stream function is shown in panel (b), while 2D and 3D mode structures are shown, respectively, in panels (c) and (d) assuming an ad-hoc radial envelope function [8.36].

Building upon the EP-stability workflow described above, and harnessing its modularity, Lauber et al. [8.32] created the newly written ATEP code as part of the EUROfusion Enabling Research project, which bears the same name. Within this numerical framework, the linear gyrokinetic mode information is utilized to calculate the phase space fluxes appearing in the PSZS governing equation, introduced in the previous section. To obtain these fluxes, the HAGIS code [8.31] is used assuming various perturbation amplitudes, allowing the implementation of the double averaging procedure already described. Since the current analysis focuses on quasi-linear diffusive transport, the phase space fluxes can be immediately linked to transport coefficients. These coefficients are evaluated on the final 3D grid used in the ATEP code, consisting of particle energy (per unit mass) $\mathcal{E} = \frac{v^2}{2}$, particle pitch Λ, and the toroidal component of the canonical angular momentum P_ϕ. Careful interpolation of these coefficients is required since the effect of resonant transport can be quite relevant and localized in the phase space, which is the main motivation of this analysis.

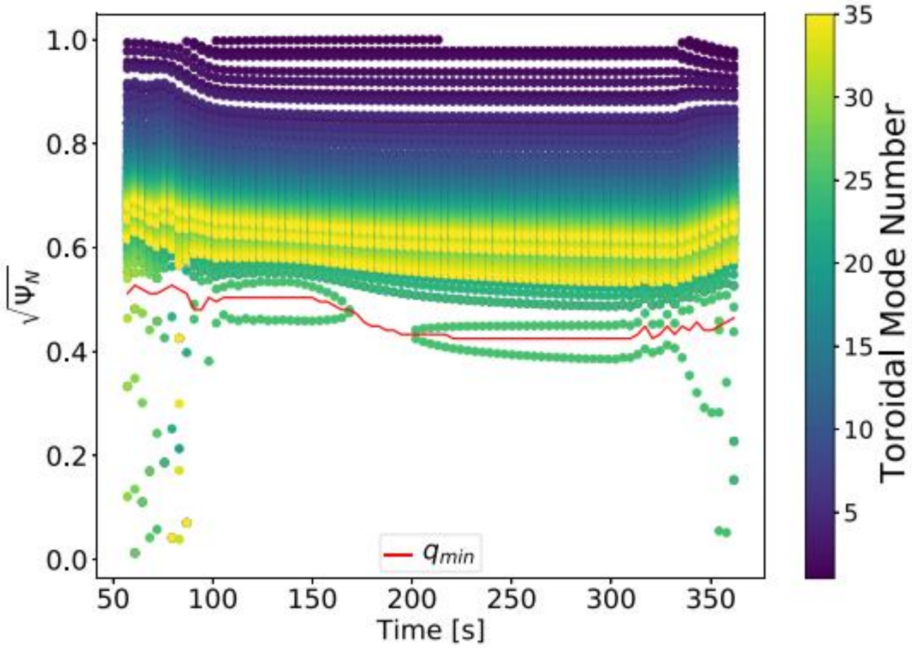

Fig. 8.2: Tracking of the radial position (normalized poloidal flux) of TAE modes with given toroidal mode number n *in an ITER* $Q = 10$ *scenario. Courtesy of A. Popa [8.14]*

As an example, in Fig. 8.4 we show some plots of the orbit-average of $\delta\dot{P}_\phi$ caused by single Toroidal Alfvén eigenmode as appearing in the PSZS equation in the quasi-linear limit.

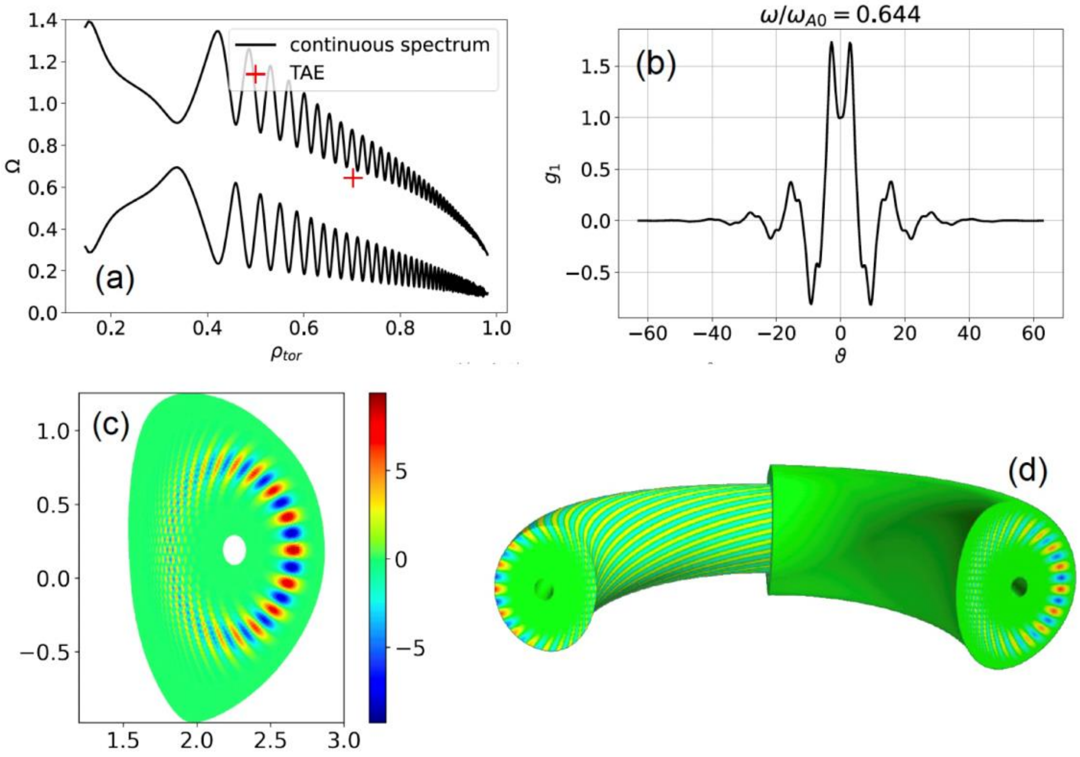

Fig. 8.3: (a) Continuous spectrum (n=20) and location of TAE in DTT; (b) normalized parallel mode structure of the magnetic stream function at ρ_{tor}*=0.702; 2D (d) 3D mode structure (n=20) obtained with an ad-hoc radial envelope. Courtesy of G. Wei [8.36].*

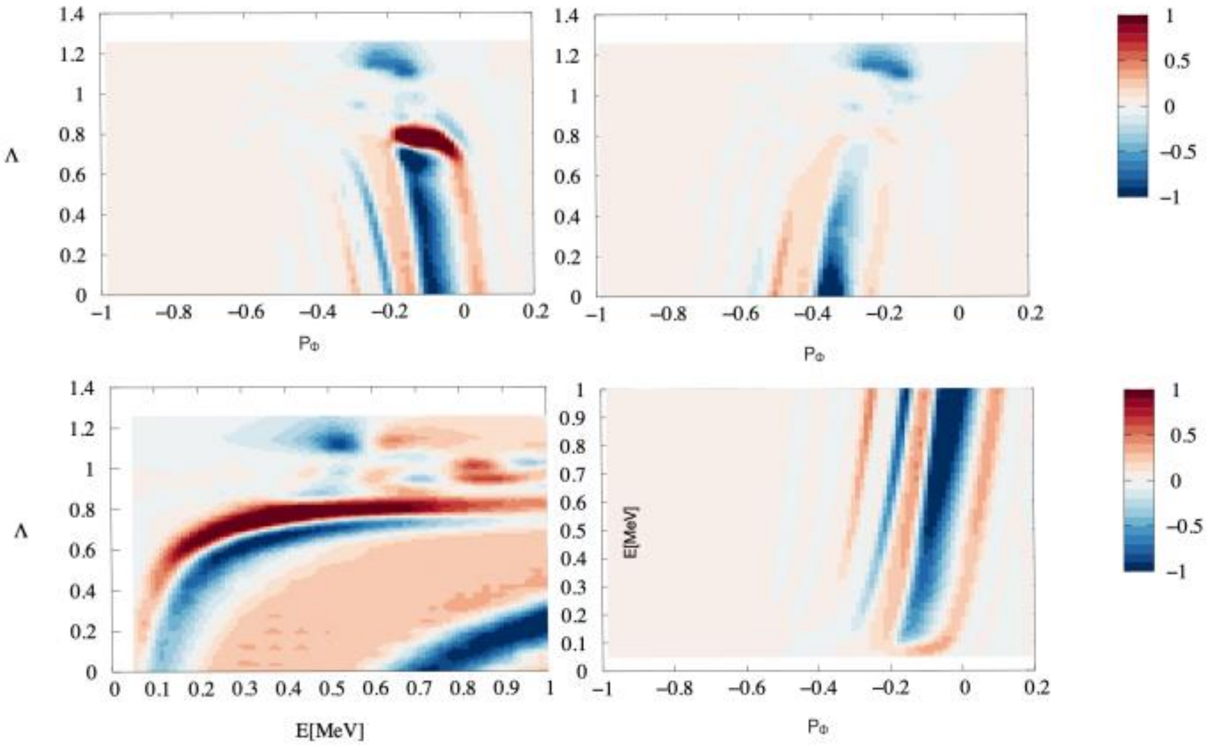

Fig. 8.4: Calculation of the orbit average of $\delta\dot{P}_{\phi}$ produced by a single $n = 13$ TAE mode for an ITER pre-fusion scenario. The plots on top left describes for fixed energy E (500 KeV) co-passing and trapped particles, on the top right counter-passing and trapped particles, while plots at the bottom show the structure of the $E - \Lambda$ space for fixed $P_{\phi} = -0.2$ (left) and in $P_{\phi} - E$ space for fixed $\Lambda = 0.12$. Courtesy of P. Lauber [8.32]

The next step of the ATEP code [8.32] consists in evolving a given distribution function using the PSZS equation. The distribution function, as generated by heating systems or by other IMAS-compatible codes, can be loaded and evolved in time. In Fig. 8.5, as an example, we show the modification of the PSZS distribution function between two times of the workflow.

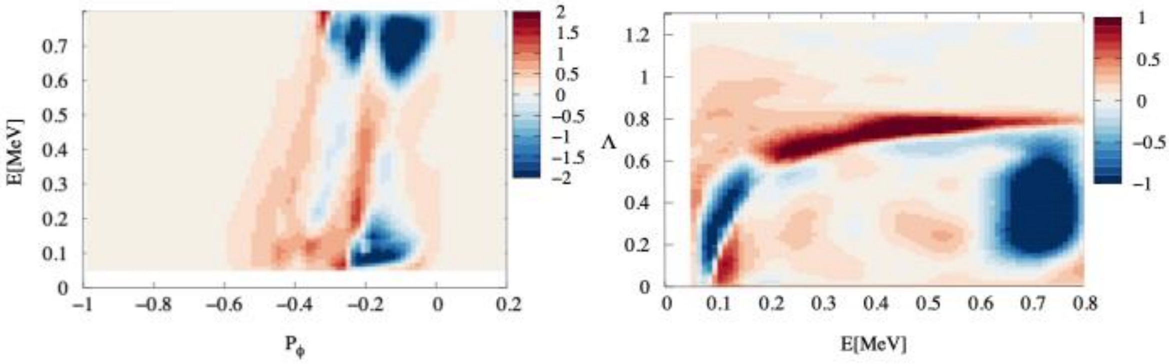

Fig. 8.5: Modification of the PSZS distribution function between two times as calculated by the ATEP code. The effect of localized, resonant transport is clearly shown. Here, an integration over third CoM coordinate (left over Λ, right over P_{ϕ}) has been performed. Courtesy of P. Lauber [8.32]

Consistently with this analysis, all the moments of the PSZS distribution, such as the related current and pressure, can be evaluated at each time step and eventually passed to a transport code or directly compared with DTT diagnostics results.

In conclusion, it is of utmost importance to emphasize the active development of these workflows, or similarly capable alternatives, for ensuring the accurate scientific exploitation of DTT. Such tools are crucial for validating theoretical results by means of a comparison with experimental data and synthetic diagnostics, thereby establishing a solid framework for the hierarchy of reduced transport models introduced earlier. By prioritizing the ongoing evolution and enhancement of these tools, the DTT project can ensure the reliability, accuracy, and credibility of its findings. In this respect, it is noteworthy emphasizing that, given the flexibility of these tools and their natural embedding within the IMAS framework, results of analyses will be most naturally linked with synthetic diagnostics, particularly those specifically developed for EP physics (see Chapter 7). Good illustrative examples of this case are provided by the imaging neutral particle analyzer (INPA), recently developed at DIIID [8.37] and ASDEX Upgrade [8.38].

For these reasons, a workflow has recently been developed by the ITER organization [8.41] to transform 5D/6D distributions into 3D CoM (Constants of Motion) distributions. These marker distributions can originate either from Fokker-Planck codes such as ASCOT and NUBEAM, or from experimental measurements. The markers are then projected onto a Cartesian 3D CoM grid, weighted by the Jacobian of the transformation. The CoM Jacobian is computed using the 6D particle pusher developed for the XTOR-K code, a kinetic-MHD code, which calculates the poloidal bounce/transit time at each vertex based on the orbits information. A spline representation is then used for the CoM distributions, which allows a precise computation of their gradients in CoM space, essential for the numerical stability and accuracy of δf codes. This spline representation also enables all first-principles and linear codes to be directly connected to the CoM workflow through a unique input, in order to provide a precise assessment of the stability of EP-driven modes via code benchmark, using a hierarchy of models ranging from quasi-linear to fully gyrokinetic. An example of distribution transformation is provided in Fig. 8.6, using a NUBEAM simulation based on a JET-DT plasma. The trapped contribution is split in co-going and counter-going parts with $\sigma = \pm 1$, to provide smooth CoM distributions across the trapped-passing boundary. The accuracy of such a transformation is currently being tested with highly resolved ASCOT simulations. The CoM workflow is also able to compute the particle angular frequencies in CoM phase space, using the orbits calculated on the Cartesian CoM grid. Such a feature enables the computation of both wave-particle resonance lines and transport coefficient terms in the PSZS theory. A larger number of particle markers is needed for this workflow, the accuracy of the transformation being a function of the CoM grid resolution and of the number of markers per CoM grid cell.

It has recently become possible to selectively probe and reconstruct 3D phase-space distribution functions experimentally, allowing testing phase space transport theories against experimental data. The most developed example of these new techniques is the recent reconstruction of a 3D phase-space distribution function and the 3D phase-space redistribution during a sawtooth crash at ASDEX Upgrade [8.42]. The investigated sawtooth crash transported ions from the plasma center within the q=1 surface towards the periphery outside the q=1 surface. The necessary diagnostic weight functions for such a 3D phase-space inversion have been derived and understood for fast-ion D-alpha spectroscopy (FIDA) [8.42], neutron emission spectroscopy (NES) and gamma-ray spectroscopy (GRS) [8.43] and it has become possible to relate energetic particles measurements by FIDA, NES and GRS to particular regions in 3D phase space [8.43]. These first 3D phase-space diagnostic explorations were done in the coordinates (E, R_m, Λ_m) where E is the energy, R_m the maximum major radius of the orbit, and Λ_m the corresponding pitch value, which are convenient for tomographic inversion and are equivalent to the CoM space coordinates used in this Section. From these works, the phase-space sensitivity of energetic particle diagnostics directly in CoM space has also been fully understood. Typical phase-space sensitivities for different positions of a measurement volume, e.g. of a FIDA diagnostic, and for different detected Doppler shifts in a measured spectrum appear in Fig. 8.7 [8.44], which aid the design of the FIDA system at COMPASS-Upgrade that is currently in progress. The phase-space sensitivity of NES and GRS can be determined for specific measurement volumes or sightlines. Hence, it is possible to selectively probe phase space transport phenomena in CoM space using experimental measurements. Tomographic inversion of the measurement data is also possible [8.42] if at least two FIDA viewing fans with about 10 sightlines each are available, in addition to gamma-ray and neutron emission spectroscopy systems. Such 3D inversions turned out to be difficult, but recently the use of physics informed prior information has become possible, reflecting slowing-down physics in plasmas [8.50]. This cogent prior information likely allows CoM space inversion. Meanwhile, the timely and conscientious investigation of positioning and lines of sight of various diagnostic systems as well as corresponding data acquisition become vital for full exploitation of machine capabilities.

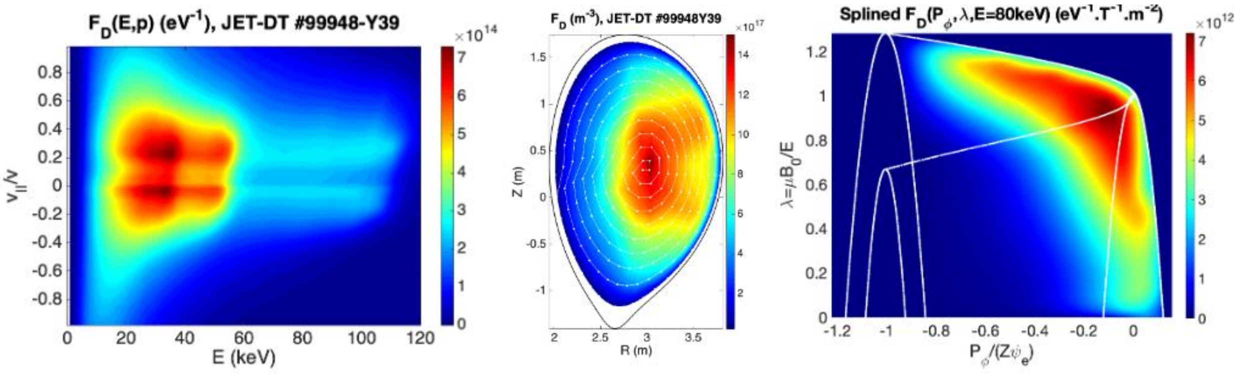

Fig. 8.6: (a-b) NUBEAM distribution function, respectively displayed in the $(E, v_\parallel/v)$ *and* (R, Z) *diagrams. (c) CoM distribution in the* (P_φ, λ) *phase space diagram at E = 80 keV for co-going particles*

Thus, with good diagnostic coverage it will be possible to hold up the theoretical predictions of phase-space flow, such as those made in Figs. 8.4 and 8.5, against experimental data. The need to use prior information to enable a full inversion of the fast ion phase space also applies to DTT. As the device is an advanced superconducting tokamak, we expect that the availability of multiple (or even single, but optimized) lines of sight for each fast ion diagnostic may prove difficult, as the choice of the diagnostics setup for each system will have to be compromised against more stringent engineering constraints as compared to current devices. Under such circumstances, the weight-function based methods outlined above may have a triple role. A first one is that, during the design phase, they can inform on preferred choices for the lines of sight of EP diagnostics within the engineering constraints, and with the aim of covering the largest possible area of the EP phase space by the combined used of the DTT EP diagnostics suite. Once fully designed, a second role comes from the analysis of the actual DTT EP diagnostic systems and their lines of sight, in order to identify which areas of the phase space can or cannot be measured. This will also guide the proposal of experiments to validate EP theory, for example by informing which effects can and cannot be validated by the available set of experimental measurements and, perhaps, highlight the needs for further diagnostics. A third role finally comes from the combined use of numerical simulations and synthetic measurements. For example, we can use numerical predictions of phase-space transport, such as those shown in Figs. 8.2 and 8.3, as cogent prior information and then locate any discrepancy between actual measurements and synthetic measurements based on these numerical predictions in phase space. This technique requires much less experimental data than a full tomographic inversion of the EP phase space, which may perhaps not be viable at DTT, due to the constraints on lines of sight and systems mentioned above. A demonstration of the combined use of predictions and measurements to identify discrepancies with respect to models of the EP dynamics has been made for a 2D velocity space [8.51] and it is expected to work also in 3D CoM space, although its demonstration still needs to be made. An Enabling Research project in 2024-2025 and a Joint

Experiment in the ITPA Topical Group for Energetic Particle Physics to be started in 2024 will further explore these ideas.

As a final remark, it is worthwhile stressing that the EP diagnostic system with its crucial role could/should be harmonized with the likewise crucial fluctuation diagnostic system (see Sec. 4 of Chapter 7 for more details). In fact, simultaneous knowledge of fluctuation spectra and ensuing transport processes are indispensable elements of a modern plasma device for the full exploitation of its capabilities.

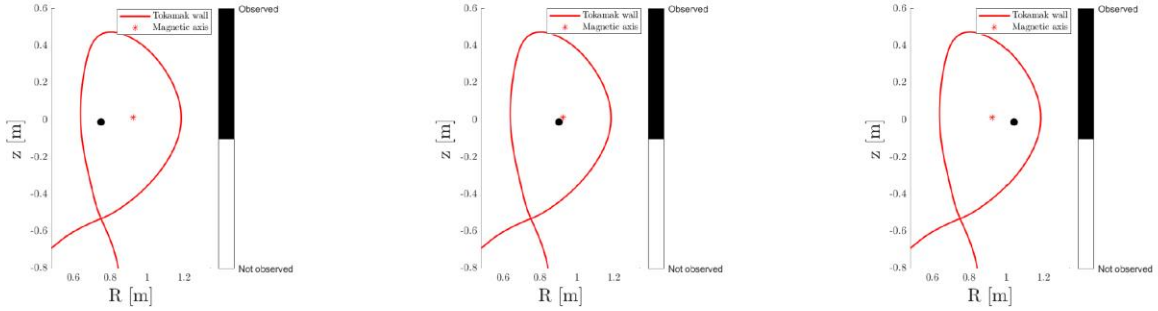

(a) Observe high-field side (b) Observe around magnetic axis (c) Observe low-field side

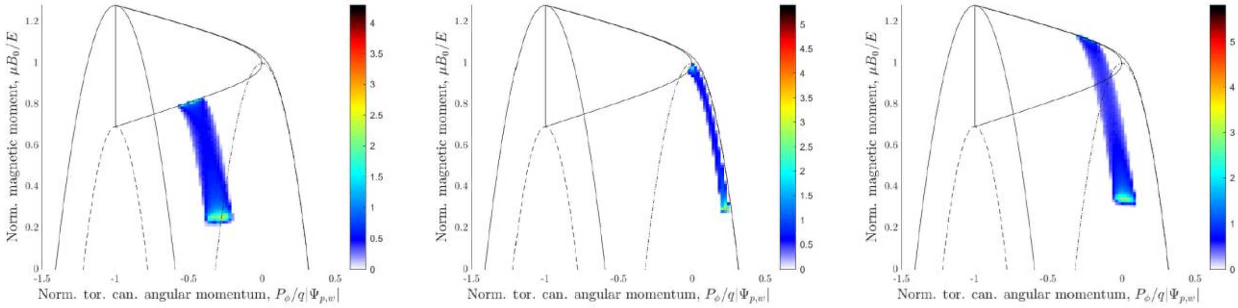

(d) $\varphi = 26.4°, E = 95keV$ (e) $\varphi = 26.4°, E = 95keV$ (f) $\varphi = 26.4°, E = 95keV$

Fig. 8.7: Weight functions for a projected velocity u corresponding to 25.44keV for φ = 26.4, contributing to the ongoing design of the FIDA system at COMPASS-Upgrade. The energy plots shown are all for E = 95keV. The measurement volume in a) is centred around (R = 0.75m, z = −0.01m). The measurement volume in b) is centred around (R = 0.90m, z = −0.01m). The measurement volume in c) is centred around (R = 1.04m, z = −0.01m). Courtesy of M. Rud [8.44]..

8.5 Novel approaches and open problems

As outlined in Chapter 1, due to the significance and uniqueness of the parameters involved, DTT will undertake the formidable task of addressing particle and power exhaust as an integrated problem in conditions relevant to fusion reactors. The primary objective of the project is to investigate the impact of various magnetic configurations in combination with the local divertor radiation to minimize the power directed towards the divertor tiles and to control particle fluxes. This aims at improving our understanding and strategies for effectively managing particle and power exhaust in reactor-relevant plasmas.

Due to the presence of neutral particles, impurities, and relatively cold plasma in the divertor region, an accurate description of the underlying physics processes is essential, but, at the same time, poses several issues that remain open problems. This encompasses a broad range of phenomena, spanning from plasma to atomic physics and addressing interactions among different species (both ionized and non-ionized) and the wall. Despite the inherent complexity, an accurate description of these phenomena is necessary to describe the behavior of the divertor region comprehensively. Choosing the best kinetic description is essential because it will address the particle and power exhaust issues in reactor-relevant conditions with an unprecedented core-edge integration. Meanwhile, the generally used reduced models are based on a hierarchy of equations obtained from the moments (integrals in the velocity space) of the Boltzmann equation, where the closure, i.e., the relation of the highest order moment with the moments of lower order, is given by a model in which the role of collisions is typically considered dominant. To enhance the accuracy of traditional edge turbulence simulations based on these Braginskii-type equations, it is crucial to incorporate theories capable of capturing kinetic effects arising from long mean free path and finite orbit sizes. This is particularly important considering that DTT will operate under high-density and low-collisionality conditions, closely resembling those of ITER and DEMO. By accounting for these kinetic effects, the simulations can better reproduce the complex plasma behavior expected in reactor-relevant plasmas. Various challenges related, for example, to the relative ordering of the characteristic length-scales characterizing the theory, due e.g., to the transition region between closed and open flux surfaces, must be addressed. The general theoretical framework should be continuously refined to advance our understanding of plasma physics in complex fusion devices. Issues that are presently attracting significant interest for the extension of gyrokinetic analysis to the pedestal and edge plasma regions relate to the validity of gyrokinetic ordering in the steep gradient region and with the construction of a fully nonlinear gyrokinetic collision operator.

In plasma conditions relevant to reactors, energetic particles have a significant influence on both turbulent transport between the core plasma region and the plasma edge and the divertor itself, if they are transported without adequately releasing their energy through thermalization. This condition not only affects the efficiency of the self-sustaining process of thermonuclear reactions but may also significantly alter the divertor operational mode, due to the presence of a significant population of supra-thermal alpha particles. Accurately describing these processes requires the use of advanced plasma models, which can still be based on the well-established hierarchy of equations derived from moments of the Boltzmann equation with kinetic closure relations, as proposed in Ref. [8.27]. Similar to the analysis of turbulent transport in the core, the interplay of multiple scales is a crucial aspect of transport in the edge and divertor regions. Furthermore, due to the transition between closed and open magnetic flux surfaces across the separatrix, the radial profiles of the plasma may vary on short scale lengths in the edge region, affecting the separation between macro- and micro-scales.

Various state of the art gyrokinetic codes, such as GTC, GENE, ORB5, etc., are addressing the issue of core-edge coupling using the approach of unstructured mesh to cross the separatrix and efficiently treat both close and open magnetic surfaces in the SOL (Scrape-Off Layer) region. Besides the aforementioned challenges to the gyrokinetic ordering in the steep gradients pedestal and SOL regions, and the necessity of developing a fully nonlinear gyrokinetic collision operator, it is mandatory for nonlinear gyrokinetic codes to develop capabilities to simulate electromagnetic fluctuations in the SOL. Reviewing the state of the art of nonlinear gyrokinetic codes dealing with these problems is beyond the present scope. However, we nonetheless want to mention the potential impact of such studies by recalling the recent results by the XGC1 code [8.45], showing that, even in the electrostatic approximation limit, it is possible to demonstrate that the power fall-off length is significantly broadened [8.46] with respect to the well-known Eich scaling [8.47]. A fully nonlinear electromagnetic global gyrokinetic approach may nonetheless be insufficient to address the complex phenomenology that characterizes fluctuations in the transition region from core to pedestal and SOL regions. In fact, the kinetic behaviour of the low-temperature SOL plasma naturally brings in dependences on fluctuations in the whistler wave range. Meanwhile, reconnection events possibly associated with nonlinear microtearing dynamics near the separatrix may be related with excitations of lower hybrid frequency spectra. These issues naturally call for a hybrid approach such that described in Ref. [8.28], where the GeFi (Gyrokinetic electron Fully kinetic ions) code solves equations for electromagnetic potentials using a moment approach and a fully kinetic description for ions and a gyrokinetic description for electrons. Adopting this theoretical framework may also offer the possibility of using different closures of the same equations, thereby producing a hierarchy or reduced descriptions within the same unified formulation, especially when adopting the GeFi theoretical framework based on $\boldsymbol{E}$ and $\boldsymbol{B}$ fields rather than on the four-potential [8.29]. In fact, in this way, it would be possible to progressively shift from kinetic hybrid, to gyrokinetic, to fluid-kinetic and, finally, to collisional closures. In other words, this would enable to compare the predictive capability of existing numerical tools, such as SOLPS, which are routinely used for ITER modelling, with more advanced approaches with increasingly higher fidelity. For these reasons, this novel approach has a great potential to enable addressing fundamental open problems that DTT will face as focus of its mission.

Since the scaling of EP transport dependence on β_h/β (ratio of EP and thermal betas) is of crucial importance for future burning plasmas, the experimental variation of this ratio around projected values is of great theoretical interest. More specifically, the ratio of EP energies and thermal background temperatures exhibits a sensitive influence on mode stability, saturation levels and EP transport. To this end, DTT as a W-machine will be able to apply similar strategies as other W-devices for reaching burning-plasma-relevant ratios: by allowing a controlled W influx, the thermal plasma β and thus background Landau damping can be reduced while keeping the NBI power and energy maximal. Mode drive and saturation levels have been shown to increase substantially, facilitating dedicated non-linear EP studies with DEMO-relevant parameter ratios [8.48, 8.49]. An additional novel element in these studies are the super-Alfvénic beam energies at DTT that enable mode destabilisation via the primary resonance, i.e., $v = v_{Alfvén}$ being another step closer to burning plasma conditions.

8.6 Headlines of the research programme for theory and simulation

In this section, we summarize the main headlines of the DTT research programme for the theory and simulation subject, according to the various operation phases of DTT.

Headline number	**Headline contents**	**Priority (+,++, +++)**	**ITER**	**DEMO**
Construction Phase 2022-2029				
C.8.1	Verification of Phase 1 scenarios and extended/kinetic MHD modelling with high fidelity theory-based tools. Predict and prepare Phase 1 Experimental programme.	++	*	*
C.8.2	Set up IMAS infrastructure and workflows, e.g. ATEP code	+++		
Phase 1 2029-2034				
1.8.1	Verification of Phase 1 scenarios and extended/kinetic MHD modelling with high fidelity	++	*	*

	theory-based tools. Predict and prepare Phase 2 Experimental programme.			
1.8.2	Validation of IMAS workflows under Low EP (ICRH) Pressures and Currents and scenario optimization	++		
Phase 2 2034-2038				
2.8.1	Verification of Phase 2 scenarios and extended/kinetic MHD modelling with high fidelity theory-based tools. Predict and prepare Phase 3 Experimental programme	+++	*	*
2.8.2	Validation of IMAS workflows description of new EP transport regimes with NNBI and high current and scenario optimization	++	*	*
2.8.3	Development of reduced models for describing DTT's full power EP transport	++	*	*
Phase 3 2038-…				
3.8.1	Verification of Phase 3 scenarios and extended/kinetic MHD modelling with high fidelity theory-based tools. Predict and prepare Phase 3 Experimental programme	+++	*	*
3.8.2	Validation of IMAS workflows with full power plasmas and scenario optimization	++	*	*
3.8.3	Development of reduced models for describing DTT's EP transport	++	*	*

8.7 References

[8.1] https://wiki.euro-fusion.org/wiki/Project_No10
[8.2] https://wiki.euro-fusion.org/wiki/TSVV-10
[8.3] https://www.afs.enea.it/zonca/CNPS/
[8.4] Pizzuto, A., et al. Nuclear Fusion 50.9 (2010): 095005.
[8.5] Kadomtsev B B, 1975 Sov. J. Plasma Phys. 1 295
[8.6] Lackner K, Coster D, Schneider R, and the ASDEX-UPGRADE Team, 1998 Czech. J. Phys. 48 (Suppl. S2) 167
[8.7] Romanelli F et al. 2004 Fus. Sc. Technol. 45 483
[8.8] FAST-Team, Technical Report, ENEA/FPN-FAST-RT-07/001
[8.9] Chen, Liu, and Fulvio Zonca, Nuclear Fusion 47 (2007): 886.
[8.10] Zonca, Fulvio, et al., Plasma Physics and Controlled Fusion 57 (2015): 014024
[8.11] Chen, Liu, and Fulvio Zonca., Reviews of Modern Physics 88.1 (2016): 015008.
[8.12] Guo, et al., NF Fec 2023
[8.13] Lauber, et al., NF Fec 2023
[8.14] Popa, V-A., et al., Nuclear Fusion 63.12 (2023): 126008.
[8.15] Chen, L., Z. Lin, R. B. White, and F. Zonca, Nucl. Fusion 41, 747 (2001).
[8.16] Guzdar, P. N., R.G. Kleva, A. Das, and P. K. Kaw, Phys. Rev. Lett. 87, 015001 (2001).
[8.17] Diamond, P. H., K. Itoh, S.-I. Itoh, and T. S. Hahm, Plasma Phys. Controlled Fusion 47, R35 (2005).
[8.18] Chen, L., and F. Zonca, Phys. Rev. Lett. 109, 145002 (2012).
[8.19] Wang, T., et al., Physics of Plasmas 25 (2018): 062509

[8.20] Wang, T., et al., Physics of Plasmas 26 (2019): 012504
[8.21] Zonca, F., et al., New Journal of Physics 17 (2015): 013052
[8.22] Falessi, M. V., and Fulvio Zonca, Physics of Plasmas 26.2 (2019).
[8.23] Zonca, F., et al., Journal of Physics: Conference Series 1785 (2021): 012005
[8.24] Falessi, M. V., et al, New Journal of Physics 25, 123035
[8.25] Popa, V-A., et al., arXiv preprint arXiv:2306.08442 (2023).
[8.26] Donnel, Peter, et al. Plasma Physics and Controlled Fusion 63.2 (2020): 025006.
[8.27] Chen, Liu, et al, SCIENCE CHINA Physics, Mechanics & Astronomy 64 (2021): 245211
[8.28] Lin, Y., X. Y. Wang, Z. Lin and L. Chen, Plasma Phys. Control. Fusion 47 (2005): 657
[8.29] Chen, L., Y. Lin, X. Y. Wang and J. Bao, Plasma Phys. Control. Fusion 61 (2019): 035004
[8.30] Lauber P., Günter S., Könies A. and Pinches S. 2007 J. Comput. Phys. 226 447–65
[8.31] Pinches, S.D., Comp. Phys. Comm., 111 (1998)
[8.32] Lauber, P. et al., FEC 2023 submitted to NF
[8.33] Falessi, Matteo Valerio, et al., Physics of Plasmas 26.8 (2019).
[8.34] Falessi, M. V., et al Journal of Plasma Physics 86 (5), 845860501
[8.35] Lu, Z., Zonca, F., Cardinali, A. (2012). Physics of Plasmas, 19(4)
[8.36] Wei, G., submitted to Phys. Plasmas (2024).
[8.37] Du, X.D. et al., Phys. Rev. Lett. 127, 235002 (2021).
[8.38] Rueda-Rueda, J. et al., presented at the 29th Fusion Energy Conference, Oct.16-21 (2023), London, UK
[8.39] C. De Piccoli et al., EFTC conference 2023.
[8.40] O. Asunta et al. Computer Physics Communications, 188:33–46, 2015.
[8.41] G. Brochard et al. 29th International Tokamak Physics Activity on Energetic Particles (ITPA-EP), May 2023.
[8.42] Stagner, L., et al. Nuclear Fusion 62.2 (2022): 026033
[8.43] Järleblad, L. et al. Nuclear Fusion 62.11 (2022): 112005.
[8.44] M. Rud et al 2024 Nucl. Fusion in press https://doi.org/10.1088/1741-4326/ad4bf4
[8.45] Ku, S. et al., Phys. Plasmas 25, 056107 (2018)
[8.46] Chang, C. S., Phys. Plasmas 28, 022501 (2021)
[8.47] Eich, T. et al, Nucl. Fus. 53, 093031 (2013)
[8.48] Horváth, L., et al. Nuclear Fusion 56.11 (2016): 112003.
[8.49] Lauber, Ph., et al. The 28th IAEA Fusion Energy Conf.. 2021.
[8.50] Madsen, B., et al., Plasma Phys. Control. Fusion 62 (2020) 115019
[8.51] Salewski, M., et al. Nuclear Fusion 56 (2016) 106024.

Chapter 9

FUSION TECHNOLOGY DEVELOPMENTS

S. Brezinsek, C. Day, G. Dose,
R. Bonifetto, J.W. Coenen, M. Dalla Palma, M. Firdaouss, T. Giegerich, M. Iafrati, M. Missirlian,
S. Peruzzo, M. Richou, M. Wirtz

DTT provides great opportunities for characterising and testing fusion relevant components for heat and particle exhaust for metallic devices such as ITER, DEMO and beyond. This chapter addresses current technology gaps and defines development goals to bridge them. It describes areas in which DTT will be used as enabler to bring to maturity materials and technologies in the fields of plasma-facing materials and components for the divertor and the first wall as well as for fuelling and pumping.

9.1 Introduction

DTT will carry out a complementary fusion technology programme in order to fulfil the holistic goal of developing integrated core-edge scenarios, scalable to reactor-class devices such as ITER and DEMO, where good plasma performances are achieved together with acceptable conditions at the wall, especially with respect to lifetime and safety, and ultimately solving the challenges for the tokamak-based magnetic confinement fusion power plant. The unique capabilities of DTT allow crucial contributions in a plethora of fusion technologies utilising in particular flexibility in the assessment of divertor solutions. As a clear priority, the present chapter will focus on the technology development of plasma-facing components (PFCs) in the divertor and the main chamber, and the systems responsible for heat and particle exhaust, in close relation with the DTT mission. The possibility of a wider technological programme remains for later phases of the experiment. The state-of-the-art plasma-facing components developed for ITER are currently the most challenging, since ITER decided to operate as full-W facility, but cannot be directly extrapolated to a power plant reactor. New plasma-facing materials and design concepts for components compatible to high neutron and particle fluxes are necessary in order to improve the performance and operation stability, as well as increase lifetime in view of future fusion reactors with high duty cycle and high fluence, equivalent to approximately five full-power burning years before components replacement is required. Such new technologies need to be qualified under representative fusion-relevant conditions provided by DTT, such as long pulse, high field, high power density and high plasma density. This aspect, separately for materials and components, is addressed in sections 9.2 and 9.3. In particular, DTT complements the portfolio of metallic tokamaks in Europe and provides unique opportunities for the comparison of different concepts, materials and components in one reactor-relevant device next to the operation of ITER.

The divertor of a fusion power plant does not only have to withstand the high heat loads, it also has to allow for efficient exhaust of particles, neutralised at the target plate, and to ensure stable plasma operation. It is therefore in the scope of DTT as divertor test-bed to provide opportunities for assessing and characterising DEMO-relevant vacuum pumping and fuelling technology and demonstrate solutions. This aspect is addressed in section 9.4.

It is important to note that all experimental work shall be complemented by detailed engineering analysis in order to calibrate and verify tools that then can be reliably employed for scale-up and proper dimensioning of DEMO-like components, as well as to validate procedures and processes.

Finally, the DTT construction by itself offers unique opportunities to learn in view of a future reactor build.

9.2 Plasma-Facing Materials

The heat load expected in reactor components needs the use of materials satisfying requirements of plasma compatibility, structural integrity, and lifetime. Moreover, neutron irradiation and tritium retention conditions shall be complied. Those requirements limit the numbers of suitable candidates for plasma-facing surfaces and structural materials.

Key issues of plasma-facing materials to be addressed are:

- re-crystallisation of tungsten as refractory material with significant reduction in toughness
- narrow operation temperature range for copper alloys as heat sinks (about 250-350 °C for CuCrZr)

- high local stresses due to discrete material interfaces
- not self-healing properties

After testing and qualifying pure W-armoured PFC in WEST and the expected first ITER divertor operation in the early 2030s under tokamak conditions, DTT shall be used at a later stage to test innovative concepts and accompany ITER research. This is why advanced material solutions are currently under development to address the potential issues that can occur in DEMO (cracking, oxidation, thermal fatigue, neutron damage, etc.) or any reactor-like facility. DTT has the unique capability of providing a large area (hundreds of cm² in the divertor, and thousands of cm² in the main first wall) specifically dedicated to material studies at reactor-relevant fluxes of heat and particles as well as at relevant impact energies and plasma conditions. Thereby, the access time to the materials tested in DTT is due to specially designed integrated facilities systems that are short in comparison to present-day steady-state metallic tokamaks.

Candidate advanced tungsten-based armour and heat sink materials, and associated processes to be tested comprise the following list of currently most promising investigated materials for both the divertor and the first wall:

- fiber-reinforced tungsten composites (Wf/W, Wf7Cu)
- tungsten alloys based on nanostructuring
- functionally graded materials (W/Fe, W/Cu) with optimised spatial fraction in order to minimise the local stresses under the plasma exposure
- self-passivating tungsten alloys (W-Cr-Ti, W-Cr-Y)
- porous tungsten (or other refractory material) as self-healing materials (W foam filled with lithium)
- thick tungsten coatings (plasma-sprayed W),
- 3D printed tungsten (latticed W)
- liquid metals (Sn) to prepare a liquid metal divertor solution.

The further development of these materials, currently developed pre-dominantly in the European Research programme (EUROfusion work packages WPMAT, WPPRD, WPDIV), or even new concepts emerging by the time of DTT availability, will have to be combined with thermo-mechanical simulations of plasma exposure (thermal transient and mechanical models also using optimisation algorithms), cyclic heat flux testing of samples and strong interaction with material manufacturers to determine the characteristic material properties.

DTT will be equipped with long-term samples, to be integrated in the first wall, as well as a sample manipulator for short-term exposure. Specially designed divertor and first wall test modules will be made available for dedicated campaign phases, offering the possibility to compare plasma-facing materials solutions under reactor-relevant controlled tokamak conditions next to each other. These experiments will bridge to the research in other laboratory experiments focusing on individual aspects of the qualification, such as high plasma fluence impact (linear plasma facilities), high repetitive heat flux impact (electron beam and ion beam facilities) or neutron-damage aspects (facilities in hot cells). They will close the gaps to the reactor conditions, which only in an integrated manner can be obtained in a magnetically confined reactor itself.

A combination of in-situ measurements, such as spectroscopy, infrared (IR) thermography, laser-induced breakdown spectroscopy (LIBS), laser induced desorption spectroscopy (LIDS), etc. and post-mortem analysis, such as Thermal Desorption Spectrometry (TDS), Nuclear Reaction Analysis (NRA), Secondary Ion Mass Spectrometry (SIMS), LIDS, LIBS metallography, etc. as well as microscopy, such as Electron

BackScattered Diffraction (EBSD) and energy dispersive spectroscopy (EDS), is necessary to characterize the materials and their evolution over the DTT operational phases.

One additional technology gap was found to be on electrical properties of insulating materials under reactor-like environment conditions. A particular aspect for such testing is the in-situ characterization of materials for insulation of plasma-facing components (as necessary for glow discharge cleaning electrodes and in-vessel sensors).

9.3 Plasma-Facing Components

DTT will also provide a test-bed for technologies used in the manufacturing of the PFCs of DEMO. Both divertor and main first wall components will be tested in reactor-relevant integrated scenarios, and at the thermohydraulic condition expected in DEMO or other next-step reactor facilities.

9.3.1 Divertor test modules

Once the technology for building actively cooled components is developed with these materials, an integrated component test has to be carried out. A key role for the confirmation of material choices on the level of a component will be played by the so-called Divertor Test Modules (DTMs), see Figure 9.1. DTMs are cassettes, which are located at privileged locations, directly in front of the ports dedicated to the divertor remote handling at DTT. Therefore, the extraction and substitution of such modules will require the least amount of downtime of the device. Moreover, the divertor water system of DTT is designed to accommodate a dedicated, separated cooling apparatus for the DTMs, which can operate at the coolant conditions of pressurized water reactors (up to 250 °C, up to 15 MPa). The DTMs are the main tool for integrated divertor materials and components testing in DTT.

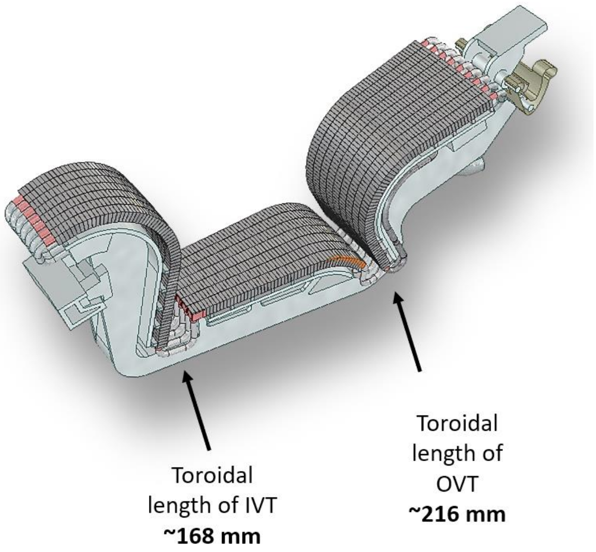

Figure 9.1: Model of a DTM with toroidal dimensions.

Such testing can go from ´only material´ qualifications used for the PFCs, over embedded instrumentation (e.g. integrated in the manufacturing process by 3D printing), up to testing breaking technologies, such as liquid metals for PFC including different designs, but keeping the toroidal symmetry of the device intact. Interesting aspects for instrumented testing categories are

- hohlraum cavities in IR camera view,
- Bragg-fibres,
- interlayers of Mo or Rh for erosion measurements by spectroscopy or LIBS, or
- variable roughness or surfaces structures in visible range (reflection).

In addition to the high power handling capabilities of high heat flux actively cooled divertor components for future machines, thermal loads on the top surface of these components can induce specific issues in case of leading edges. The study of different variants of shaped surface is thus required in order to learn how to best protect leading edges and avoiding overloading in specific areas (e.g. poloidal/toroidal gaps for W-monoblock technology). The experimental data shall be compared with thermo-mechanical calculations and extensive PWI code simulations to extrapolate from the DTT results to the operation point of DEMO. It should be noted that different advanced divertor concepts might have different optimizations, thus flexibility must be ensured if no down-selection of solutions after the first phase of operation will be done.

The integral component testing in a DTM allows also studying joining techniques (e.g. stable joints between /W/Cu/Steel) and manufacturing technologies. A promising novel approach is advanced manufacturing (additive manufacturing, laser sintering/melting, infiltration) which allows complex geometries and transitional structures with control of material microstructure. 3D printing is a potential method for low-cost production of shaped and optimized W components. DTT can act as an integrated test facility at the main chamber and divertor components for this technology, which has high potential to reduce the post-processing and shaping of monoblocks in order to avoid leading edges.

Another key objective of DTT is the testing of pre-damaged components, which is currently outside of the scope of present-day devices operating at high magnetic field. This will allow directly reaching defined and high damage and ageing levels, and to understand limits of acceptability by the impact different damage types have on the associated loss of performance (degradation of the armour material and energy extraction capability of the component). Analyzing the evolution of such defects and their impact is crucial for the engineering design of the components for future devices towards improved lifetime. Many types of damage have to be applied to the components:

- artificial cracks (pre-cracked or damaged by melting events simulated by e-beam/laser/plasma loads),
- interfacial defects,
- irradiation damage simulated by using synchrotron-irradiation (30 MeV) and its combination with other pre-damaging,
- W ion self-damage or proton damage,
- He-induced damage and embrittlement,
- recrystallization (pre-recrystallized tiles and in-situ recrystallization),
- melting/solidification,
- misalignment,
- damage induced by thermal shocks and ELM-like loading (repetitive thermal cycles).

A complementary aspect to the characterisation of pre-damaged components is their performance after repair (molten and solidified, laser repair, in-operando erosion/coating), in order to demonstrate the whole lifecycle of such a component. In this context, additional to ex-situ repair, DTT offers the opportunity to develop and test an in-situ repair system.

A second DTT divertor is also planned to be installed. The first divertor design in DTT is optimized for a single null configuration, but it is also compatible with a number of different magnetic equilibria (XD, DN, NT) at reduced maximal plasma current. However, DTT shall ultimately be used to operate the best performing optimized divertor solution. The selection shall be done in conjunction with alternative divertor research and DEMO compatibility studies within the European research programme and beyond. A roadmap for decision shall be included to give timely input. This needs to be correlated with the DTT divertor physics programme.

According to the ITER Research Plan, a second divertor for ITER is foreseen after few years into the Fusion Power Operation (FPO) phase (DT operation). Design-to-manufacturing will require a minimum of ~ 7 years. Consequentially, the design activities for the ITER second divertor would begin when DTT is in its Phase 3, being the only European tokamak that will have plasma parameters relevant for ITER while providing a P/R ~ 15 MW/m, as needed to test PFCs for ITER. DTT can then be a test-bed for the technology of the second ITER divertor and its behaviour in a tokamak environment (PWI, toroidal shaping, assembly, thermal fatigue, etc.).

9.3.2 Thermohydraulics

The DTT PFCs come with a complex active cooling structure. It is a unique opportunity to develop detailed thermal and thermohydraulic models of the DTT plasma-facing systems. Both the (nominal) plasma operation and selected accidental transients (disruption with runaway electron generation, …) will be investigated. For validation of the models, the numerical results of the predictions (temperature distribution, local melting of the plasma facing materials) will be compared to the measurements during DTT operation to validate (and if necessary improve/calibrate) the models. The essential benefit of this is twofold. Firstly, it provides the possibility to use the thermal models to estimate the real thermal loads on the DTT plasma facing materials (only then, the results of the DTM tests can be interpreted properly). Secondly, the validated thermal models are available for upscaling to DEMO and power plant level, and deriving the correct cooling strategy. It can also serve as test case to learn to which extent the full model (FEM representation of the conservation equations) can be simplified to lumped-parameter models.

Suitable diagnostics must be added to the DTT machine, allowing the measurement of the surface temperature distribution (by cameras) and temperature sensors at selected relevant locations also in the bulk material and coolant flow.

The comparison between numerical predictive simulations and the measurements will allow identifying possible weak points in the models. In that case, the modelling issues will then be fixed to finally have a reliable, validated model. The latter will be applied to predict the behaviour of the EU DEMO plasma facing components, according to their design and the nominal heat loads and operation, possibly suggesting improvements in their geometry, material or cooling design.

9.3.3 First wall module

DEMO will be equipped with blanket modules, covered with actively cooled PFCs made with EUROFER97 as heat sink material and thin W as plasma-facing material. Such a design has been tested by manufacturing at medium scale only. DTT has the capability to install full-scale DEMO blanket modules (which have a toroidal extension of ~1.5 m) if put along the poloidal direction. Therefore, DTT can be used as test-bed for the comprehensive validation of PFCs having such a dimension. This comprises DEMO relevant steady state radiative loading (0.5 – 1 MW/m²), thermal shocks (~100 MW/m² over some 10 ms) and compatibility with the plasma environment (fuel retention, erosion, etc.). In particular, the latter plasma-wall interaction aspects are of high interest to validate a) the W layer thickness and W deposition technology to ensure the required lifetime and b) quantify the D transport in the W and structural material. In particular, also components with pre-damage (self-damage and He implantation) simulating different phases of reactor wall lifetime and neutron doses can be tested to study the power handling and fuel retention. In principle also advanced first wall material concepts, e.g. with self-passivating alloys to prevent LOCA (loss of coolant accident) damages can be studied in a later phase.

It is therefore planned to utilize one single first wall module as a test bed for a DEMO first wall mock-up. For this purpose, a dedicated cooling circuit shall be allocated to such a module, reflecting the choice of the blanket cooling concept that will be eventually selected by the DEMO design team, such as water-cooled lithium lead (WCLL) or Helium cooled pebble bed (HCPB). Due to the design choices that still have to be made, as well as the need of DTT to be at its full-power capabilities to provide the proper loading, such experimental campaign has to be planned in the later stages of Phase 3.

9.4 Matter control

Matter control is a critical aspect of tokamak operation, especially for the divertor. Ad hoc actuators are being developed for DEMO, due to its specific needs and performance space. DTT shall provide a test-bed for the technologies foreseen for a fusion reactor, or alternatively investigate different solutions to mitigate the risk (see Figure 9.2). In the following, we specifically refer to the EU DEMO design concepts.

9.4.1 Fuelling

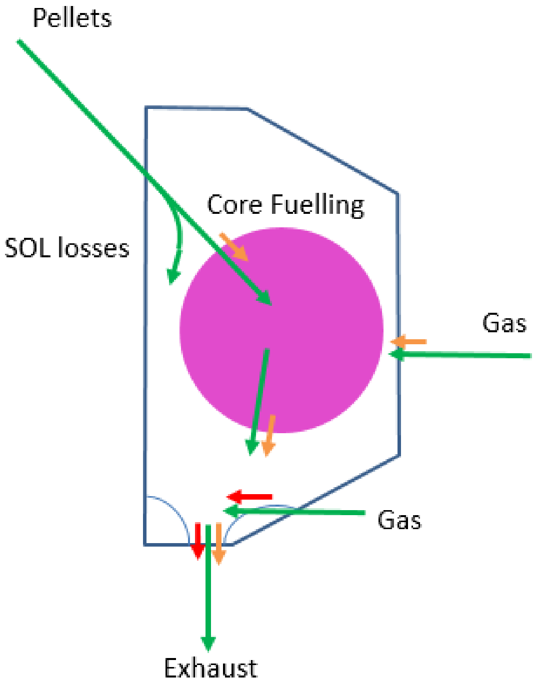

Figure 9.2: Illustration of the matter actuators.

DEMO requires a high speed, repetitive (of the order of 10 Hz), continuous, very accurate and reliable pellet injection system for various fuelling tasks, in particular density control of the plasma core. Core fuelling is a function that, on the scale of a high-energy reactor plasma, cannot be provided by gas injection. A number of concepts are under discussion. Due to deuterium-tritium fuel cycle implications, the chosen reactor scale acceleration concept of the pellet injection system will be based on a centrifuge [9.1]. Such a system is definitely first-of-its kind. While existing pellet injectors (such as at JET) were relying on component delivery from outside EU, the running EUROfusion programme is developing a novel purely European design of a reactor relevant pellet injection system [9.2]. DTT will also install a pellet launching system for core density control from the high field side and potentially ELM pacing. In view of the low maturity of the DEMO technologies, it is still under discussion, which technologies DTT will opt for. Due to the risks of the DEMO pellet injection concept, but also to mitigate risks of the chosen DTT pellet launching system, it is proposed to develop the two concepts (DEMO and DTT) synergistically together, so that – in case unforeseen showstoppers turn up – one can as quickly as possible change over to the other technology. To enable this, DTT will evaluate the operational limits of the DTT pellet system in view of a potential DEMO application.

In this context, DTT is planned to test the technology performance of an advanced design of the new EU pellet launching system, which will become available by 2027. Such a design will already represent the second generation of this development, which starts in 2026 with a principle validation in the EU pellet test-bed in the fuel cycle test facility DIPAK located at KIT [9.3]. The operation of the system will rely on cryocoolers, so that there is no interface to the DTT cryoplant. Such testing is aiming at demonstrating the technology of the system, for which it will come with its own integrated set of diagnostics. For studies of the interaction of pellets and plasma, the setup would make use of the existing DTT infrastructure.

The DTT Phase 1 starting in 2029 goes also very well together with the operation of the pellet launching system in JT-60SA Phase OP2 in 2026 [9.4]. The comparison between the JT-60SA and the DTT systems will allow investigating not only pellet injection technology characteristics, but will add the opportunity to study injection physics with two different technologies on the scale of a real plasma.

9.4.2 Pumping

To reduce tritium inventory, DEMO is using continuous vacuum pumps for divertor pumping, comprising customized vapor diffusion and liquid ring pump technology, together with a metal foil pump as primary pump. These are first-of-a-kind technologies that ask for a strong maturation programme [9.5]. While the vapor diffusion and ring pumps can be representatively tested in other facilities, this is not completely possible for the metal foil pump. In particular, the operation of the pump under non-uniform external magnetic fields is a potentially critical issue that needs investigation, as well as final confirmation that possible performance losses are acceptably small [9.6]. DTT will install a test metal foil pump in or attached to a divertor port (ports # 4 or 5), to gain operational experience in view of later operation at DEMO.

Ideally, the design and size of the test metal foil pump is very close to that of the DEMO pump, illustrated in Figure 9.3. The metal foil pump is a static pump that does not require an operating fluid, but needs just electric power and cooling, so that it can be easily integrated in DTT. The metal foil pump technology is considered to be transformative for the fuel cycle, so that DTT could provide a unique impact contribution.

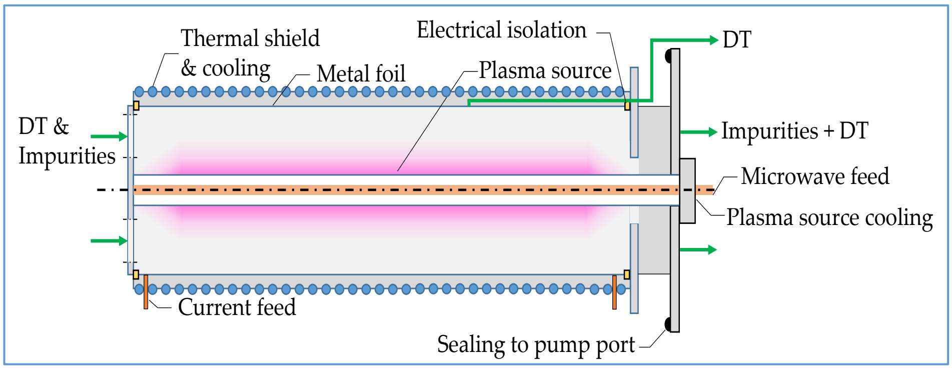

Figure 9.3: Concept design of the DEMO metal foil pump .

Another objective of DTT will be the investigation of a variable pumping speed on divertor performance. The divertor pumping system is the main actuator to influence the pressure field in the sub-divertor volume and with this the particle exhaust performance of the divertor itself. However, such influence of the pumping speed of the divertor pumping system has never been studied parametrically in a high-density tokamak experiment. The supporting modelling suffers from the fact that the collisionality of the neutral gas flows is difficult to describe. From other machines, it is well known that predictions of the particle fluxes/divertor neutral pressures are often up to an order of magnitude lower than the measurements indicate. It is hence considered an absolute necessity to improve the modelling capability in order to better agree with experimental data and to reach full predictive capability.

The DTT divertor pumping system is based on nine identical cryogenic pumps located in the lower vertical ports, as shown in Figure 9.4. It is planned to build them in such a way that they can be switched on and off in groups. DTT will perform a parametric set of experiments with variable pumping speed under different densities (fuelling rates) in order to provide the experimental baseline to validate a predictive modelling tool for the sub-divertor. Pumping speed reduction will also add asymmetry to the flow pattern, the measurement of which can be used to validate the 3D modelling capability of a sub-divertor neutral gas code (in particular DIVGAS [9.7]). Such a tool is absolutely essential for the transfer of the DTT divertor design (pumped by a cryopumping system) back to the DEMO environment, where a different pumping system will be employed. DIVGAS is seen as a main tool to develop a metric usable to judge requirements coming from divertor particle exhaust.

This activity is utilizing the as-installed cryopumping system. In order to produce most relevant data, this activity benefits from the planned rich divertor neutral (and partial) pressure diagnostic set.

Part of an effective solution for the power handling capability in a fusion reactor will mandatorily comprise the development of a robust scheme for real-time divertor detachment control, to make sure to dissipate the thermal power coming from the plasma, and to avoid damage in the divertor PFCs. Proper actuators must be implemented, able to provide a timely response of the control system. DTT will be equipped with a divertor gas injection system, which is traditionally used in tokamaks. However, on DEMO scale, the achievable timescales for divertor buffering of 0.1s to > 1s might be too slow to react on disturbances from the plasma, especially during ramp-up and ramp-down. As a risk mitigation strategy, DTT shall investigate alternative actuators and qualify for their requirements during detachment control and during ramp-up [9.8]. Candidate technologies are supermolecular beam injection (SMBI) and micro shattered pellet injection (MSPI), another novel first-of-a-kind approach. DTT is providing the perfect environment for their validation under relevant operation conditions. While the SMBI does only ask for gas piping, the MSPI would have to be installed close to the divertor area (i.e. to some ten metres distance). This installation requires some infrastructure (power supply and cooling water for cryocoolers, hydrogen, helium and seeding gas supply, control system interface) and the usual divertor diagnostics (e.g. Thomson Scattering, Langmuir probes or spectroscopy). The footprint of this system is ~3 m² (without infrastructure and cubicles that can be located further away).

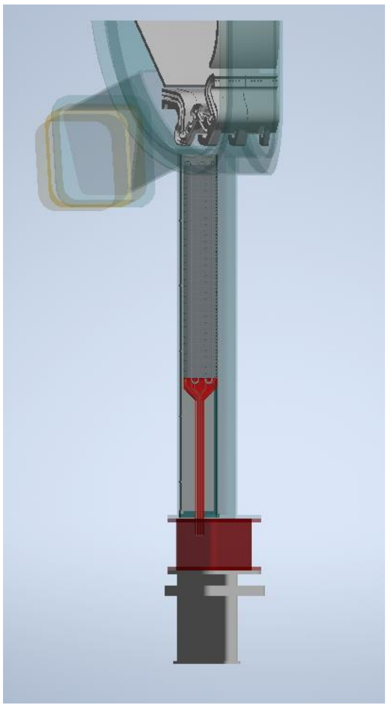

Figure 9.4: Vertical port with cryopump..

In parallel to the experimental validation activities, a modelling campaign should be performed. This allows not only validation of the technical system but also the validation of modelling tools for the divertor plasma control loop, which are not yet available for the time being, and for the neutral rarefied gas flows.

9.5 Headlines of the research programme for fusion technology

In this section, we summarize the main headlines for topics related to fusion technology, indicating the relevant time frames and relating them with the ITER and DEMO projects.

Headline number	Headline contents	Priority (+, ++, +++)	ITER	DEMO
Construction Phase 2022-2029				
C.9.1	Develop and utilize modelling tools for advanced materials under cyclic load conditions, in order to identify sets of materials and conditions for testing	++	*	*

C.9.2	Develop, design and integrate a specific set of observation systems (IR, UV-VIS spectroscopy, thermocouples etc.) for the DTM and FW module in the portfolio of DTT diagnostics	+++	*	*
C.9.3	Prepare an initial set of components reflecting the first divertor material selection for DTT divertor	+++	*	*
C.9.4	Establish and integrate the specific test environment for material and components testing in DTT (DTM, FW module)	+++	*	*
C.9.5	Establish and integrate a specific test environment and infrastructure in DTT for fuelling and pumping tests	+++	*	*
Phase 1 2029-2034				
1.9.1	Commission DTM and associated diagnostics. DTM equipped with standard DTT divertor materials for reference	+++	*	*
1.9.2	Integrated PFC and material testing (different sets) using the DTM at basic power and particle fluxes	+++		*
1.9.3	Assess performance of the first set of advanced materials and components in DTM. Comparison with DTT standard divertor materials and components.	+++	*	*
1.9.4	Calibrate thermohydraulic models of actively cooled PFCs	+++		*
1.9.5	Commissioning of fuelling and pumping test components	+++		*
1.9.6	Validate the launching performance of the DEMO pellet injection system	+++		*
1.9.7	Validate the performance of a test metal foil pump in a representative tokamak environment	+++		*
1.9.8	Extract the gas supply requirements for stable control of the DEMO SN divertor	+++		*
1.9.9	Provide parametric variation of divertor pressure (pumping speed, fuelling rate) with corresponding plasma simulation cases to benchmark particle exhaust conditions with the DIVGAS code	++	*	*
Phase 2 2034-2038				
2.9.1	Integrated plasma-facing component and material testing (different sets of advanced concepts) using the DTM at elevated power and particle fluxes	+++		*

2.9.2	Assess performance of applied sets of advanced materials and components in DTM. Selection of the second divertor components solution for DTT.	++	*	*
2.9.3	Commission FW module and associated diagnostics. FW module equipped with one standard DTT first wall material for reference.	++		*
2.9.4	Characterise a FW module equipped with different plasma-facing materials made of W	++		*
2.9.5	Explore the engineering limits of DEMO relevant fuelling and pumping technology	++		*
Phase 3 2038-…				
3.9.1	Integrated component testing and qualification in DTM at maximum power and particle fluxes and at high fluence, mimic reactor conditions.	+++		*
3.9.2	Integrated component testing and qualification in FW module at high fluence, mimic reactor conditions	++		*

9.6 References

[9.1] P.T. Lang et al., Fusion Engineering and Design 185 (2022) 113333.
[9.2] B. Ploeckl et al., Fusion Engineering and Design 199 (2024) 114142.
[9.3] J. Ayllon-Guerola et al.,European machine enhancements for the JT-60SA tokamak, AAPPS-DPP23 Conference, Nagoya, Japan, Nov. 2023.
[9.4] C. Day et al., Fusion Engineering and Design 179 (2022) 113139.
[9.5] Y. Kathage et al., Plasma 6 (2023) 714-734.
[9.6] C. Tantos et al., Nuclear Fusion 64 (2024) 016019.
]9.7] C. Day, L.R. Baylor, Plasma Physics and Technology Aspects of the Deuterium-Tritium Fuel Cycle for Fusion Energy, IAEA TecDoc (2024).

Appendices

APPENDIX A: DTT parameters

Table A.1. Main DTT parameters (scenario E)

Major radius (m)	2.19
Minor radius (m)	0.7
Volume (m^3)	35
Plasma current (MA)	5.5
Toroidal field (T)	5.85
Elongation at separatrix	1.78
Triangularity at separatrix	0.45
Line-averaged electron density (10^{20} m^{-3})	1.5
Total injected power (MW)	45
ECRH power (MW)	29
ICRH power(MW)	6
NBI power (MW)	10
Pulse length (s)	100

Table A.2. DTT physics parameters

P_{sep}/R [MW/m]	15
β_N [%]	1.6
ρ^* at mid-radius [10^{-3}]	3.8
ν^* at mid-radius [10^{-2}]	1.2
ρ^* at pedestal [10^{-3}]	2.7
ν^* at pedestal [10^{-2}]	5.0
Fast particles ρ^* [10^{-2}]	2.4
Fast particles β [10^{-2}]	1.0
q_{95}	3.0
Greenwald density [10^{20} m^{-3}]	3.6
Energy confinement time (s)	0.4

Here the reference orientations of the toroidal magnetic field, of the plasma current, and of the NBI are defined. These references are introduced in connection with the general reference system of the machine and, in particular, with the direction of the Z-axis (reference). **Note that the directions of I_p and B_T can be changed depending on the plasma scenarios.**

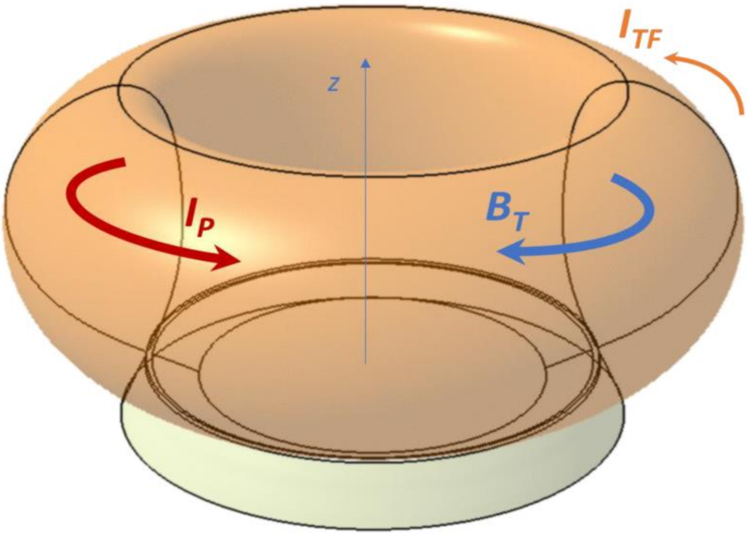

Figure A.1: Field and currents orientation.

	Reference orientation with respect to the Z-axis
Toroidal Magnetic Flux density	clockwise when seen from above
Plasma current	counter-clockwise when seen from above
NBI	counter-clockwise when seen from above

APPENDIX B: DTT tokamak description

In this Appendix, the main parameters of the DTT tokamak are presented in a series of tables.

Toroidal Field coils

Parameter for TF coils	
SC material adopted	Nb_3Sn
I_{op} (kA)	42.5
B_{peak} (T)	**11.9**
Number of modules	18
Casing material	316LN
TF module mass [kg]	15000 (excl. Gravity supports)
Nominal max ripple	2.9e-3
Number of turns per module (3 regular DP + 2 side DP)	3x(9x2)+2x(9+6)=84
Conductor size [mm x mm]	28.9 x 22,2
Conductor void fraction	26.4%
Conductor strands	480 Nb_3Sn + 180 Cu
Max terminal to ground voltage [kV]	5.8
DC test [kV]	10
Min T_{margin} (K)	>1.2
sDP max & rDP hydraulic length [m]	110
sDP short hydraulich length [m]	72
Mass flow rate per module [g/s]	40
He inlet temperature [k]	4.3
He inlet pressure [bar]	5.4
Turn insulation (fiberglass) [mm]	1.0
$\tau_{discharge}$ [s]	5
Max holding time before discharge [s]	1.5
Max voltage	
J_E on conductor (A/mm^2)	**67**
J_E on WP (A/mm^2)	**56**

Poloidal Field coils

Parameter for PF1/6 coils	
SC material adopted	Nb3Sn
Max I_{op} (kA)	28.3
B_{peak} (T) (self field)	**9.1**
Number of pancakes	4 QD + 1 DP
Number of turns	360
mass [kg]	15000 (excl. supports)
Conductor size [mm x mm]	29.1 x 22.7
Conductor void fraction	29.8%
Conductor strands	180 Nb_3Sn + 216 Cu
Min T_{margin} (K)	>1.8
hydraulic length [m]	180
Ave. radius – width [mm]	1400 – 510
Distance from tokamak equatorial plane – height [mm]	2760 – 590.4

Parameter for PF2/5 coils	
SC material adopted	NbTi
Max I_{op} (kA)	27.1
B_{peak} (T) (self field)	**4.2**
Number of pancakes	8 DP
Number of turns	160
mass [kg]	18000 (excl. supports)
Conductor size [mm x mm]	28.6 x 25
Conductor void fraction	27.9%
Conductor strands	162 NbTi + 324 Cu
Min T_{margin} (K)	>1.9
hydraulic length [m]	190
Ave. radius – width [mm]	3079.5 – 279
Distance from tokamak equatorial plane – height [mm]	2534 – 516.8

Parameter for PF2/5 coils	
SC material adopted	NbTi
Max I_{op} (kA)	27.1
B_{peak} (T) (self field)	**4.2**
Number of pancakes	8 DP
Number of turns	160
mass [kg]	18000 (excl. supports)
Conductor size [mm x mm]	28.6 x 25
Conductor void fraction	27.9%
Conductor strands	162 NbTi + 324 Cu
Min T_{margin} (K)	>1.9
hydraulic length [m]	190
Ave. radius – width [mm]	3079.5 – 279
Distance from tokamak equatorial plane – height [mm]	2534 – 516.8

Central Solenoid coils

Parameter for CS coils	
Number of modules	6
SC material adopted	Nb_3Sn
Max I_{op} (kA)	34
B_{peak} (T) (self field)	**13.6**
Required magnetic flux [Wb]	16.2
mass [kg]	50000 (excl. supports)
Min T_{margin} (K)	>1.0
Max radius [mm]	755

In-vessel coils

Parameter for **not-axisymmetric coils**	Nominal value
Number of not-axisymmetric coils	9 (top) + 9 (equat.) + 9 (bottom) =27
Turns (top – equatorial - bottom)	16 – 20 – 20
Conductor type	ASDEX-U like conductor
Conductor size (copper diameter and hole) [mm]	16 - 9
Nominal max voltage [V]	400
Maximum current [kA]	2,5
Frequency range [Hz]	1-10
Operation mode	Steady state (error filed correction) + pulsed (ELMs correction)

Parameter for **divertor coils**	Nominal value
Number of divertor coils	3
Turns (minor radius – central – major radius)	7 – 12 – 12
Conductor type	ASDEX-U like conductor
Conductor size (copper diameter and hole) [mm]	16 - 9
Nominal max voltage [V]	500-600
Maximum current [kA]	5
Frequency range [Hz]	1-10

Parameter for **stabilization coils**	Nominal value
Number of stabilization coils	2
Turns (upper – lower)	20
Conductor type	ASDEX-U like conductor
Conductor size (copper diameter and hole) [mm]	16 - 9
Nominal max voltage [V]	4000
Maximum current [kA]	6
Frequency range [Hz]	1-1000

Cryoplant

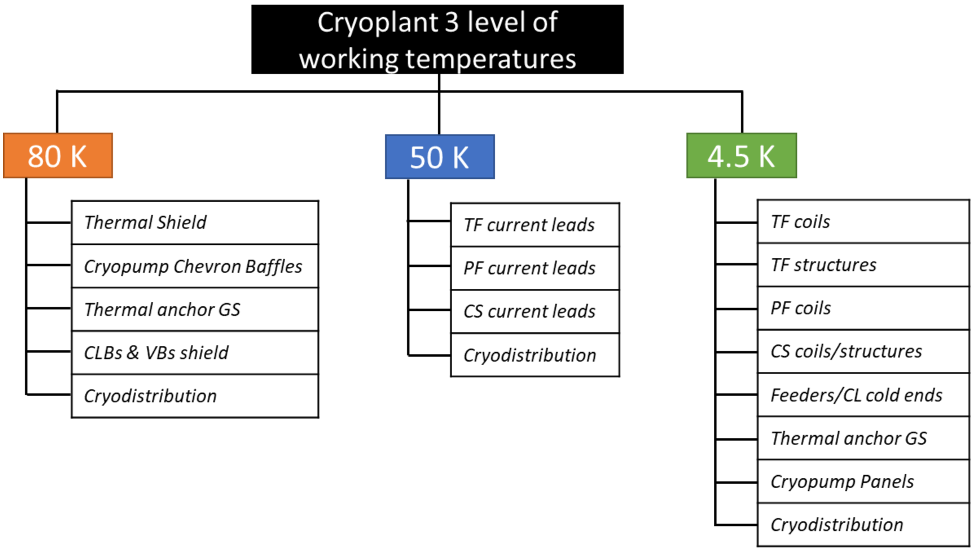

80 K User	Required heat load (W)	NOTES	P_{inlet} (bar)	P_{outlet} (bar)	T_{inlet} (K)	T_{outlet} (K)	Flow rate (g/s)	Heat load (W)	Eq. Heat Load @4.5 (W)	Pressure Eq. Load @4.5 (W)
Thermal Shield	30900	Estimate based on old CAD model, only radiation. Data to update	15	13	80	100	297	30900	1109	407
Cryopump Chevron Baffles	3770	Data based on preliminary design. Conduction not considered	15	14	80	100	45	4458	161	30
Thermal anchor GS	1800		15	14	80	90	45	2343	91	30
CTBs & VBs shield	4000	Preliminary estimate	15	14	80	100	56	5840	209	37
Cryodistribution	950	Preliminary estimate (n. of valves, pipes layout to be defined)								
TOTAL	**41420**									

50 K User	Required flow rate (g/s)	NOTES	P_{inlet} (bar)	P_{outlet} (bar)	T_{inlet} (K)	T_{outlet} (K)	Flow rate (g/s)	Heat load (W)	Eq. Heat Load @4.5 (W)	Pressure Eq. Load @4.5 (W)
TF current leads	18.95	Conservative estimate based on correlations available in literature and considering peak current	4	1	50	300	18.95	24605	1638	947
PF current leads	24.97		4	1	50	300	24.97	32422		
CS current leads	27.95		4	1	50	300	27.95	36291		
Cryodistribution	Negligible									
TOTAL	***71.87***							***93318***		

4 K User	Load per cycle (pulsed) (kJ)	Average power (POS+DWE) (W)	NOTES	P_{inlet} (bar)	P_{outlet} (bar)	T_{inlet} (K)	T_{outlet} (K)	Flow rate (g/s)	Heat load (W)	Eq. Heat Load @4.5 (W)	Pressure Eq. Load @4.5 (W)
TF coils	2100	576		5.4	4.2	4.3	4.7	540	594	817	260
TF structure	1823	506		5.4	4.2	4.3	5.54	180	1098	978	166
Thermal anchor GS (6 K)		450									
TF feeders		300		5.4	4.2	4.3	5.1	105	327	316	87
PF coils	1552	430		5	4	4.3	4.65	485	484	650	202
CS coils	748	210	Loads are estimated from old design version of CS coils	5	4	4.3	4.63	255	232	322	104
PF/CS Feeders		300		5	4	4.3	5.54	48	309	274	39
Cryopump panels		150	Conduction not considered	5	4.5	4.5	4.8	180	195	214	40
Cryodistribution		270	Preliminary estimate (n. of valves, pipes layout to be defined)	5	4.5	4.5	4.8	180	195	214	40
TOTAL		***3192***									

Heat loads during POS

LOOP	Utilities	DP (bar)	$\dot{m}$ (g/s)	T_{in}/T_{out} avg (K)	Eq. Heat load @4.5K (W)	Eq. pressure drop load @4.5K (W)	Circulator dissipation load @4.5K (W)	Total equivalent load @4.5K
1	- TF WP - TF case + thermal anchor - TF feeders	1.2 (5.4-4.2)	825	4.3/4.98	2170	513	1088	**3771**
2	- PF coils - CS coils - PF feeders - CS feeders	1 (5-4)	788	4.3/4.72	1277	348	866	**2491**
3	- Cryopanels	0.5 (5-4.5)	180	4.5/4.8	214	40	-	**254**
4	- Thermal shield - Cryop. chevron baffle - Th. Anchor GS TF + VB/CTB thermal shield	2 (15-13)	443	80/100	1655	606	-	**2261**
5	- CL TF - CL PF - CL CS	3 (4-1)	71.87	50/300	1638	947	-	**2585**
			48	50/300	1094	632	-	**1726**
				TOTAL	**11362 W** **10503 W (lower $\dot{m}$ on CL)**			

Heat loads during STS

LOOP	Utilities	Average heat load during POS (W)	Average heat load during STS (W)		DP (bar)		$\dot{m}$ (g/s)		T_{in}/T_{out} avg (K)		Total equivalent load @4.5K	
			TFC ON	TFC OFF								
1	- TF WP - TF case + thermal anchor - TF feeders	1952	**1240**	**820**	1.2 (5.4-4.2)	0.5 (5-4.5)	825	300	4.3/4.98	5/5.5	**3771**	**1020**
2	- PF coils - CS coils - PF feeders - CS feeders	1055	**727**		0.5 (5-4.5)		300		5/5.5		**1020**	
3	- Cryopanels	185	**<185**		0.5 (5-4.5)		180		4.5/4.8		**254**	
4	- Thermal shield - Cryop. chevron baffle - Th. Anchor GS TF + VB/CTB thermal shield	41420	**41000**		2 (15-13)		443		80/100		**2261**	
5	- CL TF - CL PF - CL CS	93318	**51935**		3 (4-1)		71.87		50/300		**2585**	
					TOTAL		**7140 W (TFM off)**					

Vacuum vessel

Parameter	Expected value
Torus vacuum pressure [Pa]	<1.0E-6
Cryostat vacuum pressure [Pa]	<1.0E-3
Leak rate of the individual vessel multi-sector specified for both inter-shell volume and plasma side volume [Pa m^3 s^{-1}]	<1.0E-9
Leak rate of the individual port assembly [Pa m^3 s^{-1}]	<1.0E-10
Leak rate of the inter-ply of the individual bellows [Pa m^3 s^{-1}]	<1.0E-10
Local leak rate [Pa m^3 s^{-1}]	<1.0E-10
Vacuum Vessel operational temperature range [°C]	20-110
Baking temperature [°C]	240
Number of manufactured sectors	3 (2 x 170° + 1 x 20°)
Number of ports	82
Number of gravity supports	6
Nominal distance of inner leg surface from tokamak vertical axis [mm]	1400
Overall diameter (incl. Ports) [mm]	11108
Overall height (incl. Ports) [mm]	9298
Weight of main vessel body [kg]	36900
Volume of the shielding water [m^3]	13.5
Volume of the VV – plasma side [m^3]	99.7
Mass flow rate of the shielding water [kg/s]	20
Water pressure [Mpa]	0.4
Nominal temperature [°C]	60
Strong baking temperature with Nitrogen [°C]	Up to 200 (165 for ducts)
Light baking temperature with water [°C]	Up 110

APPENDIX C: ASTRA time dependent simulations of various plasma scenarios at reduced power, field and current

In this Appendix details are provided of the methodology used for the time dependent simulations carried out with the ASTRA transport code [C.1, C.2], whose results for the full power, full field and current scenario E are described in Section 2.6. We also provide here the results of ASTRA simulations for other scenarios at reduced power, field and current, namely scenario A, C and E at half field/half current, high β_N.

C.1 Simulation methodology

ASTRA is coupled with the TGLF-SAT2 [C.3] quasilinear model for the turbulent transport, the NCLASS [C.4] model for the neoclassical calculations, the FACIT [C.5] routines for the calculation of the neoclassical transport coefficients of the impurity densities and the IMEP [C.6] routines for the calculation of the H-mode pedestals. The simulations cover the whole confined plasma radius, up to the separatrix and are time-dependent. The evolution of the whole plasma discharge, from the early ohmic limiter phase up to the H-mode flat-top phase, is simulated. All the different phases (L-mode, L-H transition and H-mode) are treated in a single simulation, with the plasma parameters at the L-H transition determining the H-mode pedestals. The electron temperature T_e, the ion temperature T_i, the electron density n_e, the impurity densities, and the plasma current density j_p are predicted in these simulations.

The time-dependent plasma boundaries are calculated by the nonlinear solver of CREATE [C.7] and prescribed in the ASTRA simulations. The plasma equilibrium is calculated self-consistently using the SPIDER [C.8] (or the equivalent FEQUIS [C.9]) routines. The heating power deposition profiles are calculated as follows: for the NBI power deposition RABBIT is used [C.10]; Gaussian profiles are used for the ECRH power deposition; for the ICRH power deposition profiles both Gaussian profiles and PION [C.11] simulations are used, depending on the scenario. The choice of using Gaussian profiles for the ECRH is dictated by the need of simplifying, since a calculation of the time-dependent values of the ECRH gyrotrons angles throughout the ramp-up would be required for using the TORBEAM [C.12] routines. The radial position of the peak of the Gaussian and the Gaussian width have been adjusted to be similar to the ECRH deposition profiles obtained in JINTRAC runs [C.13]. The simulations cover the whole plasma radius, with the boundary at the plasma separatrix (i.e. at $\rho_{tor} = 1$, where $\rho_{tor} = \sqrt{\Phi/\Phi_b}$, Φ being the toroidal magnetic flux and Φ_b being its value at the separatrix). The values of T_e at the separatrix are calculated using the 2-point model [C.14]; the boundary value of T_i is imposed to be 1.1 T_e; the value of boundary n_e is imposed to be $0.4 \cdot \overline{n}_e$, where $\overline{n}_e$ is the line-averaged density.

At the L-H transition, that is reached once the power crossing the separatrix (P_{sep}) is above the power threshold predicted by the Martin scaling [C.15] (P_{LH}), the IMEP routines are called for the calculation of the plasma pedestal. The calculation of the pedestal is then repeated every time the power crossing the separatrix is increased by 20%. After the L-H transition, the boundaries for the evolution of temperatures and electron density is moved to $\rho_{tor} = 0.9$, with the pedestal profiles calculated by IMEP fixed outside this radius. The profiles of the plasma current and of the impurity densities are calculated on the whole plasma radius even after the L-H transition.

A feedback control of the line-averaged density is obtained, during the phases prior to the L-H transition, through a feedback control on the influx of the neutral particles at the separatrix (similar to what it is done in [C.16]), a method that resembles the gas puff control in experimental conditions. The line-averaged density is kept proportional to the Greenwald density limit [C.17], $n_G = I_p/(\pi \cdot a^2)$, this meaning that it evolves proportionally to the plasma current. At the L-H transition, the IMEP routines consider the plasma parameters self-consistently for the calculation of the pedestal, the only free parameter being the neutral particles density influx at the separatrix ($S_{n,sep}$). The value of $S_{n,sep}$ that is passed to IMEP can have an important effect on the pedestals. Higher values of $S_{n,sep}$ give higher pedestals in the electron density, reducing the pedestal in temperatures, and viceversa. In our simulations, we pass to IMEP values of $S_{n,sep}$ that give values of the pedestal density similar to the one assumed in ref. [C.13].

The impurity density boundary values are calculated through a feedback control on the level of the radiated power. Tungsten (W) is always considered in the simulations, with an additional lighter impurity, nitrogen, neon or argon (N, N_e or A_r) depending on the scenario. The boundary value of the W density is set to be proportional to the lighter impurity one. Two different approaches for the calculation of the impurity density profiles are used. One simply calculates the impurity charge at a specific radial position following the formulas in Ref. [C.18] and keeps an almost constant value of Z_{eff} on the whole plasma radius. In this way, no calculation of the impurity transport coefficients with NCLASS and with TGLF-SAT2 is needed. The other method uses FACIT and TGLF-SAT2 for the calculation of the neoclassical and turbulent impurity density transport coefficients, with an evolution of the impurity density profiles and with a Z_{eff} that depends more strongly on the radial position. The difference between the two methods, in terms of global plasma parameters, is found to be small. As the calculation time of TGLF-SAT2 strongly depends on the number (and mass) of the species considered in the simulation, the first method is much faster. In any case, the effect of the main ion dilution, due to the presence of the impurities, is taken into account in TGLF-SAT2 (this is possible because TGLF does not require a plasma quasi-neutrality).

The radial electric field E_r is calculated self-consistently using local quantities at the low field side mid-plane, considering the ion diamagnetic velocity contribution and assuming neoclassical theory for the poloidal main ion velocities. As observed experimentally, the E_r profile shows a minimum close to the separatrix and goes to values close to zero at the separatrix, in order to reconcile with the positive values of E_r in the scrape off layer (SOL) dictated by the SOL physcis. For this reason, and due to the lack of a proper model for the turbulent contribution to the parallel and toroidal velocities, we force the E_r profile to reach a desired value (zero in our cases) outside $\rho_{tor} = 0.995$. A parabolic function for the E_r profile outside this position is used. The effect of the external flow shear, γ_{ExB}, related to E_r, has been found important for the edge region of the plasma ($0.9 < \rho_{tor} \leq 1$). The reduction of the turbulent fluxes in TGLF-SAT2 by γ_{ExB}, even if not as strong as found in a dedicated study using gyrokinetic simulation [C.19], has anyway an important impact on the edge transport coefficients, leading to the formation of a non-stiff region in the density and temperature profiles outside $\rho_{tor} = 0.9$. This affects the level of neutral particles influx at the separatrix necessary to keep the desired plasma density. Previous simulations, carried out without the effect of E_r, indicated that a gas-puff beyond the experimental capabilities was necessary for DTT. Once the effect of γ_{ExB} is taken into account, the level of gas-puff required in the simulation to keep the desired level of line-averaged density is found to be within experimental capabilities, even though pellet injections will be probably necessary for DTT during the H-mode phase [C.20].

The effect of the sawtooth instability is also retained in the simulation. This is done using a simplified Kadomtsev model that acts only on the plasma current profile and that is triggered in the region of the plasma with safety factor $q < 1.0$. The effect of the sawtooth instability on the temperature and density profiles is taken into account adding artificial averaged transport coefficients, i.e. constant additional transport coefficients that are activated after the first sawtooth activity in the plasma and that acts within the magnetic reconnection position.

C.2 Scenario A SN baseline

The DTT scenario A will operate at $B_T = 3$ T, $|I_p| = 2$ MA and with eight ECRH gyrotrons, i.e. with 7.2 MW of auxiliary heating in the plasma. The ECRH power is deposited close to the plasma axis, at $\rho_{tor} = 0.2$, with the same Gaussian deposition profiles used for the scenario E (see Figure 2.8). One pair of gyrotrons (1.8 MW) is turned on at t=2 s, after the limiter phase, while the remaining three pairs are switched on 200 ms after the end of the current ramp-up, around t=5.2 s, triggering the L-H transition. Nitrogen (N) and tungsten (W) are used as impurities in this case, using a ratio between the N and the W concentration at the separatrix of $n_W/n_N = 0.005$. The imposed level of radiated power is set to a quarter of the total auxiliary heating power, $P_{rad} = 0.25 \cdot P_{heating}$. The ratio between the electron line-averaged density and the Greenwald density during the ramp-up phase is kept around $\overline{n}_e/n_G = 0.45$: with this value, an L-H power threshold of $P_{LH} = 5.5$ MW is expected from the Martin scaling.

The time-evolution of some plasma parameters of interest is shown in figures C.1 and C.2. The evolution of $\overline{n}_e$ follows the ramp in current, as desired, and shows a clear jump at the L-H transition around *t=5.2* s. In our case, $\overline{n}_e/n_G$ goes from approximately 0.45 during the L-mode phase, to approximately 0.75 during the H-mode phase. Values of the internal inductance, l_i, and of the poloidal beta, β_{pol} , are found to be within the level of acceptance for DTT. The poloidal magnetic flux at the separatrix, $\Psi_{\rho=1}$, reaches a value of $\Psi_{\rho=1} = 5$ Vs at the L-H transition. The loop voltage is $V_{loop} = 0.15$ during the H-mode phase. Considering these two numbers and considering the fact that DTT will have a total magnetic flux $\Psi_{\rho=1} = 19.7$ Vs available before the ramp-down phase, the flat-top phase of the DTT scenario A can be maintained, from a pure flux consumption side, for around 100 seconds.

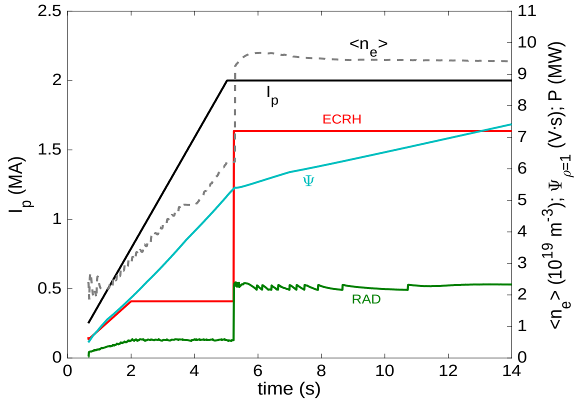

Figure C.1: Time evolution for scenario A of the plasma current (Ip), of the plasma auxiliary heating powers (ECRH, NBI, ICRH), of the power radiated within the separatrix (RAD), of the poloidal magnetic flux at the separatrix (Ψ) and of the line-averaged electron density (<n_e>).The jump in <n_e>, closely following the strong increase in ECRH heating at t=5.2 s, indicates the transition into H-mode.

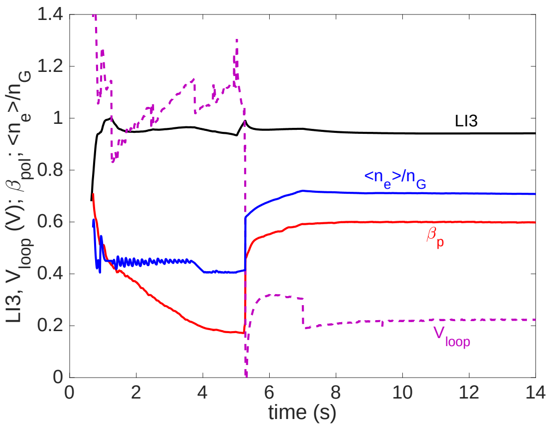

Figure C.2: Time evolution for scenario A of the plasma inductance (LI3), of the plasma loop voltage (V_{loop}), of the plasma poloidal beta (β_{pol}]) and of the ratio between the line-averaged density and the Greenwald density (<n_e>/n_G). The jump in all of these parameters, at t=5.2 s, is due to the transition into H-mode.

The time evolution of the plasma profiles of n_e, T_e, T_i is shown in figure C.3 a-c. The evolution of the impurity densities, for the case in which FACIT is used, is shown in figure C.3 f-g. The evolution of n_e follows the ramp in current, while the evolution of T_e, T_i follows the ramp in heating power. At the L-H transition, a pedestal top $T_{e,ped} = T_{i,per} = 1.2$ keV is expected, with $n_{e,ped} = 8.2 \cdot 10^{19}$ m^{-3}. The boundary (at the separatrix) values of n_e, T_e during the H-mode phase are $T_{e,b} = 100$ eV and $n_{e,b} = 2.7 \cdot 10^{19}$ m^{-3}. The core value of T_e reaches $T_e = 5$ keV, while T_i arrives at $T_i = 3.5$ keV. n_e reaches high values $n_e = 12 \cdot 10^{19}$ m^{-3}, with, as pointed before, a line-averaged density around 0.75, the Greenwald density limit being $n_G = 1.3 \cdot 10^{20}$ m^{-3}.

Values of β_N, ν_e^*, ρ^* during the flat-top phase of scenario A are reported in Table 2.5. An H factor $H_{98} \approx 1.1$ is expected in this case.

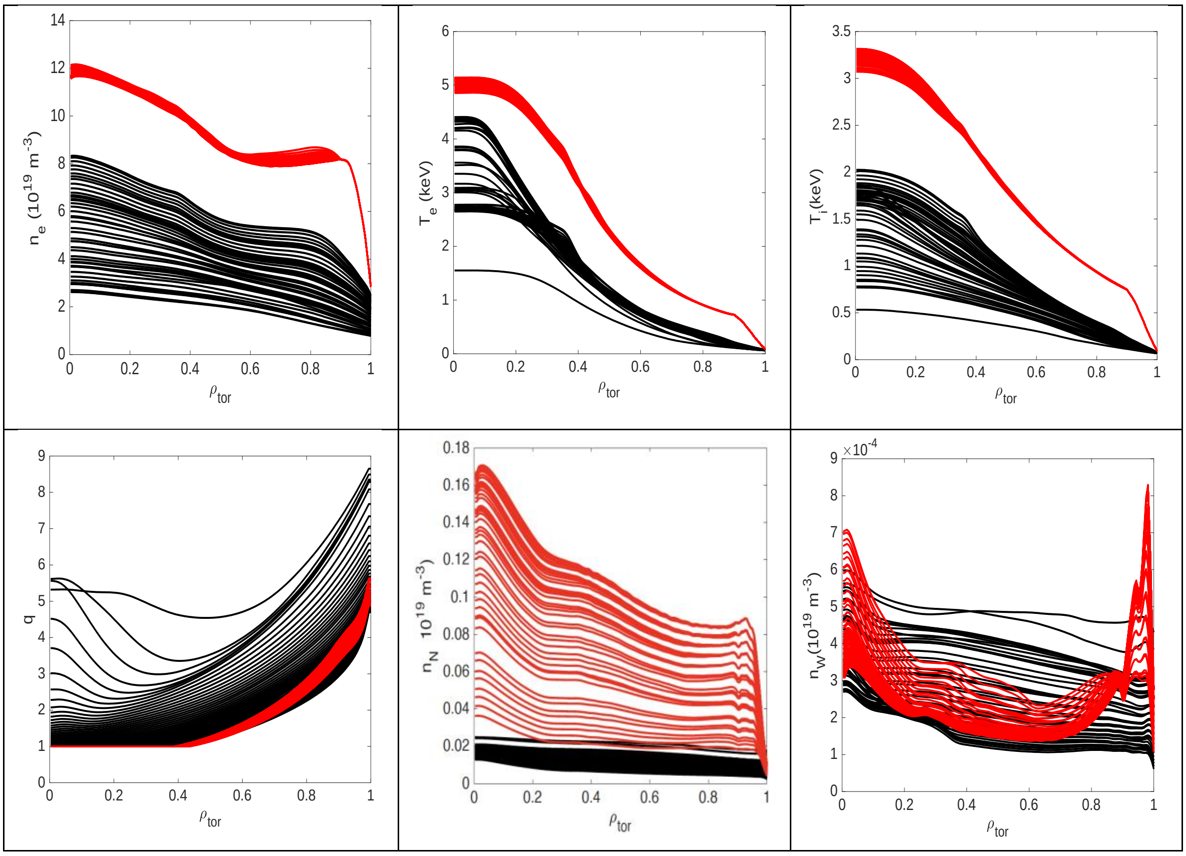

Figure C.3: Time evolution for scenario A of the profiles of n_e, T_e, T_i, q, Z_{eff}, N and W density . The black lines indicate the L-mode phase of the plasma, with Te increasing with increasing power. The red lines indicate the H-mode phase of the plasma, with the profile fixed, outside ρ_{tor}=0.9, to the pedestal calculated by IMEP.

C.3 Scenario C SN baseline

The DTT scenario C will operate at $B_T = 3$ T, $|I_p| = 4$ MA and has 14.4 MW of ECRH and 3 MW of ICRH auxiliary heating in the plasma. The ECRH heating is deposited close to the plasma axis, at $\rho_{tor} = 0.2$, with the same Gaussian deposition profiles used for the scenario E (see Figure 2.8). The first pair of gyrotrons (1.8 MW) is turned on at *t=2* s, one additional pair of gyrotrons is switched on every 2 s. At *t=10.2* s, 200 ms after the end of the ramp in current, all the remaining gyrotrons and the ICRH are switched on, triggering the L-H transition. For the ICRH power deposition, we use, in this case, Gaussian profiles similar to the ECRH one: the ICRH is deposited close to the plasma axis, at $\rho_{tor} = 0.2$, with 2 MW absorbed by the ions and 1 MW by the electrons. This is an approximation of what is used in Ref. [C.13], where a direct calculation of the ICRH power deposition with PION is made. The L-H power threshold predicted by the Martin scaling using, in our case, a ratio between the electron line-averaged density and the Greenwald density of $\overline{n}_e/n_G = 0.45$, is close to the limit of the auxiliary heating, and no transition is observed with only ECRH heating. At this power level, Neon (Ne) is used as seeding gas. Ne and W are modelled as impurities in this case, using a ratio between the Ne and the W concentration at the separatrix of $n_W/n_{Ne} = 0.015$. The imposed level of P_{rad} is set equal to the 25% of the total auxiliary heating power. If larger P_{rad} is considered, the possibility of triggering the L-H transition becomes more uncertain for this scenario.

The time evolution of some plasma parameters of interest is shown in Figure C.4. The evolution of $\overline{n}_e$ follows the ramp in current, as desired, and shows a clear jump at the L-H transition around *t=10.3* s. In our case, $\overline{n}_e/n_G$ goes from approximately 0.4 during the L-mode phase, to approximately 0.56 during the H-mode phase. Values of the internal inductance, l_i, and of the poloidal beta, β_{pol}, are found to be within the level of acceptance for DTT. The poloidal magnetic flux at the separatrix reaches a value of $\Psi_{\rho=1} = 9.3$ Vs at the L-H transition. The loop voltage is $V_{loop} = 0.15\ V$ during the H-mode phase. Considering these two numbers, the flat-top phase of the DTT scenario C can be maintained, from a pure flux consumption side, for around 70 seconds.

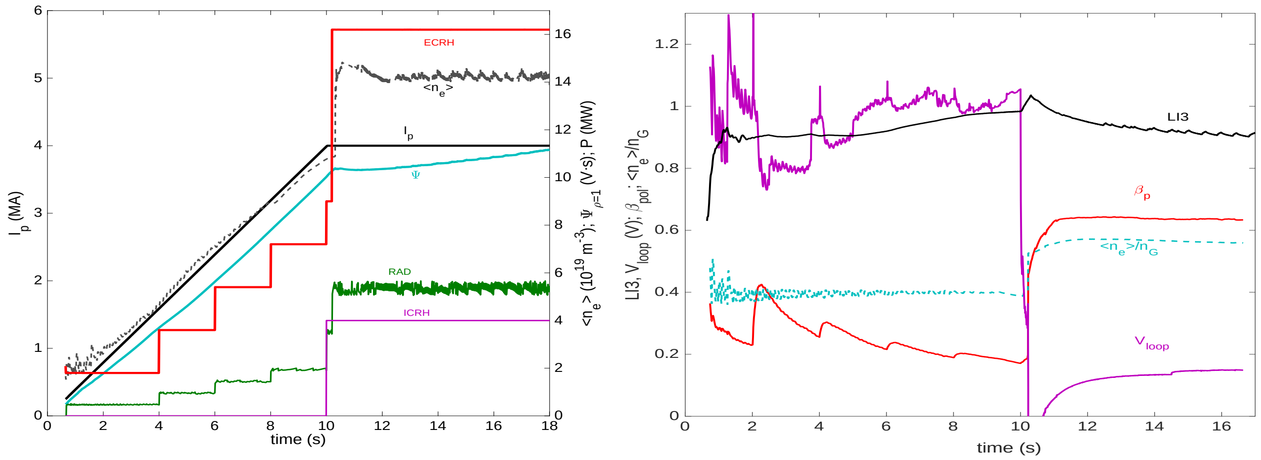

Figure C.4: Same as Figure C.1 and C.2 for Scenario C.

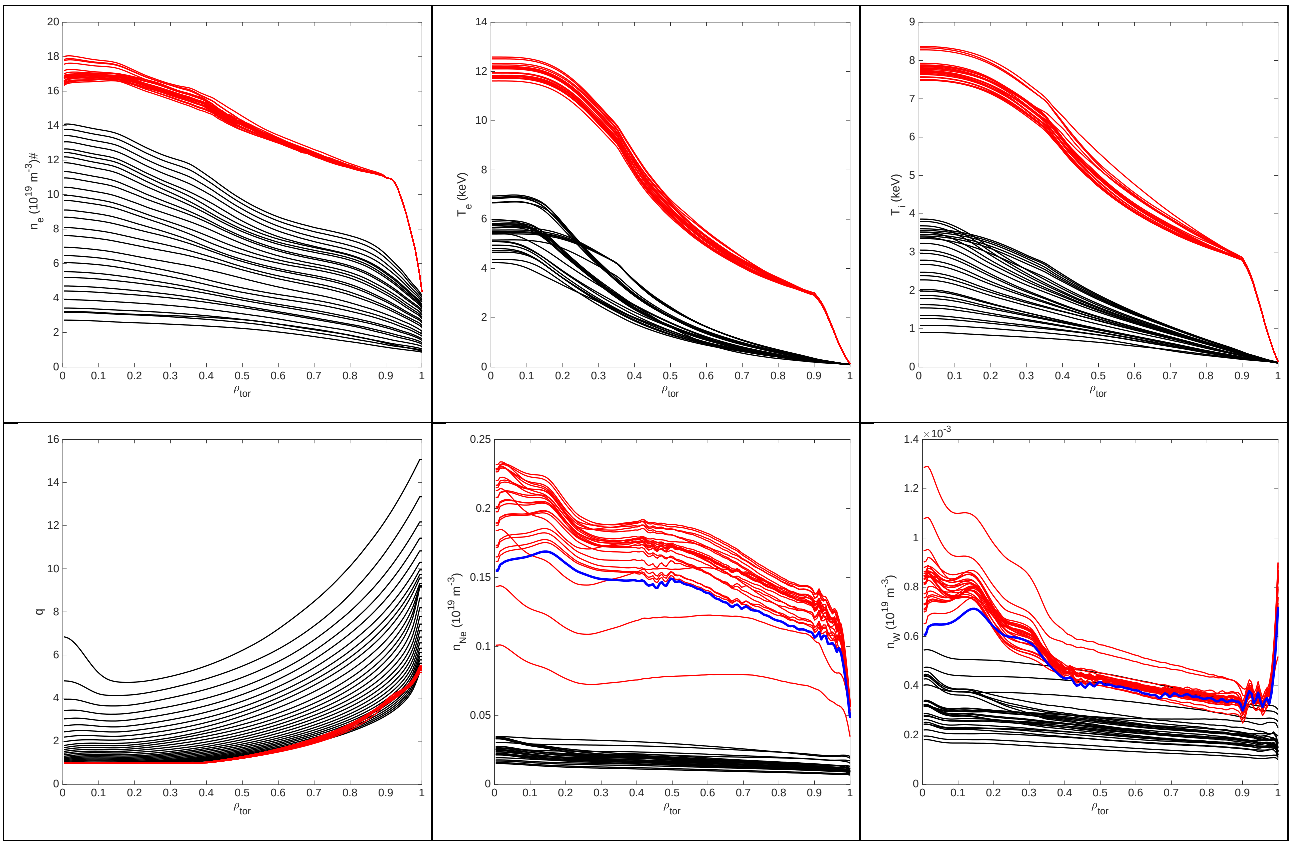

Figure C.5: Time evolution for scenario C of the profiles of n_e, T_e, T_i, q, Z_{eff}, Ne and W density. The black lines indicate the L-mode phase of the plasma, with the electron temperature increasing with increasing power. The red lines indicate the H-mode phase of the plasma, with the profile fixed, outside ρ_{tor}=0.9, to the pedestal calculated by IMEP. The blue line refers to the last time simulated.

The time evolution of the plasma profiles of n_e, T_e, T_i are shown in figure C.5. The evolution of n_e follows the ramp in current, while the evolution of the temperatures follows the ramp in heating power. At the L-H transition, a pedestal top $T_{e,ped} = T_{i,ped} = 2.2$ is expected, with a pedestal top $n_{e,ped} = 12 \cdot 10^{19}$ m^{-3}. The boundary (at the separatrix) values of density and temperature during the H-mode phase are $T_{e,b} = 130$ eV and $n_{e,b} = 4.2 \cdot 10^{19}$ m^{-3}. The core value of T_e reaches $T_e = 8$ keV, while T_i reaches $T_i = 6$ keV. The electron density reaches high values of $n_e = 18 \cdot 10^{19}$ m^{-3}, with, as pointed before, a line-averaged density around 0.56, the Greenwald density limit being $n_G = 2.6 \cdot 10^{20}$ m^{-3}. Values of β_N, ν_e^*, ρ^* during the flat-top phase of scenario C are reported in Table 2.5. An H factor $H_{98} \approx 1.1$ is expected in this case.

C.4 Scenario E half field/half current high β_N

The DTT high-β_N scenario operates at $B_T = 2.9$ T, $|I_p| = 2.9$ MA and at full power with 29 MW of ECRH, 6 MW of ICRH and 10 MW of NBI as auxiliary heating. For these simulations, we have used the same boundary shapes as for scenario A. The ECRH and ICRH power deposition are the same as the scenario E case with the ECRH power deposited fully on-axis. The NBI power deposition is calculated by RABBIT. Of the 10MW of NBI injected in the power, around 8 MW are absorbed in this case. Only one pair of ECRH gyrotron (1.8 MW) is switched on at t=2 s, while the rest of the heating power (for a total of 45 MW) is switched on at t=5.2 s, at the end of the current ramp-up phase. The line-averaged density during the ramp-up phase is kept, in this case, around 0.45 the Greenwald density, $n_G = 3.6 \cdot 10^{20}$ m^{-3}. Neon (L-mode) and Ar (H-mode) and W are used as impurities in this case, using a ratio between the Ne/Ar and the W concentration at the separatrix of $n_W/n_{Ne} = 0.015$. The imposed level of radiated power is set to 25% of the total auxiliary heating power.

The time-evolution of some plasma parameters of interest is shown in Figure C.6. The evolution of the line-averaged density follows the ramp in current, as desired, and shows a clear jump at the L-H transition around *t=5.2* s. In our case, $\bar{n}_e/n_G$ goes from approximately 0.43 during the L-mode phase, to approximately 0.7 during the H-mode phase. Values of l_i and of β_{pol} are found to be within the level of acceptance for DTT. The poloidal magnetic flux at the separatrix reaches a value of $\Psi_{\rho=1} = 6.3$ Vs at the L-H transition. The loop voltage is $V_{loop} = 0.015$ during the H-mode phase. Considering these two numbers and considering the total magnetic flux available before the ramp-down phase of DTT, the flat-top phase of the DTT high-β_N scenario can be maintained, from a pure flux consumption side, for more than 100 seconds.

The time-evolution of the profiles of n_e, T_e, T_i is shown in Figure C.7. The evolution of n_e follows the ramp in current, while the evolution of the temperatures follows the ramp in heating power. At the L-H transition, pedestal tops in the electron and ion temperatures of $T_{e,ped} = 1.4$ keV and $T_{i,ped} = 1.3$ keV are expected, with an electron density pedestal top of $n_{e,ped} = 10 \cdot 10^{19}$ m^{-3}. The boundary (at the separatrix) values of density and temperature during the H-mode phase are $T_{e,b} = 100$ eV and $n_{e,b} = 3.3 \cdot 10^{19}$ m^{-3}. The core value of the electron temperature reaches $T_e = 11$ keV, while the ion temperature arrives at $T_i = 5.5$ keV. The electron density reaches high values of $\bar{n}_e = 12.6 \cdot 10^{19}$ m^{-3}, with, as pointed before, a line averaged density around $\bar{n}_e/n_G$ =0.7, the Greenwald density limit being $n_G = 1.8 \cdot 10^{20}$ m^{-3}. Values of β_N, ν_e^*, ρ^* during the flat-top phase of the DTT high-β_N scenario are reported in Table 2.5. An H factor $H_{98} \approx 1$ is expected in this case.

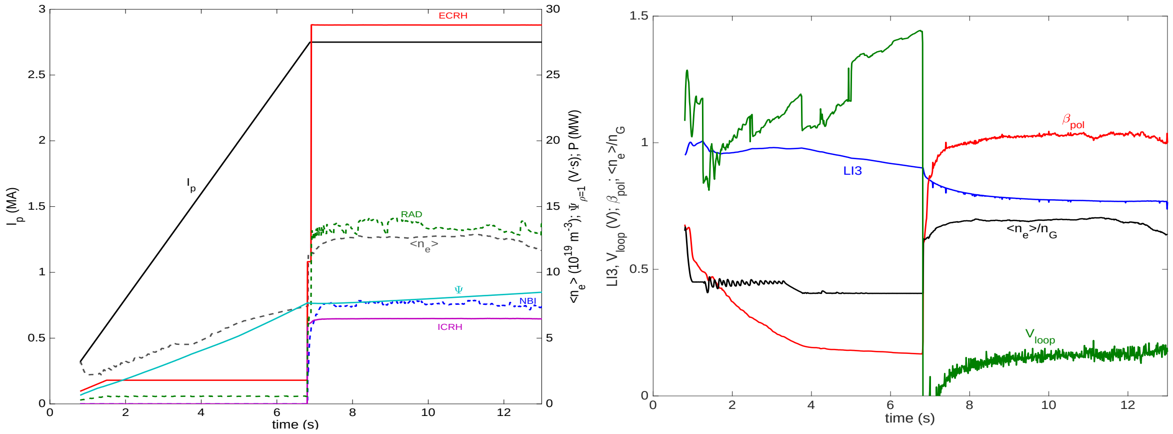

Figure C.6: Same as Figure C.1 and C.2 for Scenario E half field/half current.

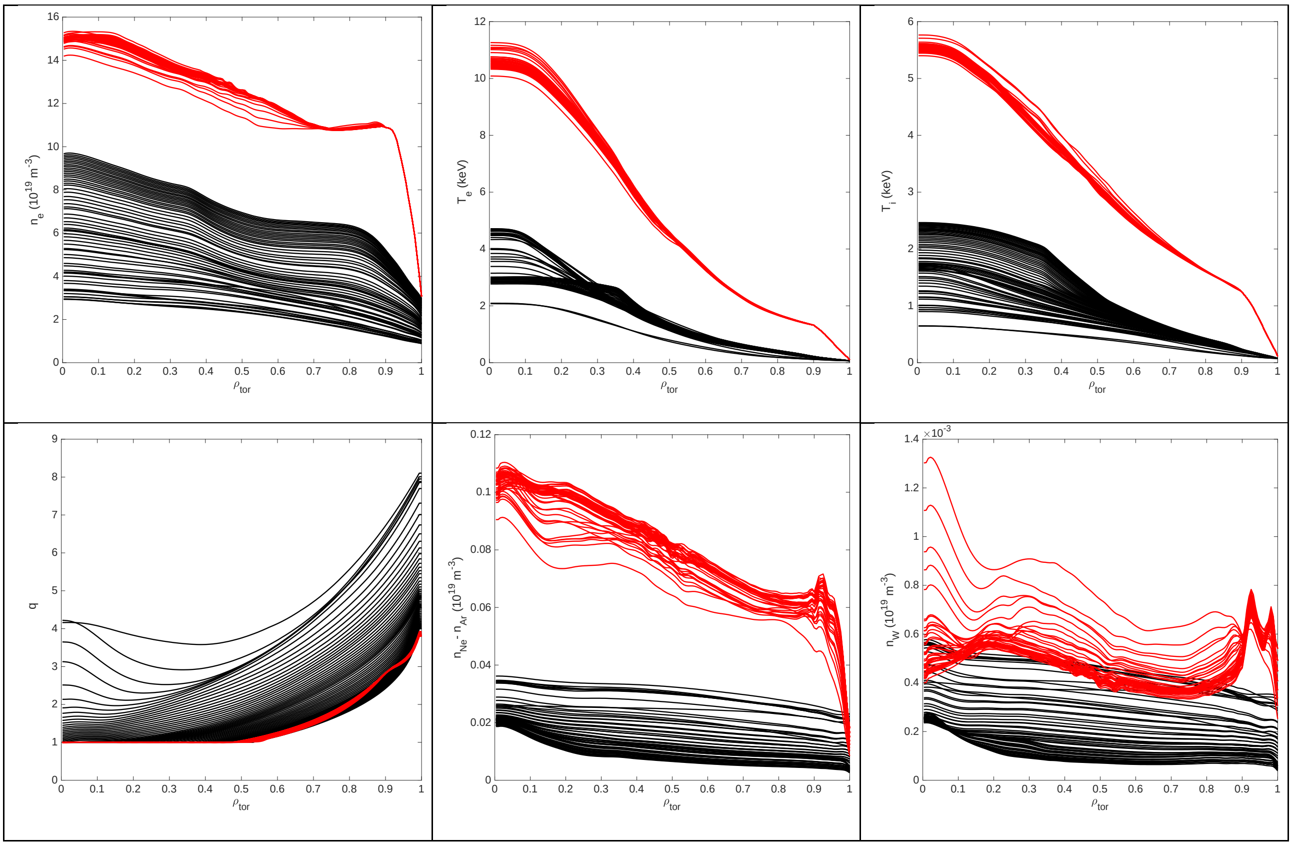

Figure C.7: Time evolution for Scenario E half field/half current of the profiles of n_e, T_e, T_i, q, Z_{eff}, Ne and W density. The black lines indicate the L-mode phase of the plasma, with the electron temperature increasing with increasing power. The red lines indicate the H-mode phase of the plasma, with the profile fixed, outside ρ_{tor}=0.9, to the pedestal calculated by IMEP.

C.5 References

[C.1] G. Pereverzev, P. N. Yushmanov, "ASTRA Automated System of TRansport Analysis in a Tokamak", Report of the Mak-Planck-Institut für Plasmaphysik, IPP 5/42 (Garching Germany, 1991)
[C.2] Fable e., et al., Nucl. Fusion 53 (2013) 033002
[C.3] Staebler G. M., et al., Nucl. Fusion 62 (2022) 0420
[C.4] Houlberg W.,et al, Phys. Plasmas 4 (1997) 3230
[C.5] Fajardo D., et al., Plasma Phys. Control. Fusion 64 (2022) 05501
[C.6] Luda T., et al., Plasma Phys. Control. Fusion 65 (2023) 034001
[C.7] Albanese R., et al., Fusion Eng.Des. 96–97 (2015) 664
[C.8] The SPIDER code. Solution of tokamak plasma equilibrium problem with anisotropic pressure and rotation, A.A. Ivanov, A.A. Martynov, S.Yu. Medvedev and Yu.Yu. Poshekhonov, 2012, https://api.semanticscholar.org/CorpusID:94369725
[C.9] Fable E., et al., Nuclear Fusion 53 (2013) 033002

[C.10] Weiland M. et al., Nuclear Fusion 58 (2018) 082032
[C.11] Eriksson L-G, et al., Nucl. Fusion 33 (1993) 1037
[C.12] Poli E., et al., Comp. Phys. Comm. 225 (2018) 36
[C.13] Casiraghi I., et , Plasma Phys. Control. Fusion 65 (2023) 035017
[C.14] Kallenbach A., et al., Nuclear Materials and Energy (2018)
[C.15] Martin Y R , et al., J. Phys.: Conf. Ser. 123 (2008) 012033
[C.16] Angioni C., et al., Nucl. Fusion 62 (2022) 066015
[C.17] Greenwald W., Plasma Phys. Contr. Fusion 44 (2002) R27
[C.18] JENSEN D.E., et al., Atomic Data and Nuclear Tables, Vol.20 (1977) 397
[C.19] Bonanomi N., et al, to be submitted to Nuclear Fusion
[C.20] Baiocchi B., et al Nucl. Fusion 63 (2023) 106009

APPENDIX D: Plasma facing components

D.1 Divertor

The DTT divertor is composed of 54 Cassette Assemblies (CA) or modules installed at the bottom part of the vacuum vessel (Fig. D.1). Each module includes the Cassette Body (CB) or cassette and three plasma-facing components (PFCs), namely the Inner Vertical Target (IVT), the Outer Vertical Target (OVT), and the Dome (Fig.D.2). The full divertor procurement package includes fifty-six divertor modules, three for each 20° sector plus two spares. Fifty-two are standard modules and four are the so-called divertor test modules (DTM).

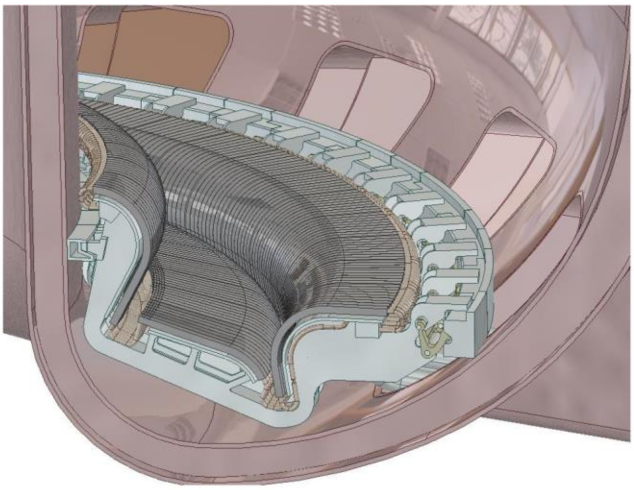

Fig. D.1 The DTT divertor system

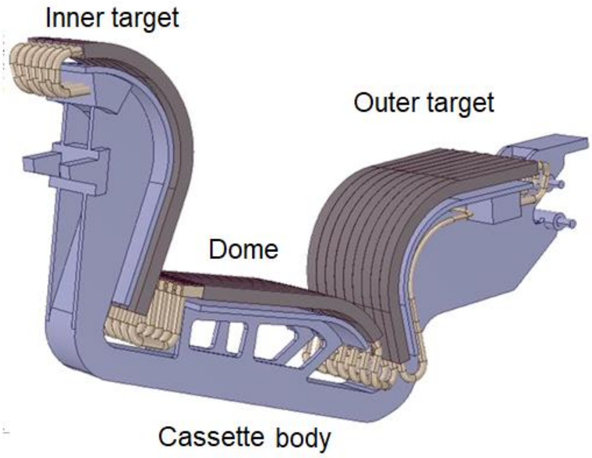

Fig.D.2 The DTT cassette assembly or module

The CB provides neutron shielding for the Vacuum Vessel and magnet coils and routes the coolant to the PFCs. The IVTs and OVTs and Dome intercept the magnetic field lines, and therefore shall have to remove the heat load coming from plasma via conduction and convection during the normal and transient operations as well as during the off-normal events. The curved upper part of the IVTs and OVTs provides a baffle for neutral particles. The dome, depending on plasma scenario, can work only as a baffle for neutrals or as a target for charged particles and baffle for neutrals. The PFCs also protect the CB and diagnostics from direct interaction with the plasma.

In a standard module the PFC configuration is based on the W monoblock (MB) concept, i.e., CuCrZr actively cooled tubes protected by W massive tiles. This choice relies on proven technologies already qualified for ITER (5000 cycles at 10 MW/m^2, followed by 300 cycles at 20 MW/m^2). The PFCs are cooled in series and the water coolant is routed via the CB. Each Divertor cassette is connected to the primary cooling loop through a pair of radial pipes entering the vessel from port 4.

The divertor system has an allocated maximum volume in order to accommodate the needs of different plasma configurations and also to be compliant with the available space for its extraction through the port 4 of the four remote handling (RH) sectors (1,4,10,15, see Fig. D.3) . The RH window is limited vertically to 650mm and toroidally to 350mm. A rough estimate of the weight of a single divertor module is 300 kg.

Poloidal and toroidal gaps between monoblocks (or cassettes) and inevitable radial misalignments between toroidally neighbouring monoblocks expose monoblock edges to high heat flux densities flowing parallel to magnetic field lines. Table D.1 summarizes the findings of the toroidal shaping for the divertor PFCs to compensate inter-cassette radial misalignment. The tilting is applied only to the IVT and OVT strike point region. No tilting is applied to the dome and OHT part of OVT: in this case, the radial misalignment is compensated by steep bevels given to the monoblocks of the two extreme plasma facing units, left and right side (so called roof shaping).

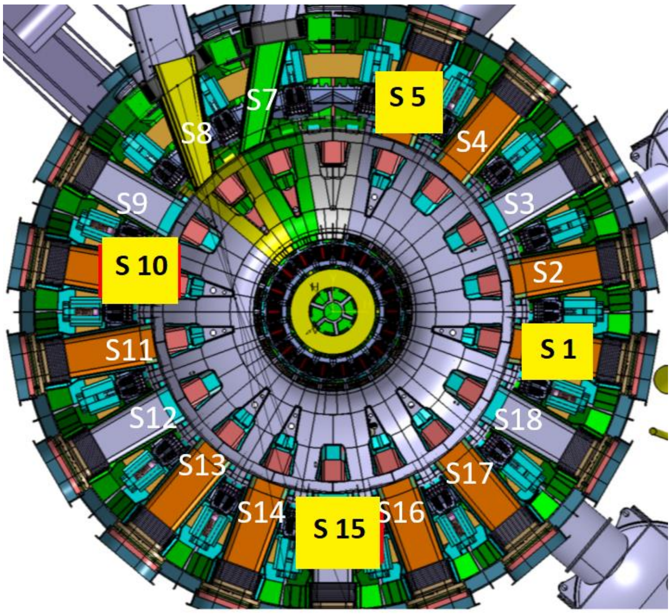

Fig. D.3: Plant view of DTT sectors, the yellow-labelled rectangles are the divertor RH sectors

PFC	Grazing angle α (°)	Inter-cassette gap-g$_{CAS-}$ (mm)	Inter-cassette total gap (mm)	Field line radial component (mm)	Inter cassette radial step (mm)	MB width (mm)	PFC toroidal width	Tilt angle (°)	h bevel* (mm)
IVT	2(SN)	7.5	10.5	0.37	2	24	171.0	0.797	-
OVT	2(SN)	10	13	0.45	2	24.5	224.5	0.625	-
Dome	5.2(NT)	9.5	12.5	1.14	2	25.5	181.5	0	3.14
OHT	1.3(NT)	12	15	0.34	2	27.5	251,5	0	2.34

Table D.1 Toroidal shaping of divertor PFC (global tilting).

** These bevels are doubled to consider the effect of dome and OHT profile symmetrical shape)*

Previous R&D and ITER prototyping results have shown that the achievable monoblock tolerance in radial direction is ±0.3 mm. Therefore, this potential small misalignment has to be compensated by monoblock toroidal shaping. A simple solution for monoblock plasma facing surface shaping is a planar toroidal bevel of height sufficient to protect the worst-case radial misalignment (as said 0.3 mm). The chosen bevel height for the different PFCs is summarized in Table D.2. Figure D.4 gives a qualitative picture of PFC shaping.

According to the DTT Balance of Plant Auxiliary System Process Basis of Design, the maximum power to be absorbed by the divertor is 32 MW. The 54 modules composing the DTT divertor are cooled in parallel by pressurized water with a total mass flow rate of about 570 kg/s. The inlet water conditions foresee a pressure of 50 bars and a temperature that can be selected for each tokamak campaign between 30 °C and 130 °C with a maximum variation of ± 5 °C. The estimated total pressure drop (cassette in-out) shall not exceed 2 MPa.

Each divertor module is provided of a shut-off valve for leak detection. Moreover, in the four RH sectors all the three modules are instrumented with pressure monitor and inlet-outlet flow meter and termocouples.

PFC	Grazing angle α (°)	Inter-MB gap (mm)	Field line radial component (mm)	Inter MB radial misalignment (mm)	h bevel (mm)	Bevel angle (°)	h total bevel* (mm)	Monoblock width (mm)
IVT	2(SN)	0.5+0.2	0.024	0.3	0.32	0.764	-	24
OVT	2(SN)	0.5+0.2	0.024	0.3	0.32	0.748	-	24.5
Dome	5.2(NT)	0.5+0.2	0.063	0.3	0.36	-	3.50	25.5
OHT	1.3(NT)	0.5+0.2	0.016	0.3	0.32	-	2.66	27.5

**The height of total bevel is the sum of inter-cassette and inter-MB bevels for dome and OHT. This applies only to side PFUs because the other PFUs are flat.*

Table D.2: Monoblock toroidal shaping

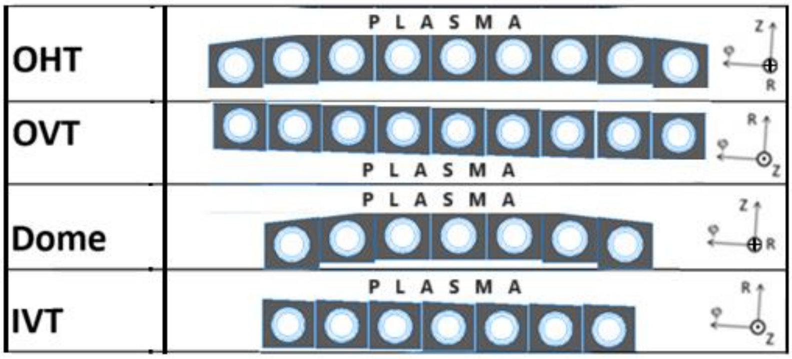

Fig. D.4: PFC toroidal shaping (note different axes' orientation).

The main characteristics of the DTT divertor are summarised in Table D.3.

Parameters for **divertor**	Nominal value
Number of divertor modules	54 (50 standard + 4 test modules)
Max inlet pressure of standard modules [MPa]	5
Max inlet pressure of test modules [MPa]	15*
Max inlet temperature of standard modules [°C]	130
Max inlet temperature of test modules [°C]	250*
Number of targets per module	4
Number of plasma facing units at **inner** vertical target per module	7
Number of plasma facing units **dome** per module	7
Number of plasma facing units at **outer** vertical target per module	9
Nominal length of target (inner – dome – outer vertical – outer horizontal) [mm]	211 – 261 – 180 – 142
W armour thickness [mm]	3

*hydraulic system of test modules to be upgraded in Phase 2 of DTT operations

Table D.3: main characteristics of the DTT divertor

D.2 First wall

The first wall (FW) design is still in progress. As shown in Fig. D.5, the FW modules are divided into different sub-systems depending on the poloidal position inside the Vacuum Vessel (VV): Outboard FW (**OFW**), Top FW (**TFW**) and Inboard FW (**IFW**), with the last in turn segmented in Limiter IFW (**LIFW**) modules and Standard (**SIFW**) modules. Indeed, the need for an operating flexibility and robustness imposes the presence of inboard limiters and it was decided that 50% of the IFW is covered by limiter modules.

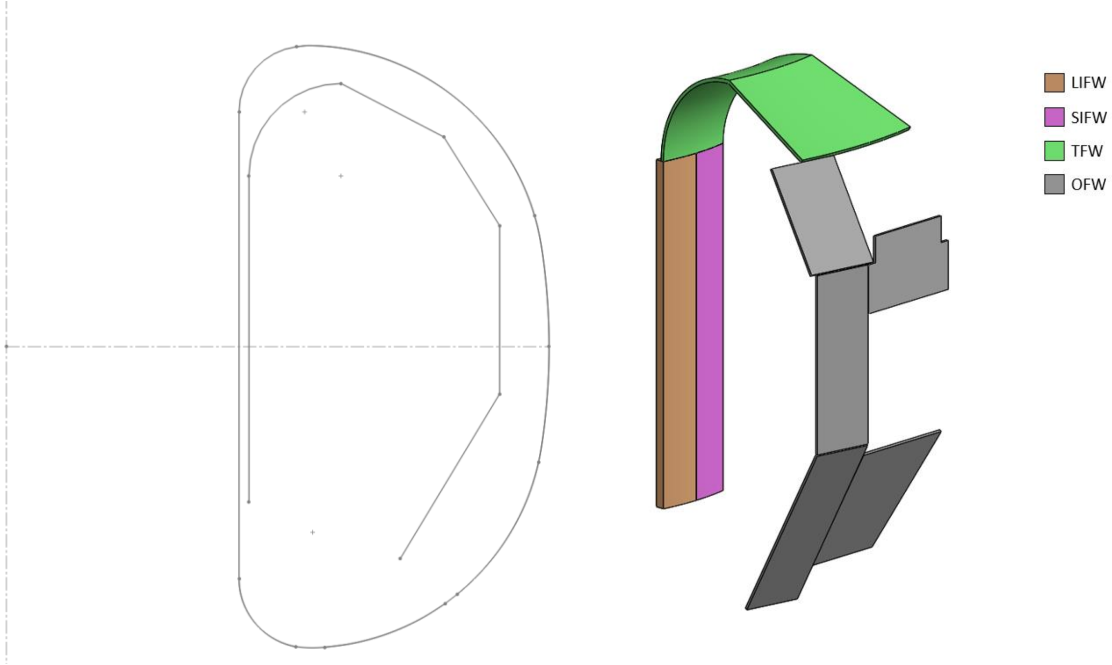

Fig; D.5 - CAD model of a toroidal sector of the DTT FW, highlighting the sub-systems.

The Plasma-Facing Components (PFCs) of the DTT FW are designed to exhaust a relevant fraction of the plasma power and to shield the VV and the other In-Vessel Components (IVCs) from the particle and photon flux coming from the plasma. Moreover, the design of the FW modules is driven by several requirements and constraints, coming from the interfacing with the other systems of DTT:

- The cooling requirements of the FW modules must comply with the primary Water-Cooling System.
- The integration with the other in-vessel components and the diagnostics must be taken into account to define the dimensions and the geometry of all the FW modules.
- The compatibility with the Remote Handling (RH) system provides constraints both for the size of the FW modules, which must be inserted and removed through the allocated ports, and the attachment system to the supports, that must have a remotely operable interface.
- The FW must comply with the plasma shaping of the magnetic equilibria that will be tested.

The maximum thermal power to be absorbed by the DTT FW is 32 MW, exclusive of the power radiated in the ports and the one deposited on the ICRH antennas. Given this thermal power and the desired temperature difference (20 °C), the whole water mass flow required by the FW is 381 kg/s, provided at the inlet conditions of 60 °C and 40 bar. The inlet temperature value must be kept constant during the entire shot with a tolerance of ± 5 °C, and the maximum pressure drop in the section of circuit inside the vacuum vessel is 10 bar. The whole water mass flow of 381 kg/s is distributed in all the FW modules through a system of circuits connected in parallel.

The **LIFW** consists of 18 modules (one per sector). Each LIFW module covers 10° per sector (the remaining 10° occupied by a SIFW module). The conceptual layout of a LIFW plasma facing unit (PFU) is based on the ITER-like W-monoblock with a CuCrZr coaxial pipe as heat sink. Each module is made of seven continuous coaxial pipes extending poloidally over a length of 1960 mm and is connected in parallel to the others with the feeding pipes passing through duct 1.

The **SIFW** consists of 18 modules (one per sector). Each SIFW module covers 10° per sector (the remaining 10° occupied by a LIFW module). Each module is made of seven continuous coaxial pipes extending poloidally over a length of 1960 mm and is connected in parallel to the others with the feeding pipes passing through duct 1.

The **OFW** is segmented in five modules per sector. Each OFW module is made of a plate shaped plasma-facing unit (PFU), two separated manifolds (inlet/outlet) and a back plate. Each module is connected in parallel to the others and the feeding pipes pass through the adjacent ducts (port 2, 3, 4). The back plate is necessary to limit the bending of the PFU due to the thermal load. The PFU is connected to the back plate only at its centre, thus allowing the differential expansion between the parts. The OFW module assembly is fixed to a support system directly welded to the VV and must be designed complying with the RH requirements. Currently, the thicknesses reserved for the overall dimensions of the PFU and the back plate are 15 mm and 45 mm, respectively.

The **TFW** is segmented in two poloidally adjacent modules per sector, positioned respectively at a smaller (module TFW #1) and a larger radius (module TFW #2). Both modules have a toroidal extension of 20°. In order to decrease the necessary mass flow rate, the two modules of a sector are hydraulically connected in series and the feeding pipes pass through duct 1. For reasons of compatibility with the RH, the hydraulic connection must take place outside the duct.

APPENDIX E: Heating and current drive systems

The Heating systems of DTT are described in the following articles:

ECRH: S. Garavaglia et al., Fusion Eng. Des. **168** (2021) 112678
NBI: P. Agostinetti et al., IEEE Transactions on Plasma Science **50** (2022) 4027
ICRH: S. Ceccuzzi et al., Fusion Eng. Des. **146** (2019) 361

A general overview can be found in:

G. Granucci et al., Fusion Eng. Des. **122** (2017) 349

Here below a synthetic summary on the three systems characteristics is presented.

ECRH System

Frequency: 170 GHz for the first 16 gyrotron, 140-170 for the next 16 ones (to be confirmed)
Power Unit output: 1 MW
Total Installed power: 32 MW (to be confirmed after DTT Phase 1)
Pulse length: 100s
Launched Mode: Ordinary (OM) or Extraordinary mode (XM) (via polarization control)
Cut-off density: 3.4 10^{20} m^{-3} (OM 1st harmonic) and 1.7 10^{20} m^{-3} (XM 2nd harmonic)
Power Modulation: 0-100% up to 1 kHz, pulse length limited with modulation up to 5 kHz
Power control: with on/off duty cycle, via beam voltage (to be confirmed).
Gyrotron feeding: in couple (one Power Supply for two gyrotrons) → single power step = 2 MW
Transmission efficiency from source to plasma: 90% (target, to be confirmed)
Launcher type: independent front steering for each beam, launching mirrors *real time* controlled in both directions (poloidal and toroidal)
Poloidal Mirror speed: 40°/s equivalent to 0.6 $\Delta\rho_t$/s (in average for all the mirror positions)
Launching port distribution: 6 units for each ECH port 3 (equatorial), 2 units for each ECH port 2 (upper);
Total ECH sectors: 4
Poloidal steering span: 35° from 0.05 to 0.9 ρ_t (depending on the launcher position)
Toroidal steering: ±25°
Minimum waist at R_{RES} : 44.5 mm for the equatorial launcher and 15 mm for the upper launcher

NBI System

Type: Negative Neutral Beam Injector
Number of Injectors: 1
Equatorial toroidal inclination: 30° at R=3.4 m (beam average tangency radius R_{tang} = 1.95 m)
Energy: 510keV
Pulse length: 50s
Injected atoms: D or H
Power at Vacuum Vessel: 10 MW (0.5 MW power losses in the duct)
Energy Control: from 10% to 100% of energy, linear from ≈ 250 to 500KeV
Power Control: quasi linear from 4 MW to 10 MW
Beam dimension at plasma centre: 190 mm (horizontal) x 440 mm (vertical)

ICRH System

Frequency Range: 60 – 90 MHz

Power Sources type: 8 Solid State Amplifier (SSA)

Unit Power (P_{max}): 1.2 MW

Source power control: 5% accuracy from $P_{max}/2$ to P_{max}

Max rate of power modulation: around 500 Hz

Pulse length: 50s

Power Transmission efficiency: 70%

Number of Antennas: 4 (one pair of antennas fed by 4 SSA)

Antenna Type: 3-strap antenna with adjustable radial position

Phasing: 0-π-0 or 0-0-0

Launched Spectrum for 0-π-0 phasing:

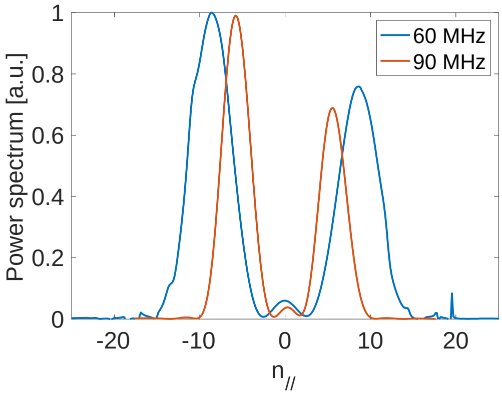

Frequency	Peak n//
60 MHz	8.6
90 MHz	5.6

APPENDIX F: Diagnostic systems

Diagnostics for Machine/Divertor Protection and Plasma Control (basic feedback control functions as density, plasma current, equilibrium etc…) are included in the Phase 1 DTT Diagnostic Equipment (Table F.1) and these design activities have priority in the diagnostic procurement plan.

A final assessment and optimization of Phase 1 equipment will be subject to a revision of the costs and of the integration and interface activities, both after completion of the ongoing design. An essential input will also be the definition of the experimental programmes planned for Phase 1 of the present DTT Research Plan. Diagnostics with an impact on the in-vessel components are necessarily included in Phase 1 equipment, as well as some diagnostics of relevance for machine operation and, at the same time, of low impact on implementation.

Table F.1: A strategy for Phase 1 DTT Diagnostic Equipment

Diagnostic	**Measured Parameter**	**Machine Protection**	**Essential For Operation**	**Scientific Programme**
Bolometers cameras core and divertor	Radiation Total, profile		X	
SXR Imaging	Fluctuations, MHD - SXR profile			X
SXR Sensors	Fluctuations, MHD - SXR profile			X
Interferometer Vertical (Central LOS)	Fluctuations, density electron		X	
Interferometer Tangential	Fluctuations, density electron	X	X	
Charge Exchange and Diagnostic Neutral Beam Charge Exchange (CXRS)	Temperature ions, Profile: core/pedestal/SOL Rotation, toroidal – poloidal			X
Diagnostic Neutral Beam Injection (DNBI) and MSE Polarimeter	Safety factor, Profile Current			X
SXR Crystal spectrometer	Impurities, density profile			X
SXR spectrometer (XUV1) and (XUV2)	Impurities, species monitoring		X	
Visible D alpha array and Divertor	Neutrals Density and Fluctuations ELMs and L-H transition, Recycling	X	X	
Visible spectrometer survey and Divertor	Wall, chemical composition monitor, isotope ratio / Impurities, radiation power of each species and ionisation front (Divertor)		X	
Visible Z_{eff} Bremsstrahlung	Impurities, Z_{eff} profile		X	
VUV spectrometer Edge	Wall, density and detachment and enrichment			X
VUV Spectrometer Survey	Impurities, species monitoring	X	X	
Neutrons Activation Foils (NAS)	Neutrons, Yield		X	
Neutrons Yield Monitors	Neutrons, flux monitor		X	
Biaxial LTCC Coils IN-VESSEL	Plasma shape & equilibrium reconstruction - Vertical		X	

	speed estimation - MHD fluctuation			
Biaxial Pick-up Coils EX-VESSEL and IN-VESSEL and DIVERTOR	Plasma current & centroid position estimation - Plasma shape & equilibrium reconstruction - Vertical speed estimation	X	X	
Current Shunt IN-VESSEL and DIVERTOR	Halo and Eddy currents	X	X	
Diamagnetic Loops Compensation Coils EX-VESSEL and IN-VESSEL	Plasma magnetic energy estimation			X
Diamagnetic Loops EX-VESSEL and IN-VESSEL	Plasma magnetic energy estimation			X
Flux Loops EX-VESSEL and IN-VESSEL	Plasma shape & equilibrium reconstruction - Loop voltage estimation - Eddy current estimation	X	X	
Hall Probes EX-VESSEL	Plasma shape & equilibrium reconstruction - Magnetic calibration			X
Optic Fiber Plasma Current - EX-VESSEL	Optic fiber plasma current measurement			X
Partial Rogoski Coils IN-VESSEL and DIVERTOR	Halo and Eddy currents	X	X	
Rogoski Coils EX-VESSEL	Plasma Current	X	X	
Saddle Loops EX-VESSEL	Backup for: Plasma shape & equilibrium reconstruction - Error field reconstruction	X	X	
Cameras IR SLOW and FAST	Temperature electron, First Wall and Divertor	X	X	
Cameras VIS	Wall, sources and main gas / Offline inspection	X	X	
Electron Cyclotron Stray Detection Bolometers and Sniffer probes	Wall / Stray EC	X	X	
Langmuir probes FW EXTERNAL - INNER and DIVERTOR	Density electron & Temperature electron, density (low power) profile / leg position	X	X	
Long Term Samples (LTS)	Wall, Plasma Wall Interaction			X
Microbalance probes redeposition	Wall, redeposition layers			X
Neutrals Gas Analyzer	Neutral Gas Composition (Physics)		X	
Optical sensors of deformation-strain sensors (FOS) DIVERTOR	Strain and stress deformation	X	X	
Penning spectroscopy	gas pressure and composition (Divertor)			X
Thermocouples DIVERTOR	Wall, temperature	X	X	
Thermocouples FW EXTERNAL and INNER	Wall, temperature		X	
ECE Electron Cyclotron Emission Radiometer and Michelson Interferometer	Temperature electron, Profile and Temperature electron, Profile (fast)		X	
Thomson Scattering Core-Edge (Inner) LIDAR	Density electron Profile / Temperature electron Profile (core/pedestal/SOL)		X	

Runaway Electron Imaging Spectrometer (REIS)	Runaway electrons spectrum		X	
Hard-X-Rays/Gammas Rays Monitors	Hard-X and Run-Away Monitor	X	X	

In addition to Phase 1 equipment, a number of advanced diagnostic systems of Phase 2 ("Research Programme") (Table F.2) is being presently envisaged, in order to assess their allocation on the machine and in nearby laboratories and to assess interface and integration issues. The guideline for the strategy has been to identify a complete, although improvable, diagnostic equipment. A final selection and optimization of the Phase 2 diagnostic equipment strategy should follow closely the evolutions of the DTT Research Plan.

Table F.2: A strategy for Phase 2 DTT Diagnostic Equipment

Diagnostic	**Measured Parameter**
Bolometer cameras, toroidal asymmetries studies	Radiation Total, Tomography
Bolometers cameras Tomography	Radiation Total, Tomography
SXR Tomography	Fluctuations, MHD - SXR Tomography
Interferometer Divertor	Density electron, profile Divertor
Interferometer/Polarimeter Vertical	Fluctuations, density electron / Safety factor, Safety factor: Profile
Phase Contrast Imaging (PCI)	Fluctuations, density electron
Laser Blow Off	Impurities transport / Runaways mitigation
Multi-spectral Imaging system Divertor (Visible Filtered Camera)	Impurities profiles - Detachment monitor
Tracer-encapsulated solid pellet (TESPEL)	Impurities transport
VUV spectrometer imaging Divertor	Impurities, monitor (Divertor) and physics of the plasma-divertor detachment mechanism
Neutron Gammas Cameras	Neutrons, emission profile
Time-Of-Flight neutron spectrometer (TOF)	Fast ions energy spectrum / Neutrons Spectrum
Toroidal Alfven Eigenmodes diagnostic heads (TAE)	Alfven Eigenmodes (TAE)
BES beam emission spectroscopy	Fluctuations, density, electron
Event Detection Intelligent Fast Camera	Wall, sources and main gas / fast
Gas Puffing Imaging	Plasma Fluctuations
Langmuir probes reciprocating	Flow, plasma SOL
Laser Induced Breakdown Spectroscopy-(LIBS-Divertor)	Wall, embedded content (divertor)
Laser Induced Breakdown Spectroscopy(LIBS)	Wall, embedded content
Sample Introduction System (SIS)	Wall, Plasma Wall Interaction
Thermal He Beam	Density electron / Fluctuations
ECE Electron Cyclotron Emission Radiometer in Line	MDH activity

ECE Michelson Oblique ECE	Distribution function, electron (strong e heating)
ECE Turbulence Coherent	Fluctuations, MHD imaging - ELMs dynamics - NTM detect. & control
Reflectometry Density Profile Reconstruction (DPR)	Density profile
Reflectometry Plasma Position (PPR)	Plasma position and shape
Reflectometry Turbulence (TR)	Turbulence drift velocity
Thomson Scattering Divertor and Edge (External)	Density electron / Temperature electron (Divertor)
Cherenkov probe	Runaways electrons
Runaway Electron Imaging Spectrometer (enhanced performance)(REIS2)	Runaways electrons spectrum
Fast Ion Loss Detector (FILD)	Fast Ions Loss
Fast ions Deuterium alpha (FIDA-CX)	Fast ions, Energy and density
Hard-X-Rays/Gammas Rays Spectrometers	Neutrons & gammas flux / Runaways Electrons flux and spectrum - profile
Hard-X-Rays/Gammas Rays Tomography	Neutrons & gammas flux / Runaways Electrons flux and spectrum - tomography
Neutral Particle Analyzer	Fast ions, energy spectrum of fast ions

A preliminary port allocation of DTT diagnostics for Phase 1 is shown in Fig. F.1.

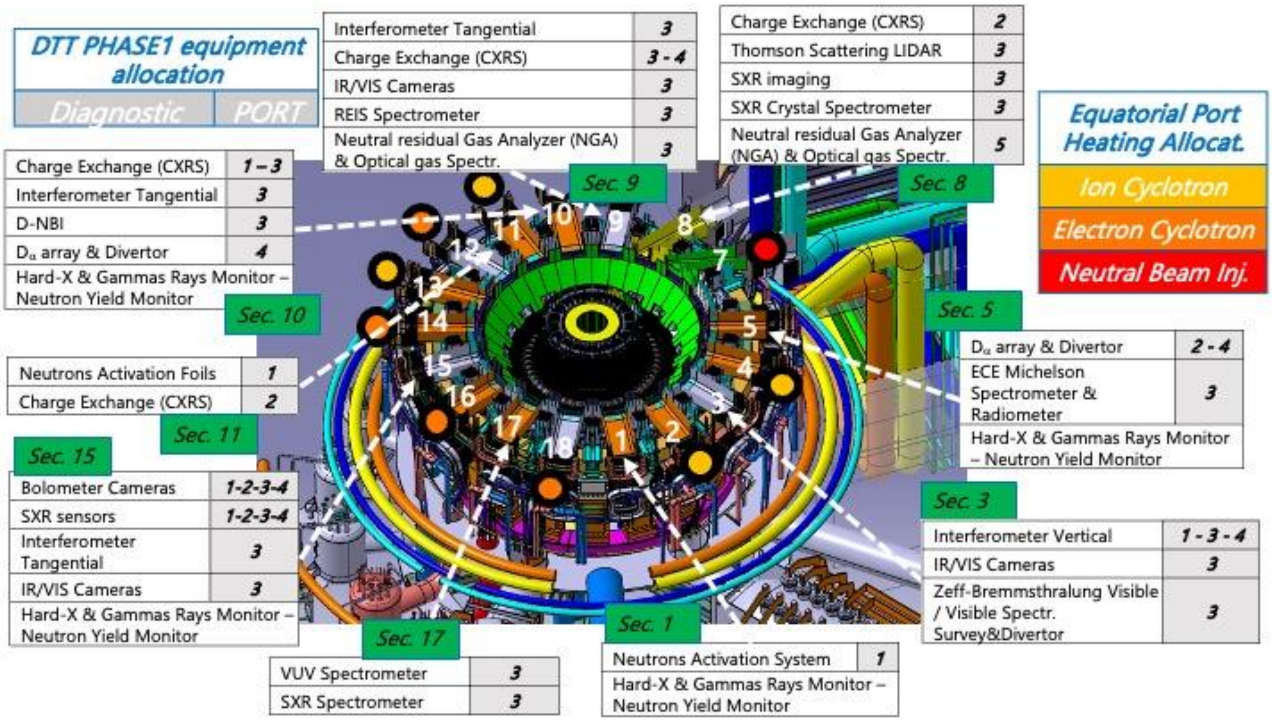

Sec. 10

Diagnostic	PORT
Charge Exchange (CXRS)	1 – 3
Interferometer Tangential	3
D-NBI	3
D_α array & Divertor	4
Hard-X & Gammas Rays Monitor – Neutron Yield Monitor	

Sec. 9

Interferometer Tangential	3
Charge Exchange (CXRS)	3 - 4
IR/VIS Cameras	3
REIS Spectrometer	3
Neutral residual Gas Analyzer (NGA) & Optical gas Spectr.	3

Sec. 8

Charge Exchange (CXRS)	2
Thomson Scattering LIDAR	3
SXR imaging	3
SXR Crystal Spectrometer	3
Neutral residual Gas Analyzer (NGA) & Optical gas Spectr.	5

Sec. 5

D_α array & Divertor	2 - 4
ECE Michelson Spectrometer & Radiometer	3
Hard-X & Gammas Rays Monitor – Neutron Yield Monitor	

Sec. 3

Interferometer Vertical	1 - 3 - 4
IR/VIS Cameras	3
Zeff-Bremmsthralung Visible / Visible Spectr. Survey&Divertor	3

Sec. 1

Neutrons Activation System	1
Hard-X & Gammas Rays Monitor – Neutron Yield Monitor	

Sec. 17

VUV Spectrometer	3
SXR Spectrometer	3

Sec. 15

Bolometer Cameras	1-2-3-4
SXR sensors	1-2-3-4
Interferometer Tangential	3
IR/VIS Cameras	3
Hard-X & Gammas Rays Monitor – Neutron Yield Monitor	

Sec. 11

Neutrons Activation Foils	1
Charge Exchange (CXRS)	2

Fig. F.1: preliminary port allocation of DTT diagnostics for Phase 1

APPENDIX G: Gas injection and pumping systems

G.1 Gas injection System

In Table G.1 the main parameters of the gas injection system (GIS) are reported. The final arrangement of injection points is presently under analysis with the aim to provide a toroidally uniform distribution of injected gas and to allow injection of the main gas (D/H or He) and impurity seeding gas from the same poloidal position in the divertor. Presently 35 injection points have been considered (see Figure G.2-G.5 and Table G.2). The piezoelectric valves are not defined yet, then for the conceptual design the characteristics of the valves used in other experiments were assumed. The maximum flow rate considered is about 20 Pa m^3/s for deuterium (nominal value for the General Atomic valves is maximum 50 Pa m^3/s for hydrogen and minimum at 8 Pa m^3/s for argon).

TABLE G.1. OVERVIEW OF THE GIS

Number of injection lines	*35*
Max single line flow rate (D)	*20 Pa m^3/s*
Max global flow rate(D)	*700 Pa m^3/s*
Gas involved	*H, D, He, Ne, Ar, Kr, etc.*

G.1.1 Gas injection distribution

In Figure G.1 the GIS schematized layout is presented. From the fire-protected zone, the lines enter the torus hall towards two ATEX (Atmosphere Explosible) cabinets (about 50 m) in which the following components are located:

- A Matrix valve to control the final valves destinations of gasses allowing directing any of the available gas to any of the injection points.
- Two intermediate volumes to store the hydrogen for the experiment operation in between cryopumps regeneration. These volumes are sized in order to have always a volume of explosive gas inside the torus hall (local tank and cryopanels) lower than the safe one.
- Flux meter dedicated to the GDC (Glow Discharge Cleaning) lines
- H_2 and B_2H_6 sensors

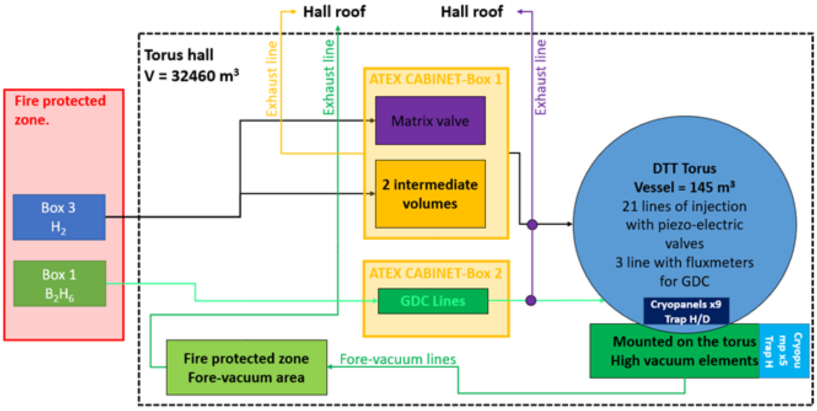

Figure G.10: GIS schematized layout

From the ATEX cabinet the pipes arrive at the piezoelectric valves located on the cryostat. The length of the pipes depends on the sector in which each piezoelectric valve is located, in a range between 5 m to 35 m.

Presently, it is considered to install the fast piezoelectric valves near the flanges of the ports with dedicated gas sensors to detect possible gas leakages at the connections between pipes and valves (see Table G.2).

TABLE G.2. INJECTION VALVES

Sector	1	2	3	4	5	6	7	8	9	10	11	12	13	14	15	16	17	18
Top. 1					🟨						🟨						🟨	
Top. 2					🟥						🟥						🟥	
Top. 3					🟨						🟨						🟨	
Top. 4					🟫						🟫						🟫	
Out eq.					🟦			🟦						🟦			🟦	
In eq.					🟩						🟩						🟩	
Div. 1					🟧						🟧						🟧	
Div. 2					🟦						🟦						🟦	
Div. 3					🟧						🟧						🟧	
Div. 4					🟫						🟫						🟫	
ICRH		🟪		🟪							🟪		🟪					

Gas injection points close to the ICRH antennas are foreseen to improve RF coupling with the plasma. For this reason, specific injection points (probably integrated in the antennas) are considered. The gasses are principally D but the system will be connected to the matrix valves, so any gas connected to the system can be used. The ICRH systems are located at sectors 2, 4, 11 and 13 of the torus. Based on the previous experience, the requested flux for every antenna is about $0.5\text{-}1.0\cdot10^{22}$ s^{-1} which is compatible with the previous maximum flow rate of a single line.

Four different positions are presently considered for the in-vessel injection points: inner wall, top vessel, external wall, bottom divertor, as shown in Figures G.2-G.5.

Top and bottom divertor: each pipe will split in the two toroidal directions with a path of 40° to provide a total of nine injection points 40° away each other. Gas injection in the gaps between divertor cassettes is presently under study. At the central part of the dome, lines are duplicated to allow D/H and seeding gas injection from the central position.

Top divertor: in principle, two different tasks should be accomplished: a) a poloidally distributed gas injection in case of single null configurations; b) a toroidally uniform gas injection in case of DN magnetic configuration that can be studied at low plasma current. It has not been decided yet how to manage these different requirements; presently at the top the bottom arrangement is replicated, but this solution is under evaluation.

At the inner wall and outer equatorial location, gas is injected through many holes in the pipes.

In all cases, the length of the pipes from the piezoelectric valves to the injection point is about 7 m. This should provide a time delay in gas injection of about 5 ms for deuterium and about two/three times more for neon/argon. This delay should be acceptable in comparison to the 900 ms global particle confinement time.

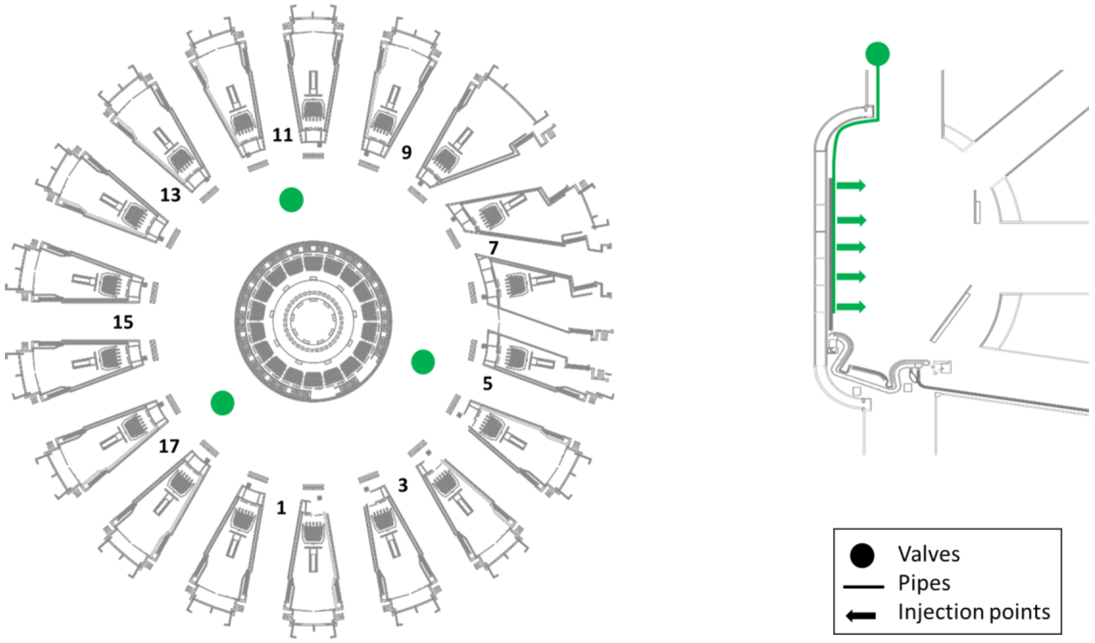

Figure G.2: Inner wall injection points

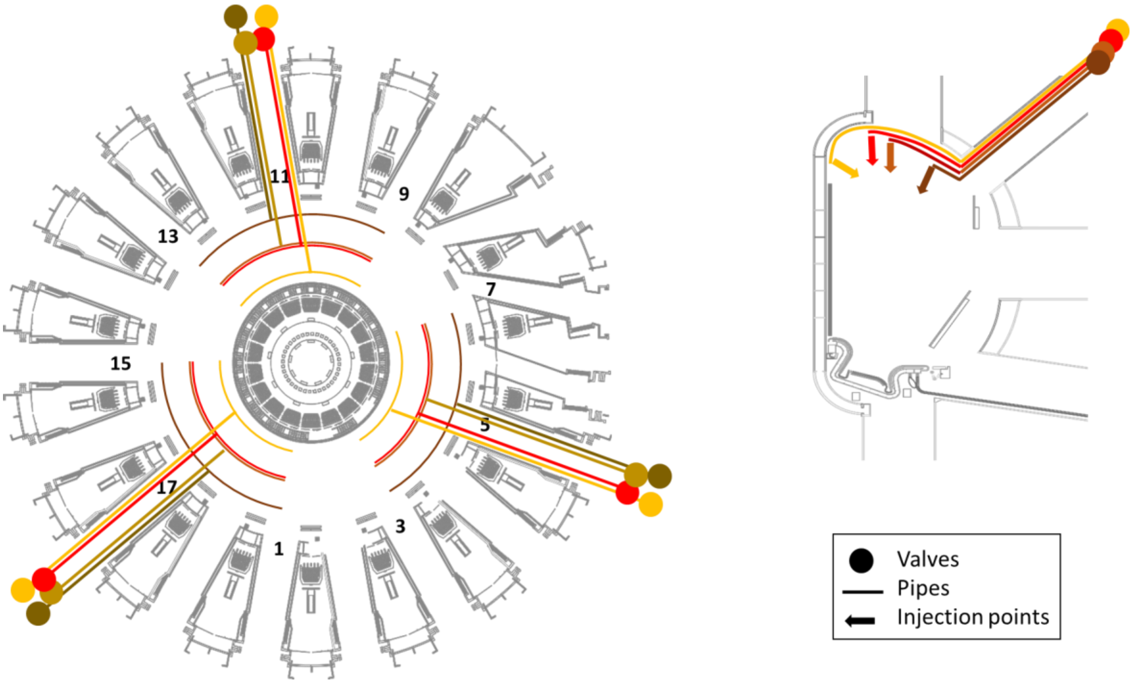

Figure G.3: Top injection points

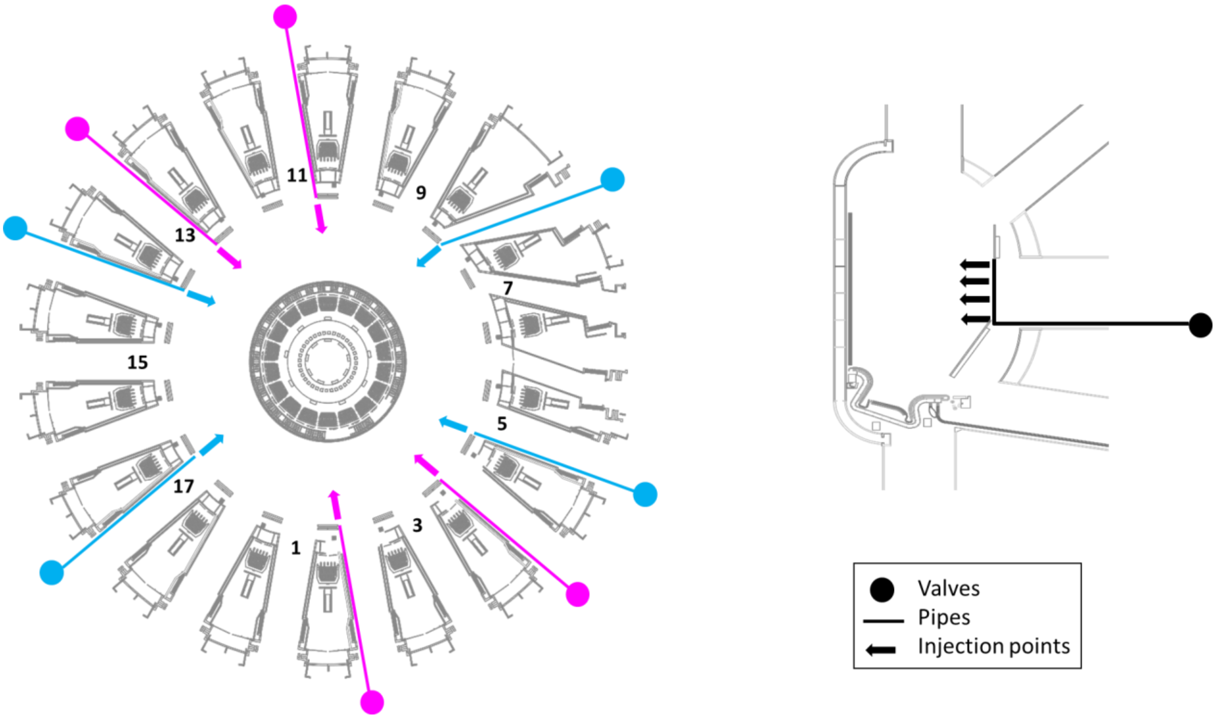

Figure G.4: Outer equatorial injection points

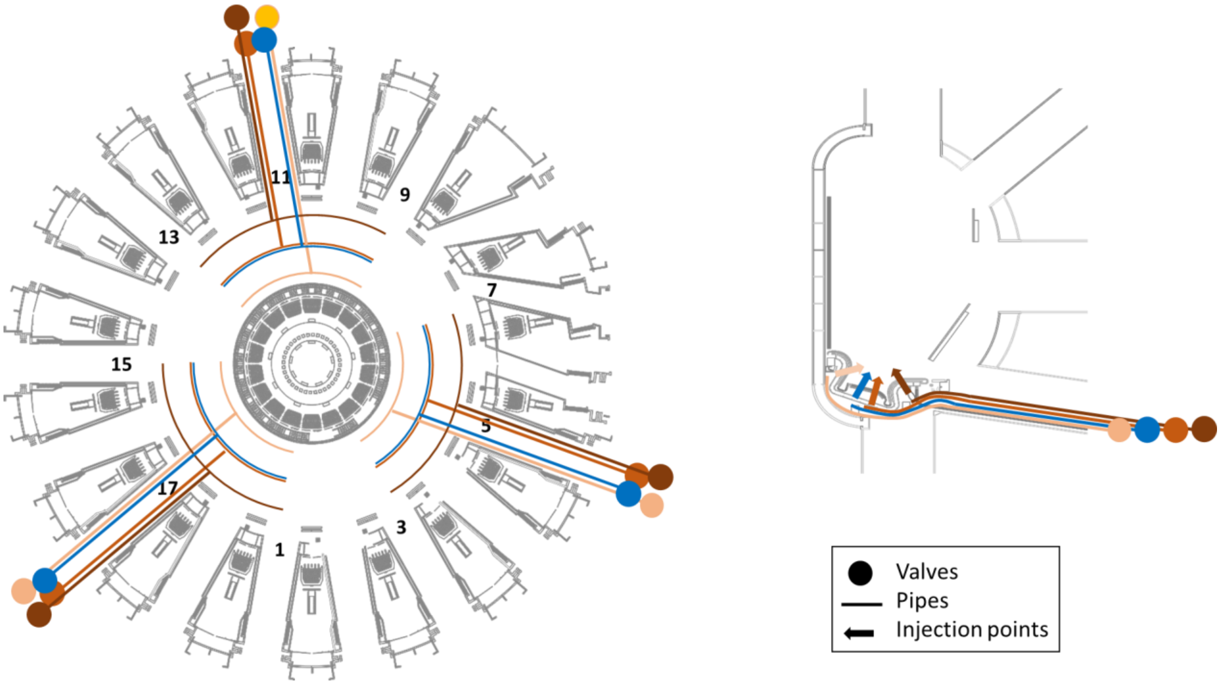

Figure G.5: Port #4 injection points

G.1.2 Glow discharge cleaning and boronization injection points

The gas injection system will provide an adequate controlled gas flow to reach the required pressure for the Glow Discharge Cleaning (GDC). The foreseen pressure range is between 0.1 to 1 Pa. Separate gas lines will be installed only for B_2H_4/B_2D_4. A stationary injection is incompatible with the piezoelectric valves (used for the fuelling); therefore, flux-meters installed in parallel to some of the piezoelectric valves are considered. In Figures G.6-G.7 the distribution of the GDC electrodes (green circle) is reported. Note that this GDC electrodes distribution is a first assumption and that it is not the final solution.

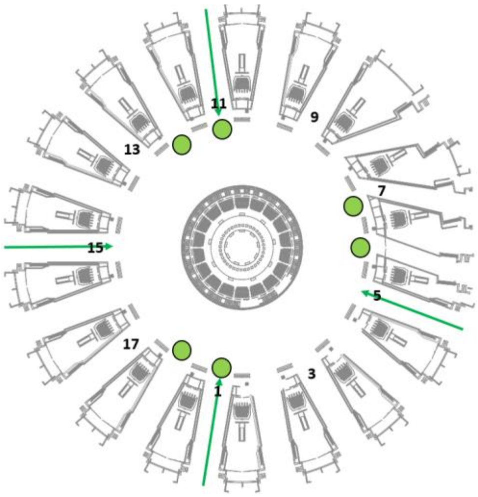

Figure G.6: Toroidal distribution of the GDC electrodes (green circle) and the injection points for the B_2H_6 (green arrows)

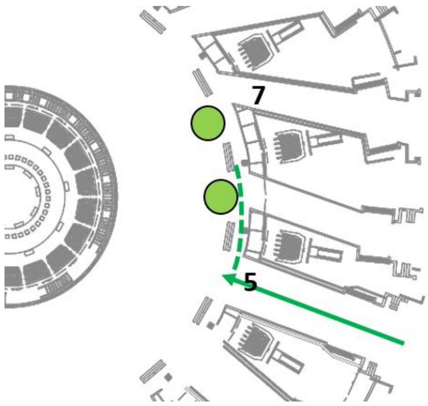

Figure G.7: Detail of a possible solution for sector 5 injection point

G.2 Divertor pumping System

In DTT ten cryopumps, connected to ten bottom vertical ports (Figure G.8), contain two cooled cryopanels each, with charcoal coating cooled to 4.5 K, and surrounded by an optically tight thermal shield system operated at 80 K. The cryopump system will provide a pumping speed of approximately 100 m^3/s at the divertor entrance. The maximum amount of trapped hydrogen will allow a full day operation with regeneration performed during the night.

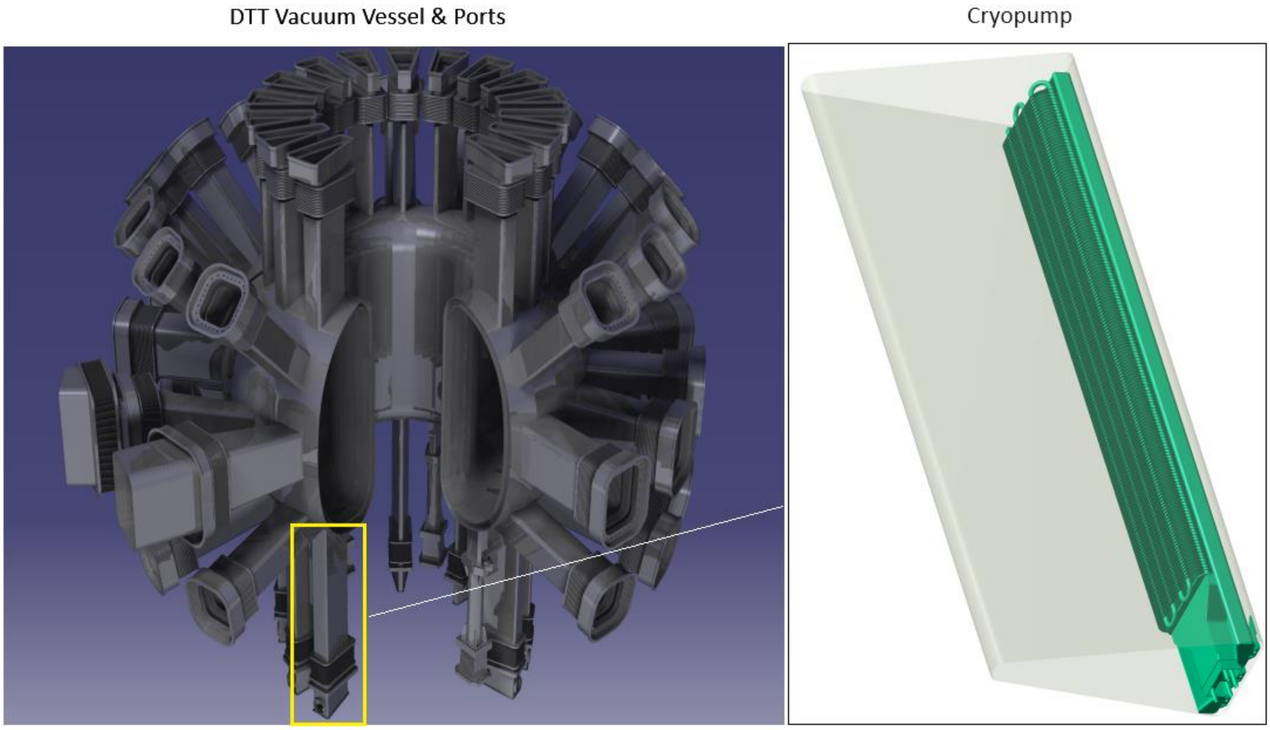

Figure G.8: Vacuum vessel and cryopumps

APPENDIX H: Numerical codes

The following numerical codes have been used or are planned to be used for the DTT research programme:

Equilibrium	
CREATE-NL+	Finite Elements solver of the free boundary dynamic plasma equilibrium problem, i.e. the MHD time evolution of 2D axisymmetric plasmas in toroidal nuclear fusion devices, including eddy currents in the passive structures, and feedback control laws for current, position and shape control. *R. Albanese et al., Fus. Eng. Des.* ***96-97*** *(2015) 664*.
EFIT	Equilibrium code that reconstructs the current profile parameters, the plasma shape, and a current profile consistent with the MHD equilibrium constraint from external magnetic measurements, based on a Picard iteration approach which approximately conserves the measurements. *L.L. Lao et al., Nuclear Fusion* ***25*** *(1985) 1421*.
HELENA	2D equilibrium code with given plasma boundary of arbitrary shape. Also calculated are the infinite-n ballooning stability and the ideal and resistive Mercier criterion. *G.T.A. Huysmans et al., CP90 Conf. on Comp. Physics, Word Sci. 1991, p.371.*
CHEASE	Accurate fixed boundary 2-D magnetic reconstruction code for MHD studies. It solves Grad-Shafranov equation in axi-symmetric toroidal geometry for thermal (one-temperature) plasma. Computes bootstrap fraction, ballooning stability, ideal interchange (Mercier) and resistive interchange stability. *H. Lutjens et al., Comput. Phys. Commun.* ***97****, 219 (1996)*
SPIDER	Numerical simulation of the tokamak plasma equilibrium with toroidal rotation and pressure anisotropy. *A.A. Ivanov, A.A. Martynov, S.Yu. Medvedev and Yu.Yu. Poshekhonov, 2012, https://api.semanticscholar.org/CorpusID:94369725*
Transport and turbulence	
QUALIKIZ	Quasilinear model based on the linear gyrokinetic code KINEZERO, which calculates the linear growth rates of unstable modes to characterise the microturbulence. It accounts for all unstable modes and sums up the contributions over a wave-number spectrum. *C. Bourdelle et al., Phys. Plasmas* ***14****, 112501 (2007)*
TGLF	The trapped gyro-Landau-fluid model solves for the linear eigenmodes of trapped ion and electron modes (TIM, TEM), ion and electron temperature gradient (ITG, ETG) modes and electromagnetic kinetic ballooning (KB) modes, with an improved description of the trapped particle response [*G. M. Staebler et al Phys. Plasmas, 14, 055909 (2007)*]. For the quasi-linear computation of the fluxes, the model is applied with the recent saturation rule 2 (TGLF-SAT2) [*G.M. Staebler et al Nuclear Fusion* ***61****, 116007 (2021)*].
GENE	Gyrokinetic Vlasov code. It solves the nonlinear gyrokinetic equations on a fixed grid in five-dimensional phase space (plus time). *T. Görler et al., J. Comp. Phys.* ***230****, 7053 (2011)*
NEO	Eulerian multi-species solver of the drift-kinetic Fokker-Planck Poisson system of equations for accurate neoclassical transport calculations [E.A. *Belli and J. Candy* Plasma Phys. Control. Fusion*, 50:095010, 2008; E.A. Belli and J. Candy,* Plasma Phys. Control. Fusion*, 51:075018, 2009; E.A. Belli and J. Candy.* Plasma Phys. Control. Fusion*,* ***54*** *015015, 2012*].
NCLASS	The NCLASS code calculates the neoclassical transport properties of a multi-species axisymmetric plasma of arbitrary aspect ratio, geometry and collisionality. It is designed to be called from a transport code that provides the plasma density and temperature profiles as well as a number of flux surface averaged geometric quantities. *W.A. Houlberg et al 1997 Phys. Plasmas* ***4*** *3230*
FACIT	The fast and accurate collisional impurity transport (FACIT) module allows calculations of impurity transport. It takes the kinetic profiles, the main ion and impurity charges and masses, and the magnetic equilibrium as inputs, and outputs the collisional transport coefficients and fluxes as well as the variables that characterize the poloidal distribution of the impurity density. *D. Fajardo et al 2022 Plasma Phys. Control. Fusion* ***64*** *055017*
MHD	
MISHKA	Ideal, incompressible MHD stability analysis of axisymmetric tokamak equilibria. The full spectrum of MHD waves (TAE modes etc.) can also be calculated, including modes driven by an external antenna. Toroidal mode numbers n=1-50 can be calculated. *A.B. Mikhailovskii et al., Plasma Phys. Rep.* ***23****, 844 (1997)*

CASTOR	Linear, resistive MHD stability analysis of axisymmetric tokamak equilibria. The full spectrum of MHD waves (TAE modes etc.) can also be calculated, including modes driven by an external antenna. Toroidal mode numbers n=1-20 can be calculated. *W. Kerner et al., J. Comp. Phys.,* ***142****, 271 (1998)*
XTOR	3D nonlinear MHD code. Includes resistive MHD effects, anisotropic thermal transport, some neoclassical effects. *H. Lütjens, J.F. Luciani, J. Comp. Phys.* ***227****, 6944 (2008)*
CARMA	Studies RWM by self-consistent coupling between MARS-F (single fluid MHD code, including the effects of plasma rotation and using various damping models to approximate the ion Landau damping) and CARIDDI (a 3D time-domain eddy currents code). *F. Villone et al., in 34th EPS Conf. on Control. Fusion and Plasma Phys., ECA Vol.* ***31F****, P5.125 (2007).*
CarMa0NL	Evolutionary equilibrium code, self-consistently coupling an axisymmetric plasma, described through Grad-Shafranov equation, with three-dimensional surrounding conducting structures, described by a volumetric integral formulation of magneto-quasi-static Maxwell equations. It allows the calculation of 3D eddy and halo currents during disruptions and the computation of related electromagnetic forces. It provides also the computation of linearized plasma response models including 3D effects, for control-related analyses. *F. Villone et al., Plasma Phys. Control. Fusion* ***55*** *(2013) 095008*
JALPHA	JALPHA is an IMAS workflow. It allows computing the ideal MHD stability diagram of an equilibrium with respect to the maximum normalized edge pressure gradient α_{max} and the normalized edge current density. It uses the HELENA equilibrium solver and the ILSA ideal linear MHD solver. *G. Falchetto et al., Nucl. Fusion* ***54*** *(2014) 043018*
JOREK	3D nonlinear extended-MHD code in realistic geometry. Includes models for free-boundary evolution with resistive wall effects, poloidal field and/or 3D coils, halo currents, massive gas injection, shattered pellet injection, runaway electrons, etc. *M. Hoelzl et al., Nucl. Fusion* ***61*** *065001 (2021)*
MARS	Full, resistive, linear MHD code in general curvilinear geometry. It can include a vacuum region described by a conformal ideally conducting wall. It is IMAS compliant. *Bondeson A., Vlad G. and Lütjens H. 1992 IAEA Technical Committee Meeting on Advances in Simulations and Modelling of Thermonuclear Plasmas (15-18 June 1992) (Montreal (Canada)) (Vienna, Austria: International Atomic Energy Agency) p 306*
MARS-F/K/Q	The MARS-* series of codes include MARS-F [1], MARS-K [2] and MARS-Q [3] so far. These are various extensions to the MARS code that solves the single fluid, ideal or resistive MHD equations with toroidal flow. MARS-F includes the capability of feedback control of an MHD instability (e.g. the RWM, plasma response). MARS-K is a MHD-drift kinetic hybrid implementation. MARS-Q is a quasi-linear expansion. *[1] Y.Q. Liu et al. Phys. Plasmas* ***7*** *(2000) 3681* *[2] Y.Q. Liu et al. Phys. Plasmas* ***15*** *(2008) 112503* *[3] Y.Q. Liu et al. Phys. Plasmas* ***20*** *(2013) 042503*
EQSTABIL Workflow	The EQSTABIL workflow is a Kepler workflow aimed at performing linear MHD stability analysis of tokamak plasma equilibria for a single or multiple toroidal mode numbers when executed. The high-resolution equilibrium actors consider axisymmetric toroidal static plasmas with isotropic pressure and the linear MHD stability models stem from single fluid ideal/resistive MHD with compressibility. It has been constructed specifically around the IMAS database. *Coelho R. et al., 42nd EPS Conference on Plasma Physics (2015) P4.178*
Europed	The Europed code for pedestal predictions implements the EPED1 model (which uses the peeling-ballooning stability as MHD constraint and the kinetic ballooning mode assumption for the transport constraint). The code employs HELENA for the equilibrium and can use several different models and codes for the bootstrap current. The standard version can use either MISKHA or ELITE for the pedestal ideal MHD stability. Implementation of CASTOR for the use of resistive MHD is currently on-going. *S. Saarelma et al., Plasma Phys. Control. Fusion* ***60*** *(2018) 014042*
GPEC	The Generalized Perturbed Equilibrium Code (GPEC) is a toroidal ideal MHD code. Its suite includes non-axisymmetric stability and perturbed equilibrium codes, such as DCON / RDCON / STRIDE (stability), GPEC per se (driven plasma response), and PENTRC (NTV torque). *J.-K. Park et al., Phys. Plasmas,* ***16*** *(2009) 056115*

Energetic particles	
HYMAGYC	Hybrid MHD-Gyrokinetic code (resistive, linear full MHD in curvilinear geometry; $k_\perp\varrho_H \sim O(1)$ Gyrokinetic equation for Energetic Particles). It is partly IMAS compliant. *G. Vlad et al., 11th IAEA TM on Energetic Particles in Magnetic Confinement Systems, P–25, 2009. G. Fogaccia et al., 2016 Nucl. Fusion **56** 112004.*
FALCON	Semi-analytical tool to study various aspects of linear physics of the Energetic Particles. *Falessi M.V., Carlevaro N., Fusco V., Vlad G. and Zonca, F. 2019 Phys. Plasmas **26** 082502*
EQUIPE	Equilibrium post processing. *Falessi M V, Carlevaro N, Fusco V, Giovannozzi E, Lauber P, Vlad G and Zonca F 2020 J. Plasma Phys. **86** 845860501*
DAEPS	Drift Alfvén Energetic Particle Stability code. *Li Y, Hu S, Zheng W and Xiao Y 2020 Phys. Plasmas **27** 062505*
HMGC	Hybrid MHD-Gyrokinetic code (visco-resistive, non-linear reduced $O(\varepsilon^3)$ MHD; $k_\perp\varrho_H \ll 1$ Gyrokinetic equation (guiding center limit) for Energetic Particles). *Briguglio S., Vlad G., Zonca F. and Kar C. 1995 Phys. Plasmas **2** 3711. Briguglio S., Zonca F. and Vlad G. 1998 Phys. Plasmas **5** 3287*
Hamiltonian mapping	Analysis tool for detailed studies of energetic particle nonlinear dynamics (to be used with, e.g., HMGC and HYMAGYC outputs). *Briguglio S, et al. 2014 Phys. Plasmas, **21** 112301*
ORBIT	Hamiltonian test particle, guiding center code, with Montecarlo collision operator. *R.B. White and M.S. Chance, Phys. Fluids **27**, 2455 (1984)*
LIGKA	Linear MHD gyro-kinetic code in realistic tokamak geometry, self-consistently treating general energetic particle distribution functions. It can be used to calculate stability boundaries of Alfvénic modes. *Ph. Lauber et al., J. Comp. Phys. **2268**, 447 (2007)*
HAGIS	Nonlinear wave-particle interaction guiding centre code. *S.D. Pinches, CPC **111**, 131 (1998)*
Integrated Workflow for Energetic Particle Stability (IMAS)	Automated time-dependent workflow for energetic particles stability analysis within the Integrated Modelling & Analysis Suite (IMAS) (Python-based), Not available at present, but ENEA-Frascati participate actively in the ENR project that developed this tool. *V.-A. Popa et al 2023 Nucl. Fusion **63** 126008*
ATEP	Phase space zonal structure transport code. *Lauber, Meng NF 2024 (submitted)*
ASCOT	Guiding-centre orbit following Monte Carlo code for studies of charged particle behaviour in realistic 3-D tokamak geometry. *E. Hirvijoki et al. 2014, Comput. Phys. Commun. **185** 1310–21*
Divertor, SOL and PWI	
EIRENE	The three-dimensional EIRENE neutral gas Monte Carlo solves the full 3D Boltzmann transport equations for the neutral distribution function. The collision term includes also neutral-neutral collisions, in addition to the atomic physics data, surface reflection data are provided by Monte-Carlo codes like TRIM. *D. Reiter et al. Fus. Sci. Technology **47** 172 (2005)* *TRIM - W. Eckstein, Computer simulation of ion–solid interactions. In Springer Series in Materials Science, Vol. 10. Springer, Berlin, (1991).*
EDGE2D	Solves a set of fluid equations describing the edge plasma, coupled to a kinetic (Monte Carlo) description of the neutrals on a 2D grid for the divertor, SOL and a small annulus of the main plasma (on closed flux surfaces). *D. Reiter, J. Nucl. Mat. **196**, 241 (1992)*
SOLPS	This solves a set of fluid equations describing the edge plasma, coupled to either a fluid or kinetic (Monte Carlo) description of neutrals on a 2D grid for the divertor, SOL and a small annulus of the main plasma (on closed flux surfaces). *R. Schneider et al., Contrib. Plasma Phys. **46**, 3 (2006)*
SOLEDGE2	This solves a set of fluid equations describing the edge plasma, coupled to either a fluid or kinetic (Monte Carlo) description of neutrals on a 2D grid for the divertor, SOL and a small annulus of the main plasma (on closed flux surfaces). The grid covers the entire SOL surface up to the wall/divertor. *H. Bufferand et al., Nucl. Mat. Energy **12**, 852 (2017)*
SOLEDGE3X	The code implements a fluid description of the edge plasma based on the drift-fluid approximation. Braginskii like equations can be solved either in 2D or in 3D. The 2D simulations can be used for two different purposes: firstly, the code can be used as a transport code in this case, a 2D symmetry is assumed. The code can also be used in 3D. It can then be used for two purposed: as a 3D transport code, for instance including non-symmetric wall elements like

	antenna limiters or as a 3D turbulence code or as a 3D turbulent code. *H. Bufferand et al., Nucl. Fusion **61** 116052 (2021)*
EMC3	The EMC3 code solves a set of Braginskii like equations in a 3D space with a Monte Carlo technique. The code is coupled to IRENE for a kinetic (Monte Carlo) description of the neutrals. *Y. Feng, et al., Contrib. to Plasma Physics **44** 57 (2004).*
BIT1	Particle-in-cell Monte Carlo code. Multiple-ion, multiple-neutral scrape-off layer transport code, taking account of plasma-wall interactions. Includes some elements of plasma-surface interactions: secondary electron collisions, and neutral recycling. *D. Tskhakaya and S. Kuhn, J. Nucl. Mat. **313-316**, 1119 (2003)*
DIVIMP	DIVIMP (divertor impurity) is an extension of the LIM (limiter impurity) Monte Carlo code. It follows the ions impurity in a 2-D (poloidal plane) orthogonal mesh. Ions production mechanism, e.g., physical sputtering, angular and velocity distributions of sputtered particles are specified, as well as yields and also the cross-field diffusion coefficient. The sputtered neutrals are followed in a Monte Carlo way until ionization. The ions are then followed in their cross-field and parallel to B motion allowing ionization to higher stages and recombination; finite rate of temperature relaxation to the local plasma values; parallel diffusive collisions; (d) the various forces acting on the parallel motion including friction, electrostatic force, and gradients. The particles are followed until they reach a solid surface, the plates or walls. Patterns are calculated. Self-consistent self-sputtering. *P.C. Stangeby and J.D. Elder , J. Nucl. Mat. **196-198** 258 (1992)*
ERO2.0	Monte-Carlo code for modelling plasma-wall interaction and 3D plasma impurity transport. It described the PFCs erosion by physical and chemical sputtering due to the plasma background ions. Like DIVIMP it follow in the 3D the trajectory of the released particles leaving the PFCs initially as neutrals and then as ions in different ionization stages due ionization through collisions with the plasma background. *J. Romazanov et al Phys. Scr. **2017** 014018 (2017)*
SMITER	SMITER code package (SMARDDA for ITER) is a graphical user interface (GUI) framework for power deposition mapping on tokamak plasma-facing components (PFC) in the full 3-D CAD geometry of the machine, taking as input a user-defined specification for parallel heat flux in the scrape-off layer (SOL) and a description of the equilibrium magnetic flux. *L. Kos et al. Fus. Eng. Design **146** 1796 (2019)*
DIVGAS	3D Solver of the Boltzmann equation to describe collisional neutral gas dynamics (Direct Simulation Monte Carlo method) and derive maps of macroscopic properties (such as flows, pressure, density, temperature, bulk velocity) in the sub-divertor and pumping area, with self-consistent description of transport properties and gas mixtures. *S. Varoutis et al., Fusion Engineering Design **121**, 13 (2017)*
Integrated operation scenarios	
ASTRA	The Automated System for Transport Analysis in a tokamak is a numerical platform which allows the development of predictive and interpretive transport modelling workflows through the solution of particle, heat and momentum equations in combination with current diffusion and free-boundary equilibrium solvers [*G.V. Pereverzev and P.N. Yushmanov, IPP-Report, IPP 5/98, February, 2002. E. Fable et al Plasma Phys. Control. Fusion **55** 124028 2013*]. It is coupled with turbulent transport models like TGLF and QuaLiKiz, as well as with the impurity transport codes STRAHL [*R. Dux et al. IPP report 10/30 (2006)*]. DTT predictions have been also obtained with the Integrated Modelling based on Engineering Parameters (IMEP) workflow, which adopts pedestal stability calculations with the MISHKA MHD code
JETTO	Solution of a set of transport equations consistent with models for sources, together with the Grad-Shafranov equation in general tokamak-related toroidal geometry. Set of 6 transport equations: poloidal flux, electron and ion temperature, ion density and toroidal rotation. It is linked with 1D core impurity transport code SANCO. *G. Cenacchi and A. Taroni, ENEA, ISSN/0393-6633, 1988*
JINTRAC	JINTRAC is a system of 25 interfaced Tokamak-physics codes for the integrated simulation of all phases of a tokamak plasma discharge. In particular, it is based on the combination of the JETTO transport code with the impurity transport code SANCO, coupled to the edge code EDGE2D / EIRENE. It includes the coupling with theoretical transport models like TGLF and QuaLiKiz. *M. Romanelli et al Plasma Fusion Research **9**, 3403023 (2014)*
METIS	0.5 D code, computing the time evolution of global plasma quantities for given waveforms of control parameters in a discharge with short CPU time. It solves current diffusion equation with

	an approximate equilibrium evolution, simplified treatment of sources and of spatial dependences. Stationary transport equations are solved on discrete time slices. *J.F. Artaud et al., Nucl. Fusion* ***58****, 105001 (2018)*
Heating and CD	
BBNBI	Monte Carlo code for simulating NBI ionization in magnetically confined plasmas. It uses a beamlet-by-beamlet representation of the injected beam and takes into account all the ionization processes in the plasma. *O. Asunta et al. 2015 Comput. Phys. Commun. 188 33–46*
GRAY	Quasi-optical propagation of a Gaussian beam of electron cyclotron waves in a general tokamak equilibrium, taking account of diffraction effects. It includes the full relativistic dielectric tensor and linear CD calculation. *D. Farina et al., Fus. Sci. Techn.* ***52****, 154 (2007)*
PION	A time dependent code that calculates the ICRH power deposition and the velocity distribution function(s) of the resonating ions. *L-G Eriksson et al., Nucl. Fusion* ***33*** *(1993) 1037*
TORIC	2D wave propagation and absorption code developed for the RF range. *[M. Brambilla, Plasma Phys. Contr. Fusion* ***41****, 1 (1999)]*
FELICE	1D antenna coupling code computing the coupling of an ICRH antenna to a hot plasma *[M. Brambilla, 1992 IPP Report 5/45]*
TOMCAT	1D wave equation solver accounting for up to 3rd harmonic heating *[D. Van Eester & R. Koch, Plasma Phys. Control. Fusion* ***40****, 1949 (1998)]*
SSQLFP	2D bounce averaged Fokker-Planck code *[M. Brambilla, Nucl. Fusion* ***34****, 1121 (1994)]*
TOPICA	3D antenna coupling code allowing to study the coupling of realistic ICRH antennas *[V. Lancelotti et al., Nucl. Fusion* ***46****, S476 (2006)]*
HFSS (Ansys)	3D antenna coupling code allowing for a plasma in front of a realistic antenna *[V. BOBKOV et al., AIP Conference Proc. AIP Press Melville NY 933 (2007) 83]*
CST	Commercial package for solving Maxwell's equations for realistic antennae *[CST GmbH, CST Microwave Studio User Manual (2009), http://www.cst.com]*
DISEMAG	Full hot plasma dispersion equation solver *[Cardinali A et al., Nucl. Fusion* ***42****, 427 (2002)]*

APPENDIX I: Synoptic table of DTT research programme headlines

A collection of the research programme topical headlines listed at the end of Chapters 2-9 is presented in Table I.1:

Table I.1. DTT programme headlines. Expected relevance to ITER and/or DEMO is indicated by a *. Lower to higher programmatic priorities are indicated by + to +++. Years are tentative.

Headline number	Chapter / Topic	Headline contents	Priority	ITER	DEMO
Construction Phase 2022-2029					
C.2.1	**2/ Scenarios**	Definition of the central solenoid desired capabilities	+++		
C.2.2	**2/ Scenarios**	Carry out integrated modelling of scenarios alternative to baseline H-mode	++	*	*
C.3.1	**3/ Divertor, SOL, PWI**	Definition of first wall shape and parameters	+++		
C.3.2	**3/ Divertor, SOL, PWI**	Definition of markers types and position in FW	++		
C.3.3	**3/ Divertor, SOL, PWI**	Definition of optimal diagnostics requirements for PEX/PWI analysis	++	*	*
C.4.1	**4/ Transport**	Additional integrated modelling of baseline and alternative scenarios, assessment of MHD stability and Energetic Particles (EP) properties.	+++		
C.4.2	**4/ Transport**	Diagnostics for plasma operation, essential profiles measurements (temperatures, densities, rotation), bolometry, SXR spectroscopy	+++		
C.5.1	**5/ MHD**	Preparatory modelling of the main DTT scenarios focused in particular on basic MHD stability (ideal/resistive low-n modes and high-n peeling-ballooning modes) and NTM avoidance and control	++		
C.5.2	**5/ MHD**	Error field modelling including plasma response in order to provide accuracy criteria for machine assembly	++	*	
C.6.1	**6/ H&CD, fuelling**	Assessment of ECRH, ICRH, NBI, matter injection performance (modelling) in connection with respective high priority tasks	+++	*	*
C.6.2	**6/ H&CD, fuelling**	Assessment of interfaces with diagnostics and control system	++	*	*
C.7.1	**7/ EP physics**	Verification of linear stability of EP driven modes on available scenarios with NNBI and ICRH using global gyrokinetic codes	++	*	*
C.7.2	**7/ EP physics**	Nonlinear simulations of EP driven modes on available scenarios with NNBI and ICRH using global gyrokinetic codes	++	*	*
C.7.3	**7/ EP physics**	Numerical study of the EP distribution function in phase space (NNBI, ICRH, NNBI & ICRH)	++	*	
C.7.4	**7/ EP physics**	Numerical study of EP test particle losses induced by magnetic field ripple and in presence of global Alfvén eigenmodes.	++	*	*
C.7.5	**7/ EP physics**	Set up IMAS infrastructure and dedicated workflows for EP physics	+++		
C.8.1	**8/ Theory & simulation**	Verification of Phase 1 scenarios and extended/kinetic MHD modelling with high fidelity theory-based tools. Predict and prepare Phase 1 Experimental programme.	++	*	*
C.8.2	**8/ Theory & simulation**	Set up IMAS infrastructure and workflows, e.g. ATEP code	+++		
C.9.1	**9/ Fusion technology**	Develop and utilize modelling tools for advanced materials under cyclic load conditions, in order to identify sets of materials and conditions for testing	++	*	*
C.9.2	**9/ Fusion technology**	Develop, design and integrate a specific set of observation systems (IR, UV-VIS spectroscopy, thermocouples etc.) for the DTM and FW module in the portfolio of DTT diagnostics	+++	*	*
C.9.3	**9/ Fusion technology**	Prepare an initial set of components reflecting the first divertor material selection for DTT divertor	+++	*	*
C.9.4	**9/ Fusion technology**	Establish and integrate the specific test environment for material and components testing in DTT (DTM, FW module)	+++	*	*
C.9.5	**9/ Fusion technology**	Establish and integrate a specific test environment and infrastructure in DTT for fuelling and pumping tests	+++	*	*

Phase 1 2029-2034					
1.2.1	**2/ Scenarios**	Development of baseline L-mode and H-mode scenarios A, B, C in SN or XD divertor configuration	+++	*	*
1.2.2	**2/ Scenarios**	Development of Negative Triangularity scenarios	+++		*
1.2.3	**2/ Scenarios**	Development of Hybrid scenarios at half power	++	*	*
1.2.4	**2/ Scenarios**	Development of high β_N AT scenarios at half field, half power	++	*	*
1.2.5	**2/ Scenarios**	First studies of small/no ELMs regimes	++	*	*
1.3.1	**3/ Divertor, SOL, PWI**	Developments and characterization study of plasma start-up and ramp-up scenarios with boronization	+++	*	
1.3.2	**3/ Divertor, SOL, PWI**	Developments and characterization of plasma start-up and ramp up scenario without boronization	+	*	*
1.3.3	**3/ Divertor, SOL, PWI**	Development and characterization of strike point sweeping method	+++	*	*
1.3.4	**3/ Divertor, SOL, PWI**	Development and characterization of SN detached configuration in L-mode	+	*	
1.3.5	**3/ Divertor, SOL, PWI**	Development and characterization of SN detached configuration in H-mode	+++	*	*
1.3.6	**3/ Divertor, SOL, PWI**	Development and characterization of XD divertor configuration	+++		*
1.3.7	**3/ Divertor, SOL, PWI**	Development and characterization of NT divertor configuration	+++		*
1.3.8	**3/ Divertor, SOL, PWI**	Optimization and characterization of boronization	++	*	
1.3.9	**3/ Divertor, SOL, PWI**	Quantification and characterization of D retention in clean W	+++	*	*
1.3.10	**3/ Divertor, SOL, PWI**	Quantification of the impact of boronization on D retention	++	*	
1.4.1	**4/ Transport**	Ohmic and L-mode transport properties at half field and half current (Scen. A,B), and full field full current (C)	+++	*	*
1.4.2	**4/ Transport**	H-mode access at half (A,B) and full field (C) with P_{ext}<20 MW and dominant electron heating	+++		
1.4.3	**4/ Transport**	First studies of effects of impurity seeding on confinement for edge-core integrated scenarios (B, C)	+++	*	*
1.4.4	**4/ Transport**	Characterize transport in edge and core in different scenarios, compare full and half field	+++	*	*
1.4.5	**4/ Transport**	Transport properties in presence of 3D ELM control, in no ELM regimes and in negative triangularity plasmas	+++	*	*
1.5.1	**5/ MHD**	Development of error field correction	+++	*	*
1.5.2	**5/ MHD**	NTM control studies (exploiting high β_N scenarios at reduced I_p and B_t)	++	*	*
1.5.3	**5/ MHD**	Development of disruption prevention and avoidance (continuing in later phases)	++	*	*
1.5.4	**5/ MHD**	RE studies (in particular, RE impacts on the wall / sacrificial limiters and, as soon as the SPI system is available, RE beam mitigation by H2 or D2 SPI) (continuing in later phases)	+++	*	*
1.6.1	**6/ H&CD, fuelling**	ECRH and ICRH initial system commissioning, asynchronous and with plasma, including optimization of coupling	+++	*	*
1.6.2	**6/ H&CD, fuelling**	ECRH and ICRH commissioning of functionalities supporting basic machine operations: wall cleaning, assisted start-up, current ramp-up and ramp-down at half and full magnetic field	+++	*	*
1.6.3	**6/ H&CD, fuelling**	ECRH and ICRH basic control functionalities: sawteeth, NTMs, impurities, density and ELM pacing at half and full magnetic field	+++	*	*
1.6.4	**6/ H&CD, fuelling**	Access to H-mode Baseline and Hybrid scenarios	++		
1.7.1	**7/ EP physics**	Optimization of experimental scenarios to observe EP driven modes on Phase 1 scenarios	++	*	*
1.7.2	**7/ EP physics**	Validation of linear and nonlinear EP dynamics simulation on Phase1 experiments.	++	*	*
1.7.3	**7/ EP physics**	Validation of EP distribution function experimental reconstruction on Phase1 experiments.	++	*	*
1.7.4	**7/ EP physics**	Validation of EP test particle losses simulations with experimental observations.	++	*	*

1.8.1	**8/ Theory & simulation**	Verification of Phase 1 scenarios and extended/kinetic MHD modelling with high fidelity theory-based tools. Predict and prepare Phase 2 Experimental programme.	++	*	*
1.8.2	**8/ Theory & simulation**	Validation of IMAS workflows under Low EP (ICRH) Pressures and Currents and scenario optimization	++		
1.9.1	**9/ Fusion technology**	Commission DTM and associated diagnostics. DTM equipped with standard DTT divertor materials for reference	+++	*	*
1.9.2	**9/ Fusion technology**	Integrated PFC and material testing (different sets) using the DTM at basic power and particle fluxes	+++		*
1.9.3	**9/ Fusion technology**	Assess performance of the first set of advanced materials and components in DTM. Comparison with DTT standard divertor materials and components.	+++	*	*
1.9.4	**9/ Fusion technology**	Calibrate thermohydraulic models of actively cooled PFCs	+++		*
1.9.5	**9/ Fusion technology**	Commissioning of fuelling and pumping test components	+++		*
1.9.6	**9/ Fusion technology**	Validate the launching performance of the DEMO pellet injection system	+++		*
1.9.7	**9/ Fusion technology**	Validate the performance of a test metal foil pump in a representative tokamak environment	+++		*
1.9.8	**9/ Fusion technology**	Extract the gas supply requirements for stable control of the DEMO SN divertor	+++		*
1.9.9	**9/ Fusion technology**	Provide parametric variation of divertor pressure (pumping speed, fuelling rate) with corresponding plasma simulation cases to benchmark particle exhaust conditions with the DIVGAS code	++	*	*
Phase 2 2034-2038					
2.2.1	**2/ Scenarios**	Improvement of all phase 1 scenarios at higher power	+++	*	*
2.2.2	**2/ Scenarios**	Development of small/no ELMs scenarios	+++	*	*
2.3.1	**3/ Divertor, SOL, PWI**	Experimental assessment of edge transport at high plasma current and comparison with λ_q scalings and theory	+++	*	*
2.3.2	**3/ Divertor, SOL, PWI**	Evaluation of transport parameters in limiter phase and in the far-SOL	+++	*	*
2.3.3	**3/ Divertor, SOL, PWI**	Optimization and characterization of detachment by impurity seeding	+++	*	*
2.3.4	**3/ Divertor, SOL, PWI**	Development and characterization of methods to control detachment	+++	*	*
2.3.5	**3/ Divertor, SOL, PWI**	Development and characterization of ELM control methods by gas-puffing, pellet RMP	++	+	
2.3.6	**3/ Divertor, SOL, PWI**	Development, control and characterization of XPR low-ELMs scenarios	++	+	*
2.3.7	**3/ Divertor, SOL, PWI**	Optimization and characterization of XD configuration with seeding	+++		*
2.3.8	**3/ Divertor, SOL, PWI**	Test new FW and divertor materials	++		*
2.4.1	**4/ Transport**	Extend all studies of Phase 1 to higher power	+++	*	*
2.4.2	**4/ Transport**	Characterize transport in high beta hybrid / advanced scenarios at high power and half field and current	+++	*	*
2.5.1	**5/ MHD**	Development of sawtooth pacing method (especially if needed for NTM avoidance)	++(+)	*	*
2.5.2	**5/ MHD**	Development of ELM control with the NAS coils	++	*	
2.6.1	**6/ H&CD, fuelling**	NBI system commissioning (asynchronous and with plasma)	+++		
2.6.2	**6/ H&CD, fuelling**	Verification of NBI power losses (in particular duct and shine-through losses) and optimization of parameters with respect to density	+++		
2.6.3	**6/ H&CD, fuelling**	Combined use and optimization of parameters of the heating and fuelling systems for scenario access and control	+++	*	*
2.6.4	**6/ H&CD, fuelling**	Control of kinetic and impurities profiles	++	*	*
2.7.1 - 2.7.4	**7/ EP physics**	Same as 1.7.1 - 1.7.4, but on Phase 2 scenarios	++	*	*

2.8.1	**8/ Theory & simulation**	Verification of Phase 2 scenarios and extended/kinetic MHD modelling with high fidelity theory-based tools. Predict and prepare Phase 3 Experimental programme	+++	*	*
2.8.2	**8/ Theory & simulation**	Validation of IMAS workflows description of new EP transport regimes with NNBI and high current and scenario optimization	++	*	*
2.8.3	**8/ Theory & simulation**	Development of reduced models for describing DTT's full power EP transport	++	*	*
2.9.1	**9/ Fusion technology**	Integrated plasma-facing component and material testing (different sets of advanced concepts) using the DTM at elevated power and particle fluxes	+++		*
2.9.2	**9/ Fusion technology**	Assess performance of applied sets of advanced materials and components in DTM. Selection of the second divertor components solution for DTT.	++	*	*
2.9.3	**9/ Fusion technology**	Commission FW module and associated diagnostics. FW module equipped with one standard DTT first wall material for reference.	++		*
2.9.4	**9/ Fusion technology**	Characterise a FW module equipped with different plasma-facing materials made of W	++		*
2.9.5	**9/ Fusion technology**	Explore the engineering limits of DEMO relevant fuelling and pumping technology	++		*
Phase 3 2038-...					
3.2.1	**2/ Scenarios**	Optimisation of all phase 1 and 2 scenarios at full power	+++	*	*
3.2.2	**2/ Scenarios**	Optimisation of small/no ELMs scenarios at full power	+++	*	*
3.3.1	**3/ Divertor, SOL, PWI**	Optimization of detachment in SN with different seeding	+++	*	*
3.3.2	**3/ Divertor, SOL, PWI**	Optimization and characterization of XD configuration	+++		*
3.3.3	**3/ Divertor, SOL, PWI**	Optimization and characterization of NT configuration	+++		*
3.3.4	**3/ Divertor, SOL, PWI**	Comparison of SN to XD and NT configurations	++		*
3.3.5	**3/ Divertor, SOL, PWI**	Estimation of wall erosion and W migration and validation of codes	+++	*	*
3.3.6	**3/ Divertor, SOL, PWI**	Evaluation of D retention after erosion/redeposition and W surface modification	+++	*	*
3.3.7	**3/ Divertor, SOL, PWI**	Development of methods for D removal	++	*	*
3.4.1	**4/ Transport**	Extend all studies of Phase 1 and 2 to full experimental capabilities	+++	*	*
3.5.1	**5/ MHD**	Studies on disruption prediction and mitigation with SPI at full performance (prepared already in previous phases)	+++	*	
3.6.1	**6/ H&CD, fuelling**	H-mode operation at full power	+++		*
3.7.1 - 3.7.4	**7/ EP physics**	Same as Headlines 2.7.1-2.7.4, but on Phase 3 scenarios, taking full advantage of the relevance of DTT regarding burning plasma regimes.	+++	*	*
3.8.1	**8/ Theory & simulation**	Verification of Phase 3 scenarios and extended/kinetic MHD modelling with high fidelity theory-based tools. Predict and prepare Phase 3 Experimental programme	+++	*	*
3.8.2	**8/ Theory & simulation**	Validation of IMAS workflows with full power plasmas and scenario optimization	++	*	*
3.8.3	**8/ Theory & simulation**	Development of reduced models for describing DTT's EP transport	++	*	*
3.9.1	**9/ Fusion technology**	Integrated component testing and qualification in DTM at maximum power and particle fluxes and at high fluence, mimic reactor conditions.	+++		*
3.9.2	**9/ Fusion technology**	Integrated component testing and qualification in FW module at high fluence, mimic reactor conditions	++		*